COMPUTATIONS OF BUBBLE DYNAMICS WITH HEAT TRANSFER

By

S. Senthil Kumar, B.Eng., M.S.

This thesis is submitted to Dublin City University as the fulfilment of the requirement for the award of the degree of

Doctor of Philosophy

Supervisor: Dr. Yan Delauré

School of Mechanical and Manufacturing Engineering

Dublin City University

2009

DEDICATED TO

MY

PARENTS

Declaration

I hereby certify that this material, which I now submit for assessment on the programme of study leading to the award of Doctor of Philosophy, is entirely my own work and has not been taken from the work of others save and to the extent that such work has been cited and acknowledged within the text of my work.

Signed: ID Number: 55130097

Date:

ACKNOWLEDGEMENT

I would like to express my sincere gratitude to my research supervisor, **Dr. Yan Delauré**, for his generous and invaluable guidance during this course of research. I am indebted to him for the exposure and the variety showered to me in their ways of approaches to various problems. I am grateful to him for his valuable suggestions and comments during the course of my research.

I would like to thank the head of the school, **Prof. Saleem Hashmi**, for providing financial support from the school during the last year of my research period. I am also thankful to the staff of school of Mechanical and Manufacturing Engineering, **Mr. Keith Hickey, Mr. Liam Domican, and Ms. Suzanne Dockery**, for providing excellent support for completion of this study.

The computations are a part of **Science Foundation of Ireland** funded project. Support of funding agencies is gratefully acknowledged.

I would like to thank **Prof. Darina Murray** and **Mr. Brian Donelly**, the Thermodynamics group in the Trinity College Dublin (TCD), Ireland for providing experimental results for validating my simulation results.

I am very much thankful to **Mr. T. Rajendra Kumar, Mr. Premchandran, Mr. Edison Chandra Seelan and Mr. Varadharajan** for their encouragement and support in all my efforts.

The encouragement and support I received from my family and my friends, especially **S. Santhana Lakshmi, Kannan, Jegatha, N. Jeyaprakash, Krishna Kumar, Rani, Kumar, Nagarajan, Ketheesan, Bipin Kumar, and P. Sasi Kumar** is beyond words.

S. SENTHIL KUMAR

ABSTRACT

KEYWORDS: Gas-Liquid Flow, Bubble, Convective Heat Transfer, Volume-of-Fluid Method, SIMPLE Algorithm.

Gas-liquid flows with heat transfer play an important role in many natural and industrial processes such as combustion, petroleum refining. In particular, the heat transfer enhancement caused by air bubble motion is of practical interest in many industrial applications ranging from boiling solar collectors to nuclear reactors. A bubble sliding over a heated obstacle increases heat transfer by displacing liquid, particularly in the wake region behind the bubble. This, in turn, increases heat transfer from the hot surface, by continuously bringing cooler liquid into contact with the hot surface and removing hot liquid from the surface. However, despite its industrial relevance, many important hydrodynamics and heat transfer phenomena associated with bubble flow, such as bubble formation, bubble coalescence, bubble breakup and bubble wake effect on heat transfer are still poorly understood.

The primary objective of this research is to develop a numerical tool to simulate multi-fluid flow problems and assess its suitability to study the enhancement effect of an ellipsoidal air bubble on heat transfer from a heated flat plate immersed in water, and the resulting flow patterns.

The Volume-of-Fluid (VOF) method is adopted to model the multi-fluid interface dynamics, where the interface is tracked and advected by Young's Piecewise Linear Interface Construction (PLIC) Method. The mass, momentum, and energy conservation equations are solved on a fixed (Eulerian) Staggered Cartesian grid using the Finite Volume formulation of Semi-Implicit Pressure Linked Equation (SIMPLE) method along with Krylov subspace and iterative multigrid solvers. In order to consider wall adhesion effects, while simulating a sliding bubble over an obstacle, the static contact angle model is adopted.

Numerous single-and multi-fluid flow problems have been computed and the results have been compared against published experimental, analytical and computational information. For single phase fluid flow, the code has been validated with the benchmark lid driven cavity problem, and for single phase heat transfer, buoyancy driven flow of air with the Boussinesq approximation has been studied. However, convective heat transfer in water cannot be modelled using the Boussinesq approximation, so a variable thermal property model has been included and validated against published experimental results. For multi-fluid flow, the code has been validated against published experimental results of rising air bubbles of different diameters.

The problem considered is that of sliding bubbles over inclined heated and non heated flat plates. The rising and sliding bubble shapes and velocity plots are presented and discussed to study the fluid flow behavior, and to study the dependance of time-resolved surface temperature distribution on bubble dynamics are produced. In order to investigate the suitability of a two-fluid flow model when the fluid interface is in contact with a surface, simulations are carried out with three contact angles and assessments of contact angle effects on bubble dynamics and on wall surface temperature are made. The effects of plate inclination on heat transfer characteristics are also highlighted. Results are analysed and discussed in order to gain an understanding of the relationship between bubble wake interaction and heat transfer performance.

It is found that the rising velocity of an air bubble sliding along the inclined plate increases monotonously as the inclination angle increases towards the vertical and that bubbles lift off from the surface with larger plate inclination angles. It is also shown that the bubble moving through the liquid phase strongly influences the heat transfer rates occurring between the hot surface and the liquid phase. The most significant effect is enhanced convection due to an increase in fluid agitation caused by bubble motion as the bubble acts as a bluff body, displacing the liquid and disrupting the thermal boundary layer at the hot surface and significantly promoting fluid mixing.

Comparison with experimental results is made in spite of the two dimensional limitation of the computational model. This is justified by the fact that the primary objective of the study is to assess the suitability of the numerical modelling methods adopted to represent the main mechanisms affecting the dynamics behaviour of the sliding bubbles. It is observed that the predicted temperature drop is more in the computations than in the experiments. This can be explained by the fact that, in the computations, the calculations are carried out using a 2D model which cannot account for lateral mixing as the bubble slides in the boundary layer. Conduction from the third direction might be effecting the experimental observations. This brings heat from the surrounding region of the plate surface in that direction. This effect can not be considered in the 2D computational model and this is a limitation of the present model. However, it gives an insight into the underlying mechanism of mixing and vortex-shedding that are responsible for increases in the heat transfer from the surface and has qualitative agreement with the experimental results. It is worth mentioning here that it is difficult to gain a good insight into processes taking place in the thermal boundary layer and how the bubble interacts with it through experiments. Computational results, on the other hand, help to understand the mechanisms that are responsible for temperature reduction.

CONTENTS

LIST OF TABLES

LIST OF FIGURES

NOMENCALTURE

A_o	central part of the operator H
C_d	drag coefficient
C_p	specific heat capacity
d	bubble diamter
div	discrete divergence operator
D	dimensional
D	width
E	Aspect ratio
Eo	Eötvös number
f	volume fraction
F	fluid flux in x-direction
F	force exerted by fluid on bubble
$\overrightarrow{F_b}$	body force
$F_e, F_w, F_n,\ F_s$	fluid fluxes for east, west, north, south directions
$F_{lim,\ 1},\ \ F_{lim,\ 2}$	limiting f values
g	acceleration due to gravity
$\overrightarrow{g}$	acceleration vector due to gravity
G	fluid flux in y-direction
Grad	discrete gradient operator
h	grid spacing
H	height
H	non-linear operator
L	length
$L,\ W$	distances between two extreme positions of outer surface of a bubble in $x,\ y$ directions
m	gradient of f
Mo	Morton number

n	outward unit normal vector
$n_x,\ n_y$	unit normal vectors in $x,\ y$ directions
Nu	Nusselt number
p	scalar pressure
Pr	Prandtl number
Q	heat input
R	bubble radius
Ra	Rayleigh Number
S	momentum source term
S	rate of strain tensor
$S_l\ S_r,\ S_t,\ S_b$	side fractions for left, right, top, bottom surfaces
t	time
T	temperature
T_0	reference temperature
$\mathbf{u}$	velocity vector
u	velocity in x-direction
U	rise velocity of bubble
v	velocity in x-direction
V	bubble volume
$\overrightarrow{V}$	fluid velocity vector
We	Weber Number
x	direction parallel to plate surface
$x,\ y,\ z$	components in $x,\ y,\ z$ directions
y	direction perpendicular to plate surface
α	thermal diffusivity
α	inclination angle
β	coefficient of thermal expansion
Γ	cell face surface area
δ	incremental difference
Δt	timestep

$\Delta x,\ \Delta y$	mesh sizes in $x,\ y$ directions
ΔT	temperature difference $(T_h - T_c)$
ϵ	machine epsilon
θ	plate inclination angle
θ_c	contact angle
κ	thermal conductivity
κ	curvature of surface
μ	dynamic viscosity
π	number pi (3.14159...)
ρ	fluid density
$[\rho]$	difference between densities of a heavier and a lighter fluids
σ	surface tension
τ	viscous stress tensor
ν	kinemtic viscosity
ϕ	level-set (distance) function
Ω_{u_i}	Cell volume
∇	vector differential operator
$\nabla.$	divergence operator

Subscripts

b	bubble
c	cold wall
c_r	critical value
d	drag
d	downstream
$e,\ w,\ n,\ s$	east, west, north, south directions
eq	equivalent
g	gas
h	hot wall
$i,\ j$	coordinates in $x,\ y$ directions

$i,\ j$	grid locations in $x,\ y$ directions
l	cell face centre
l	liquid
$l,\ r,\ t,\ b$	left, right, top, bottom surfaces of a control volume
lim	limiting value
max	maximum
p	pressure cell
p	present
t	tangential
T	terminal value
u	upstream
u_i	momentum cell
w	wall
0	reference
$1,\ 2$	first and second critical values
∞	freestream value

Superscripts

n	time indice
$*$	guess or predictor value
$\sim$(tilda)	filtered (smoothed) values
-1	reciprocal value
0	initial

CHAPTER 1

LITERATURE REVIEW

1.1 Background

Bubbly flows occur widely in both nature and industrial applications including energy production (e.g. oil transportation, steam generators, cooling systems) and chemical engineering (e.g. bubbly columns, mixing in reactors). Their significant practical importance has motivated numerous investigations during the last decades. However, despite this continuous effort, important questions remain open and thus study of bubble behaviour remains an important field in fluid dynamics. The high degree of complexity is a result of the potentially large number of interfaces that separate the gas and liquid phases, which have different physical properties. This complicates theoretical and numerical approaches since each interface moves with its own velocity and may deform, breakup and merge under the action of the fluids. The key problem in bubbly flows is to understand how the two phases interact and affect the flow patterns of the multiple fluids or phases.

The presence of bubbles in a flow is known to increase the heat transfer capability of the flow. This is true when the bubble impacts and slides along the surface. Two main factors influence this enhancement: the wake generated behind the bubble and the bubble itself acting as a bluff body displacing fluid as it moves. Engineering applications where two-phase flow occurs are wide and varied and include, for example, internal combustion engines, steam generators, boiling solar collectors, and nuclear reactors. Other applications such as the cooling of electronics could benefit from the introduction of bubble induced mixing.

Boiling is an example where flows inherently contain bubbles, due to bubble formation caused by evaporation of the liquid phase at the solid-liquid interface. In boiling, the heat transfer rate is much higher than that for single phase convection. This increase in the heat transfer is not only because of phase change at the nucleation sites but also due to the contribution of the convective motion caused by bubble dynamics. Promoting boiling, therefore, is an effective and popular method of heat transfer enhancement in many applications. In view of its many industrial applications, it is of cardinal importance to understand the influence of the many parameters that govern the flow configurations, heat transfer enhancement, and its time dependance.

In many of these applications bubble nucleation and detachment occurs as a result of evaporation of the liquid phase at a hot surface. Although this evaporation results in a certain amount of latent heat transfer, both numerical and experimental studies have shown that the predominant factor responsible for the heat transfer enhancement exhibited is the induced liquid agitation caused by bubble motion. As the bubbles move through the liquid phase they act in a similar manner to bluff bodies, displacing liquid and increasing mixing levels, particularly in the wake region behind the bubble. This has the effect of increasing the heat flux from the hot surface by encouraging liquid circulation, bringing hot fluid away from the hot surface and replacing it with colder fluid capable of absorbing more heat.

Previous studies have been performed to study the effect of sliding bubbles on heat transfer enhancement using both experimental and numerical approaches, such as the work by Thorncroft and Klausner [1] and that of Yoon et al. [2], respectively. Yoon et al. [2] conclude that bubbles can significantly increase heat transfer from the surface on which they move. Their study investigating boiling on a flat surface concluded that increased fluid agitation caused by bubble motion was the predominant cause of the heat transfer enhancement experienced, responsible for up to 80% of the overall predicted enhancement of heat flux. Thorncroft and Klausner [1] observed, in an experimental investigation using sliding bubbles in a forced convection flow, that heat transfer enhancement of up to 52% can be achieved compared to that of forced convection alone.

The presence of bubbles in a flow has been shown to increase heat transfer even without phase change. An investigation performed by Cornwell et al. [3] highlights how heat transfer can be affected by bubbles. Cornwell's study was based on a shell and tube heat exchanger, which experienced boiling over some or all of its tubes. It was noticed that, with all of the tubes held at the same heat flux, the upstream tubes were in nucleate flow boiling whereas the downstream tubes did not experience boiling at all. This meant that the heat transfer coefficient of the downstream tubes had to be higher than that of the upstream tubes, in order to hold the surface temperature of the tubes low enough to prevent the onset of boiling. Cornwell explained this by suggesting that bubbles formed due to boiling processes on the upstream tubes, proceeded to slide around the downstream tubes, thus significantly increasing the heat transfer experienced in the downstream region of the heat exchanger, allowing the temperature of the tubes to remain below that required for boiling.

In the case of the sliding bubble, the interaction between the bubble and the heated surface is a major influencing factor in the heat transfer that takes place between the surface and the bubble. A number of factors influence the behaviour of the bubble at this interface; these include bubble size, surface inclination angle, surface tension, viscosities of fluids, densities of fluids and the temperature gradient between the bubble and the surface.

Only a few experimental studies have been conducted on the dynamics of sliding bubbles and the associated heat transfer mechanisms. To the author's knowledge, no numerical study has been performed to understand the physical phenomena. In this work, two-dimensional numerical simulations have been conducted to provide an improved understanding of the process. In the following, a brief review of studies available in the literature related to this subject is provided.

1.2 Literature Review

Here, the fundamental mechanisms relevant to the flow problem considered are discussed and a literature review on some of the existing experimental and numerical studies on bubble dynamics, including rising and sliding bubbles with and without heat transfer, are presented.

1.2.1 Introduction

Simulations of two-fluid flows play an important role in many natural and industrial processes. For example, droplet deposition, mould filling, sloshing of liquids in containers or tanks, immiscible oils coating on top of or in water, droplet and bubble formation and breakup, and liquid jets issuing into gaseous environments all involve two-fluid flows with distinct interfaces that may evolve with time, and all of these flows continue to be difficult to simulate accurately and efficiently. Impressive developments in the visualization of fluid structure, detailed flow field measurements, and sophisticated numerical simulations have led to significant progress in the understanding of complex single-phase flows, however, difficulties are still encountered on both the experimental and numerical fronts for two-phase flows. To fully understand the behavior of a multi-fluid system the basic micro-mechanisms encountered in isolated fluid phases as well as the interactions between multiple structures (e.g., bubbles) need to be satisfactorily characterized. A good overview of the subject may be found in Clift et al. [4].

Numerical methods for the simulation of such flows can be categorized into two broad groups: in one, the computational mesh is deformed or adjusted at the interface between the fluids; and in the other, the mesh is kept fixed and a suitable technique is employed to deduce and track the location of the interface. The first family of methods cannot easily model complex interface deformation such as those involving interface breakup or merging. This research considers the second approach for which various numerical methods have been developed, as explained below.

1.2.2 Various Interface Tracking Methods

Multi-fluid flows in which a sharp interface exists are frequently encountered in a variety of industrial processes. It has proven particularly difficult to accurately simulate these flows. This can be attributed to (1) the fact that the interface separating the fluids needs to be tracked accurately without introducing excessive computational smearing and (2) the necessity to account for surface tension in the case of (highly) curved interfaces. In the past decade a number of techniques, each with its own particular advantages and disadvantages, have been developed to simulate complex multi-fluid flow problems. These techniques are briefly reviewed in this Section.

In *Level set* methods [5] - [11], a smooth level-set (distance) function ϕ is used to track the interface. The interface is implicitly represented by the set of points in which $\phi = 0$. Liquid and gas regions are defined as $\phi > 0$ in the liquid and $\phi < 0$ in the gas, respectively. The advection of this distance function is governed by the following equation:

$$\frac{DF}{Dt} = \frac{\partial F}{\partial t} + (\overline{u} \cdot \nabla F) = 0 \tag{1.1}$$

which expresses that the interface property is advected with the local fluid velocity. Level set methods are conceptually simple and relatively easy to implement and yield accurate results when the interface is advected parallel to one of the coordinate axes. However, in flow fields with appreciable vorticity or in cases where the interface is significantly deformed, level set methods suffer from loss of mass (volume) and thus loss of accuracy.

In *shock-capturing* methods [12], high-order shock-capturing schemes are used to treat the convective terms in the governing equations. The advantage of this method is that explicit reconstruction of the interface is circumvented, which offers advantages for unstructured grids. Although state-of-the-art shock-capturing methods are quite sophisticated, they do not work as well for sharp discontinuities typically encountered in multi-fluid flows. Moreover, they require relatively fine grids to obtain accurate solutions. Rider and Kothe [13] used a high-order Godunov method and conducted several numerical tests and concluded that in all cases the use of shock-capturing methods was inadequate.

In *marker particle* methods [13, 14] marker particles are assigned to a particular fluid and are used to track the motion (and thus the interface) of the fluid. From the instantaneous positions of the marker particles, the relevant Eulerian fluid properties, required to solve the Navier-Stokes equations, are retrieved. Marker particle methods are extremely accurate and robust and can be used successfully to predict the topology of an interface subjected to considerable shear and vorticity in the fluids sharing the interface. However, this method is computationally very expensive, especially in three dimensions. Moreover, difficulties arise when the interface stretches considerably, which necessitates the addition of fresh marker particles during the flow simulation. Similar difficulties arise when the interface shrinks. Also merging and breakup of interfaces constitute a problem; again a proper subgrid model needs to be invoked.

Volume of fluid (VOF) methods [15] - [21] use a color function $F(x,\ y,\ z,\ t)$ that indicates the fractional amount of fluid present at a certain position $(x,\ y,\ z)$ at time t. The evolution equation for F is again Eq. 1.1, which is usually solved using special advection schemes (such as geometrical advection, a pseudo-Lagrangian technique), to minimize numerical diffusion. In addition to the value of the color function the interface orientation needs to be determined, which follows from the gradient of the color function. Two broad classes of VOF methods can be distinguished with respect to the representation of the interface: simple line interface calculation (SLIC) and piecewise linear interface calculation (PLIC). Earlier work generally relied on the SLIC algorithm attributed to Noh and Woodward [22] and the Donor-Acceptor (D-A) algorithm published by Hirt and Nichols [16]. Modern VOF techniques include the PLIC method ascribed to Youngs' [17]. The accuracy and capabilities of the modern PLIC-VOF algorithms greatly exceeds that of the older VOF algorithms such as the Hirt and Nichols' VOF method [16]. A drawback of VOF methods is the so-called artificial (or numerical) merging of interfaces (i.e. coalescence of gas bubbles), which occurs when their mutual distance is less than the size of a computational cell. On the other hand, when coalescence is known to prevail, the VOF method, contrary to the Front Tracking method, does not require specific algorithms for the merging (or breakage) of the interface. Recently, van Sint Annaland et al. [23] successfully applied their three-dimensional (3D) VOF model, based on Youngs' method, to simulate the coaxial and oblique coalescence of two rising gas bubbles.

The *lattice Boltzmann* method (LBM) can be viewed as a special, particle-based discretisation method to solve the Boltzmann equation. This method is particularly attractive in cases, where multiple moving objects (particles, bubbles, or droplets) have to be treated and avoids, contrary to the classical finite-difference and finite-element methods, the dynamic remeshing that becomes prohibitive for a large number of moving objects. Ladd [24, 25] has used the LBM successfully to compute the effective gas-particle drag in particulate suspensions whereas Sundaresan and coworkers [26, 27] recently extended this technique to deformable interfaces and successfully applied this technique to study the dynamics of isolated gas bubbles rising in quiescent liquids. However, in this method problems similar to those characterising the VOF methods may arise as a result of the artificial coalescence of the dispersed elements (gas bubbles).

Front-tracking methods [28] - [31] make use of markers (such as triangles), connected to a set of points, to track the interface, whereas a fixed or Eulerian grid is used to solve the NavierStokes equations. This method is extremely accurate but also rather complex to implement because dynamic remeshing of the Lagrangian interface mesh is required and mapping of the Lagrangian data onto the Eulerian mesh has to be carried out. Difficulties arise when multiple interfaces interact with each other as in coalescence and breakup, both of which require a proper subgrid model. Contrary to LBM and VOF, the automatic merging of interfaces does not occur in front-tracking techniques because a separate mesh is used to track the interface. This property is advantageous when swarm effects in dispersed flows need to be studied. Because of this Lagrangian representation of the interface this technique offers considerable flexibility to assign different properties (such as the surface tension coefficient) to separate dispersed elements.

1.2.3 Review of VOF Methods

1.2.3.1 Introduction

Pioneering work on VOF methods goes back to the early 1970s. The first three volume tracking methods were DeBar's method (KRAKEN code [32]), Hirt and Nichols' VOF [16], and Noh and Woodward's SLIC method [22]. Ramshaw and Trapp [33], and Peskin [34] were also early pioneers in this field. Significant development of volume tracking methods was made by the new piecewise linear schemes of Youngs' (PLIC) [17] and his hydrocode [36]. Many extensions and enhancements to the work of Youngs' have occurred since its introduction. These versions are now known as PLIC methods. The VOF method has now been adopted by some general commercial Computational Fluid Dynamics (CFD) codes and casting process codes. Current development is geared towards applying high-order time integration schemes to propagation algorithms and robust methods of polyhedral truncation to 3D interface reconstruction.

1.2.3.2 Development of VOF Algorithms

The essential concepts of VOF methods are described here: An initial fluid volume is used to compute fluid volume fractions in each computational cell from a specified interface topology. This requires the calculation of volumes truncated by the fluid interface in each interface cell. Exact interface information is then lost and instead discrete volume data is produced until an interface is reconstructed. The fluid solver then generates a velocity field, and interfaces are tracked by evolving fluid volumes in time with the solution of an advection equation. At any time in the solution, exact interfaces must be inferred, based on local volume data and on assumptions of the particular algorithm. The reconstructed interface is then used to compute the volume fluxes necessary to integrate the volume evolution equation. Therefore, the principal steps of VOF methods are reconstruction of the interface geometry and time integration algorithms. There are mainly three algorithms (piecewise constant, piecewise constant stair-stepped, and piecewise linear) for the reconstruction of interface geometry and two algorithms for time integration (one dimensional or operator split, and multi-dimensional), as listed in Table 1.1. However, many improvements and enhancements have been developed subsequently to these by a number of researchers.

Table 1.1: Development of VOF algorithms

Reconstruction interface geometry		Time integration	Author(s)and references	Date
Piecewise linear, operator split	PLIC	One dimensional	DeBar [32]	1974
Piecewise constant, operator split	SLIC	One dimensional	Noh and Woodward [22]	1976
Piecewise constant, multi-dimensional	FCT	One dimensional	Zaleski [37]	1979
Piecewise constant, stair-stepped,		One dimensional	Chorin [38]	1980
multi-dimensional	D-A		Hirt and Nichols [16]	1981
Piecewise linear, multi-dimensional	PLIC	One dimensional	Youngs [17]	1982
Piecewise linear, operator split	FLAIR	One dimensional	Ashgriz and Poo [39]	1991
Piecewise linear, multi-dimensional	LVIRA	Multi-dimensional	Puckett et al. [40]	1997
	PLIC		Rider and Kothe [19]	1998
	SS		Harvie and Fletcher [41]	2000

PLIC – piecewise linear interface construction; SLIC – simplified linear interface construction; DA – donoracceptor; FCT – flux corrected transport; FLAIR – flux line segment model for advection and interface reconstruction; SS – stream scheme; LVIRA – least squares volume-of-fluid interface reconstruction algorithm.

These contributions focused on improving the algorithms for interface reconstruction or time integration to achieve either more accuracy or more efficiency. Youngs' formula is adopted in many codes involving material interfaces, as mentioned in Section 1.2.3.4. The basic feature of piecewise constant, SLIC and DA methods is that the interfaces within cells are assumed to be lines aligned with one of the logical mesh coordinates, which is a 1D operator. Since the interface normal follows from volume differences based upon the current advection sweep direction, improved methods use multi-dimensional operators which are set on a 3×3 stencil in 2D to reconstruct the stair-stepped interface within each cell. Its volume fluxes are formulated algebraically by using flux-corrected transport (FCT) methods. The piecewise constant method is only a first-order scheme. Errors induced by its algorithm result in unphysical interfaces, causing submesh-size fluid volumes to separate from the main material body. These severely impact on the overall interfacial solution of flows with vorticity or shear near the interface, where forces are significant. This method is also difficult to apply for complex topology multi-material flows. The piecewise linear method is different from piecewise constant in that it reconstructs interface lines with a slope, which is given by the interface normal. The interface normal is determined with a multi-dimensional algorithm which does not rely on the sweep direction. Recently, PLIC volume tracking methods have been used successfully. Several recent papers have discussed this subject extensively, introducing second-order time integration schemes or robust methods for truncation of arbitrary polyhedra [19]. Obviously, multi-dimensional schemes can be more accurate and efficient in calculating cell boundary fluxes compared to operator split schemes, and are described in [19, 40, 41]. The descriptions given by [19] on reconstruction and advection algorithms of volume tracking methods are provided in a clear and concise manner. Comparisons with SLIC, DA, FCT, and Youngs' PLIC schemes have been reported in [18]. Results have shown that Youngs' PLIC scheme uses a more accurate interface reconstruction in comparison to either SLIC and DA or FCT. The SS advection scheme coupled with Youngs' PLIC possibly provides more accuracy at potentially greater computational expense [41]. Comparisons of SLIC and PLIC with the level set method, marker particles and piecewise parabolic method (PPM) have been performed by [42]. Results show that marker particles and PLIC methods allow the robust calculation of difficult fluid flows with large jumps in physical properties at the fluid interface. Following volume tracking methods, and various enhancements to interface reconstruction and interface advection algorithms (named VOF-like methods [43, 44]), many methods are currently being developed for multi-fluid flows coupled with other multi-phase methods, such as VOF-DPM [45, 46], VOF-two phase flow [47], VOF phase change (vapour or solidification) [48] - [50] , VOF-level set [51]. These algorithms are necessary for numerical simulations of more complex phenomena.

1.2.3.3 Summary of VOF Literature

Methods for tracking immiscible interfaces have been reviewed during the last two decades. General reviews of early tracking methods are given in [52] and more recent ones in [53, 54]. Some general reviews of moving boundary methods are also discussed in [54]. Reviews of current algorithms for the VOF method are presented in [19, 18, 42, 55], where detailed comparisons and methods of error estimation are presented. A recent review of numerical errors for the LVIRA-VOF algorithm is given in [56], where an analysis of the effects of grid size on the numerical error related to interfacial reconstruction is presented. Such error, which might significantly affect the description of the physical phenomena, cannot be avoided by applying better and more accurate front tracking algorithms. The source of this error is the limitation of the grid cell as the VOF model cannot simulate portions of fluid which are smaller than the grid cell. One possibility for the reduction of the numerical error is adaptive grid refinement of the mesh during the simulation. The first use of adaptive mesh refinement (AMF) in a volume tracking method can be found in [57]. A recent report on AMF applications for bubble rising problems is described in [58]. For tracking immiscible interfaces in multi-fluid problems, volume-tracking methods have been popularly and successfully used since the mid-1970s. However, several methods for sharper interfaces in multiphase flow are under development. A level set method, for example, has recently been applied to multi-phase problems [59].

1.2.3.4 Applications of VOF Methods

Applications of VOF methods are found in many industrial and biohydronamics areas, either in the macro- or meso-/micro-scale, including aero-/astro-/hydro-dynamics, metallurgical, viscous, and viscoelastic flows. A few special test cases have benchmarks for the validation of interfacial topology and propagation, and verification of accuracy and efficiency. They include static interface reconstruction [17], Zaleski's slotted solid disk rotation [37, 41], Rider-Kothe single vortex and time reversed flows [19, 41, 42, 56], Rudman's hollow square/circle [41], and Rayleigh-Taylor instabilities [17, 18, 40, 47, 60, 61]. Numerous papers describe successful applications of VOF methods in various fields. A few typical engineering areas of macro-scale flows include cast filling [49], coastal/ ocean wave flow [61], dam break flow [62], coating process, liquid sloshing [63, 64], liquid/air jet [65, 66], environment/fire fighting/HVAC area, and material extrusion process. Meso-/micro-scale flows include bubble rising, drop deformation and rupturing [67, 68], drop sediment/splash, drop interaction [69], lubricating flow, and two layer flows. Examples of VOF codes [40] are KRAKEN, SURFER, SOLA-VOF code and its descendants (NASA-2D, NASA3D, RIPPLE, Tellurider (RIPPLE-3D version) and FLOW3D). SURFER (originally by Zaleski) and RIPPLE (originally by Kothe) are used by many researchers since these are free or public open source codes and further enhancements have been made [70]. Some examples of general commercial CFD codes which use VOF methods are FLOW3D, CFX, FLUENT, FIDAP, PHOENICS, STAR-CD, as well as some CAE codes for casting process, such as MAGMAsoft, ProCAST, SIMULATOR, and CAST-Flow.

1.2.4 Surface Tension Modelling

A common problem for all methods is an accurate representation of the surface tension force which is concentrated on the interface. Often, the surface tension term is computed either with the continuum surface force (CSF) model of Brackbill et al. [60] or with the continuum surface stress (CSS) formulation of Gueyffier et al. [71]. The CSF represents the surface tension effects in the form of a smoothly varied volumetric force. Different methods for estimating the curvature, normals, and the surface delta function required for

CSF model have been developed [60, 72, 18]. The sensitivity of the results to the choice of smoothing kernels and the interface orientation, as well as to degree of smoothing, is not yet well understood. The CSS method [71, 15] requires only the computation of the normals to the interface. An inaccuracy caused by these methods manifests itself, in particular, in well-known anomalous currents around a stationary bubble (see [15, 18]). In simulations with relatively strong surface tension effects, and especially in the presence of large density/viscosity jumps, the currents can progressively grow and destabilize the solution. The currents can be reduced by appropriate smoothing in the CSF and the CSS methods, but there is no way to remove them. An alternative approach is to model a correct pressure jump at the interface. In modeling the surface tension force on interface interpolants, cubic splines [20] have been found to be sufficiently smooth to ensure an accurate discretisation of the curvature. Popinet and Zaleski [20] cancelled the spurious currents by taking into account, in addition to spline interpolation which goes through a set of marker points, the interface position while discretising the pressure gradients. Also, Coward et al. [74] show that commonly used simple viscosity averages significantly reduce the accuracy of VOF models at the interface. In order to correctly introduce pressure jumps and continuity of the viscous stresses, deformable grids can be used, where element boundaries lie along the reconstructed interface. In combination with the VOF method, this approach was developed by Mashayek and Ashgriz [75]. Gao [76] employs a special mixed FEM formulation to obtain a stable discretisation of Navier-Stokes equations. The outcome of front aligned grids is that the boundary conditions at the front are satisfied accurately without any Lagrangian moving mesh system.

1.2.5 Bubbles and Drops in Free Motion

Bubbles and drops in free rise or fall in infinite media under the influence of gravity are generally grouped under the following three categories:

(a) **Spherical**: Generally speaking, bubbles and drops are closely approximated by spheres if interfacial tension and/or viscous forces are much more important than inertia forces. Fluid particles will be termed “spherical” if the minor to major axis ratio lies within 10% of unity.

(b) **Ellipsoidal**: The term "ellipsoidal" is generally used to refer to bubbles and drops which are oblate with a convex interface around the entire surface. It must be noted that actual shapes may differ considerably from true ellipsoids and that fore-and-aft symmetry must not be assumed. Moreover, ellipsoidal bubbles and drops commonly undergo periodic dilations or random wobbling motions which make characterization of shape particularly difficult.

(c) **Spherical-cap or ellipsoidal-cap**: Large bubbles and drops tend to adopt flat or indented bases and to lack any semblance of fore-and-aft symmetry. Such fluid particles may look very similar to segments cut from spheres or from oblate spheroids of low eccentricity; in this cases the terms "spherical-cap" and "ellipsoidal-cap" are used. If the fluid particle has an indentation at the rear, it is said to be "dimpled". Large Spherical- or ellipsoidal-caps may also trail thin envelopes of dispersed fluid referred to as "skirts". Photographs of freely rising bubbles in this regime are shown in Fig. 1.1

When bubbles and drops rise or fall in bounded media their shape is affected by the walls of the container. If the bubble or drop is sufficiently large, it fills most of the container cross section and the "slug flow" regime results.

1.2.5.1 Dimensional Numbers

For bubbles and drops rising or falling in infinite media it is possible to prepare a generalized graphical correlation in terms of the Eötvös number, Eo; Morton number, Mo; and Reynolds number, Re.

Dimensional analysis shows that three dimensional groups, two independent and one dependent, describe bubble behaviour in a liquid. The Morton number Mo, and the Eötvös number, Eo, are usually chosen as independent parameters.

The Morton number contains only physical properties of the fluid (Clift et al [4]). This allows fluids to be categorised into two separate groups based on their Morton number, with fluids in the "high Morton number" category having $Mo > 10^{-6}$, and fluids in the "low Morton number" category having $Mo < 10^{-6}$. Water, the liquid considered in this project has a Morton number of 1.1×10^{-11}, and is therefore a "low Morton number"

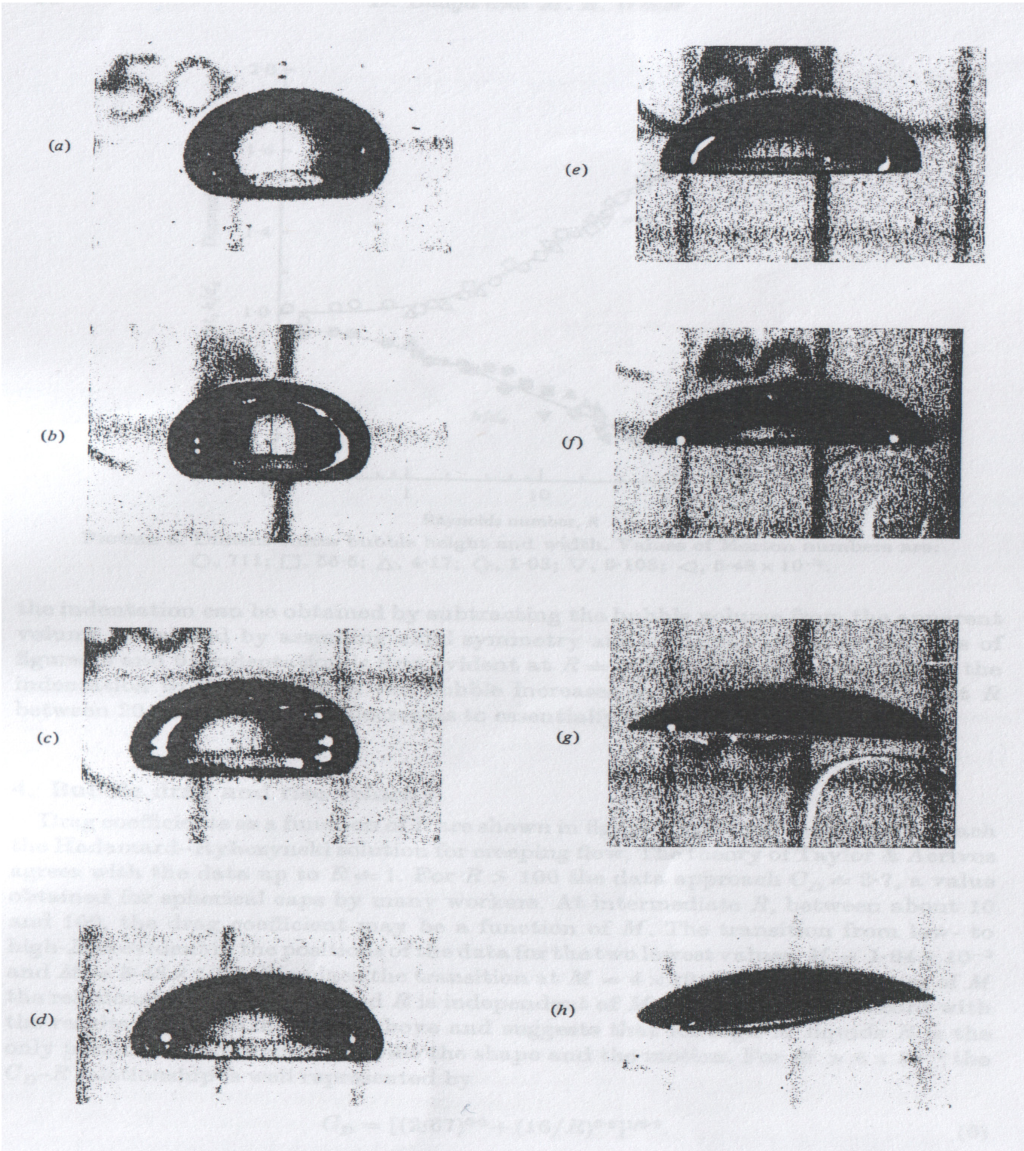

Figure 1.1: Photographs of freely rising bubbles [77].

fluid.

The Eötvös number is fundamentally a measure of the volume of the bubble, so that a functional relationship between a parameter and the Eötvös number describes how the parameter changes with bubble volume.

The choice of the dependent parameter depends on what one is interested in. The Reynolds number, Re, is the ratio of inertia forces to viscous forces, and is used mainly for determining whether a given flow will be laminar or turbulent. It is the most common parameter used to define a dimensionless rise velocity.

1.2.5.2 Terminal Bubble Shape

The dimensional numbers listed in section 1.2.5.1 can be used to predict bubble shape under various conditions. Using a plot of Re versus Eo with Mo as a parameter, as described by Bhaga et al. [77], the predicted bubble shape for single rising bubbles in Newtonian liquids at various values of Reynolds, Morton and Eötvös, numbers can be identified. This plot is shown in Fig. 1.2, while Fig. 1.3 illustrates the corresponding bubble shapes and includes descriptive abbreviations for each shape.

Figure 1.2 shows boundaries between three principal shape regimes as described above. At low Reynolds numbers, bubbles remain spherical in shape but at relatively high Re and intermediate Eo, bubbles are ellipsoidal. Spherical- and ellipsoidal-cap regimes require both Re and Eo be large. Various sub-regimes may also be mapped and some of these are included in Fig. 1.2

1.2.5.3 Bubble Trajectory

Instabilities in the path of bubbles moving through a fluid are thought to be the result of a combination of effects, namely bubble shape oscillation, wake instabilities, and surface-active impurities resulting from water contamination. Two categories of bubble trajectory are generally noticed; these are “zigzagging” and “spiralling”. Bubbles experiencing zigzagging motion will move from side to side in the vertical plane, as they rise

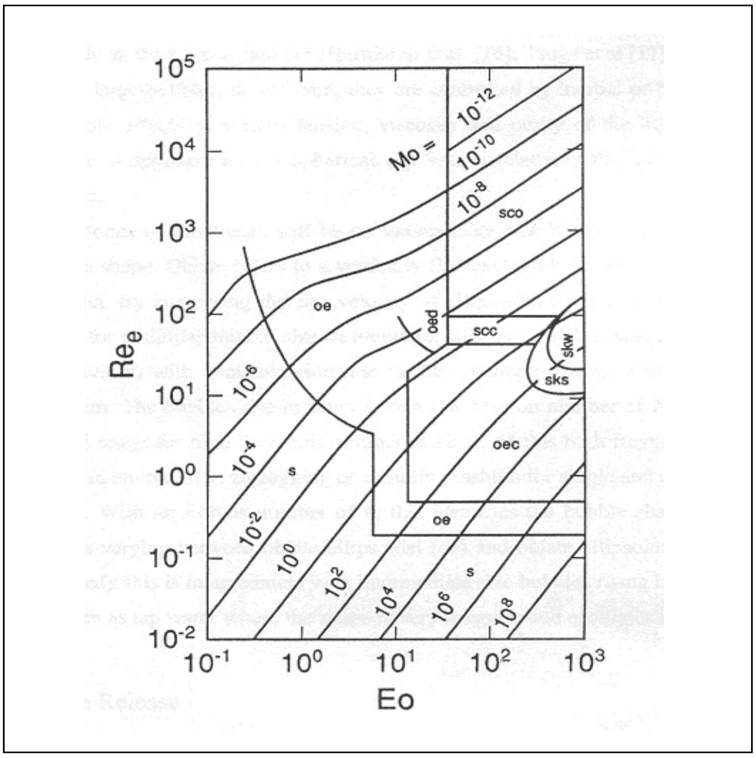

Figure 1.2: Shape-regime map for single bubbles rising in infinite Newtonian liquids [4]; For acronyms representing the bubble shapes refer to Figure 1.3 [77].

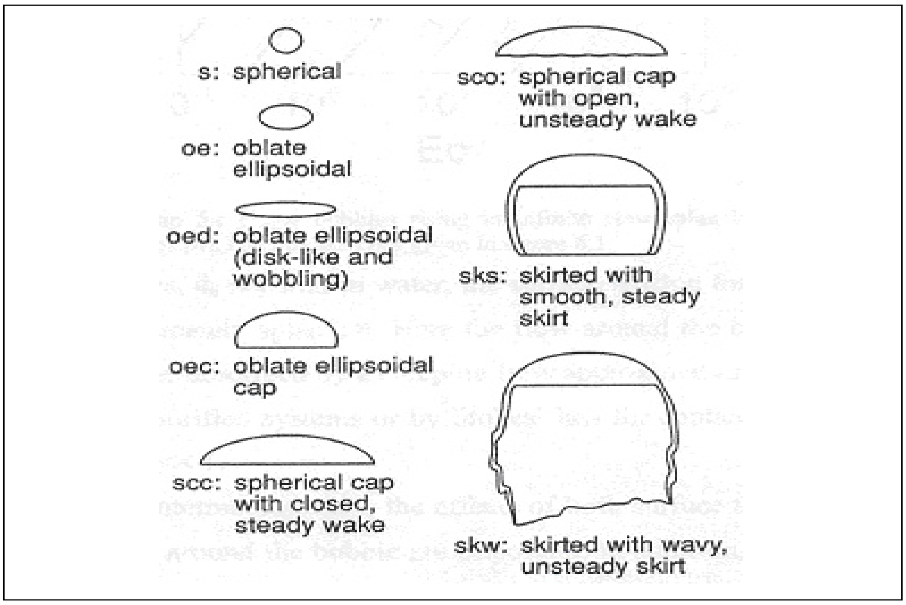

Figure 1.3: Sketches of bubble shapes observed in infinite Newtonian liquids [77].

through the fluid, whereas bubbles experiencing spiralling motion will rise through the fluid in a helical path, making circular or elliptical horizontal displacements as they rise, travelling a path similar in shape to a coiled spring (Mercier et al. [78]).

Path instability occurs essentially in the intermediate range of bubble sizes, where bubbles are roughly ellipsoidal. In a study conducted by Saffman [79], which investigated the bubble path and onset of instability in detail, trajectory instability was strongly linked to bubble size. It was noted that bubbles of equivalent radius $R_{eq} < 0.7$ mm always exhibit a straight path; this is explained by the spherical shape of bubbles of this size. For larger radii up to $R_{eq} = 1.0$ mm only zigzagging bubbles were found, and for bubbles with equivalent radii greater than 1.0 mm both spiralling and zigzagging motion was observed. Lünde and Perkins [80] remarked that the path of an individual bubble may make the transition from zigzag motion to spiralling motion, whereas the reverse of this was not observed. Saffman [79] noted that when bubbles were released in rapid succession one after another, the bubbles followed the preceding bubbles' path, suggesting that the preceding bubbles' wake has a strong effect on the trajectory of the following bubble. However it was found that for $R_{eq} < 1.0$ mm zigzagging bubbles always zigzagged, even when released in the wake of spiralling bubbles. This research also proposed that a critical bubble Reynolds number existed, at which the onset of path instability occurred and this was quantified as $Re_{cr} = 400$.

1.2.5.4 Bubble Wake

The bubble wake is the region behind the bubble where the fluid flow is affected by bubble motion. It is widely accepted that unsteadiness and vortex shedding in the bubble wake is a cause of instabilities which may arise in the bubble trajectory. Although there is a scarcity of numerical research into the wake of bubbles, similar studies into the flow regime behind a solid sphere, whose behaviour is similar to that of a bubble in surfactant-contaminated water, provide an insight into the behaviour of the bubble wake. A study carried out by Johnson and Patel [81] showed that in the case of a solid sphere, at Reynolds numbers below 210, the wake structure behind the sphere is axisymmetric. However at a Reynolds number, $Re_1 = 210$ the wake loses its axisymmetry and the flow begins to diverge regularly. After this point two vortex filaments appear, however no unsteadiness is noted until a second critical value of $Re_2 = 280$ is reached, at which point hairpin vortices are shed. Making the assumption that a contaminated bubble behaves like a solid sphere at a similar Reynolds number, it is predicted that the axisymmetry of the bubble wake breaks down at Re_1. This analytical prediction agrees quite well with experimental results from Hartunian and Sears [82] for contaminated bubbles. Experimental studies of bubble wakes have been carried out using a variety of methods. For example Lünde and Perkins [80] used dye visualisation methods, and Brücker [83] used Particle Image Velocimetry (PIV). In these studies, vortex shedding is observed to occur in the wake of zigzagging bubbles; this wake behaviour is very similar to that observed for solid spheres. Experiments carried out by Lünde and Perkins [80] showed a strong link between the wake behaviour and the path that the bubble travelled, suggesting that wake instabilities are a significant factor in determining the bubble path. It was noted that the bubble followed a helical path when the wake was steady and comprised of two vortex threads, whereas it followed a zig-zag path when the wake was unsteady and hairpin vortices were being shed in the bubble's wake. For the case of spiralling bubbles Lünde and Perkins [80] observed a double threaded wake and emphasised that this would consist of two counter rotating vortex filaments. In order to satisfactorily resolve the wake region using these methods a large amount of seeding particles or dye would need to be used, and as a result it is unrealistic to assume that the results obtained are accurate for a system using clean water with very low contaminant/surfactant levels. Bel Fdhila and Duineveld [84] concluded that above a critical contaminant concentration, the drag force exerted on the bubble increases rapidly, approaching the drag that would be expected from a solid sphere of similar diameter to the bubble. The contamination introduced by the seeding/dye may therefore explain the similarity between the reported bubble wakes, and those recorded for solid spheres. Brücker [83] studied both zigzagging and spiralling air bubbles in water, utilising both high speed imaging techniques and PIV measurements. Brücker presented a model of the entire wake region of a 6 mm diameter free rising bubble, which reconstructs the formation and shedding of three-dimensional vortices. The results obtained agree well with results obtained from the dye visualisation experiments carried out by Lünde and Perkins [80], where bubbles were released at the bottom of a tank before rising through a

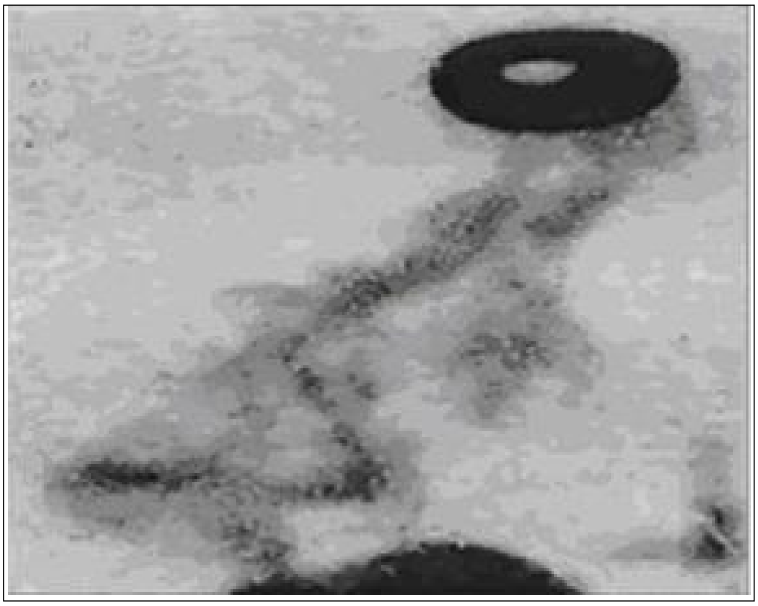

Figure 1.4: Flow visualisation of wake of free rising ellipsoidal air bubble zigzagging in water at $Re \simeq 1500$ [80].

layer of coloured dye, thus providing a visualisation of the bubble wake. An example of a wake image obtained from these experiments is shown in Fig. 1.4.

Brücker [83] sketched the vortex shed by the bubble, and this is reproduced in Fig. 1.5. The vortex may be described as a "hairpin" or closed horseshoe vortex. It is composed of two streamwise vortex filaments or legs, which are connected at the upper end by a vortex "head" and at the bottom by a vortex "tail" to form a closed contour.

From this model the zigzagging motion that the bubble undergoes can be explained by the shedding of the hairpin vortex head, as the interaction of the resulting circulation around the bubble periphery with the free stream velocity generates a transversal lift. The oscillatory characteristics of the zigzagging rise path are explained by the periodic shedding of vortices of opposite circulation on opposite sides of the bubble equatorial plane. Fig. 1.6 shows a schematic of the vortex chain formed by shedding of hairpin vortices by a free rising ellipsoidal bubble.

The influence that the wake of a bubble has on surrounding bubbles requires some examination. Stewart [86] conducted a study into the interaction of bubbles in

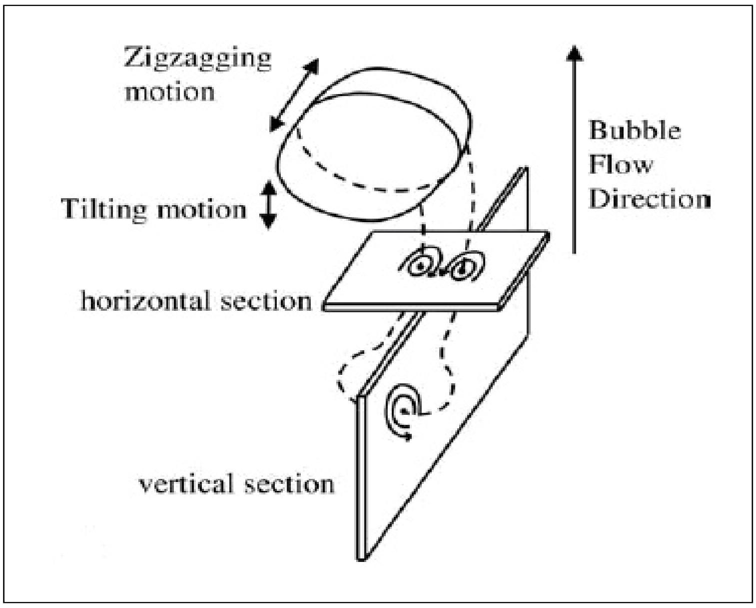

Figure 1.5: Schematic interpretation of vortex shed by free rising ellipsoidal bubble in water [85].

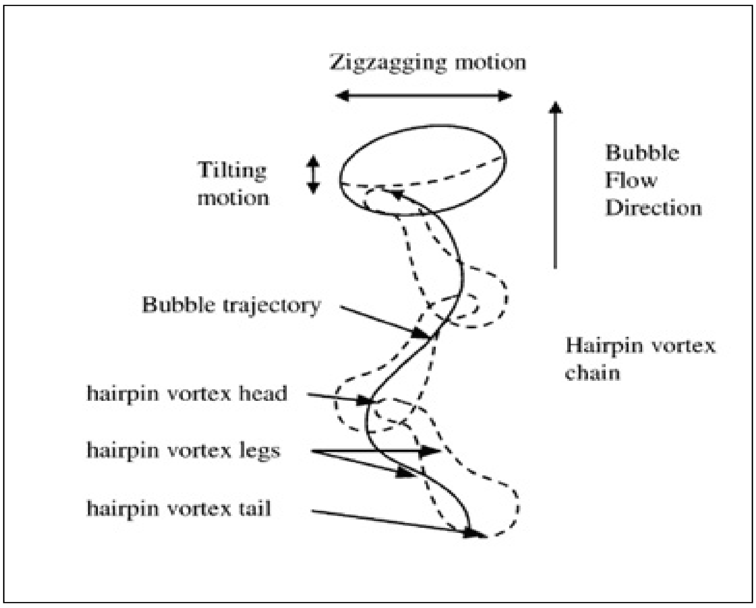

Figure 1.6: Schematic diagram of vortex chain formed by shedding of hairpin vortices from free rising ellipsoidal bubble [85].

low viscosity liquids and concluded that the bubble wake was the driving force and sole mechanism for bubble interaction. He reports that a disturbance in the wobble pattern of a trailing bubble at a distance of approximately 6 diameters behind the leading bubble is the first indication that the preceding bubble's wake region has been entered. The behaviour after this point is dependent on the Reynolds number of the bubble. For bubbles moving under high Reynolds number conditions, the trailing bubble undergoes acceleration in a series of progressively larger jumps, indicating that the wake strength of the preceding bubble is greater when close to the bubble itself, until it eventually catches the leading bubble and collides with it. For bubbles moving under low Reynolds number conditions the following bubble accelerates in a constant fashion until collision with the leading bubble occurs.

It is clear that bubble path is strongly dependent on the structure of the bubble wake. The structure of the bubble wake is dependent on the flow around the bubble itself, and as the flow around the bubble is affected by factors such as the bubble size, and the contamination levels experienced, it becomes apparent why different size bubbles, and bubbles of various contaminant concentrations, follow different rise paths.

1.2.6 Air/Water Systems

In most systems, bubbles and drops in the intermediate size range (d_{eq} typically between 1 and 15 mm) lie in the ellipsoidal regime. However, bubble and drops in systems of high Morton number are never ellipsoidal. Ellipsoidal fluid particles can often be approximated as oblate spheroids with vertical axes of symmetry, but this approximation is not always reliable. Bubbles and drops in this regime often have fore-and-aft symmetry and show shape oscillations.

Because of their practical importance, water drops in air and air bubbles in water have received more attention than other systems. The properties of water drops and air bubbles illustrate many of the important features of the ellipsoidal regime.

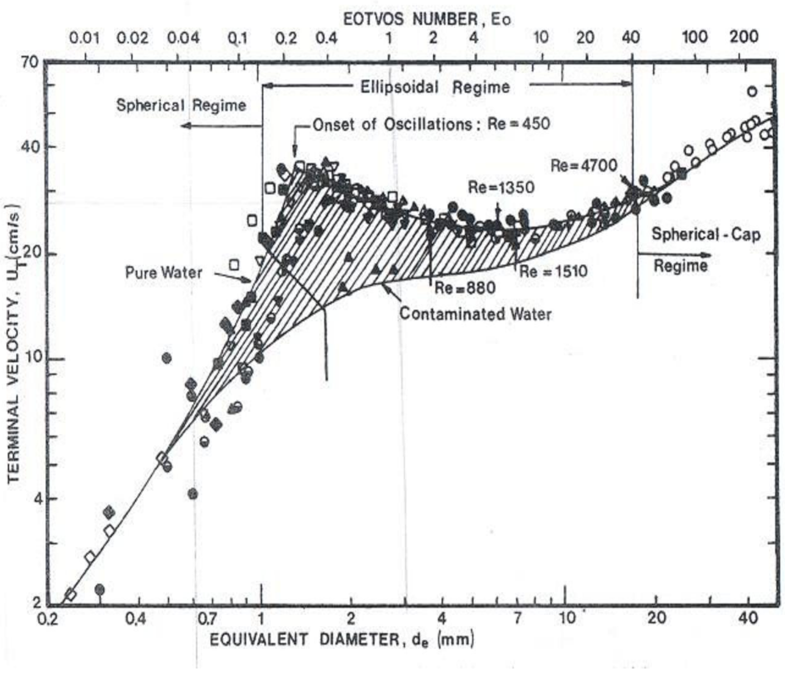

Figure 1.7: Terminal velocity of air bubbles in water at 20°C [4].

1.2.6.1 Air Bubbles in Water

Experimental terminal velocities for air bubbles rising in water are presented in Fig. 1.7 for the ellipsoidal regime and adjacent parts of the spherical and spherical-cap regime. Some of the spread in the data results from experimental scatter, but the greater cause is surface contamination. For water drops in air, surfactants have negligible effect on drag since the internal circulation is small even in pure systems. For air bubbles in water, there is little viscous resistance to internal circulation and hence the drag and terminal velocity are sensitive to the presence of surfactants.

The two curves in Fig. 1.7 are taken from [4] for distilled water and for water with surfactant added; the curve for small (spherical) bubbles, since even distilled water tends to contain sufficient surfactant to prevent circulation in the range, and; for large (spherical-cap) bubbles where surface tension forces cease to be important. Surface-active contaminants affect the rise velocity most strongly in the ellipsoidal range. For

$d_{eq} > 1.3$ mm, the uppermost curve for pure system in Fig. 1.7 is approximated closely by

$$U_T = [(1.24\sigma/\rho d_{eq}) + 0.505 g d_{eq}]^{1/2} \tag{1.2}$$

The trajectories of air bubbles in water were measured by researchers (Ref. [4]) and they found that when surface-active agents continue to accumulate during the rise, the terminal velocity may never reach steady state and may pass through a maximum (i.e. the velocity increases and then decreases). Five types of motion were observed, listed in Table 1.2 with Re based on the maximum instantaneous velocity.

Table 1.2: Motion of Intermediate Size Air Bubbles Through Water at 28.5^o C

d_{eq} (mm)	Re	Aspect Ratio (E)	Path
<1.3	<565	>0.8	Rectilinear
1.3 to 2.0	565 to 880	0.8 to 0.5	Helical
2.0 to 3.6	880 to 1350	0.5 to 0.36	Plane (zig-zag) then helical
3.6 to 4.2	1350 to 1510	0.36 to 0.28	Plane (zig-zag)
4.2 to 17	1510 to 4700	0.28 to 0.23	Rectilinear but with rocking

1.2.7 Experimental and Numerical Modelling of Rising Bubble Dynamics

The rise of a bubble in a viscous liquid is generally accompanied by deformation of the bubble. A number of experimental studies have examined this phenomena. For example, the rise of a bubble in an inviscid and a viscous liquid have been studied by Bhaga and Weber [77].

Grace et al. [87] and, in a more detailed study, Bhaga and Weber [77], systematically arranged the motion of bubbles freely rising in viscous Newtonian liquids. They showed that the Reynolds (Re), Eötvös (Eo) and Morton (Mo) numbers were essential for describing a rising bubble or falling drop motion because shape and terminal velocity of a bubble or drop were determined by these three dimensionless numbers. At the same time, their studies have provided important fundamental knowledge on bubble rise motion.

Amongst studies that have considered the deformation of a bubble in a liquid, Ryskin and Leal [88] investigated the steady state deformation of a rising axisymmetric bubble over a range of Reynolds numbers and Weber numbers using body-fitted coordinates. More recently, Unverdi and Tryggvason [28] studied the rise of two and three dimensional bubbles using a front tracking method, in which they represented the interface by an indicator function.

In the last decade, direct numerical simulation (DNS) has been recognized and used as an efficient technique for comprehending and revealing detailed flow structures and mechanisms for bubble motion in viscous liquids. As a consequence, many numerical studies of rising bubbles/drops have been presented (e.g. Sussman and Smereka [5]; Esmaeeli and Tryggvason [29, 30]; Chen et al. [89]; Son [90]; Ohta et al. [91, 92]). So far, most of the numerical simulations on bubble rise motion have been devoted to bubble rise dynamics with intermediate shape deformations and "intermediate" rise speeds. There is still a relative lack of computational studies of rising bubbles with large deformations, such as "skirted" and "spherical-cap" shapes and of rising bubbles with large Reynolds numbers. Wu and Gharib [93] reported that small air bubbles of diameter range 1-2 mm, rising in clean water have two steady shapes; a sphere and an ellipsoid. Along the same line, Tomiyama et al. [94] showed experimentally that air bubbles rising through pure and contaminated water in a surface tension force dominant regime were largely influenced by an initial shape deformation. In terms of the Eo and Mo numbers, the conditions of their study correspond to low Eo and very low Mo regions. They found that the numerical results of Yang et al. [95] conflict with the experimental studies by Wu and Gharib [93] and Tomiyama et al. [94]. Yang et al. [95] reported results using 2D-computations (a boundary fitted numerical method) which were shown to be initial-condition independent, whereas Wu and Gharib [93] and Tomiyama et al. [94] reported results which were dependent on initial-conditions.

Van Wachem et al. [96] studied bubble dynamics including the bubble shape and rising velocity. They used an advanced 3D Lagrangian interface tracking scheme to study the time-dependent behavior of gas bubbles rising in an initially quiescent liquid. Detailed experiments of single rising bubbles of different sizes were performed to compare the shape, rising velocity and pressure signal, with numerical results. Simulations of the injection of an air bubble into water were performed in a geometry of a 200-cm-high, 30-cm-wide and 15-cm-deep column, and compared with experiments. Experiments and simulations considered a bubble of 6 cm in diameter. Very good agreement between experimental and numerical results was achieved for the rising velocity of a single bubble in a two-dimensional infinite medium. The correlation derived is

$$V_b = \varphi\sqrt{gd_b} \tag{1.3}$$

where V_b is the rising bubble velocity, d_b is the bubble diameter, and $\varphi = 0.54$ for a two-dimensional geometry.

Raymond et al. [97] performed an extensive comparison between numerical and experimental results for moderate deformed bubbles concerning their drag coefficient. They carried out analysis for a range of Reynolds numbers and Weber numbers ($(Re,\ We) = [1, 100],\ [1, 5]$). They tracked the interface position by introducing a curvilinear interface-fitted non-orthogonal coordinate system. By means of a coordinate transformation, they converted the physical domain to a computational domain with known boundaries that were coordinate isolines. They generated a boundary-fitted grid around the deformed bubble at each iteration. To ensure accurate metric quantities (normal and tangential vectors, surface curvature, etc.) of the gas-liquid interface, they used a grid two-times finer than the MAC mesh (Harlow and Welch [14]). They discussed the effect of Reynolds number and Weber number on the drag coefficient and the aspect ratio.

The bubble drag coefficient, C_d, calculated in their work is defined as

$$C_d = \frac{F}{\frac{1}{2}\rho U_\infty^2 4\pi d_{eq}^2} \tag{1.4}$$

where F is the force exerted by the fluid on the bubble, calculated by integration of the local forces due to the pressure and normal viscous stress on the bubble surface. They used the bubble-equivalent diameter d_{eq} rather than the bubble width w as a reference length to facilitate the comparison of numerical and experimental results. They found that at low Reynolds numbers ($Re \approx 1-5$), the bubble deformations are small, which is in agreement with the analytical solution, and the drag coefficient is then hardly influenced by the Weber number and the drag coefficient iso-lines are almost vertical straight lines. At high Reynolds numbers ($Re \approx 10$ - 100), the bubble deformation was shown to become larger and the drag coefficient to increase significantly with the Weber number. The blending of the drag coefficient iso-lines showed that this effect is more important at a higher Reynolds number.

1.2.8 Sliding Bubble Dynamics

It is important to understand both the dynamics of sliding bubbles and their influence on the liquid flow behaviour and patterns before commencing a study into their enhancement effect on heat transfer. A thorough knowledge of the parameters which affect the dynamics of a sliding bubble in a liquid will prove extremely valuable when both predicting bubble behaviour and its effect on flow structure. A good deal of both experimental and numerical research has been carried out in the area of two-phase air-water flows, and this section aims to highlight the findings of many of these studies to provide an insight into the behaviour of both the sliding bubble itself and the flow structures it creates.

Boiling is used in many processes and is associated with very high heat transfer rates. The nucleation and growth of bubbles, and the dynamics of bubbles following detachment from their original nucleation sites, can have a significant influence on heat transfer from the heated surface (Houston and Cornwell [98]). Much attention, therefore, has been devoted to understanding heat transfer associated with sliding bubbles. The enhancement of heat transfer has been attributed to evaporation of the thin microlayer beneath the bubble, mixing in the wake of the bubbles, and to disruption of the thermal boundary layer. Models have been proposed to calculate the thickness and to quantify the heat transfer from the microlayer. Efforts have also been made to systematically study the heat transfer associated with sliding bubbles. A brief summary of pertinent literature on heat transfer associated with sliding bubbles is given next.

Research into sliding bubble phenomenon began with studies on the hydrodynamics of boiling flow in horizontal or inclined tubes. During subcooled nucleate boiling flows, especially in inclined pipes, the bubbles tend to stick to the walls and slide along the tube. The heat transfer processes are similar to those found in slug and annular flows, as there is only a thin layer of liquid between the bubbles and the wall in both the cases. Understanding the various bubbles shapes and the flow patterns present was the primary purpose of early studies on sliding bubbles.

Maneri and Zuber [99] first performed experiments on air bubbles rising along a downward facing inclined surface immersed in a pool of liquid. The experiments were conducted on a two-dimensional tank and deionized water and methanol were used as the test liquids. Both the liquid and the inclined surface were at room temperature and there was no heating involved in the study. Bubble shapes at various locations along the surface were presented. The observed motion of the air bubbles was interpreted in terms of three distinct regions:

1. inertial region, which extended from 0 - 10 degrees inclination (from vertical), where the bubble frontal radius was large, and the rise velocity was little different from the vertical value.
2. transition region, which was from 10 - 30 degrees inclination and showed a sudden increase in rise velocity.
3. property dominant region, which extended from 30 - 90 degrees from vertical, was where the frontal radius of curvature of the bubble was small, and both the geometrical and fluid properties were influencing the bubble rise velocity.

A similar, but more comprehensive study on the characteristics of bubble rising under inclined plane was conducted by Maxworthy [100]. Experiments were conducted on a water filled tank with an adjustable slotted brace, which was used to tilt the tank to required angles of inclination. Air bubbles were injected using a hypodermic syringe. Initial bubble volumes were varied from 5 to 60 ml at intervals of 5 ml. Experiments were conducted for angles of inclination (α) from vertical, ranging from 0 to 85 degrees at 5 degrees interval. As in the case of Maneri and Zuber [99], there was no heating, nor any phase change involved in these experiments. Bubble shapes, rise velocity, and bubble width were presented as a function of both bubble volume as well as the angle of inclination. A series of top-view photographs for angles of 5, 20, 50, 70 and 90° and volumes of 5, 10, 25 and 55 ml is shown in Fig. 1.8.

At very high angles of inclination from vertical, the bubbles were of the form of long ellipsoids but curved along the major axis for lower volumes. As the bubble volumes increase, for all the angles of inclination, the bubble shapes had a smooth frontal interface. The back of the bubble was often ragged, with the interface showing instability induced by the drag, and even showed smaller bubbles breaking off from the original bubble. Non-smooth interfaces on the back of the bubble were a clear feature in all the cases, as was the half oblate spheroid shape near the stagnation point. At angles close to vertical, the bubbles approached a cap bubble shape, but with center displaced from the wall as shown in Fig. 1.9. Gravitational flattening of the bubble is apparent for the smaller inclination angles and larger volumes. Measurements of bubble shape were also presented. An inviscid model to describe the bubble velocity for an angle of inclination was also proposed.

Addlesee and Cornwell [101] have attempted to estimate the liquid film thickness between a rising bubble and the inclined plate. A boundary layer analysis assuming adiabatic conditions was used and a value of 200 - 400 mm was predicted. The estimated values agreed well with the optical measurements reported in this paper, however the values were much larger than that of Cornwell and Schuller's [102] earlier work.

Houston and Cornwell [98] studied the heat transfer associated with sliding bubbles in a tube, under both evaporating and non-evaporating conditions. They compared the heat transfer rates with and without sliding bubbles. The experiments were performed in a boiling cell consisting of 34 tubes in two in-line columns. All tubes were made of stainless steel, except the tube on which measurements were made, which was made of copper. Two cartridge heaters heated the area between the sides of the cell. Heat flux was obtained from the temperature gradient along the test cylinder. R113 was used as the test liquid for both evaporating and non-evaporating cases. Based on the results they have concluded that the liquid agitation caused by the sliding bubbles was an important mechanism in enhancing the heat transfer from the surface. The evaporation under the bubble also plays an important role, however, this was not much larger than that of the turbulent convection due to sliding bubbles. Analysis of evaporation and condensation

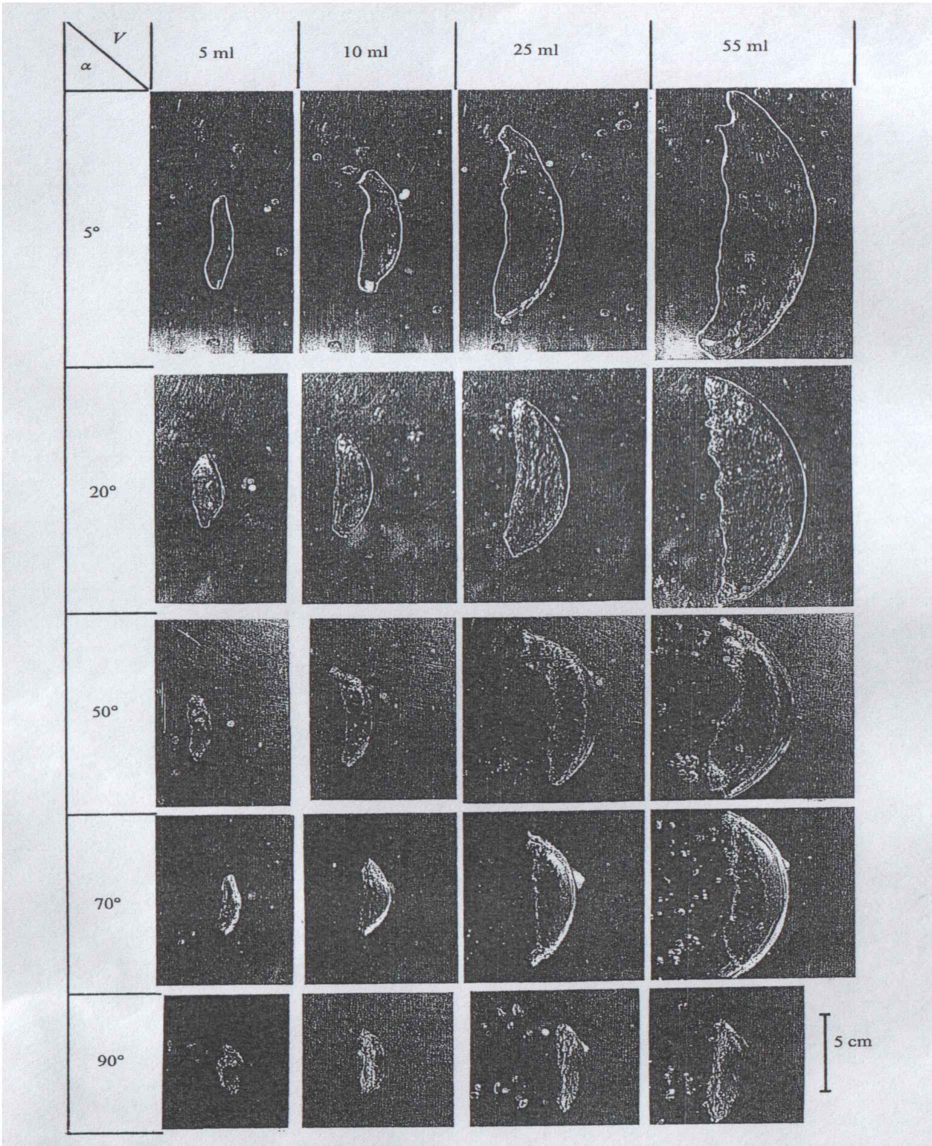

Figure 1.8: Plan view photographs of the bubbles at various values of inclination angle (α) and bubble volume (V), taken from [100].

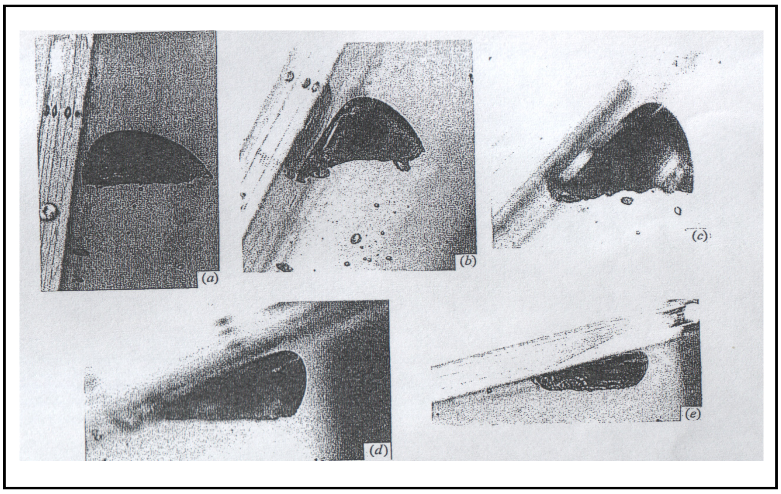

Figure 1.9: Side view photographs of the bubbles for V = 60 ml and various values of α: (a) 82°, (b) 65°, (c) 50°, (d) 25°, (e) 15°, taken from [100].

under the sliding bubble showed that the liquid layer beneath the bubble must only be a few microns thick. They also concluded, based on their analysis of evaporation and condensation under the sliding bubble, that the thickness of the liquid layer underneath the bubble should be of the order of a few microns.

Cornwell and Grant [103] also studied heat transfer to vapor bubbles sliding under a horizontal tube. Experiments were conducted on a cell containing a solid half cylinder or a shim, which served as the heater surface. For mean heat transfer studies a half cylinder with in-built cartridge heaters was used. For obtaining local temperature field, thermo-chromic paints were used on the inside of the shim. By a mirror arrangement, high-speed video images of the bubble motion could be obtained as well as thermal images from the TLC's on the heater surface. Based on the analysis of the thermal images, they concluded that both the bubble sweeping, as well as the evaporation of the thin layer beneath the bubble, were responsible for the enhancement of heat transfer.

Thorncroft, Klausner and Mei [1] studied bubble growth and detachment in vertical flow boiling over a nichrome heating surface using visual images obtained with a high speed digital camera. Both upflow and downflow configurations were studied. One of the main observations was that the vapor bubble lift off in general did not occur in upflow configurations, whereas in downward flow it occurred regularly. In upflow, vapor bubbles appeared to slide along the heater surface. Comparatively higher heat transfer coefficients were observed for upflow conditions and the increase was attributed to vapor bubble sliding.

Thorncroft, Klausner and Mei [104], examined nucleation suppression during flow boiling and proposed a criterion for differentiating a convective region from a nucleate boiling region. They also noted that there was no secondary nucleation, and concluded that such a process could not cause high heat fluxes in annular flows.

Thorncroft and Klausner [105] also examined the effect of vapor bubble sliding on forced convection boiling heat transfer. An experimental setup similar to their previous studies was used and heat transfer during both vertical up flow and downward flow was studied. Experiments were conducted using FC 87 as the fluid at saturated annular flow boiling as well as slightly subcooled conditions. The test section was a square clear tube permitting direct high-speed photography. Vapor bubbles were generated from one side of a wall, which was attached to a DC powered Nichrome heater strip. Significantly higher heat transfer coefficients were observed for up flow conditions than for down flow. This increase was attributed to the sliding bubbles that remained attached to the wall in the case of up flow. An additional set of experiments performed by injecting air bubbles, instead of vapor bubbles, also found that the heat transfer rates are higher in the case of up flow. They have concluded that, at least for the experimental conditions considered in their work, the bulk turbulent motion due to the presence of the bubbles explained the major portion of the increase in heat transfer observed in the case of sliding bubbles.

Yan, Kenning and Cornwell [106] have reported experiments on vapor bubbles sliding under inclined planes. The inclined planes were thin foils, which were electrically heated. On the upper side of the planes thermo chromic paint was applied to study the local temperature variations due to sliding bubbles. Experiments were performed with water as the test liquid, and steam bubbles were injected at the bottom of the inclined planes. The angle of inclination of the plane was varied from 45° to 75° from the vertical.

The study showed that the evaporation of the thin liquid layer under the bubble made a significant contribution to heat transfer only in the case of large bubbles. Much of the enhancement in heat transfer came from the wake region of the bubble.

In a more recent study, Kenning, Bustnes and Yan [107] reported experiments to study heat transfer to a single vapor bubble sliding on a downward facing heater surface. They have also used liquid crystal thermography to obtain the spatial variations in temperature along the heater plate. A high-speed video of bubble sliding along the plate was also simultaneously obtained. Experiments were conducted with water as the test liquid with low wall super heat (< 3 K) and for an angle of inclination of 15°. A thin layer of liquid was assumed to exist continuously, with no hot dry spots, between the bubble and the heater plate in the bubble contact area. The bubble contact area was less than the projected area of the bubble on the heater, and was estimated from the thermal images obtained. A transient conduction model was proposed for heat transfer across the thin liquid layer. Based on this model and wall temperature measurements the thin liquid layer thickness was estimated to be between 45 - 80 microns. For large non-spherical bubbles, present in high angles of inclination from vertical, the heat flow from the interface was more dominant than that from the thin liquid layer beneath the bubble. Only 10% of the heat input to the bubble comes directly from the wall, through the contact area. The remaining 90% of the heat flow was estimated to come from the previously heated liquid surrounding the bubble and from the wedge shaped region near the stagnation point on the bubble.

Bayazit, Hollingsworth and Witte [108] have also studied experimentally the enhancement of heat transfer due to sliding bubbles under boiling conditions. The surface was an electrically heated thin foil, the bottom side of which was exposed to the sliding bubbles. The upper side of the foil was coated with thermo liquid crystals (TLC)s. Heat transfer due to sliding motion of the bubbles was analyzed by studying the temperature response of TLC's. FC-87 was used as the test liquid and the bubbles were generated using a bubble generator developed for these experiments. The heater surface was at 12° inclination from horizontal and maintained at a constant heat flux of 1.6 kW/m^2. The liquid subcooling was maintained at 5 K for the experiment reported. Bubble sizes and shapes at various locations along the heater surface were reported. The wake behind the bubble was clearly shown in the thermal imagery obtained from TLC's. They have also proposed a model for the thickness of the micro-layer beneath the bubble, and estimated the temperature drop, which was compared with the experimental results. Three regimes of bubble motion were observed: spherical, ellipsoidal, and bubble-cap. Fig. 1.10 from Bayazit et al. [108] shows a collage of bubble images from a single test run with the test surface inclined at an angle of 12°, complete with a scale highlighting the image timings. From the Fig. 1.10, it can be seen that a bubble begins as a small hemispherical bubble, quickly grows and transforms into a much larger cap-shaped bubble. The large cap-shaped bubble at 560 ms from Bayazit et al. [108] is shown in Fig. 1.11. The wake behind these bubbles lies within the lines shown and marked by a shear layer which forms at the extremities of the bubble. The shear layer appears to contain small-scale turbulent structures which contribute to liquid agitation and therefore to an enhancement in heat transfer in this region. They have also commented that the transient response of the heater surface is an important issue in estimating the magnitude of augmentation of heat transfer in the case of sliding bubbles. A model for heat transfer within the microlayer underneath the bubble was used to infer the microlayer thickness. Preliminary results showed a microlayer thickness of 40-50 μm for these experiments.

Qiu and Dhir [109] presented the flow pattern and heat transfer associated with a bubble sliding along a downward facing heater surface. The test fluid was PF5060. The data was obtained for inclination angles of 5 - 75°. On a downward facing surface, a single bubble was created at an artificial cavity. The bubble shape changed from initially a sphere to elongated ellipsoids at the upper end of the surface. The smaller the inclinational angle to the horizontal was, the larger was the bubble in the sliding direction (see Fig. 1.12 - Right). An wedge-like liquid gap was observed underneath the sliding bubble on the downstream side for θ = 15 - 60°. Fig. 1.12 - Left shows the shape of a bubble sliding along the heater surface for θ = 15°. The apparent liquid wedge angle is seen to decrease when the bubble size increases. The apparent wedge angle, apparent length of the wedge and fraction of the bubble base length occupied by the wedge are listed in Table 1.3 for different heater inclination angles and at different locations along the flow path length. At

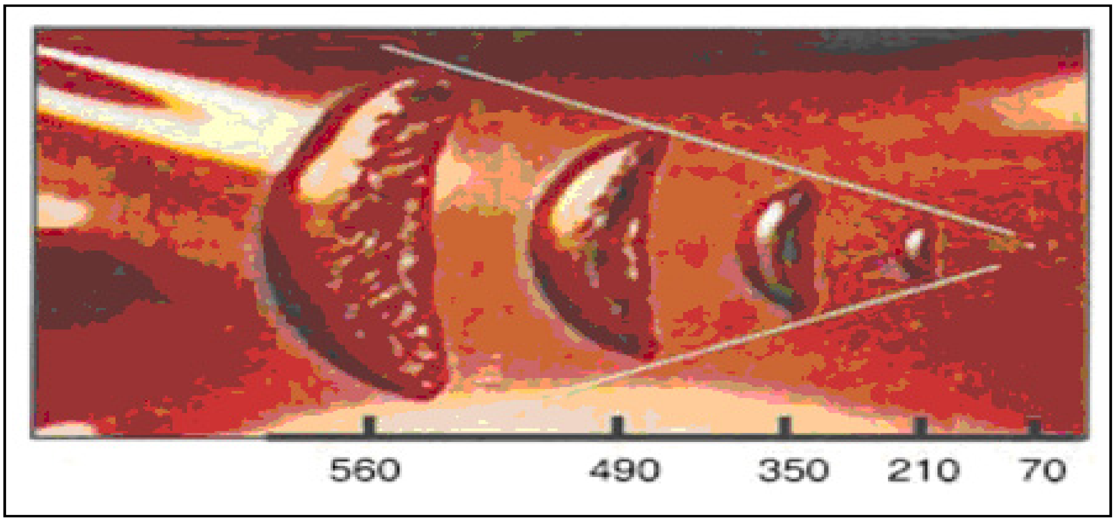

Figure 1.10: Collage of sliding bubble images with frame timing in ms [108].

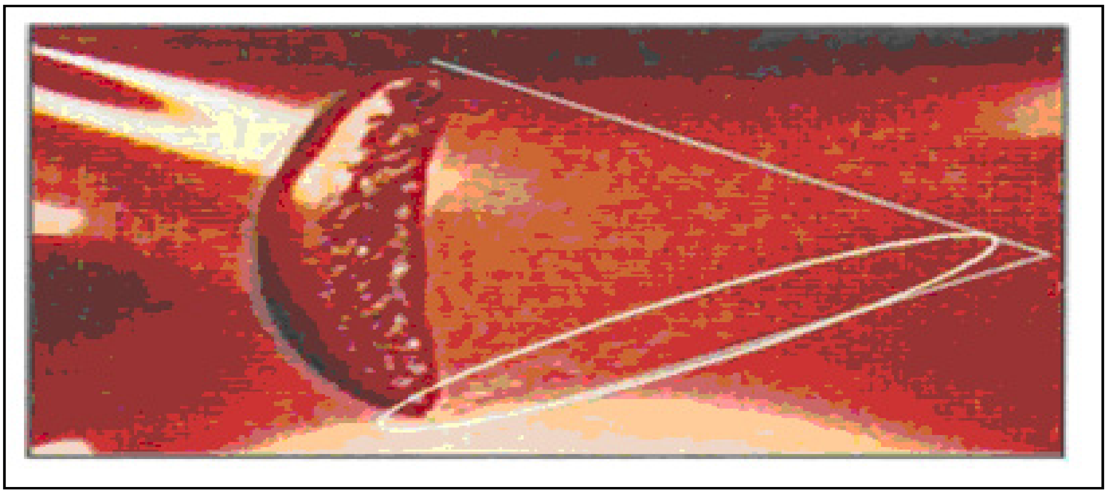

Figure 1.11: Large cap shaped bubble with a shear layer at the lower extremity [108].

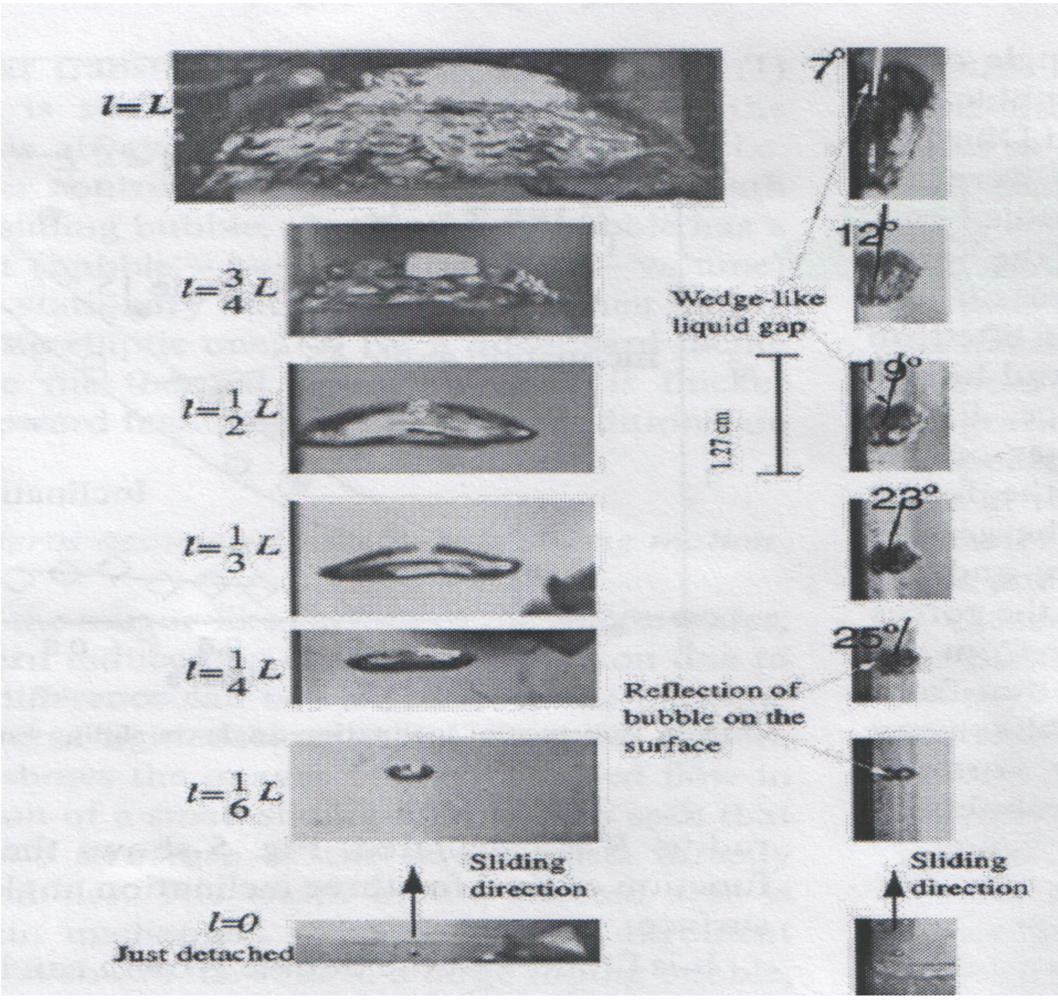

Figure 1.12: Pictures of sliding bubble shapes and liquid film layer viewed; Right: from below test surface, and Left: from the side of test surface [109].

the smaller inclination angle of 5°, bubbles were flat and in the bottom front of the bubble no apparent liquid wedge was observed. For higher inclination angles ($\geq 60°$), bubble size was small and no liquid wedge could be identified. For these cases bubble shapes are reported instead of wedge angle. Table 1.3 shows that the apparent wedge angle increases as heater inclination angle becomes larger. The apparent wedge length underneath the bubble increased with bubble size. It should be noted that the listed values are merely a rough estimation and defined as apparent dimension due to the curved wedge mouth and the lack of clarity of images.

Table 1.3: Apparent dimensions of liquid wedge under sliding bubble (apparent wedge angle\wedge length\portion of length) [109]

Heater Inclination Angle (°)	Distance From Cavity		
	l = 1/3L	l = 1/2L	l = 4/5L
5	No apparent wedge		
15	23°\0.9 mm\38%	19°\ 1.3 mm\37%	8°\ 3.0 mm\27%
32	(Not measured)		14°\1.4 mm\31%
45	19°\0.4 mm\17%	10°\0.8 mm\56%	24°\1.23 mm\41%
60	Spherical	60°\0.3 mm\60%	30°\0.4 mm\60%
75	Spherical	Spherical	Tear drop shape

Figure 1.13 from Qiu and Dhir [109] shows the wake structure of a bubble sliding along a submerged plate at an inclination angle of 15° from horizontal. Flow visualisation of the bubble's wake region confirmed that increased mixing levels in this region had the effect of increasing the heat transfer from the hot surface, by continuously bringing cooler liquid into contact with the hot surface and removing hot liquid from the surface in a constant cycle.

In order to have insight into the flow pattern around a sliding bubble, liquid velocity field around the bubble was determined using particle image velocimetry (PIV). The velocity vectors in the front and the back portions of a sliding bubble at $\theta = 30°$

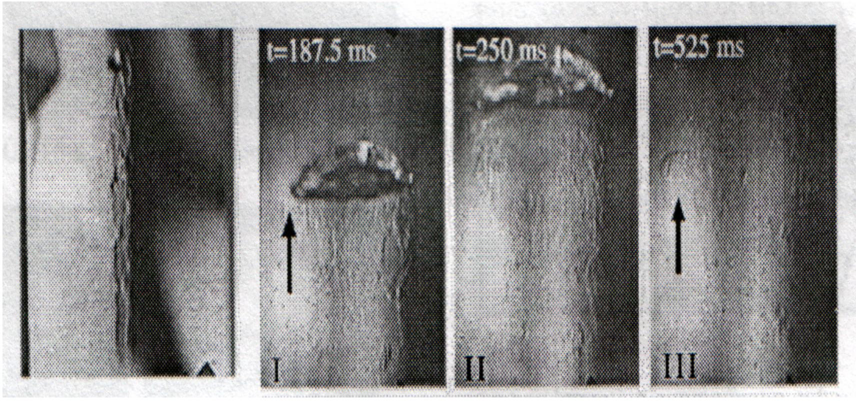

Figure 1.13: Wake structure of a sliding bubble viewed from below [109].

are shown in Figs. 1.14a and b respectively. The shape of the sliding bubble is clearly seen in these figures, with a wedge shaped gap at the leading edge of the bubble, between the bubble itself and the surface on which it slides. The PIV data shows that liquid at the front of the bubble is pushed outwards, away from the heater surface, and that at the outer interface of the bubble there is significant motion normal to the wall (heater surface). Towards the rear of the bubble, liquid is pulled inwards and a vortical structure is seen to exist, with the liquid velocities in this vortical region seen to be comparable with the overall bubble velocity. The liquid motion in this region enhances the heat transfer from the wall by bringing colder liquid from the surrounding region into the thermal layer.

A thin liquid wedge was observed between the front of the bubble and the heater surface. The angle and the length of the wedge were found to be a function of plate inclination angle and bubble size. Holographic interferometry was used to obtain the temperature field in the sub-cooled liquid. The flow pattern around and in the wake of the bubble was studied using PIV. Vortices were observed to shed from the wake of the bubble, resulting in a significant wall temperature drop.

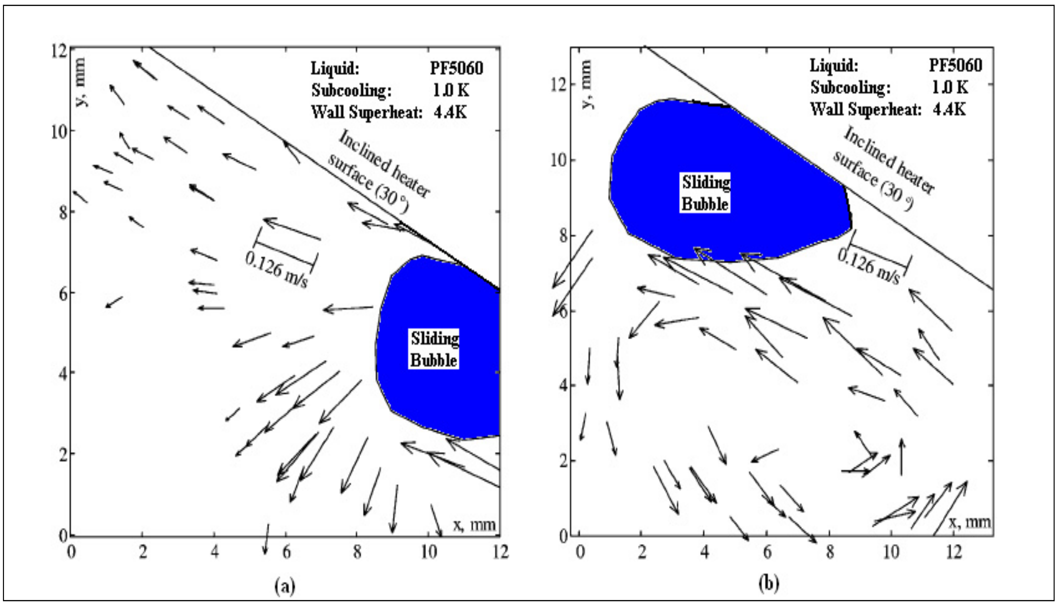

Figure 1.14: Shape and velocity field associated with a sliding bubble: (a) Front of the sliding bubble, (b) rear of the sliding bubble [109].

1.3 Motivation

It is clear from the literature review in the preceding sections that the existing studies on sliding bubble dynamics with and without convective heat transfer are mainly experimental in nature and, to the author's knowledge, to date no direct numerical computation on sliding bubble dynamics with heat transfer has been performed. Also, all studies on the influences of sliding bubble on heat transfer from surfaces considered boiling flow. In this case, bubbles grow as a result of phase change, leading to specific kind of sliding bubble flow.

Hence, it is proposed to study, by computational means, the convective heat transfer mechanisms involved in air bubble flow interacting with natural convection flow from heated flat plate immersed in water, using two-dimensional modelling. This first requires that a numerical code be built and suitability assessed.

1.4 Objectives

The primary objective of this research is to investigate the convective heat transfer mechanisms involved in air bubble flow interacting with natural convection flow from an inclined heated flat plate immersed in water, using two-dimensional numerical modelling. Specifically, the objectives are to

- develop a stable, fast and accurate numerical tool based on the Volume of Fluid (VOF) method to simulate unsteady two-dimensional two-fluid flow problems.
- validate the numerical tool by studying benchmark cases for both the single- and two-fluid flows with and without heat transfer and by comparing the numerical solutions to experimental results.
- investigate the accuracy for two-fluid flow with large property ratios across the interface.
- investigate the suitability of a two-fluid flow model when the interface is in contact with a surface.
- study the dynamics of isothermal ellipsoidal rising bubbles in an enclosed domain.
- study the dynamics of an ellipsoidal bubble sliding over an inclined flat plate held at different angles, without heat transfer.
- study the enhancement effect of an ellipsoidal air bubble on heat transfer from an inclined heated flat plate immersed in water, and the resulting flow patterns.

CHAPTER 2

MATHEMATICAL FORMULATION AND NUMERICAL METHODS

In this chapter, the mathematical formulation and the numerical methods adopted to solve the multi-fluid problems with or without heat transfer are presented. After describing the formulation, numerical assessment for single fluid flow computation will be made to establish the basis of the present approach. Then, multi-fluid computations will be assessed for various interface problems, such as translation of different interfaces and the Rider and Kothe [19] single vortex problem.

2.1 MATHEMATICAL FORMULATION

2.1.1 Governing Equations

The governing equations for unsteady, incompressible, immiscible two-fluid VOF-CSF model with heat transfer include the continuity, momentum, energy and VOF advection equations. They are written as:

$$\begin{aligned}
\nabla \cdot \overrightarrow{V} &= 0 && (2.1)\\
\rho \frac{\partial\left(\overrightarrow{V}\right)}{\partial t} + \nabla \cdot (\rho \overrightarrow{V}\overrightarrow{V}) &= -\nabla p + \nabla \cdot \tau + \rho \overrightarrow{g} + \overrightarrow{F_b} && (2.2)\\
\rho \frac{\partial (C_p T)}{\partial t} + \nabla \cdot (\rho C_p T \overrightarrow{V}) &= \nabla \cdot (\kappa \nabla T) && (2.3)\\
\frac{\partial f}{\partial t} + \nabla \cdot (f \overrightarrow{V}) - f(\nabla \cdot \overrightarrow{V}) &= 0 && (2.4)
\end{aligned}$$

where ρ is the fluid density, $\overrightarrow{V}$ the fluid velocity, p the scalar pressure, τ the viscous stress tensor, $\overrightarrow{F_b}$ a body force, $\overrightarrow{g}$ the acceleration due to gravity, C_p the specific heat capacity, κ the thermal conductivity, T the temperature and f the volume fraction.

Although the incompressible continuity equation is used, spacial variations in density will be accounted for in the momentum equations (see Section 2.2.1.3 for details). In Eq. (2.4), the velocity divergence, $\nabla \cdot \overrightarrow{V}$ is retained since $\nabla \cdot \overrightarrow{V}$ is not zero but $O(\epsilon)$, where ϵ is small number dependent on the machine epsilon and the convergence criterion of the Poisson pressure solution. The nonlinear advection term is written in conservative from. The viscous stress tensor τ is defined according to the Newtonian formulation:

$$\tau = 2\mu S. \qquad S = \frac{1}{2}\left[(\nabla\overrightarrow{V}) + (\nabla\overrightarrow{V})^T\right] \tag{2.5}$$

where S is the rate-of strain tensor and μ is the coefficient of dynamics viscosity.

The mixed properties used in Eqs. (2.2) & (2.3) can be defined as [19, 20]:

$$\rho = f\rho_g + (1-f)\rho_l \tag{2.6}$$

$$\mu = f\mu_g + (1-f)\mu_l \tag{2.7}$$

$$\kappa^{-1} = f/\kappa_g + (1-f)/\kappa_l \tag{2.8}$$

$$[\rho C_p] = f\rho_g\left(C_p\right)_g + (1-f)\rho_l\left(C_p\right)_l \tag{2.9}$$

$$C_p = \frac{[\rho C_p]}{\rho}$$

where the subscript l denotes liquid and the subscript g denotes gas. The scalar function f is generally known as the volume fraction or VOF function. The discrete representation of the function f is equal to 1 in cells fully filled by the liquid phase and equal to 0 in cells filled by the gas phase but takes a value bounded by 0 and 1 in cells where the interface lies (as shown in Fig. 2.14).

2.2 NUMERICAL METHODOLOGY

The numerical simulation of free-surface flow composed of two immiscible fluids involves two coupled tasks: (1) resolve the flow field and temperature and (2) update the position of the interface. The first task is completed by solving the Navier-Stokes equations and the energy equation. It is implemented numerically via the SIMPLE method, where the velocity is first determined from the momentum equations with the initialised pressure field not satisfying continuity. If the pressure field is correct, the resulting velocity will satisfy continuity. As the pressure is unknown, there is a need to calculate it. In the second step, the Pressure Poisson Equation (PPE) is solved and the pressure field is used to correct the preliminary velocity prediction, thus recovering the continuity constraint. Then, the energy equation is solved to compute the temperature field. The second task is carried out via the Volume of Fluid (VOF) method [16]. The VOF method updates the field of volume fraction of one fluid in each cell. The advantage of the VOF method is that there is no major constraint due to topological changes of interface. Thus, the VOF method has been widely used to track the interface of two immiscible fluids, such as water and air. In the present work, the surface tension is taken into account using the Continuum Surface Force(CSF) method [60], where the surface force is transformed into a body force, F_b, which is non-zero only in an interface region of limited thickness.

2.2.1 Fluid Flow Field Equation Solver

2.2.1.1 Finite Volume Formulation

The equations are discretised by Finite Volumes on an orthogonal staggered C-grid (Fig. 2.1), with the primary variables evaluated at the cell centers. The convective flux coefficients are derived by a first order upwind scheme while the diffusive flux coefficients are obtained by central differencing and the equations are discretised in time by implicit first order Euler differencing. The discretised forms of Eqs. (2.1) and (2.2) can be written using a symbolic operator notation:

$$\Omega \cdot \frac{\rho^n}{\delta t}\left[(u_i)^{n+1} - (u_i)^n\right] = H\left(u_i^{n+1}\right) - \Omega_{u_i} \cdot Grad_{u_i}\left(p^{n+1}\right) + \Omega_{u_i} \cdot S_i \tag{2.10}$$

$$Div_p\left(u^{n+1}\right) = 0 \tag{2.11}$$

where the superscript $n+1$ and n represent two successive time steps, the subscript i refers to the coordinate directions and S_i is the momentum source term. In Eq. (2.10), $Grad_{u_i}\left(p^{n+1}\right)$ is the i component of the discrete gradient operator approximated by central differencing at the u_i - momentum cell centre. Ω_{u_i} results from the Finite Volume integration and is the corresponding cell volume. In Eq. (2.11), $Div_p\left(u\right)$ is the discrete divergence operator over the continuity or pressure cell. It is evaluated by integrating the

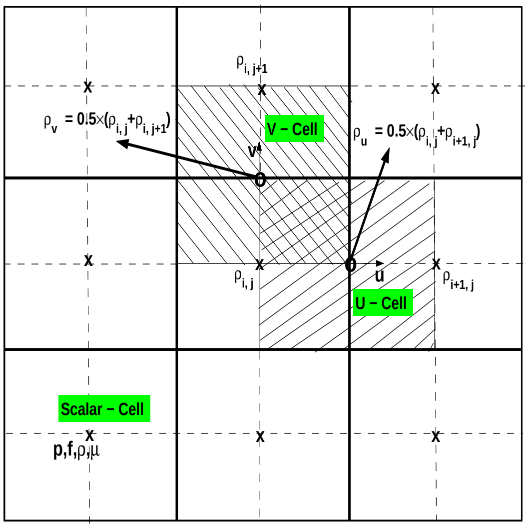

Figure 2.1: The schematic diagram of staggered grid arrangement.

continuity equation, Eq. (2.1), and applying Gauss' divergence theorem, giving:

$$Div_p\left(u^{n+1}\right) = \sum_l \left(\Gamma n \cdot u^{n+1}\right)_l \tag{2.12}$$

The summation is carried out over the continuity cell faces and all terms indexed with the subscript l are evaluated at the corresponding face centre. n is the outward unit normal vector to the cell face and Γ is the cell face surface area.

The operator $H\left(u_i^{n+1}\right)$ accounts for the diffusive and convective terms:

$$H\left(u_i^{n+1}\right) = div_{u_i}\left(\rho^n u_i^{n+1}\mathbf{u}^{n+1} - \mu^n \mathbf{Grad}_{u_i}\left(u_i^{n+1}\right)\right) \tag{2.13}$$

where ρ^n is the average cell density for momentum equations calculated as shown in Fig. 2.1. div_{u_i} is the discrete divergence operator over the u_i -momentum cell and is approximated by integration over the u_i -momentum cell and application of the Gauss divergence theorem giving:

$$H\left(u_i^{n+1}\right) = \sum_l \left[\Gamma n \cdot \left(\rho^n u_i^{n+1}\mathbf{u}^{n+1} - \mu^n \mathbf{Grad}_{u_i}\left(u_i^{n+1}\right)\right)\right]_l \tag{2.14}$$

In this case the summation is carried out over the u_i -momentum cell faces. $\mathbf{Grad}_{u_i}\left(u_i^{n+1}\right)$ is the discrete gradient operator to be evaluated at each cell face centre. $H\left(u_i^{n+1}\right)$ is a non-linear operator and, in order to solve Eqs. (2.10) and (2.11), it must be linearised or split according to the solver's splitting methodology [110]. A similar discretisation is used to solve the energy equation, Eq. (2.3). We assume (i) constant fluid properties in each fluid when modelling isothermal flows and variable fluid properties in each fluid when modelling non-isothermal flows; (ii) phase change and pressure work and viscous dissipation in the energy equation are ignored.

2.2.1.2 SIMPLE Pressure Correction Method

The SIMPLE pressure-velocity coupling method [111, 112] is implemented in this study to solve the set of Navier-Stokes equations. The method is based on an iterative segregated solution of the momentum equations and of a pressure correction equation within each time step. The pressure correction equation provides the necessary coupling between pressure and velocity. It does not exist a priori as one of the Navier-Stokes equations but is derived from the continuity and momentum equations. The first step in this iterative method is to obtain an estimate of the velocity field from a guess value of the pressure p^* , which may be its value at the previous time step p^n. This predictor step involves the solution of the following implicit equations for u_i^* .

$$\left[\Omega_{u_i} \cdot \frac{\rho^n}{\delta t} - A_0\right] (u_i^*) = H' (u_i^*) - \Omega_{u_i} \cdot Grad_{u_i} (p^n) + \Omega_{u_i} \cdot S_i + \Omega_{u_i} \cdot \frac{\rho^n}{\delta t} (u_i^n) \tag{2.15}$$

where $A_0(u_i^*) = H (u_i^*) - H' (u_i^*)$ is the central part of the operator $H (u_i^*)$. This splitting of the operator means that the central part of the operator is treated implicitly in the corrector step (Eq. (2.17)) which has been shown to reduce the error amplification factors for a given δt [16].

The explicit terms in Eq. (2.15) include the discrete form of the source term from Eq. (2.10) but also the pressure gradients as well as an additional term due to the flow velocity at the previous time step. The latter term must be retained in the derivation of the pressure correction equation since it is not necessarily divergence free. A simplified discrete correction equation can be derived by subtracting Eq. (2.15) from:

$$\left[\Omega_{u_i} \cdot \frac{\rho^n}{\delta t} - A_0\right] \left(u_i^{n+1}\right) = H' (u_i^*) - \Omega_{u_i} \cdot Grad_{u_i} \left(p^{n+1}\right) + \Omega_{u_i} \cdot S_i + \Omega_{u_i} \cdot \frac{\rho^n}{\delta t} (u_i^n) \tag{2.16}$$

giving:

$$\left[u_i^{n+1} - u_i^*\right] = -\Omega_{u_i} \cdot \left[\Omega_{u_i} \cdot \frac{\rho^n}{\delta t} - A_0\right]^{-1} \cdot Grad_{u_i} \left(p^{n+1} - p^n\right) \tag{2.17}$$

Combining Eq. (2.17) and Eq. (2.11) gives the pressure correction equation, which can be solved for $(p^{n+1} - p^n)$:

$$Div_p \left[\Omega_{u_i} \cdot \left(\Omega_{u_i} \cdot \frac{\rho^n}{\delta t} - A_0\right)^{-1} \cdot Grad_{u_i} \left(p^{n+1} - p^*\right)\right] = Div_p \left(u_i^*\right) \tag{2.18}$$

Once Eq. (2.18) is solved, $\left[u_i^{n+1} - u_i^n\right]$ can be evaluated from Eq. (2.11). The semi implicit operator splitting of Eq. (2.16) (taking $H'\left(u_i^*\right)$ on the right hand side instead of $H'\left(u_i^{n+1}\right)$) represents the most significant approximation of the SIMPLE method. It leads to a pressure correction giving a velocity field that satisfies the momentum equations reasonably well but does not generally give satisfactory continuity residuals. Depending on the flow parameters, several iterations within each time step may be required to achieve momentum and continuity residual convergence. Alternative splitting schemes have been developed [17] but, for the sake of simplicity, are not considered in this study.

The solver must include appropriate boundary and initial conditions. All boundaries are treated as walls and all boundary conditions are of the Dirichlet type for the velocity field. For the temperature field, both Dirichlet and Neumann boundary conditions are used for walls. The fluid is initially at rest throughout the domain and the initial pressure is specified according to the hydrostatic law.

The linearised momentum equations have been solved using the Krylov subspace iterative method, while the pressure correction equation is solved with a Multigrid solver. For any given numerical test, the same iterative method is used as a smoother for the momentum equations and for the Multigrid scheme at all grid levels. The iterative solver considered is an RILU preconditioned BiCGStab with an RILU parameter of 0.95. The Multigrid iterations involve repeated calls of the μ-cycles until the specified convergence criterion is met. The absolute residuals used to test convergence are evaluated using an l2 norm. A continuity residual lower or equal to 10^{-4} is necessary for the unsteady multifluid flow solver to converge. This, in turn, requires that the momentum and pressure correction residuals be reduced to at least 10^{-7}. In this study, all numerical tests were performed with convergence threshold residuals for the momentum and pressure correction equations equal to 10^{-8}.

2.2.1.3 Density Averaging

Equation (2.15) does not account for changes in density between the momentum cell faces when modelling the convective fluxes of $H'(u_i^*)$. The mean density calculated at the centre of the momentum cell as shown in Fig. 2.1 is used instead for all terms of the momentum equations.

On the other hand, the term, $\left(\Omega_{u_i} \cdot \frac{\rho^n}{\delta t} - A_0\right)$ in the pressure correction (Eq. (2.18)), does account for the variation in density across the scalar cell. It is evaluated at the centres of scalar cell faces coinciding with the centres of neighbouring u and v momentum cells as shown in Fig. 2.1. The density at the centres of the cell faces is calculated based on an arithmetic mean value (for example $\rho_{i+1/2,j} = 0.5 \times (\rho_{i,j} + \rho_{i+1,j})$). The term, A_0 is calculated using the non-linear operator, H (Eq. (2.13)) which accounts for the diffusive and convective fluxes. It is worth highlighting that, the present density modelling approach differs from that of the projection method [72] generally used in all published numerical studies of multi-fluid flow by VOF methods.

2.2.2 Surface Tension Force Estimation

This section is a brief summary of the CSF calculation of the surface force terms in the momentum equations which is due to Kothe et al. [72] and Brackbill et al. [60]. The CSF formulation makes use of the fact that numerical models of discontinuities in finite volume and finite difference schemes are really continuous transitions within the fluid properties. The "color" function, f, varies smoothly from one fluid to another over a distance of $O(h)$, where h is a length comparable to the resolution afforded by a computational mesh with spacing δx. It is not appropriate, therefore, to apply in a finite difference scheme a pressure jump induced by surface tension at a free surface "discontinuity". Surface tension should act everywhere within the transition region, namely through the volume force F_b.

The volume force in the CSF model is easily calculated by taking first and second order spatial derivatives of the color data. At each point within the free surface transition region, a cell centered value F_b is defined which is proportional to the curvature κ of the constant VOF surface at that point. The volume force always tends to force the free surface to seek a minimum surface energy configuration. Reconstruction models, on the other hand, tend to introduce numerical noise from computed surface pressures, often leading to unphysical free surface disruptions in the form of spurious currents. In addition to providing a more accurate finite difference representation of surface tension without the topological restrictions, the CSF model is easy to implement computationally [72].

The dynamics stress balance is realised through the CSF-ALE model [60] incorporated in the momentum equation, Eq. (2.2), by introducing a volume force F_b. The localised volume force F_b is calculated from the volume fraction data by

$$F_b = \sigma \kappa(x) \widetilde{\mathbf{n}} \frac{\nabla \widetilde{f}(x)}{[f]} \tag{2.19}$$

where κ is the curvature of surface and the $\sim$(tilda) denotes filtered (smoothed) values and the square bracket denotes the difference between the maximum and the minimum values of the function inside the brackets. The above model produces an artificial acceleration in the lighter fluid when the density ratio of the two fluids is large. This acceleration is the main source of spurious currents'. In problems where the surface tension forces dominate the viscous forces, the spurious currents can cause interface oscillations and deform or destroy the interface. Brackbill et al. [60] recommended adding a density scaling factor in order to reduce the formation of such spurious accelerations and proposed the following equation instead of Eq. (2.19):

$$F_b = \sigma \kappa(x) \widetilde{\mathbf{n}} \frac{\nabla \widetilde{f}(x)}{[f]} \frac{\rho(x)}{[\rho]} \tag{2.20}$$

where $\rho(x)$ is the local value of the density obtained by Eq. (2.6) and $[\rho]$ is the difference between the density of the heavier and the lighter fluids.

The interface characteristic parameters, the outward normal vector $\widetilde{n}$ and curvature κ, are calculated as

$$\widetilde{\mathbf{n}} = (\widetilde{n}_x, \widetilde{n}_y) = -\nabla f, \qquad \hat{\mathbf{n}} = \frac{\widetilde{\mathbf{n}}}{|\widetilde{\mathbf{n}}|} \tag{2.21}$$

$$\kappa = (\nabla \cdot \hat{\mathbf{n}}) = -\frac{1}{\widetilde{\mathbf{n}}}\left[\left(\frac{\widetilde{\mathbf{n}}}{|\widetilde{\mathbf{n}}|} \cdot \nabla\right) |\widetilde{\mathbf{n}}| - (\nabla \cdot \widetilde{\mathbf{n}})\right] \tag{2.22}$$

Brackbill et al. [60] have rewritten the curvature in terms of $\widetilde{n}$ and $|\widetilde{n}|$ to ensure that the main contribution from the finite difference approximation of κ, comes from the center of the transition region rather than the edges. This can be achieved by an Arbitrary Lagrangian Eulerian (ALE)-like scheme or MAC method. In both approaches, the color function is chosen to be the fluid density, which resides at cell centers. The curvature $\kappa_{i,j}$ therefore also will be cell-centered. Both approaches were tested and it was found that the ALE scheme works better than the MAC method with the present solver giving more stable flows. As the governing equations are discretised on the staggered grid in the present solver, the surface tension forces have to be calculated at cell faces for the momentum equations. It is found that an averaging of F_b from cell centers gives better results for the staggered grid approach. Hence the ALE-like scheme, discussed in the nest section, is used in the present solver.

The CSF method has the ability to use the smoothed or mollified VOF function $\widetilde{f}_{i,j}$ for the calculation of the curvature $\kappa_{i,j}$ in the volume force Eq. (2.20), which is different from the unsmoothed function $f_{i,j}$ used to calculate the normal vector in that equation. This enables the algorithm to calculate a smoother curvature for accuracy, and has been found to decrease the number of pressure solution iterations required.

The smoothed VOF function is computed by convolving f with a B-Spline of degree l (de Boor [113]; Brackbill et al. [60]), $\beta^{(l)}(|X' - X|; H)$, (with $l = 2$) where $\beta^{(l)} \neq 0$ only for $|X' - X| < (l + 1)h/2 = 3h/2$. The smoothed VOF function is given by:

$$\widetilde{f}_{i,j} = \sum_{i',j'=1}^{k} f_{i,j} \beta^{(l)}\left(x'_{i',j'} - x_{i,j}\ ; h\right) \beta^{(l)}\left(y'_{i',j'} - y_{i,j}\ ; h\right) \tag{2.23}$$

where the sum gathers contributions from the nine values (for $l = 2$ in 2-D) of $f_{i,j}$ within the support of β^2. In our case this formulation becomes simply:

$$\widetilde{f}_{i,j} = \frac{9}{16} f_{i,j} + \frac{3}{32}\left(f_{i+1,j} + f_{i-1,j} + f_{i,j+1} + f_{i,j-1}\right) \tag{2.24}$$

$$+\frac{1}{16}\left(f_{i+1,j+1} + f_{i+1,j-1} + f_{i-1,j+1} + f_{i-1,j-1}\right) \tag{2.25}$$

This formula may be applied iteratively by multiple passes through the mesh for increased degrees of smoothing. Our experience has shown that one to three passes are optimal. Hence most calculations are carried out with one pass.

2.2.3 ALE-like Scheme:

Vertex-centered normal vectors are obtained by differentiating the color function in the four surrounding cells. For example, the normal vector at the top right vertex of cell (i, j) is given by

$$\widetilde{n}_{x\ i+1/2,\ j+1/2} = \left(\frac{\widetilde{f}_{i+1,j} + \widetilde{f}_{i+1,j+1} - \widetilde{f}_{i,j} - \widetilde{f}_{i,j+1}}{2\Delta x}\right) \tag{2.26}$$

$$\widetilde{n}_{y\ i+1/2,\ j+1/2} = \left(\frac{\widetilde{f}_{i,j+1} + \widetilde{f}_{i+1,j+1} - \widetilde{f}_{i,j} - \widetilde{f}_{i+1,j}}{2\Delta y}\right) \tag{2.27}$$

The curvature follows from an indirect differentiation of the unit normal $\widetilde{n}$, as given by the two terms on the RHS of Eq. (2.22). The first term, the derivative of $|\widetilde{n}|$ along the cell-centered unit normal $\widehat{n}_{i,j}$, is given by

$$\left(\frac{\widetilde{n}_{i,j}}{|\widetilde{n}_{i,j}|} \cdot \nabla\right)|\widetilde{n}| = \left(\frac{\widetilde{n}_x}{|\widetilde{n}|}\right)_{i,j}\left(\frac{\partial|\widetilde{n}|}{\partial x}\right)_{i,j} + \left(\frac{\widetilde{n}_y}{|\widetilde{n}|}\right)_{i,j}\left(\frac{\partial|\widetilde{n}|}{\partial y}\right)_{i,j} \tag{2.28}$$

$$= \left(\frac{\widetilde{n}_x}{|\widetilde{\mathbf{n}}|}\right)^2_{i,j}\left(\frac{\partial\widetilde{n}_x}{\partial x}\right)_{i,j} + \left(\frac{\widetilde{n}_x\widetilde{n}_y}{|\widetilde{\mathbf{n}}|^2}\right)_{i,j}\left(\frac{\partial\widetilde{n}_x}{\partial y} + \frac{\partial\widetilde{n}_y}{\partial x}\right)_{i,j} + \left(\frac{\widetilde{n}_y}{|\widetilde{\mathbf{n}}|}\right)^2_{i,j}\left(\frac{\partial\widetilde{n}_y}{\partial y}\right)_{i,j} \tag{2.29}$$

Other vertex-centered normal vectors can be found in a similar fashion by translating the i and j indices in the above expression. The curvature in Eq. (2.22) is calculated at cell centers. The divergence of $\widetilde{n}$ for cell $(i,\ j)$ is calculated from the vertex-centered normals and is given by

$$(\nabla.\widetilde{n})_{i,j} = \left(\frac{\partial\widetilde{n}_x}{\partial x}\right)_{i,j} + \left(\frac{\partial\widetilde{n}_y}{\partial y}\right)_{i,j} \tag{2.30}$$

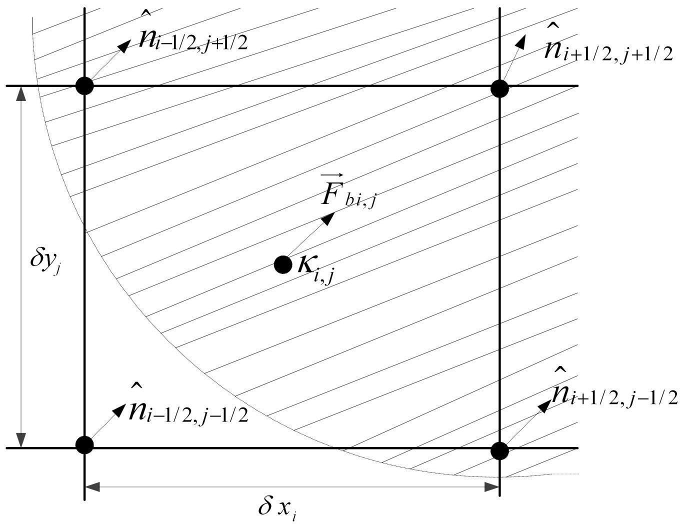

Figure 2.2: A cell centered volume force due to surface tension $F_{b\ i,j}$ is derived from a free surface curvature κ at the cell center and unit normals $\widehat{n}$ at the 4-cell vertices.

where

$$\left(\frac{\partial \widetilde{n}_x}{\partial x}\right)_{i,j} = \frac{1}{2\Delta x}\left[\widetilde{n}_{x\ i+1/2,\ j+1/2} + \widetilde{n}_{x\ i+1/2,\ j-1/2} - \widetilde{n}_{x\ i-1/2,\ j+1/2} - \widetilde{n}_{x\ i-1/2,\ j-1/2}\right] \tag{2.31}$$

$$\left(\frac{\partial \widetilde{n}_y}{\partial y}\right)_{i,j} = \frac{1}{2\Delta y}\left[\widetilde{n}_{y\ i+1/2,\ j+1/2} + \widetilde{n}_{y\ i+1/2,\ j-1/2} - \widetilde{n}_{y\ i-1/2,\ j+1/2} - \widetilde{n}_{y\ i-1/2,\ j-1/2}\right] \tag{2.32}$$

The cell-centered normal is the average of vertex normals:

$$\widetilde{n}_{x\ i,j} = \frac{1}{4}\left(\widetilde{n}_{x\ i+1/2,\ j+1/2} + \widetilde{n}_{x\ i+1/2,\ j-1/2} + \widetilde{n}_{x\ i-1/2,\ j+1/2} + \widetilde{n}_{x\ i-1/2,\ j-1/2}\right) \tag{2.33}$$

$$\widetilde{n}_{y\ i,j} = \frac{1}{4}\left(\widetilde{n}_{y\ i+1/2,\ j+1/2} + \widetilde{n}_{y\ i+1/2,\ j-1/2} + \widetilde{n}_{y\ i-1/2,\ j+1/2} + \widetilde{n}_{y\ i-1/2,\ j-1/2}\right) \tag{2.34}$$

The face centered values of $F_{bi,j}$ at the right and top faces are required for the momentum equations and are calculated from cell centered values:

$$F_{bi+0.5,j} = 0.5 \times (F_{bi+1,j} + F_{bi,j}) \tag{2.35}$$

$$F_{bi,j+0.5} = 0.5 \times (F_{bi,j+1} + F_{bi,j}) \tag{2.36}$$

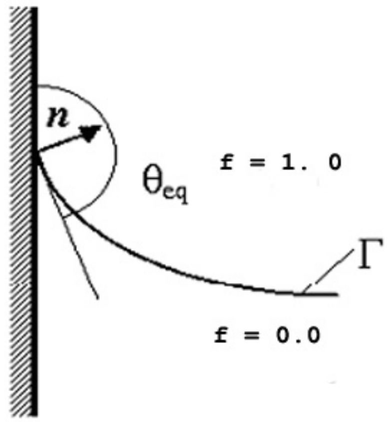

Figure 2.3: Schematic diagram of the static contact angle θ_{eq} for a wetting fluid.

2.2.4 Wall Adhesion - Boundary Condition

A special phenomenon, called wall adhesion, occurs at the contact point between the interface and the solid wall. The forces between the molecules of a fluid and the molecules of a solid give rise to adhesion between them. The fluid molecules with the strongest adhesion force crowd towards the solid and 'wets' the wall. This effect needs to be accounted for and can be prescribed as a contact angle (wetting angle) between the interface and the solid wall. This angle is not only a property of the fluid but also dependent on the smoothness and geometry of the wall. Brackbill et al. [60] defined the normal to the interface $\widehat{n}$ at the wall (as shown in Fig. 2.3) as follows:

$$\widehat{n} = \widehat{n}_{wall}\ \cos\theta_{eq} + \widehat{n}_t\ \sin\theta_{eq} \tag{2.37}$$

where θ_{eq} is the static contact angle, $\widehat{n}_t$ lies in the wall and is normal to the contact line between the interface and the wall, and $\widehat{n}_{wall}$ is the unit wall normal directed into the wall. The unit normal $\widehat{n}_t$ is computed using the equation below with the fluid color $\widetilde{f}$ reflected at the wall.

$$\widehat{n}_t = -\frac{\nabla f}{|\nabla f|} \tag{2.38}$$

As explained by Kothe et al. [72], using static contact angle is a physical approximation because θ_{eq} is assumed to be a constant. when in reality it depends on the local wall and fluid conditions (i.e., velocity, viscosity and surface tension). However, the mechanism of dynamic contact angle is complex and has not been resolved yet. The dynamic contact angle depends in a complex way on material and fluid dynamics properties. Studies have used the static contact angle approach successfully [72, 114, 16] to model multi-fluid flows including bubble flow. It is still uncertain however, whether this approach is suitable when the air-water interface does not necessarily interact the solid surface, for example as in the case of a bubble sliding along the solid surface.

2.2.5 Numerical Stability

The numerical difference equations are subject to linear numerical stability conditions that are detailed in Hirt and Nichols [16]. Material cannot move more than one cell in one time step yielding the Courant condition.

The timestep Δt at time t^n is determined by restrictions due to the CFL condition, gravity, and surface tension [60];

$$\Delta t \leq \left(\sqrt{\frac{1}{4\pi\gamma}} \Delta x^{3/2}, \frac{\Delta x}{|\mathbf{U^n}|}, \frac{\Delta x}{\sqrt{2g\Delta x}} \right) \tag{2.39}$$

2.2.6 Validation - Single Phase Flow

To validate the Navier Stokes solver, three single phase benchmark problems are considered. The governing equations, Eqs. (2.1) - (2.4), are solved with volume fraction, $f = 0$ for single-fluid flow problems. The first problem considered is the laminar lid-driven cavity flow to verify the viscous terms. The second test case is the buoyancy driven flow of air with the Boussinesq approximation in a square cavity with vertical walls differentially heated. This case demonstrates the coupling of energy equations with the flow equations. However, convective heat transfer in water can not be modelled using the Boussinesq approximation, so a variable thermal property model has also been included and validated against published experimental results.

2.2.6.1 Lid Driven Cavity Flow

The lid driven cavity flow problem is considered here to provide an outline solver validation for single fluid flow modelling. The Reynolds number considered is 1000 and corresponds to a lid horizontal velocity of 1 m/s with cavity's dimensions of 1m× 1m. The horizontal velocity u along the vertical cavity centreline and the vertical velocity v along the horizontal cavity centreline, at 30 s physical time, which can be considered to represent steady state, are compared in Fig. 2.4 to benchmark data from [115]. These results were obtained with a V-cycle Multigrid scheme using the SSOR smoother and six grid levels. The discrepancies shown between the resulting velocity profiles and the benchmark data are consistent with observations by Gjesdal et al [116]. They can be attributed to the relatively high level of numerical diffusion of the upwind scheme and can be corrected by substituting a higher order advection approximation (not done here) as shown by Gjesdal et al. [116] who implemented a 1/3 kappa discretisation scheme.

2.2.6.2 Buoyancy-induced convection

Buoyancy driven flows, especially in two-dimensions, have been the subject of extensive study for over 50 years. de Vahl Davis [117] presented a study which provides a benchmark solution for the problem of a two-dimensional flow of Boussinesq fluid in a square cavity, which is heated on the left, cooled on the right, and insulated on the top and bottom boundaries. The results of de Vahl Davis [117] were produced, for Rayleigh numbers in the range $1 \times 10^3 - 1 \times 10^6$, using a stream-vorticity formulation discretised by a second-order finite difference method on a regular mesh. Later, more accurate results obtained by a second order finite volume method on higher resolution non-uniform grids were presented in Hortmann et al. [118]. In addition to the study by de Vahl Davis [117] and Hortmann et al. [118]) additional results have been reported, e.g. Shyy(1994), Ferziger and Peric (1996), and Wan et al. (2001).

The governing equations, Eqs. (2.1) - (2.4), are used to model the buoyancy induced convection of air with the Boussinesq approximation. This means that ρ is assumed constant in all terms except in the body force term of the y momentum equation due to

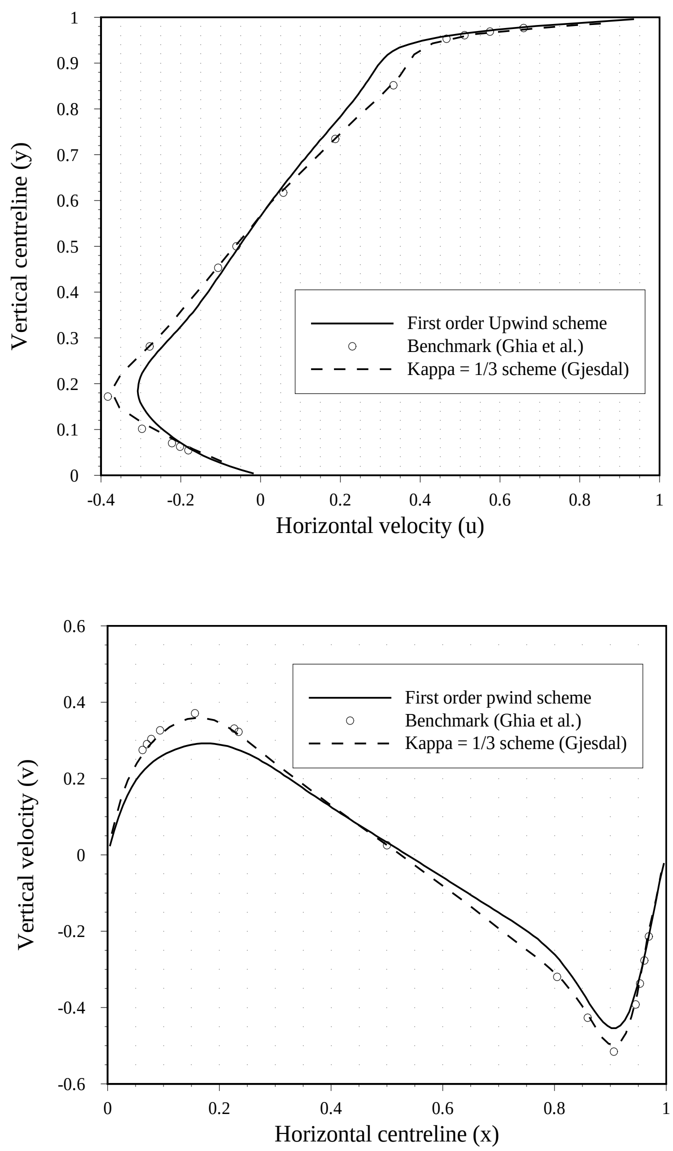

Figure 2.4: Comparison of velocity fields for Lid Driven Cavity Flow. Top: u-velocity along vertical axis. Bottom: v-velocity along horizontal axis.

the gravity acceleration where it is replaced by $\rho_0(1-\beta(T-T_0))$. This term times the gravity acceleration is the buoyancy force and it couples the momentum equation with the energy equation. Here β represents the coefficient of thermal expansion and is the thermodynamic property of the fluid that provides a measure of the amount by which the density changes in response to a change in temperature at constant pressure. This is given by

$$\beta = -\frac{1}{\rho}\left(\frac{\partial \rho}{\partial T}\right)_p \tag{2.40}$$

In the Boussinesq approximation, the density difference, which is the main driving force for the flow, is approximated as a pure temperature effect (i.e., the effect of pressure on density is neglected). This approximation is employed very extensively for natural convection. An important condition for the validity of this approximation is that $\beta(T-T_0)) \ll 1$. Therefore, the approximation is valid for small temperature differences. However, it is not valid near the point of maximum density for water at 4°C, where β is zero and changes sign as the temperature varies across this value. For large temperature differences, this approximation is generally not applicable.

The dimensional parameters describing the problem are the Rayleigh number (Ra) and Prandtl number(Pr), defined as

$$\begin{aligned} Pr &= \nu/\alpha \\ Ra &= \frac{g\beta\Delta T L^3}{\nu\alpha} \end{aligned}$$

where $\triangle T = T_h - T_c$ is the difference between the hot wall temperature, T_h, and the cold wall temperature, T_c, and α is the thermal diffusivity. All the thermal properties are calculated at the reference temperature $T_0 = (T_h + T_c)/2$. The free convection problems we consider below are completely determined by the Prandtl and Rayleigh numbers.

Differentially heated square cavity: Simulation of the free convection is performed in a differentially heated two-dimensional square cavity (Fig. 2.5). The problem involves a square box of side length $L_x = L_y = L$ filled with a Boussinesq fluid characterized by a Prandtl number, $Pr = 0.71$. The vertical walls are kept at a constant temperature, T_h and T_c, respectively while the horizontal lid and bottom are insulated

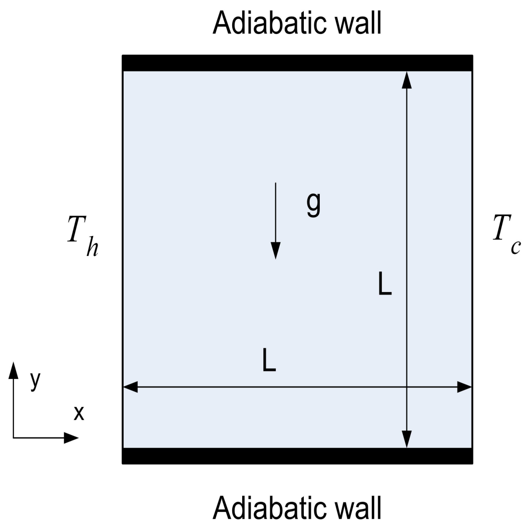

Figure 2.5: Geometry and boundary conditions for the thermally driven cavity problem.

with zero heat flux. The boundary condition for the velocity is no-slip on the four walls. The direction of gravity is downwards, in the negative y-direction.

The computations are made for $Ra = 10^3,\ 10^4,\ 10^5$ and 10^6, all in the laminar flow regime. The time step is chosen smaller for larger Ra since the velocity is known to increase with Ra from previous published results. The streamlines and isotherms are shown in Figs. 2.6 - 2.9 for $Ra = 10^3,\ 10^4,\ 10^5$ and 10^6, respectively. Simulations are performed using a grid of 161×161 points. The grid size is chosen in order to be able to compare with de Vahl Davis' results under the same conditions. The results show good agreement with the benchmark solutions of de Vahl Davis [117] and Hortmann et al. [118]. As Ra increases, one observes (i) the skewed symmetry solutions of the velocity and temperature fields with respect to the cavity centre, and (ii) higher heat transfer rate along the hot walls.

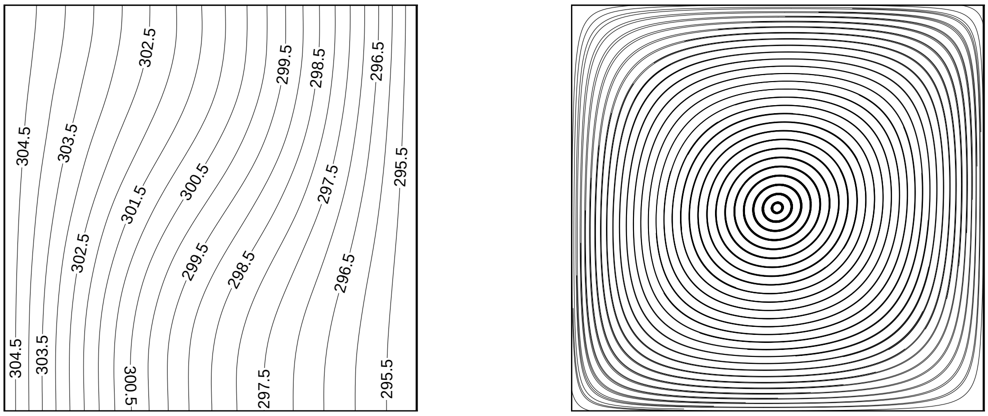

Figure 2.6: Streamlines and temperature distribution for the side-heated buoyant cavity flow at $Ra = 10^3$

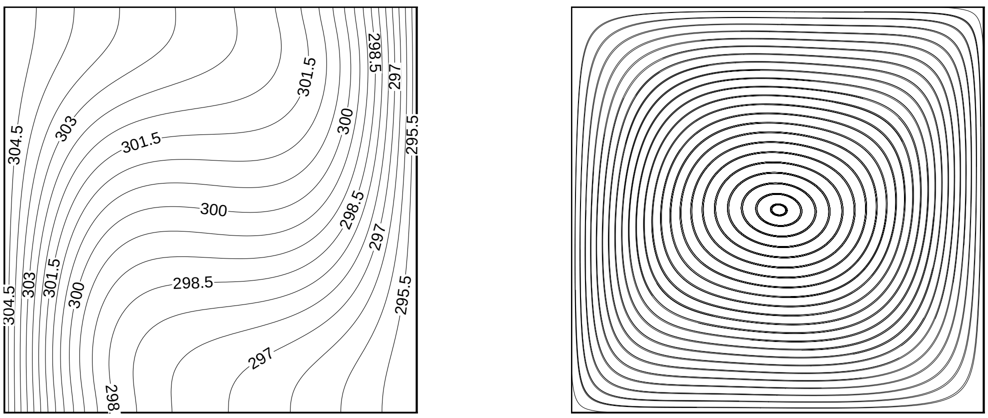

Figure 2.7: Streamlines and temperature distribution for the side-heated buoyant cavity flow at $Ra = 10^4$

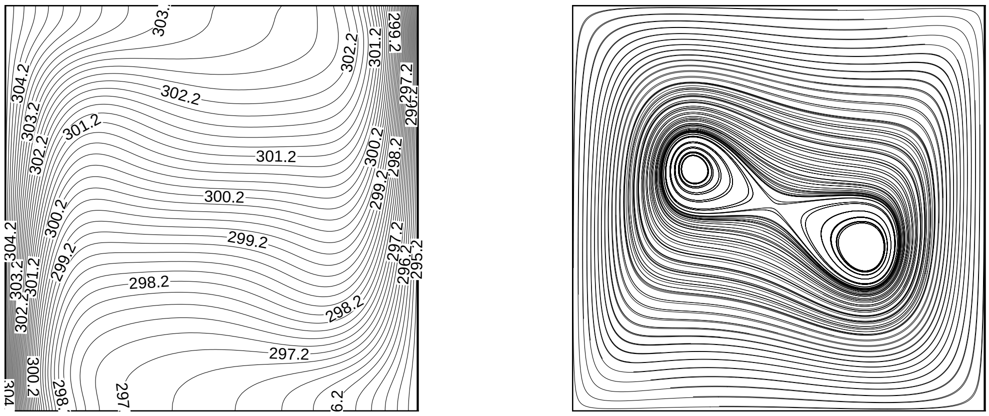

Figure 2.8: Streamlines and temperature distribution for the side-heated buoyant cavity flow at $Ra = 10^5$

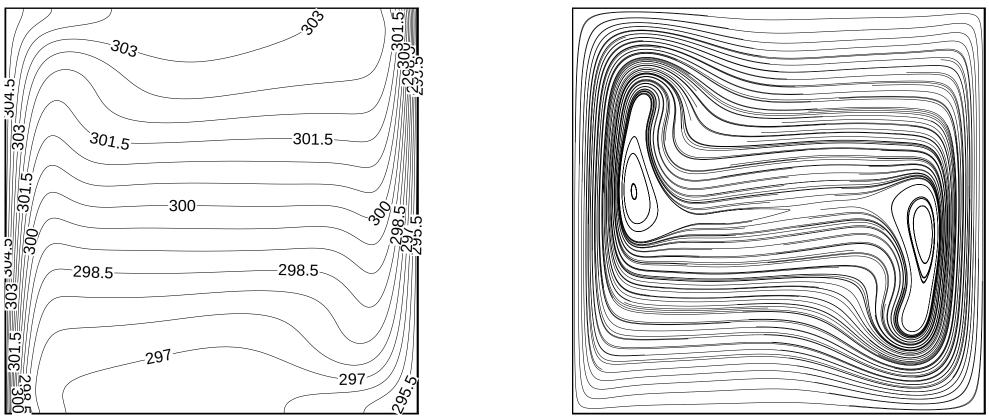

Figure 2.9: Streamlines and temperature distribution for the side-heated buoyant cavity flow at $Ra = 10^6$

Table 2.1: Comparison of present steady-state results with some previously reported solutions (de Vahl Davis [117] and Hortmann et al. [118]); $\bar{N}u_{x=0}$ = average Nusselt number over left wall.

Case	$Ra = 10^4, Pr = 0.71$			
Method	Navier-Stokes Equations and Energy Equation with SIMPLE Method		Stream Function-Vorticity	Finite Volume Formulation
Present Grid	81×81	161×161	De Vahl Davis and Jones (1983)	Hortmann et al. (1990) (161×161)
V_{max}	20.01	19.90	19.617	19.624
$\bar{N}u_{x=0}$	2.2561	2.2447	2.238	2.2446

Case	$Ra = 10^5, Pr = 0.71$			
Method	Navier-Stokes Equations and Energy Equation with SIMPLE Method		Stream Function-Vorticity	Finite Volume Formulation
Present Grid	81×81	161×161	De Vahl Davis and Jones (1983)	Hortmann et al. (1990) (161×161)
V_{max}	70.342	70.189	68.59	68.646
$\bar{N}u_{x=0}$	4.525	4.470	4.509	4.527

Case	$Ra = 10^6, Pr = 0.71$			
Method	Navier-Stokes Equations and Energy Equation with SIMPLE Method		Stream Function-Vorticity	Finite Volume Formulation
Present Grid	81×81	161×161	De Vahl Davis and Jones (1983)	Hortmann et al. (1990) (161×161)
V_{max}	221.352	220.743	220.559	219.861
$\bar{N}u_{x=0}$	8.916	8.706	8.825	8.863

The most important diagnostic connected to the free convection cavity flow is the average Nusselt number, which expresses the non-dimensional heat flux across the cavity. The Nusselt number is usually calculated at a vertical line, typically the hot wall and a line through the cavity centre. The Nusselt number is calculated using the formula below:

$$\bar{Nu} = Q_{covection}/Q_{heat\ diffusion} \tag{2.39}$$

where

$$Q_{convection} = \kappa \int_0^{L_y} \left(-\frac{\partial T}{\partial x}\right)_{x=0} dy, \qquad Q_{heat\ diffusion} = \kappa\ L_y(T_h - T_c)/L_x$$

and L_x and L_y are the height and length of the cavity, respectively. Thus, the Nusselt number averaged over the left vertical wall can be written as

$$\bar{Nu} = \frac{\displaystyle\int_0^{L_y} \left(-\frac{\partial T}{\partial x}\right)_{x=0} dy}{L_y(T_h - T_c)/L_x} \tag{2.38}$$

Numerical trials were performed to establish the most suitable grid for the present study. The results given in Table 2.1 for $Ra = 10^4$, 10^5 and 10^6 are shown to agree with the benchmark solutions of de Vahl Davis [117] and Hortmann et al. [118]. The distributions of temperature and vertical velocity component along the cavity mid-plane (y=1/2) are also shown in Fig. 2.10. The above results validate the ability of the present numerical method to solve coupled fluid flow and heat transfer problems with the Boussinesq model. Next, natural convection of water is considered to verify the heat transfer formulation of variable thermal properties of the fluid.

2.2.6.3 Natural Convection of Water With Variable Thermo-physical Properties

A common anomaly found in liquid water is that density reaches a maximum value at one specific temperature and hence the boussinesq approximation cannot be used in the mathematical model for natural convection.

Water cooling inside a closed cavity with vertical isothermal walls at different temperatures and adiabatic walls has been investigated by many researchers. Various

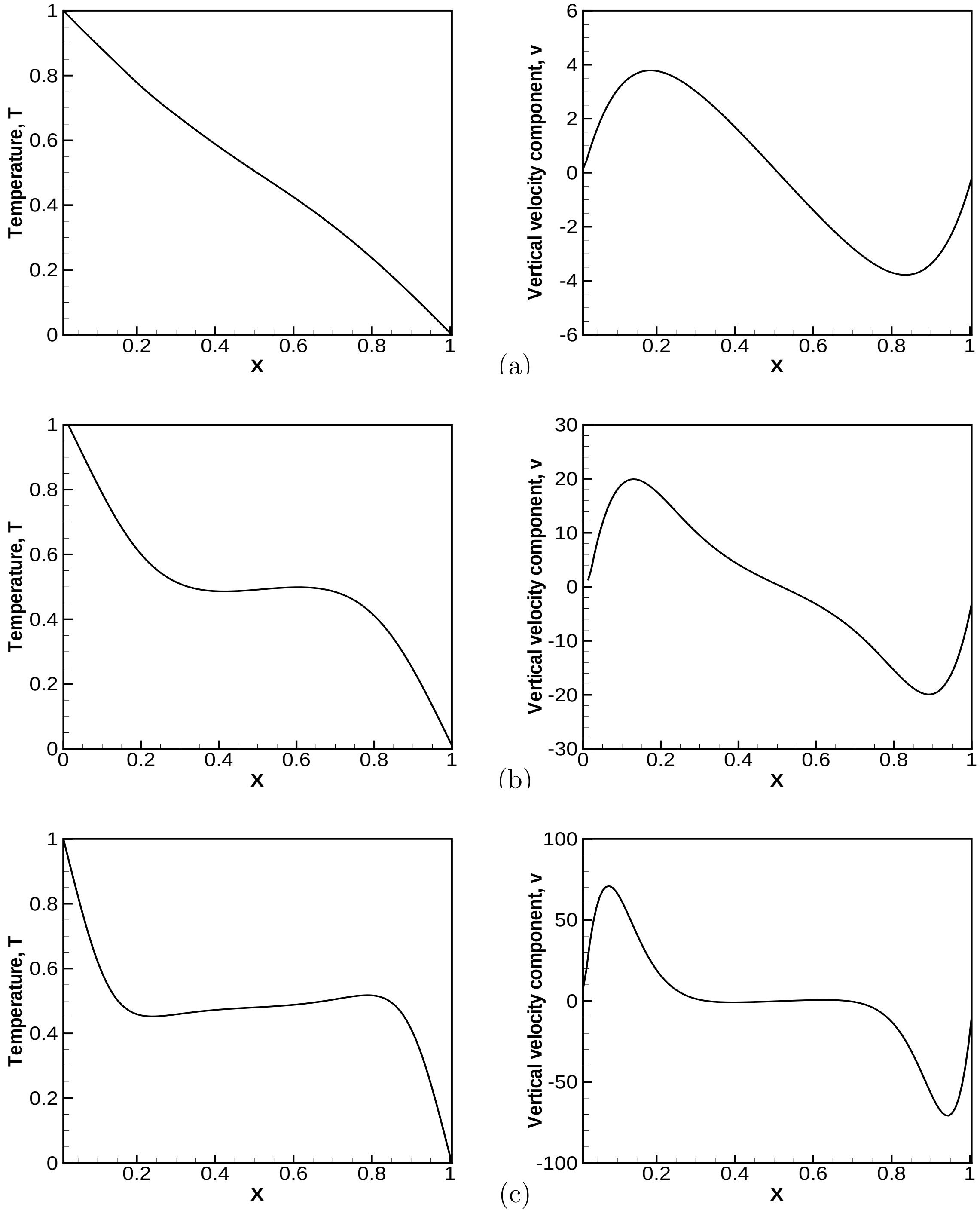

Figure 2.10: Temperature and vertical velocity component distributions in the cavity midplane (y=1/2). (a) $Ra = 10^3$, (b) $Ra = 10^4$ and (c) $Ra = 10^5$.

studies on the natural convection of water near its maximum density for different ranges of the Rayleigh number (experimental as well as computational) have been carried out (Braga and Viskanta [119], McDonough and Faghri [120], Nishimura et al [121], and Banaszek et al. [122]). Experiments on natural convection at high Reliegh numbers were performed by Braga and Viskanta [119] in the Rayleigh number range $10^7 - 10^8$. They also investigated numerically the transient natural convection. McDonough and Faghri [120] presented an experimental and numerical analysis of the transient natural convection of water. Nishimura et al. [121] used a time-dependent penalty finite-element model to describe the natural convection of water in a rectangular enclosure when $10^5 \leq Ra \leq 10^6$. Banaszek et al. [122] predicted natural convection in freezing water by using a semi-implicit method that was compared with an experimental study. All the simulations reported have been obtained using a two-dimensional model of heat transfer.

Ho and Tu [123] investigated, by experimental and numerical means, the natural convection of water near its maximum density at high Rayleigh numbers. They observed oscillatory convection flow and temperature fields in the enclosure and predicted oscillations were in a good agreement with the measured time period of the cyclic travelling wave motion of the maximum density contour. Kandasamy and Kumar [124] studied the natural convection of water near its density maximum in the presence of a uniform magnetic field. They observed that the effect of the magnetic field on the natural convection is to inhibit the heat transfer rate. Pantokratoras [125] studied natural convection of water near the density extremum along a vertical plate with sinusoidal surface temperature variation. They modelled, in particular, an inner boundary layer near the plate with periodic characteristics. Tong and Koster [126] studied numerically the transient natural convection of a water layer near its density maximum. The results illustrated that the temperature difference which determines the position of the maximum density plane in the water layer, can alter the flow field and heat transfer substantially. Recently Sundravadivelu and Kandasamy [127] derived a nonlinear 4th degree polynomial approximation for the density-temperature relation.

In most of the analysis pertaining to the convection of water in enclosures, except the latter study, a linear temperature-density relationship was taken. However in practice this will never happen as the density of water varies with temperature in a nonlinear fashion, attaining its maximum density around 4° C and decreasing when deviating from that temperature. As a result, the Boussinesq approximation, which is based on the linear behavior of the density-temperature relation, is strictly not applicable to these fluids if large T variations are considered. This property, known as density inversion, can significantly change the flow field and heat transport in an enclosure. But the complete Navier-Stokes equations are not only coupled through the density with the energy equation, but also through other temperature dependent transport properties such as viscosity, thermal conductivity and specific heat capacity. The transport properties of liquid vary appreciably for a small change in temperature. For example, the dynamic viscosity of water reduces by about 50 percent for a temperature rise from 10 to 40° C.

Here the model is investigated with the effects of temperature dependent fluid properties, namely density, viscosity, thermal conductivity and specific heat capacity, on free convection of water. To demonstrate the effect of variable physical properties on the flow and heat transfer, nonlinear empirical temperature correlations for water are used.

Problem Definition

To validate the model of heat transfer with variable thermal properties, the benchmark problem of cooling of pure water inside a cavity is studied. Initially water is at rest at a uniform temperature of 10° C. Suddenly one of the vertical walls is put at uniform temperature $T_c = 0°$ C, while the opposite wall is kept at the initial temperature $T_h = 10°$ C. The horizontal walls are considered adiabatic. Fig. 2.11 shows the geometry and boundary conditions of the physical problem.

Empirical correlations for the thermo-physical properties

Water at atmospheric pressure is considered and the empirical correlations, suggested by Shang et al. [128], are adopted.

$$\rho(T) = \left[-4.88 \times 10^{-3}(T-273)^2 + 999.9\right] kg\ m^{-3} \tag{2.39}$$

$$\mu(T) = exp\left[-1.6 - 1150 \cdot T^{-1} + (690 \cdot T^{-1})^2\right] \times 10^{-3}\ kg\ m^{-1}\ s^{-1} \tag{2.40}$$

$$\kappa(T) = \left[-8.01 \times 10^{-6}(T-273)^2 + 1.94 \times 10^{-3}(T-273) + 0.563\right]\ W\ m^{-1}\ K^{-1} \tag{2.41}$$

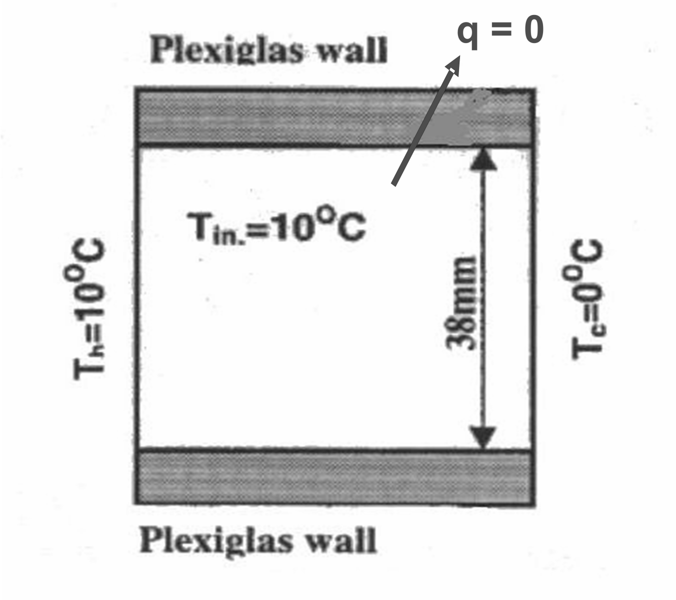

Figure 2.11: Geometry and thermal boundary conditions for natural convection of freezing water.

Here, T is taken as the absolute temperature in Kelvin. The correlations, Eqs. (2.39) - (2.41), were deduced on the basis of experimental data for water over the temperature range 0 - 100° C. The deviation of Eqs. (2.39) - (2.41) from the experimental data was reported to be within 0.35% and 0.18% respectively. Corresponding variations of ρ, μ and κ with temperature are shown in Fig. 2.12. It is readily seen that the relative variation of the density with temperature is small compared to the significant variations of the thermal conductivity and, to a large extent, of the viscosity. It is well known that the specific heat capacity, C_p, is practically independent of the temperature for most liquids. For water, as considered herein, the variation of C_p over the temperature range 0 - 100 ° C is less than 1%. We therefore take $C_p = C_{p0}$= 4200 $J\ Kg^{-1}\ K^{-1}$ in accordance with Shang et al. [128]. An immediate implication of the above assumptions is that the Prandtl number $Pr = \mu C_p/\kappa$ varies from about 13 at 0° C to approximately 1.76 at 100° C, which represents a reduction by a factor of about 7. This substantial decrease of Pr with T is primarily due to the reduction of μ but also due to the 20% increase in κ from 0° to 100° C.

The dimensional parameter describing the problem is the Rayleigh number (Ra), defined as

$$Ra = \frac{g\beta L^3 \triangle T}{\alpha\nu} \quad \text{with } \beta = -\frac{1}{\rho}\frac{d\rho}{dT} \tag{2.42}$$

where $\triangle T = T_h - T_c$ is the difference between the hot wall temperature T_h and the cold wall temperature T_c. The expansion coefficient β can be obtained by differentiating Eq. (2.39).

The computations are performed for $Ra = 2 \times 10^5$ in order to compare with the experimental results of Banaszek et al. [122]. The results are obtained on different uniform grid sizes (60×60 and 128×128) to ensure that the solution is close to the benchmark results. With 128×128, the solution agrees reasonably well with the benchmark results of Banaszek et al. [122]. Fig. 2.13 shows the temporal flow pattern and temperature field at various times. As can be seen from Fig. 2.13c, a clockwise vortex starts forming at $t = 17$ s and the size of it increases as time progresses and it penetrates deeper and deeper into the cavity center. After about 20 minutes of real time, a steady state is reached. At this stage, the circulation zone in the lower, cold corner, fills approximately one-fifth of the cavity (Fig. 2.13e). It is seen that, at steady state, the computed flow pattern is similar to that found from experiments. The vertical velocity along a line in the x-direction passing through the center of the cavity is also compared in Fig. 2.13f. It may be noted that the result approaches the experimental profile as the number of grid points increases.

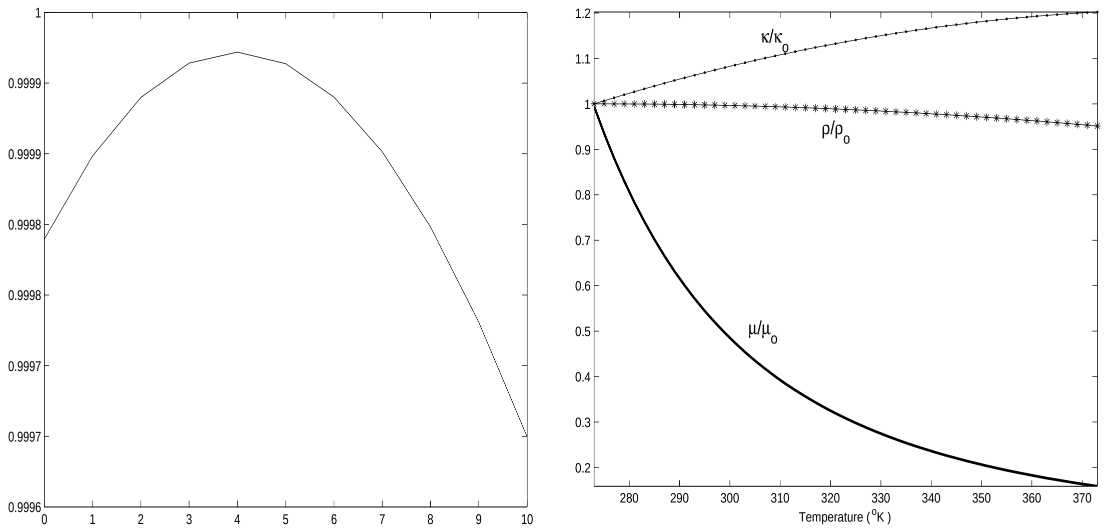

Figure 2.12: Variable thermal properties of water with respect to temperature. (a) Density versus Temperature, (b) Density, Viscosity and Thermal conductivity versus Temperature [128].

2.2.7 The Interface Tracking Algorithm

In this section the method used for tracking the interface between two fluids, say a dark fluid and a light fluid, is presented, for a two-dimensional, incompressible, non-reacting flow. We consider the problem of advancing a front in a known divergence free velocity field $\mathbf{u} = (u, v)$. We begin by discretising the domain with a uniform grid with spacing $h = \Delta x = \Delta y$. With each grid cell we associate a number $f_{i,j}$ that represents the fraction of the (i, j)th cell that is occupied by dark fluid.

Various tracking methodologies have been developed, including markers [20], level sets [7] and volume tracking [16]. The VOF method is a popular volume tracking algorithm that has proven to be a useful and robust tool since its development over two decades ago. It has therefore become a frequent choice in Eulerian models of interfacial flows, especially those flows where interfaces undergo topology changes (e.g., merging, breakup, etc.).

Rider and Kothe [19] and Rudman [18] have written a comprehensive review of volume tracking methods and a brief overview is presented here. Volume tracking

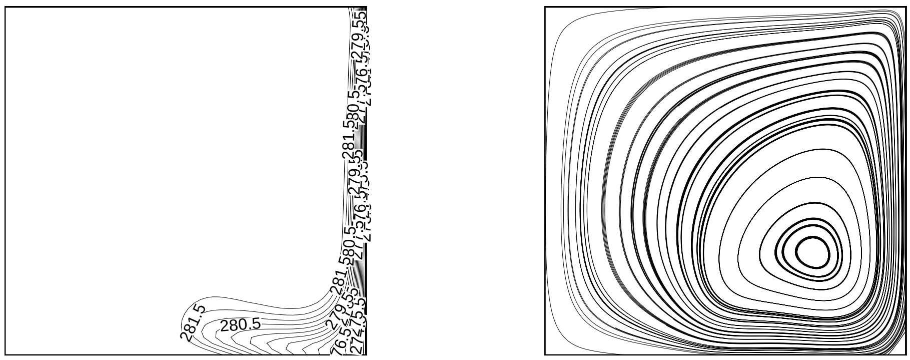

(a)

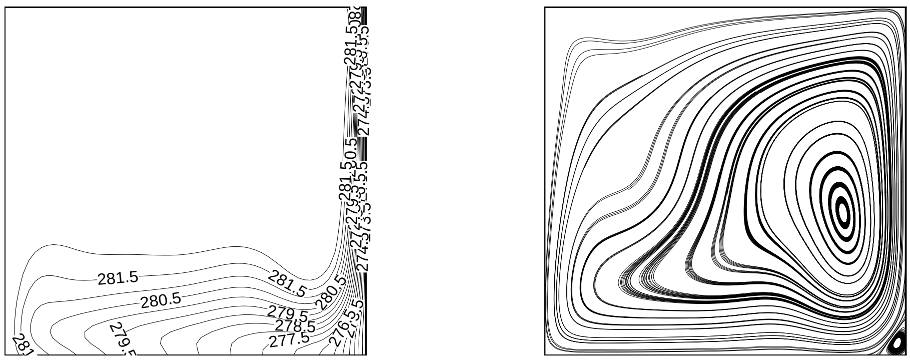

(b)

(c)

(d)

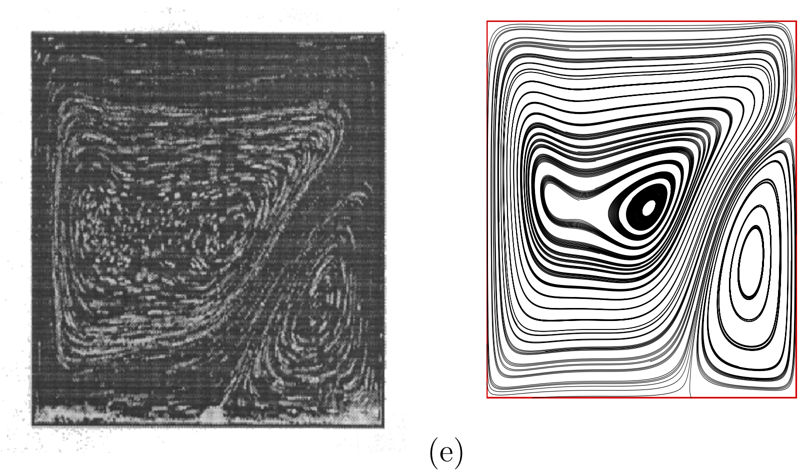

(e)

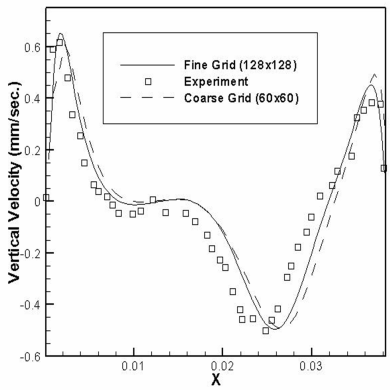

(f)

Figure 2.13: Temporal flow field and temperature field at various times; (a) $t = 17$ s, (b) $t = 50$ s, (c) $t = 100$ s, (d) $t = 500$ s and (e) steady state; Left: Experiment [122]; Right: Present Computation, and (f) Comparison of the vertical velocity along the x-direction at the center of cavity.

methods have their origin in the Volume of Fluid (VOF) scheme of Hirt and Nichols [16], whereby interfaces were modelled in a piecewise-constant manner. Many well known codes, including RIPPLE [72] and FLOW-3D [129], utilised such algorithms. Today, such methods are largely considered obsolete, and have been replaced by algorithms that approximate an interface with a straight line (in 2D) or a plane (in 3D) at any orientation to a mesh cell. Such methods are referred to as piecewise-linear interface calculation (PLIC) methods; examples include the work of Youngs [17], Rider and Kothe [19], and Scardovelli and Zaleski [15].

In the volume of fluid (VOF) method the interface evolution is described using a discrete function, f, whose value in each cell of the computational mesh, in two fluid problems, is the fraction of the cell volume occupied by the fluid, so that it is equal to one in cells full of fluid, zero in empty cells, and a value between zero and one in a mixed cell containing the interface. This volume fraction is a discretised form of a function, f, which is continuous everywhere except at the interface, where it jumps from zero to one, and satisfies a standard advection equation, Eq. (2.4).

The initial distribution of the discrete volume fraction is determined from the initial interface geometry. At each time step, the interface is first "reconstructed" in each cell from the f distribution, and is then advected by solving Eq. (2.4), using geometric considerations to compute volume fluxes through cell boundaries. This is illustrated in Fig. 2.14. The different VOF methods can be distinguished by the features of the interface reconstruction algorithm and the method used for time integration of the volume fraction equation. Successive improvements in the VOF method have kept the method competitive with more recent methods such as front tracking [20] or level set [7] methods.

2.2.7.1 The Interface Reconstruction Algorithm

This section describes the implementation of Youngs' PLIC-VOF [17] technique as used in this work. In order to advance the solution of Eq. (2.4) in time we first need to construct an approximation to the interface given the values of the volume fraction $f^n_{i,j}$ at time $t = n\Delta t$. An algorithm for doing this is referred to as a volume-of-fluid *interface*

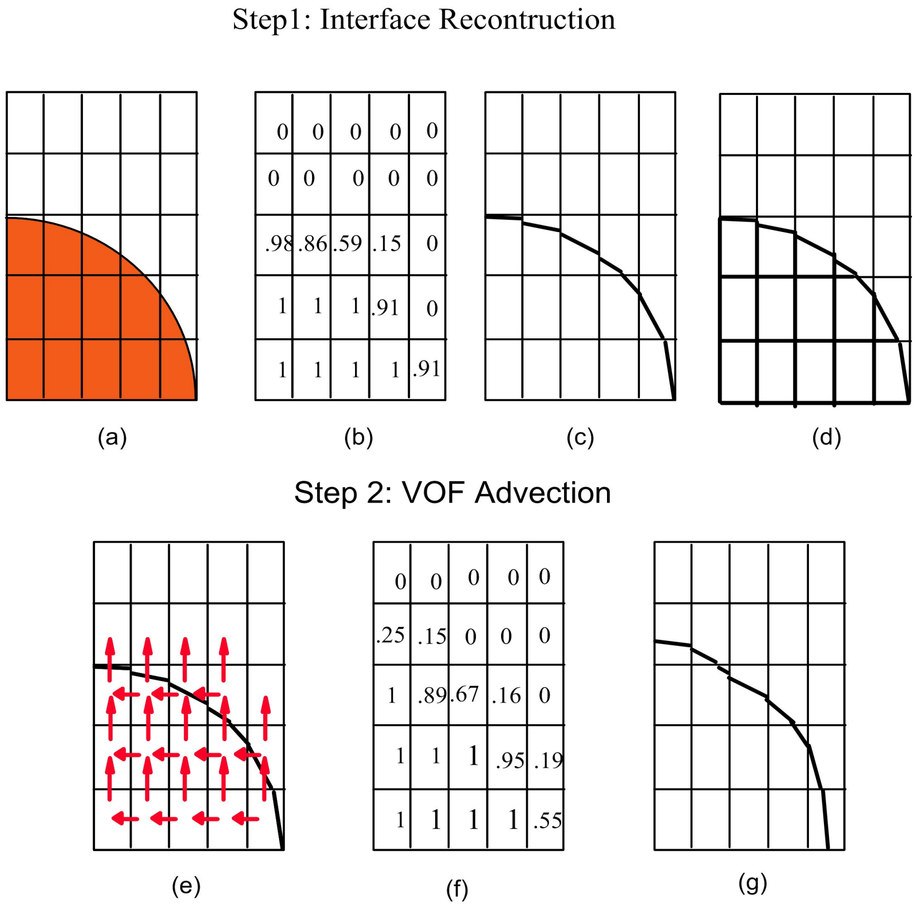

Figure 2.14: Schematic diagram of Youngs PLIC-VOF algorithm steps; (a) True Interface, (b) Volume Fraction Values, (c) Piecewise Linear Approximation, (d) Calculation of Cell Areas, (e) Velocity Field Calculated from N-S Solver, (f) New Volume Fractions after Advection and, (g) Interface Position after Advection.

reconstruction algorithm.

In the PLIC method, the interface is approximated by a straight line with appropriate inclination in each cell. The straight lines are not necessarily connected to each other at the cell faces. That is, the interface line at each cell is determined independent of the neighboring interface lines, and their ends need not necessarily be connected at the cell faces. Non-connecting lines are also commonly used by others (Zaleski [15] and Kothe et al. [19]). Each line is determined so that it is perpendicular to an interface normal vector, and it divides the cell surface into two regions that match the given f for the cell. This guarantees maximum robustness and simplicity, while sacrificing little in accuracy. The method's successive steps are illustrated in Fig. 2.14.

The interface normal vector $\mathbf{n}$, (a unit vector perpendicular to the interface) is to be determined for each cell. An example of this algorithm is shown in Fig. 2.15. This is achieved using the gradient of f:

$$\mathbf{n} = -\frac{\nabla f}{|\nabla f|} \tag{2.43}$$

where the gradient of f at the cell centre is calculated using the values of f at its nine immediate neighboring points. The nine neighboring points for point $i,\ j$ are:

$$\begin{pmatrix} f_{i-1,j+1} & f_{i,j+1} & f_{i+1,j+1} \\ f_{i-1,j} & f_{i,j} & f_{i+1,j} \\ f_{i-1,j-1} & f_{i,j-1} & f_{i+1,j-1} \end{pmatrix}$$

Assuming $\Delta x = \Delta y = h$, then the x and y components of the gradient of $f_{i,j}$ are:

$$m_{x\ i,j} = [f_{i+1,j+1} - f_{i-1,j+1} + 2(f_{i+1,j} - f_{i-1,j}) + f_{i+1,j-1} - f_{i-1,j-1}] \tag{2.44}$$

and

$$m_{y\ i,j} = [f_{i+1,j+1} - f_{i+1,j-1} + 2(f_{i,j+1} - f_{i,j-1}) + f_{i-1,j+1} - f_{i-1,j-1}] \tag{2.45}$$

And the x and y components of the unit normal vector are:

$$n_{x\ i,j} = -\frac{m_{x\ i,j}}{\sqrt{m_{x\ i,j}^2 + m_{y\ i,j}^2}} \tag{2.46}$$

and

$$n_{y\ i,j} = -\frac{m_{y\ i,j}}{\sqrt{m_{x\ i,j}^2 + m_{y\ i,j}^2}} \tag{2.47}$$

where, n_x and n_y are components of $\mathbf{n}$. Once the normalised unit normal vector $\mathbf{n}$ is calculated, a straight line (as shown in Fig. 2.15) is positioned perpendicular to it in such a way that it matches with the value of f in the cell.

Defining the angle θ to be

$$\tan\theta = \frac{n_x}{n_y}$$
$$\cot\theta = \frac{n_y}{n_x}$$

Depending upon the values of n_x and n_y, sixteen different cases may occur. They are shown in Fig. 2.17, where the numbers 1 - 4 are to denote the first, second, third and fourth quadrants, respectively, and the labels I, II, III and IV denote the subcase for each quadrant. When $\mathbf{n}$ is in the first quadrant ($0 \leq \theta \leq \pi/4$), the different cases that may occur are shown in Fig. 2.16. The area delimited by a line perpendicular to $\mathbf{n}$ can be either a triangle ($F \leq F_{lim,\ 1}$), a quadrilateral ($F_{lim,\ 2} < F \leq F_{lim,\ 2}$) or a pentagon ($F > F_{lim,\ 2}$), depending on $f_{i,j}$. The same cases can be found in each quadrant as shown in Fig. 2.17. Each case can be identified by using Algorithm 1.

Once the case has been identified, the two ends of the straight line in each cell (i.e., side fraction) need to be determined. The side fractions of each are named as S_r, S_l, S_t and S_b for the right, left, top and bottom, respectively as shown in Fig. 2.16. To calculate the values of $S_l,\ S_r,\ S_b,\ S_t$, we need to specify the limiting values of F for a particular $\mathbf{n}$. The limiting values are:

$$F_{lim,\ 1} = \frac{n_x}{2n_y} \tag{2.48}$$

$$F_{lim,\ 2} = 1 - F_{lim,\ 1} \tag{2.49}$$

Algorithm 1 PLIC-VOF Algorithm

if $tan\theta \leq 1$

  $F_{lim1} = n_x/(2n_y)$

  $F_{lim2} = 1 - F_{lim1}$

  if $F \leq F_{lim1}$

    Case I

  if $F_{lim1} < F < F_{lim2}$

    Case II

  if $F \geq F_{lim2}$

    Case IV

else

  $F_{lim1} = n_y/(2n_x)$

  $F_{lim2} = 1 - F_{lim1}$

  if $F \leq F_{lim1}$

    Case I

  if $F_{lim1} < F < F_{lim2}$

    Case III

  if $F \geq F_{lim2}$

    Case IV

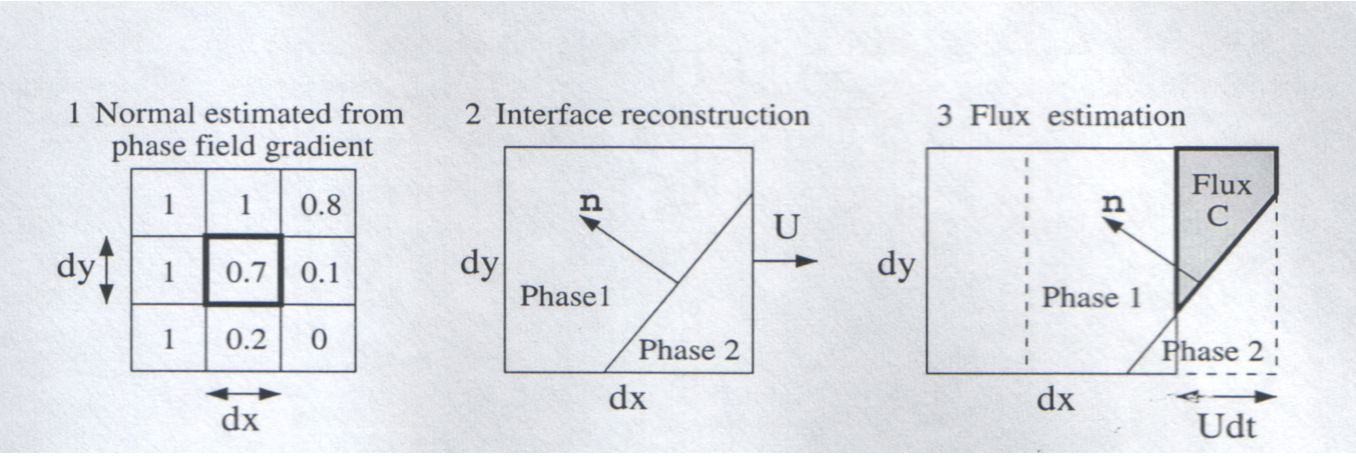

Figure 2.15: Two-dimensional transport of Youngs' PLIC-VOF method, taken from [130].

For each of the three cases, the side fractions follow immediately from simple linear or second-order equations. In local coordinates, assuming $\Delta x = \Delta y = 1$, the values of side fractions can be calculated as listed in Appendix A. Once these are known, the fluid fluxes into and from each cell can be calculated geometrically. The fluid fluxes are named as F_e, F_w, F_n and F_s for the east, west, north and south, respectively. A straightforward way to calculate the Youngs fluxes is presented with the help of Fig. 2.15 in the x direction. The definite value of fluid phase fluxes in the first quadrant is given in Appendix B.

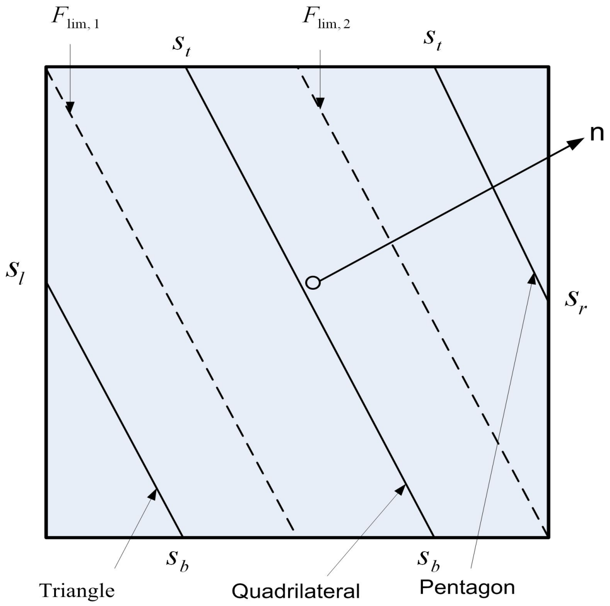

Figure 2.16: The Interface configuration in the first quadrant.

2.2.7.2 The Volume-of-Fluid Algorithm

The second step in the solution of Eq. (2.4) is an algorithm for evolving the volume fractions in time. Suppose that at time $t^n = n\Delta t$ we have values of the velocity field $(u_{i\pm1/2,j}, v_{i,j\pm1/2})$ defined at the centers of cell edges and that these velocities satisfy a discrete form of Eq. (2.1).

$$\frac{(u_{i+1/2,j} - u_{i-1/2,j})}{\Delta x} + \frac{(v_{i,j+1/2} - u_{i,j-1/2})}{\Delta y} = 0 \tag{2.50}$$

Given an approximation of the interface in each cell for which $0 < f^n_{i,j} < 1$ we wish to determine the volume fraction $f^{n+1}_{i,j}$ at the new time. We refer to the algorithm for doing this as Volume of Fluid *advection algorithm*. An example of this algorithm is shown in step 2 of Fig. 2.14.

In our work we have used a first order un-split advection algorithm [72], which is based on the standard conservative finite difference update of Eq. (2.4),

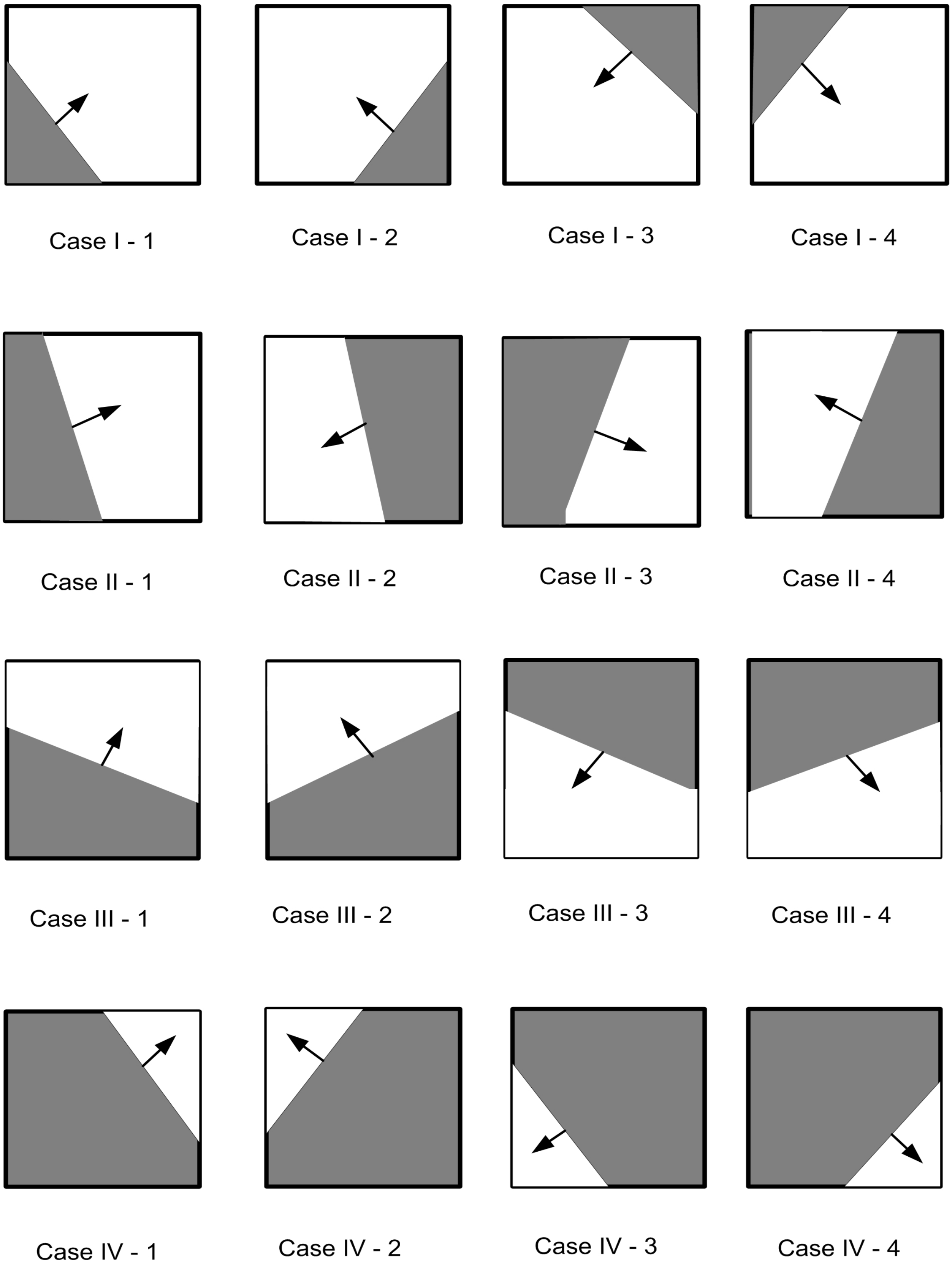

Figure 2.17: Different possible cases of interfaces in the four quadrants.

$$f_{i,j}^{n+1} = f_{i,j}^{n} + \frac{\Delta t}{\Delta x}\left[F_{i-1/2,j} - F_{i+1/2,j}\right] + \frac{\Delta t}{\Delta y}\left[G_{i,j-1/2} - G_{i,j+1/2}\right]$$
$$+\Delta t f_{i,j}^{n}\left[\frac{(u_{i+1/2,j} - u_{i-1/2,j})}{\Delta x} + \frac{(v_{i,j+1/2} - u_{i,j-1/2})}{\Delta y}\right] \tag{2.51}$$

where $F_{i-1/2,j} = (fu)_{i-1/2,j}$ denotes the flux of f across the left edge of the (i, j)thcell and $G_{i,j-1/2} = (fv)_{i,j-1/2}$ denotes the flux across the bottom edge of the (i, j)th cell, etc. Ordinarily the last term in Eq. (2.51) would be zero if continuity was satisfied. It has been found desirable to include it numerically (Brackbill et al. [60]) because, although it is small, it is not exactly zero and of the order of $\epsilon\Delta t$, where ϵ is the tolerance for the continuity equation.

2.2.8 Validation of PLIC-VOF Implementation

In this section, a series of tests are reported to assess the PLIC-VOF methodology for capturing interfaces between two immiscible fluids. The tests are used to investigate the proper implementation of the convection procedure and of the PLIC-VOF interface capturing methodology. Of particular interest here are some tests of the PLIC-VOF methods only, with pure advection problems using given velocity fields. They involve flow calculations free from gravitational forces, surface tension, and other stresses or forces. The tests involve the transport of fluid bubbles of different shapes, such as triangle, square with hole, and circle, placed in a uniform velocity and shearing flow. In the case of uniform flow, the bubble should be convected through the grid without changing its shape, In the case of shearing flow, the bubble will undergo topology changes, like deformation and distortion.

2.2.8.1 Translation of Different Interface Shapes

The first series of tests involve translating a triangle, a square with a hole and a circle through a uniform velocity field. A uniform grid size of 128 × 128 in a 3×3 units square domain is used and the initial interface placed as shown in Fig. 2.18. The time step is determined such that the Courant number is equal to 0.125. In the case of the triangle and square with hole, a constant velocity, $u = 1$, $v = -1$, is used. Figs. 2.18a and 2.18b show the contours of volume fraction of the triangle and square with hole at different times. It can be seen that, at time $t = 1$ s, the interfaces moved a unit distance in both x and y directions as expected and is convected through the grid without changing its shape significantly. It is shown, however, that smoothing occurs at sharp corners. This is primarily caused by the finite difference approximation of the interface normal by the 9 point stencil (Eqs. (2.44) - (2.45)) and cannot be avoided. Refinement of the mesh, however can minimise this smoothing effect. In the case of the circle, a constant velocity, $u = 0,\ v = -1$, is used but other parameters are unchanged. The contours of the volume fraction of the circle are shown at different times in Fig. 2.18c. In this case, there is no corner and the original interface is maintained after time $t = 1$ s. These findings show the ability of the present interface tracking algorithm and advection procedure to translate shapes in a zero divergence and irrotational flow. The results are in line with published results [18]. However, translation enables only a minimal assessment of the interface tracking algorithm integrity and capability because topology change is absent. Additional tests involving flows with nonuniform vorticity must be considered before a complete assessment can be made. We therefore consider in the next section a 2D test problem that sufficiently challenge the algorithm capabilities, provide meaningful metrics for measurement of algorithm performance, and are easy to implement.

2.2.8.2 Circle in Shear Flow

In order to validate deformation and distortion of interfaces,which is omnipresent in multiphase flow, Rider & Kothe [19] introduced two tests where a circle is subjected to shearing flow. We have repeated their single vortex problem with our implementation. These problems, characterized by flows having non-uniform vorticity, were introduced recently in [15] to test interface tracking methods with interfaces undergoing topology changes. Beside inducing topology change, the test problems are representative of interfacial flows in real physical systems, e.g., Rayleigh-Taylor, Richtmeyer-Meshkov, and Kelvin-Helmholtz instabilities, where sharp gradients in fluid properties lead to vortical flow. A proper assessment of interface tracking methods should therefore impose strong vorticity at the interface. Our test problems possess vortical flows that stretch and potentially tear any

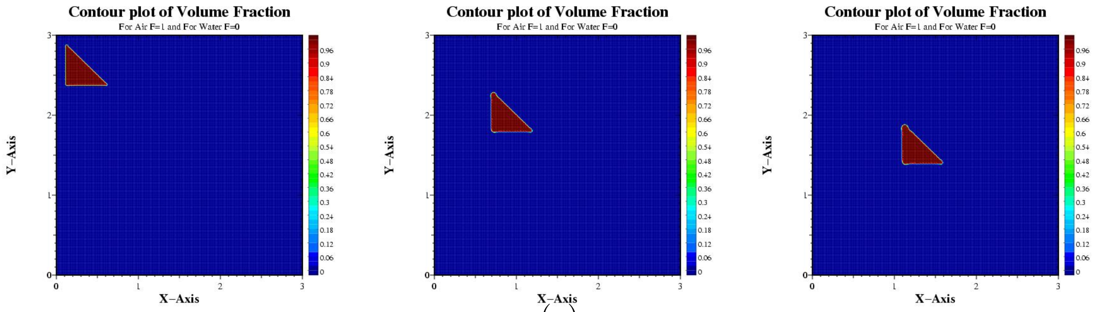

(a)

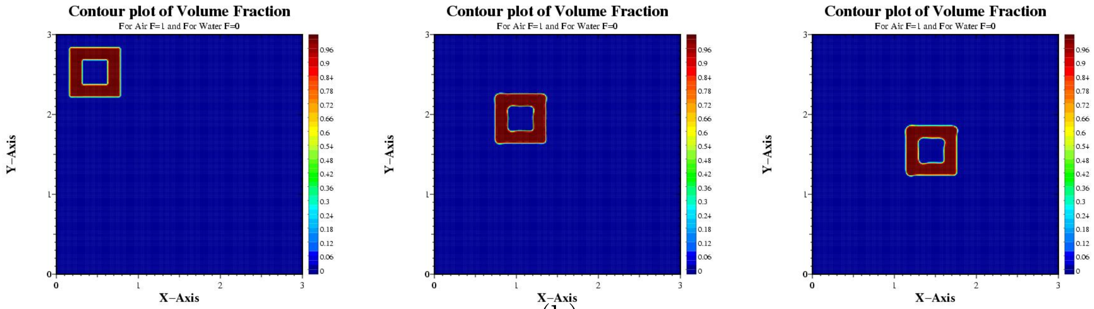

(b)

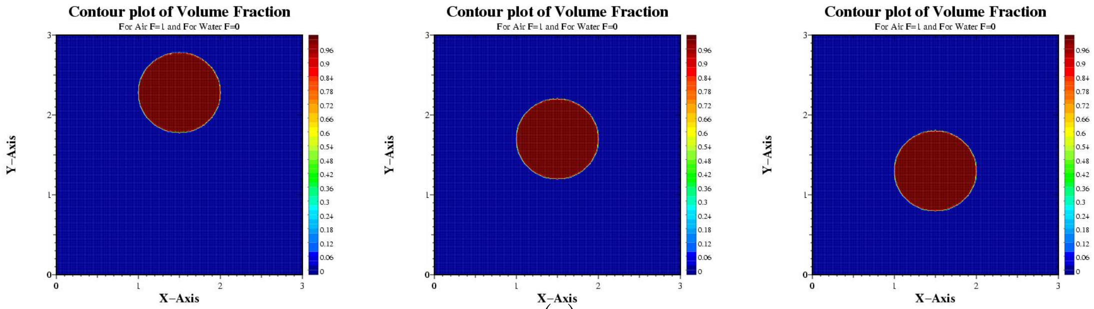

(c)

Figure 2.18: Translation of different interface shapes; right to left: $t = 0.0$, 0.5 and 1.0 s; top to bottom: triangle, square with hole and circle shapes.

interfaces carried within the flow. The problem contains a single vortex that will spin fluid elements, stretching them into a filament that spirals towards the vortex center. This flow field causes fluid elements to undergo large topological changes. In the converged limit, fluid elements will not tear, instead forming thin filaments. The imposed velocity fields are given by:

$$
\begin{aligned}
u &= -\sin^2(\pi x)\sin(2\pi y) \\
v &= \sin^2(\pi y)\sin(2\pi x)
\end{aligned}
$$

A circle (radius 0.15) is centered at (0.50, 0.75) in a unit square computational domain. The domain is partitioned with 128×128 orthogonal, uniform cells. A scalar field is initialized to unity and zero inside and outside the circle, respectively. For the cells containing the circular interface, the scalar field is set to a value between zero and one, in proportion to the cell volume truncated by the circle. This field represents a characteristic (or color) function, which for the purpose of the research is the fluid volume fraction for a circular fluid body. Fig. 2.19 shows the comparison of the solution from the present method with that of Rider & Kothe [19]. The numerical result is quite similar to the corresponding result of [19] with their PLIC-VOF method, except that the tail of our spiral is broken into droplets. This again confirms the proper implementation and capability of the method adopted in the present code.

2.3 Overall Solution Algorithm

There are three major stages followed at each time step (see Fig. 2.20)

1. Semi-implicit finite volume representations of the momentum equation, Eq. (2.10), are used to calculate new approximate velocities (u^{n+1}, v^{n+1}) at the new time level $n+1$ using initial conditions or previous time level n values (u^n, v^n) and p^n. The volume forces at the interface are calculated using Eqs. (2.19) - (2.36) and Eq. (2.37) through the CSF algorithm (Kothe et al. [60]).
2. Pressure and velocities in each mesh cell are adjusted iteratively to satisfy the continuity equation, Eq. (2.11), by using the update Eq. (2.17). Once the corrected

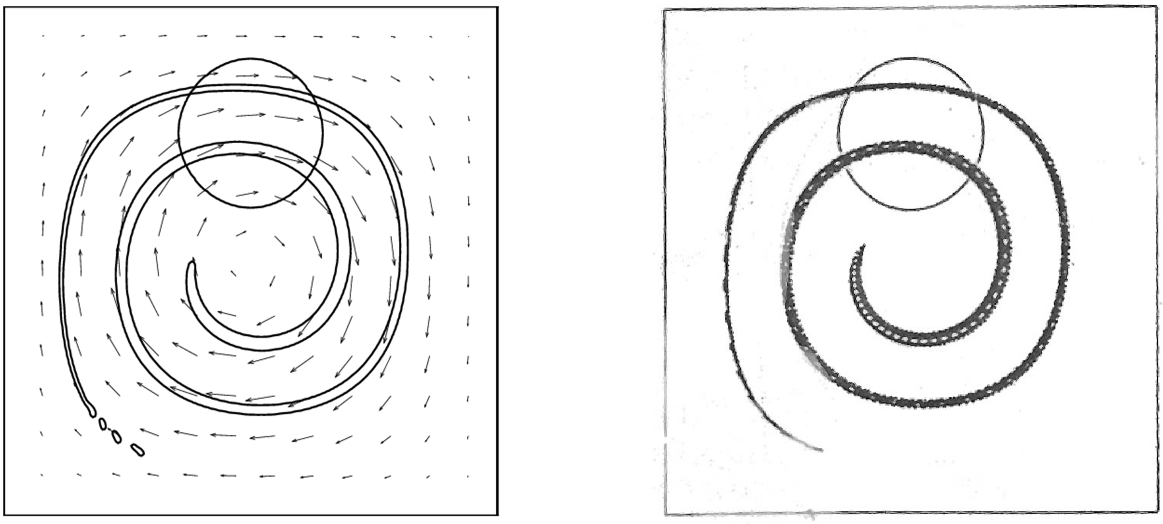

Figure 2.19: A circle fluid body placed in the single-vortex flow field. Left: The velocity field, the initial circle, and the solution using our PLIC-VOF method. Right: The solution of the same problem obtained by Rider and Kothe [19]

.

velocities are known, the energy equation is solved using the same procedure as for the momentum equations.

3. The volume of fluid advection equation is used to update the VOF function f^n to f^{n+1} using the Youngs' advection algorithm, Eq. (2.51), with divergence correction, Eq. (2.50), as discussed by Kothe et al. [19].

The above cycle is repeated for all subsequent time interval. Stability criteria based on viscous, inertia and surface tension analyses establish the size of the basic time step(Hirt and Nichols [16]) using Eq. (2.39).

2.4 Summary

In this chapter, the mathematical formulation and the numerical methodology employed have been described. The main aspects are summarised below:

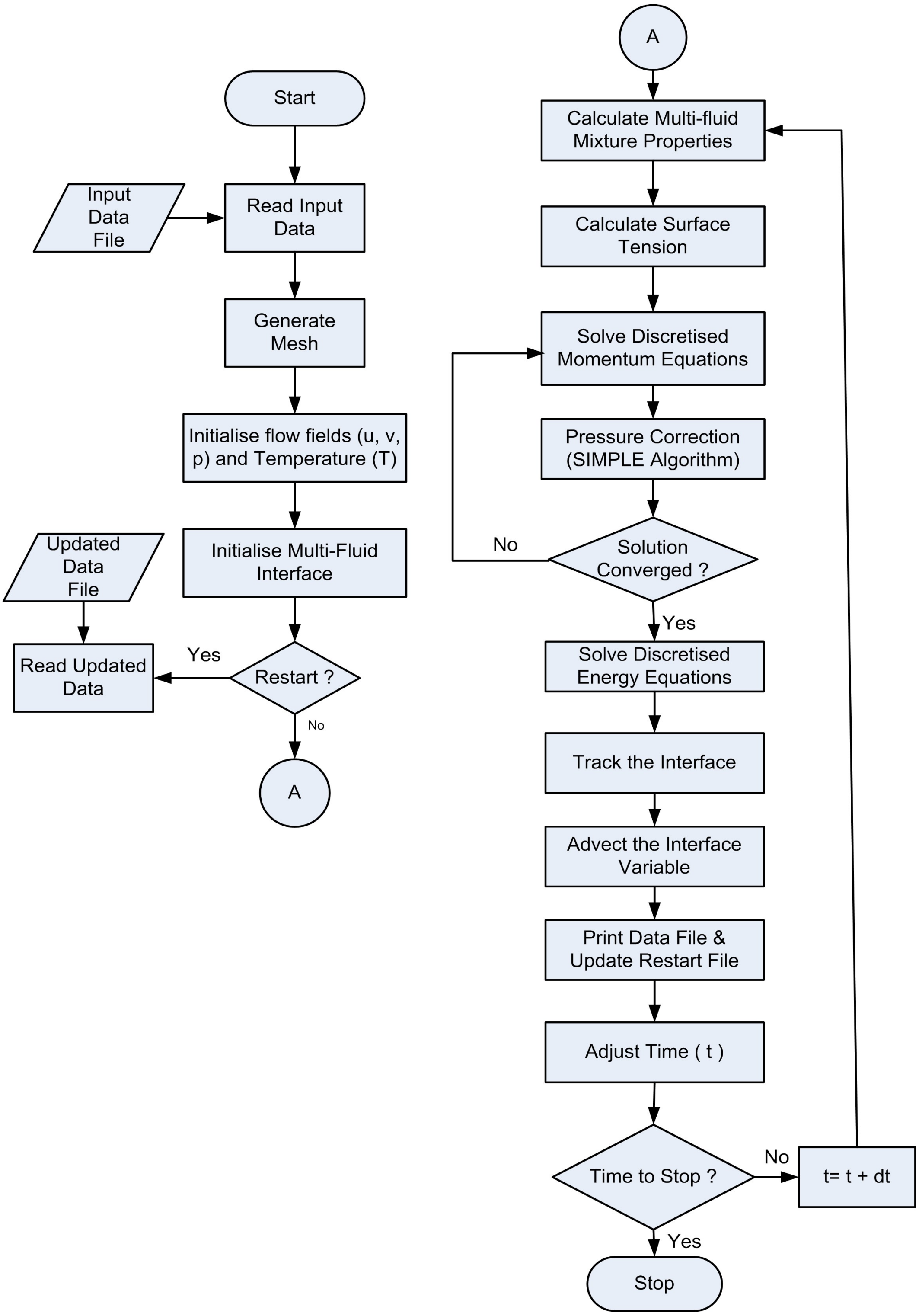

Figure 2.20: Overall Program Flow chart.

- A SIMPLE algorithm is employed to solve the mass, momentum and energy conservation equations. The equations are discretized using the finite volume formulation. A multigrid technique is implemented to accelerate the calculation of the pressure equation. The solution of mass and momentum equations is validated by the study of a lid driven cavity benchmark problem. The coupling of the mass and momentum equations with the energy equation is validated by the study of natural convection in a square cavity having its vertical walls differentially heated. The variable thermo-physical properties formulation is investigated through the problem of natural convection of water with an empirical relationship of properties to temperature.
- The two-fluid problem is solved numerically using the volume of fluid (VOF) method. The interface is tracked by the piecewise linear interface construction technique. The surface tension force is modelled as a continuum body force in the momentum equations. The accuracy and the implementation of the method are investigated through a series of tests of translation of different interfaces and of the Rider and Kothe single vortex problem.

CHAPTER 3

DYNAMICS OF RISING BUBBLES IN VISCOUS LIQUIDS

In this chapter, computations of free rising bubbles in viscous liquid are presented and discussed. The computations are performed for different fluid properties and flow parameters. The simulation results are compared with reported numerical and experimental observations of terminal bubble shapes, terminal velocities, and aspect ratios. Drag coefficients are also calculated for a range of bubble types and compared with results presented by Raymond and Rosant [97]. The main purpose is to assess the SIMPLE-VOF solver developed in this study as it relies on a specific density interpolation in cells containing the multi-fluid interface and also to assess limitations of the 2D model approach.

3.1 Introduction

The study of droplets and free rising bubbles by buoyancy in viscous liquids has received considerable attention over the years. The bubble as it rises can deform to spherical, ellipsoidal, skirted, spherical cap shapes (Clift et al. [4]) depending on three dimensionless parameters:

- the Eötvös number, Eo

$$Eo = \frac{g\Delta\rho d_{eq}^2}{\sigma} \tag{3.1}$$

- the Morton number, Mo

$$Mo = \frac{g\mu_l^4\Delta\rho}{\rho_l^2\sigma^3} \tag{3.2}$$

- the Reynolds number, Re

$$Re = \frac{\rho_l v_\infty d_{eq}}{\mu_l} \tag{3.3}$$

where g is the acceleration due to gravity, $\Delta\rho$ the difference between the densities of the heavier and lighter fluids, d_{eq} the equivalent diameter of the bubble, σ the surface tension coefficient, μ_l the viscosity of the liquid, ρ_l the density of the liquid, and v_∞ the terminal velocity of the bubble.

Dimensional analysis shows that three non-dimensional groups, two independent and one dependent, describe bubble behaviour in a liquid. The Morton number, Mo, and the Eötvös number, Eo, are usually chosen as independent parameters. The Morton number contains only physical properties of the fluid (Clift et al. [4]). Thus, for a given isothermal incompressible two-fluid system, it is a constant. It represents the ratio of gravitational forces times viscous forces to surface tension forces. The Eötvös number is fundamentally a measure of the volume of the bubble and it is the ratio of buoyancy forces to surface tension forces, so a functional relationship between the Morton number and the Eötvös number can be used to describe how the bubble changes shape as a function of gravitational, surface tension and viscous forces.

The choice of the dependent parameter depends on what one is interested in. The Reynolds number, Re is the ratio of inertia forces to viscous forces, and is used mainly for determining whether a given flow will be laminar or turbulent. It is the most common parameter used to define a dimensionless rise velocity.

The different bubble shape regimes have been classified on a map in terms of Eo, Mo, and Re (Grace [87]; Clift et al. [4]). Amongst published experimental studies, detailed visual descriptions can be found in Hnat and Buckmaster [131], Bhaga and Weber [77] and Clift et al. [4].

The bubble shapes vary greatly in different flow regimes as a function of the non-dimensional parameters described before. The terminal shapes of single rising bubbles under a range of Reynolds and Eötvös numbers were observed and reported in the work by Bhaga and Weber [77]. Generally, small bubbles, which have low Reynolds or Eötvös number ($Re < 1$ or $Eo < 1$), rise in a steady fashion and maintain their spherical shape. The shape of larger bubbles, with intermediate Reynolds and Eötvös numbers ($1 < Re < 100$ and $1 < Eo < 100$), are affected significantly by the flow conditions. Various bubble shapes (oblate ellipsoid, disk-like, oblate ellipsoidal cap, skirt bubble, and spherical-cap) have been found in various flow regimes by experimental investigation. In spite of the difference in shapes, the bubbles rise steadily in the liquid along a straight path. With further increase of the Reynolds number ($100 < Re < 500$), the bubble shape may become toroidal in the high Eötvös number ($100 < Eo < 500$) regime; spherical-cap in intermediate Eötvös number regime ($30 < Eo < 100$), and oblate ellipsoid in the low Eötvös number regime ($1 < Eo < 30$). As the bubble size increases further, a turbulent wake develops behind the bubble that leads to unsteady bubble motion. The bubble may rise in a wobbly path, oscillate about a mean shape and even break up or coalesce.

One of the earliest numerical studies was reported by Ryskin and Leal [88] for the steady motion of an axisymmetric bubble rising in a liquid. Their method employed an orthogonal curvilinear grid that conforms to the bubble shape. They considered the bubble to be a void and the bubble shape was determined based on the normal stress balance at the bubble interface. Good agreement was obtained between their numerical solution and the experiments of Hnat and Buckmaster [131]. Dandy and Leal [132] further developed the method to consider bubble/drop fluid flows. They investigated the effect of the density and viscosity ratios on the bubble/drop shapes and the associated flow structure. Their results were in good agreement with experimental results. In the method of Ryskin and Leal [88] and Dandy and Leal [132], the surface of the bubble/drop was considered as a sharp interface. In the last decade, the motion of bubbles and drops due to gravity have been simulated successfully using front tracking methods (Unverdi and Tryggvason [28]), VOF methods (Gueyffier et al. [71]; Chen et al. [89]) and level-set methods (Sussman et al. [5]; Son [90]). Raymond and Rosant [97] performed an extensive comparison between their numerical and experimental results for moderate deformed bubbles concerning the bubble drag coefficient and deformation. Their numerical model was derived with a surfactant-free assumption in order to reduce the computational cost. The interface position was tracked by introducing a curvilinear interface-fitted non-orthogonal coordinate system. By means of a coordinate transformation, the physical domain was converted to a computational domain with known boundaries that are coordinate isolines. The values predicted by their numerical model were found to be in good agreement with experimental results. Ye et al. [133] successfully simulated bubble rising due to buoyancy using a sharp interface method, referred to as a cut-cell approach, in which the governing equations for each phase are solved simultaneously on a fixed Cartesian grid. Recently, van Wachem et al. [96] developed a novel 3D model using an advanced Lagrangian VOF interface tracking scheme to study rising gas bubble dynamics of different sizes. They combined their method with a novel least-square method to get an accurate estimate of the normal of the interface to achieve an accurate interface reconstruction. Results obtained with their model were in good agreement with their experimental results for bubble shapes and rise velocity.

In this chapter, we assess the suitability of the present SIMPLE PLIC-VOF method of two-fluid flows to model free rising bubbles for different fluid properties and flow parameters. In order to do so, the results obtained with the present numerical method for rising bubbles in viscous liquids are compared with reported numerical and experimental results.

3.2 Results and Discussion

In this section, the numerical study of the rise by buoyancy of a bubble of lower density (fluid 2) in a continuous phase of higher density (fluid 1) is presented. Several computations are performed for a wide range of physical properties using realistic values for the density and viscosity ratio. To assess the present computational method, the results are compared with those of Raymond and Rosant [97]. Table 3.1 lists the physical fluid properties of different fluids used for the various simulations and chosen according to the experimental test cases by Raymond and Rosant [97]. Table 3.2 lists the simulation parameters and corresponding dimensional numbers for each fluid.

The present computational setup is illustrated in Fig. 3.1. Fluid 2 is initially a spherical bubble of different diameters ranging from 3 mm to 9 mm. Both liquid and bubble are assumed to be stationary in the initial state. No-slip boundary conditions are

Table 3.1: The physical properties of fluid used in the experiments of Raymond et al. [97]

Series	Experiment			
	Viscosity (μ_l) (Pa S)	Density (ρ_l) (kg/m^{-3})	Surface Tension (σ) (N/m)	Mo
S1	0.687	1250	0.063	7.5287
S3	0.242	1230	0.063	0.1057
S5	0.0733	1205	0.064	7.4492×10^{-4}
S6	0.0422	1190	0.064	9.7757×10^{-5}

Table 3.2: The simulation parameters for the rising of different sized bubbles in series fluids

Bubble diameter (m)	S1		S3		S5		S6	
	Mo	Eo	Mo	Eo	Mo	Eo	Mo	Eo
0.003	7.5287	1.7501	0.1057	1.7221	7.4492×10^{-4}	1.6607	9.7757×10^{-5}	1.6400
0.005	7.5287	4.8615	0.1057	4.7836	7.4492×10^{-4}	4.6131	9.7757×10^{-5}	4.5556
0.007	7.5287	9.5285	0.1057	9.3759	7.4492×10^{-4}	9.0416	9.7757×10^{-5}	8.9290
0.009	7.5287	15.7512	0.1057	15.4990	7.4492×10^{-4}	14.9464	9.7757×10^{-5}	14.7602

applied at all confining walls. The gravity vector is aligned with the vertical boundaries and pointing upwards so that the bubble rises upwards due to buoyancy force. The time required for the bubble to start rising depends upon the density and viscosity differences between the two fluids, the size of the bubble and surface tension.

Computed shapes are compared with the corresponding data obtained from the bubble diagram published by Grace [87] while rise velocities are compared with the experimental results of Raymond et al. [97]. As far as the author knows this study is the first attempt to make a systematic comparison between simulation and experiment (Grace diagram) over a wide range of physical properties using at the same time realistic values for the density and viscosity ratio. The effect of the domain size and the typical number of required computational cells inside the gas bubble were determined before carrying out this parametric analysis.

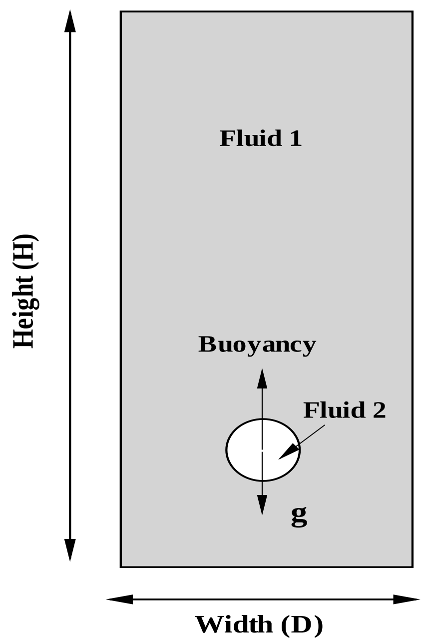

Figure 3.1: Schematic of the computational setup for a single bubble rising by buoyancy.

3.2.1 Wall effect

The size of the solution domain in the horizontal direction should be large enough so that the boundary effects on the rising bubble can be ignored in the simulation, and the bubble can be assumed to rise in an infinite quiescent liquid. Two sets of simulations were carried out to assess the influence of the size of the computational domain on the terminal velocity. The effect of domain width is shown in Fig. 3.2a for simulation conditions S5 and a bubble diameter of 5 mm, as shown in Tables 3.1 and 3.2. The terminal velocity of the bubble is calculated with four different widths of the channel, 0.02 m, 0.025 m, 0.03 m and 0.04 m. It is clearly shown that the terminal velocity approaches the experimental value of Raymond et al. [97] as the width of the channel increases up to 0.04 m. It is found that the boundary effect is negligible when the horizontal size of the solution domain is about eight times of the bubble diameter ($D \geq 8d$), which is then adopted in this work.

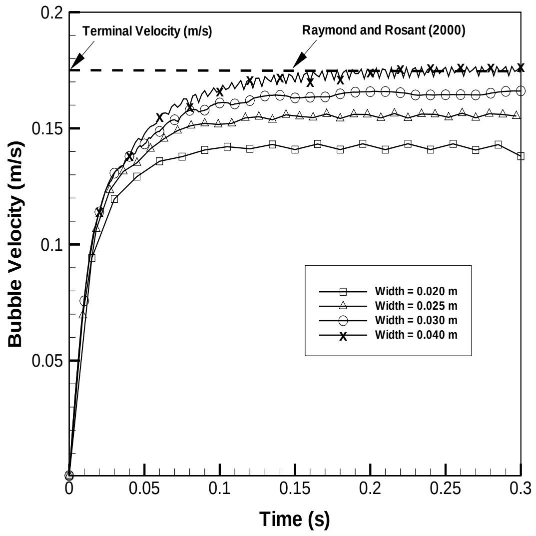

(a)

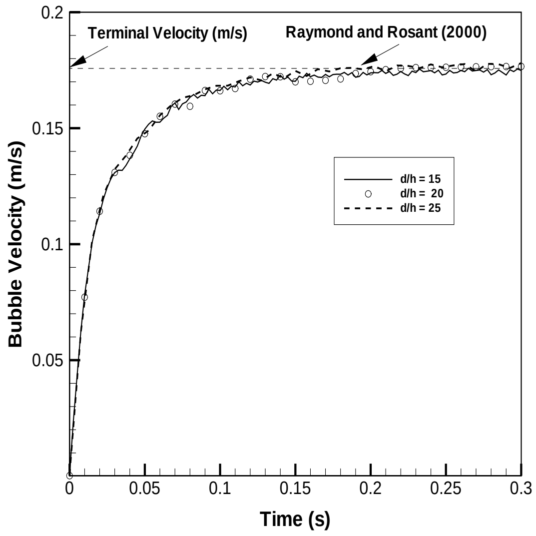

(b)

Figure 3.2: (a) Effect of width of the infinite channel column on the terminal velocity versus time and (b) Effect of number grid cells inside the bubble on the terminal velocity versus time.

3.2.2 Grid resolution effect

Another issue concerns the optimal number of computational cells initially present inside the gas bubble. In all the simulations, a uniform mesh is adopted in both the x and y directions to solve the governing equations. The grid resolution is investigated for a case with S5 fluid ($Mo = 7.4492 \times 10^{-4}$ and $Eo = 9.0416$) corresponding to a bubble size of 5 mm in diameter.

Three different mesh sizes of G1 (120×360), G2 (160×480), and G3 (200×600) are considered for the simulations. For the 120×360 grid, the number of cells per diameter (d/h) is 15, for 160×480 grid, d/h = 20 and for 200×600 grid, d/h = 25. The effect of mesh size on predicted bubble rising velocity is shown versus time in Fig. 3.2b. The difference between the results on the coarse and fine grid is small. When the mesh is coarse, about fifteen grids across the bubble, although the mean bubble rise velocity is well predicted with similar accuracy as those with the fine mesh (G3), there are significant fluctuations in the bubble rising velocity. When the mesh is fine, the fluctuations are negligible. Hence, the computations carried out are based on background mesh G3 and the bubble is meshed with about twenty-five grids across its diameter.

3.2.3 Effect of the bubble size

The effect of the bubble size is investigated with different bubble diameters for each series of fluid. The instantaneous bubble shapes for the different bubble diameters with the S3 fluid are shown in Fig. 3.3. It can be seen from Fig. 3.3 that the bubble deforms from spherical to ellipsoidal shapes as the diameter of the bubble increase. When the bubble diameter $d = 3$ mm, the shape is spherical and when $d = 9$ mm, it is ellipsoidal. The same behaviour was noticed by Bhaga and Weber [77] and Raymond et al. [97] for a rising bubble in liquid under different flow regimes. This is due to the fact that Reynolds and Eötvös numbers increase as the bubble diameter increase. As Re and Eo increase, spherical to ellipsoidal bubble shapes are predicted. These terminal shapes will be verified in Section 3.2.4. The dependance of the terminal velocity and shape on the initial bubble diameter will be reviewed in this section.

Figures 3.4a, b, c and d show the evolution of the bubble velocity versus time as it reaches its terminal velocity, for different diameters of the bubble for S1, S3, S5 and S6 fluids, respectively. It can be seen from the these figures that the velocity of the bubble slowly increases from zero and reaches a steady state value (i.e the terminal velocity). The time taken for the bubble to reach this steady level increases as the diameter of the bubble increases for any given background fluid. As stated previously, it has been proven that the terminal velocity depends on the size of the bubble among other parameters. It is also found that there is an increase in the terminal velocity as the bubble diameter increases for a fixed value of background fluid. The same trend in the velocity evolution and time taken to reach that value is noticed for S3, S5 and S6 fluids. However, there are some discrepancies in the terminal velocity for larger bubbles ($d > 5$ mm) of series S5 and S6, respectively. This may be due to the fact that as the bubble becomes larger or the liquid Morton number becomes smaller, the bubble may rise in a wobbly path [4], and the two dimensional assumption of bubble flow is not valid. In this situation, a three dimensional model is needed to predict the bubble velocity and shape instead of the two

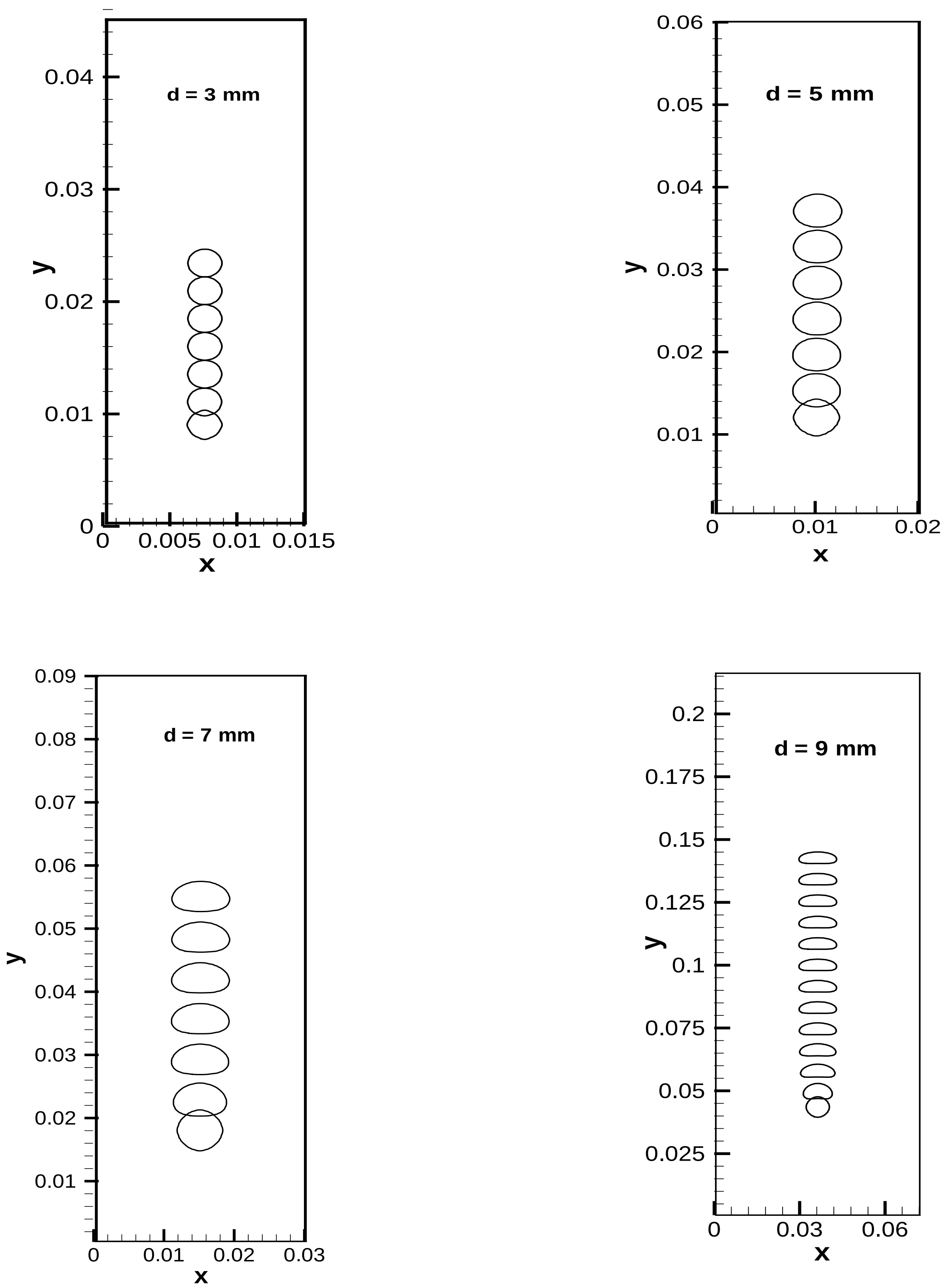

Figure 3.3: Effect of the bubble diameter on the instantaneous shapes of air bubble rising in S3 series fluid.

dimensional model used in this study. On the other hand, these results suggest that a 2D model predicts correctly the balance of forces and mechanisms affect the free rise velocity.

Figures 3.5a and b present the comparisons of bubble terminal velocity and bubble aspect ratios, respectively, between simulations and experiments with different liquid properties and bubble sizes. The aspect ratio is defined as the bubble height in the y direction divided by the bubble width in the x direction. It can be seen from Fig. 3.5 that the terminal velocity increases as the bubble diameter increases for a given fluid while the aspect ratio decreases. Generally, the simulations provide good predictions of bubble terminal shape when compared with the experimental results of Raymond et al. [97] whereas the terminal velocity compares well when the Morton number (Mo) is larger than 1.0×10^{-4} or the bubble size is smaller than 5 mm. These limitations are most likely due to a breakdown of the two dimensional flow assumption. In this case, a three dimensional flow model is needed to predict the bubble velocity instead of the two dimensional model used in this study.

3.2.4 Comparison with Grace Bubble Diagram

Grace [87] has analyzed a large body of experimental data on shapes and rise velocities of bubbles in quiescent viscous liquids and has shown that this data can be condensed into one diagram, provided that an appropriate set of dimensionless numbers (Mo, Eo and Re) is used. To the author's knowledge, the present study is the first attempt to make a systematic comparison between VOF simulations and experimental results, as summarised in Grace's diagram, over a wide range of physical properties, using at the same time realistic values for the density and viscosity ratios. A copy of this diagram, taken from Clift et al. [4] is reproduced in Fig. 3.6 while Fig. 3.7 illustrates the various bubble shapes experienced including the descriptive abbreviations for each shape.

The simulation results for a number of important regimes given in the bubble diagram of Grace, corresponding to the value taken from Raymond et al. [97] (see Table 3.2) are presented. In Table 3.3, the values of the selected Morton and Eötvös numbers are given for simulations of bubbles in different regimes for each series of fluid. In this table,

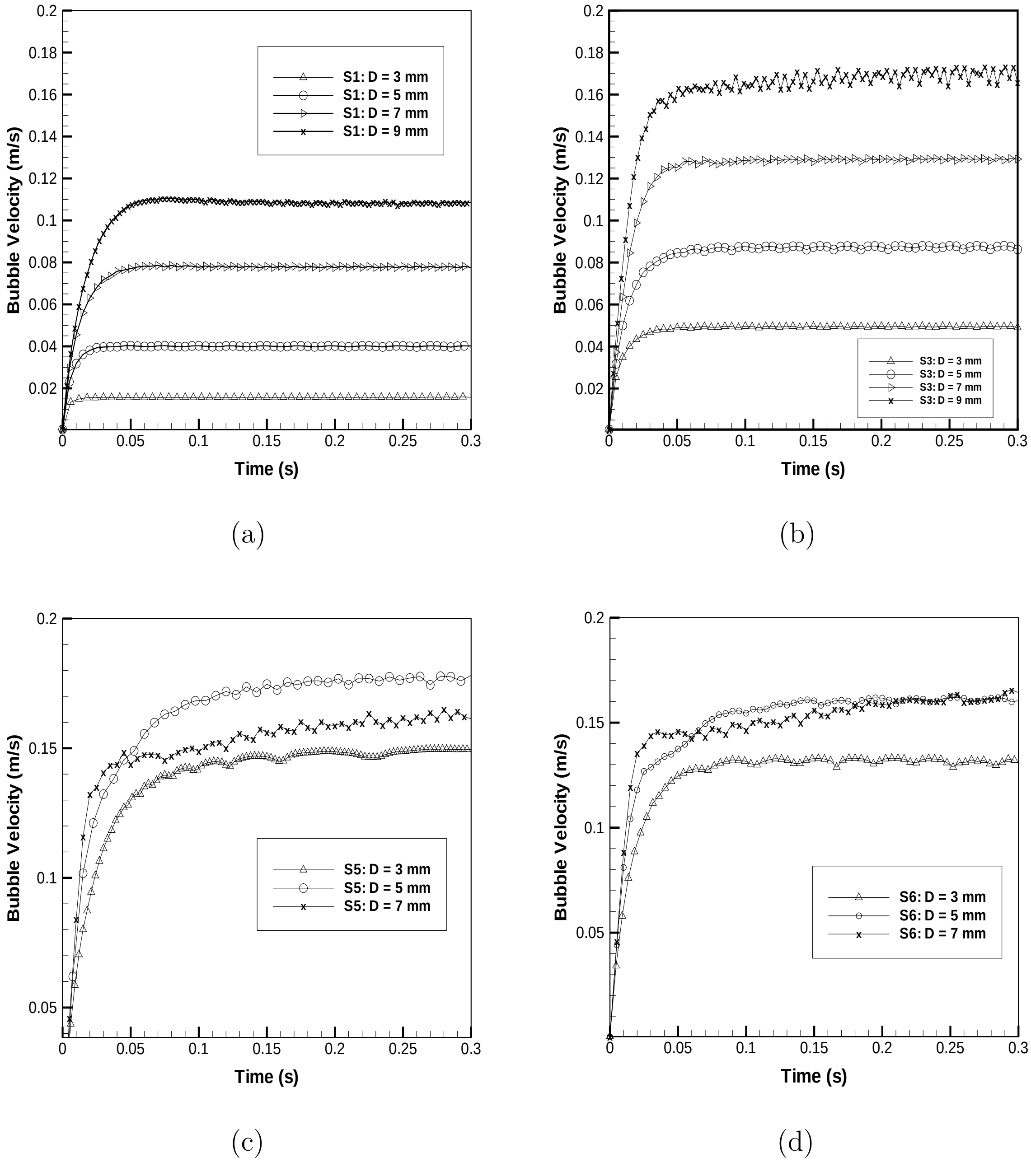

Figure 3.4: Terminal velocity versus time for different bubble diameters and for different fluid properties: (a) S1 fluid (b) S3 fluid (c) S5 fluid (d) S6 fluid.

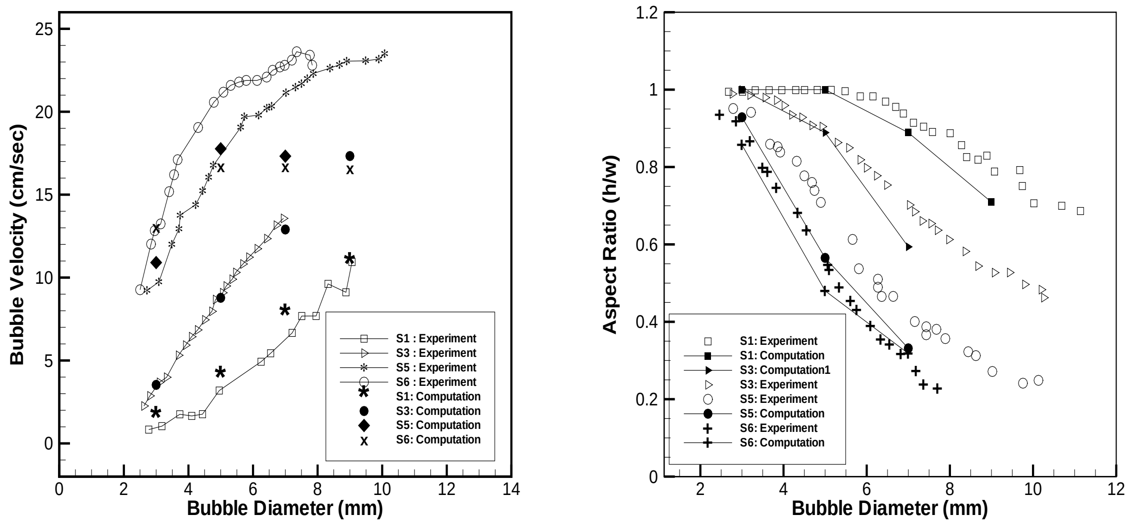

(a) (b)

Figure 3.5: Effect of bubble diameter on the terminal velocity (a) and on the aspect ratio (b) for different fluid properties.

$v_{\infty P}$ and $v_{\infty R}$ represent, respectively, the computed bubble terminal velocity and the bubble terminal velocity obtained by Raymond et al. [97]. For each regime, a code is placed on the Grace diagram and the corresponding shape of the bubble is listed in Table 3.3. Computed shapes and rise velocities of gas bubbles are compared with the corresponding data obtained from the bubble diagram published by Grace [87] and the data from Raymond et al. [97], respectively. In Table 3.4, snapshots are given of the computed shapes of the bubbles. It is also verified that the computed terminal velocity is in good agreement with that of Raymond et al.'s experimental results [97] apart from results, with fluid S1, corresponding to the largest Morton number. The bubble shapes also compare very well with the data obtained from the bubble diagram of Grace [87].

3.2.5 Effect of Mo and Eo

The effects of the Morton (Mo) and Eötvös (Eo) numbers on the bubble steady state shape are investigated next. In Table 3.4, the computed rising terminal bubble shapes

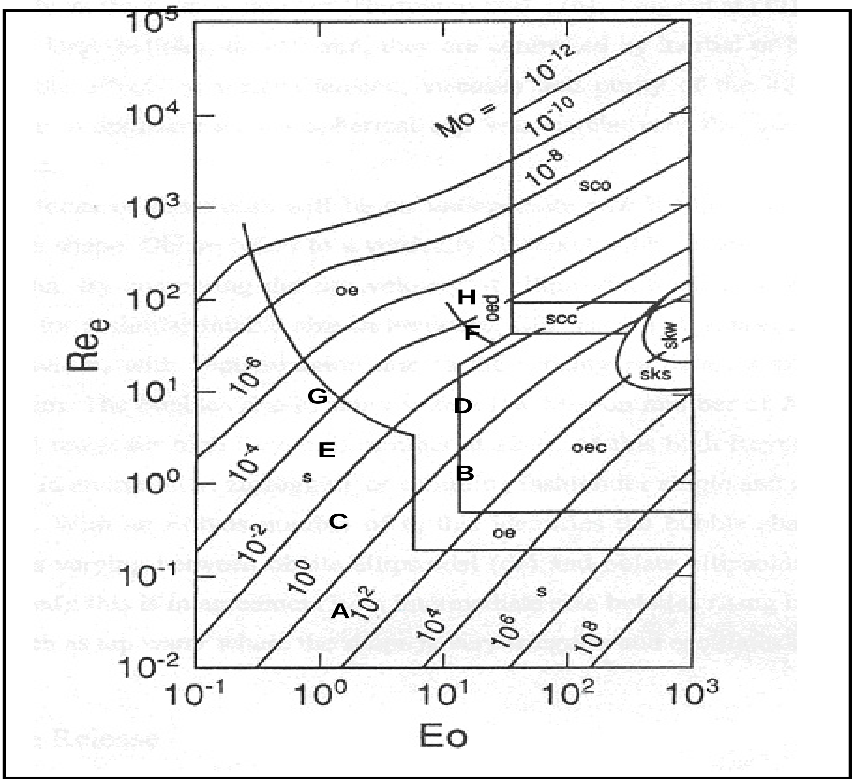

Figure 3.6: Shape-regime map for single bubbles rising in infinite Newtonian liquids [4].

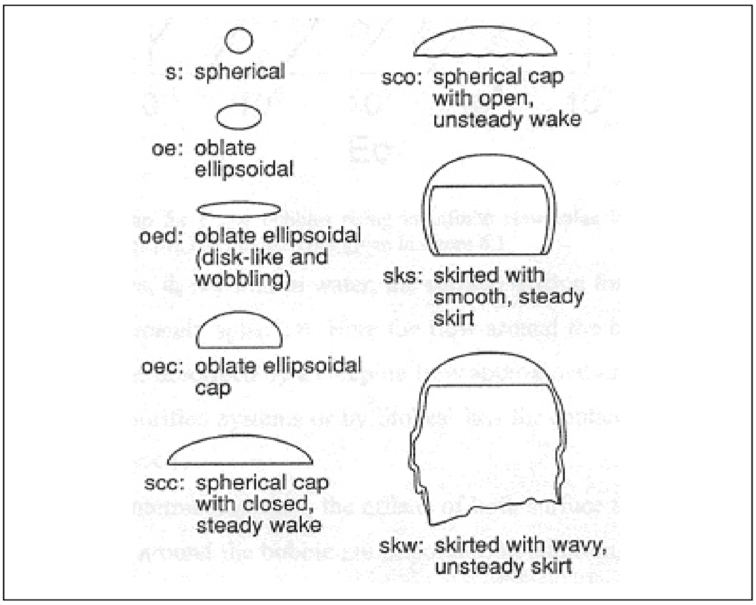

Figure 3.7: Sketches of bubble shapes for corresponding acronyms in Figure 3.6 [77].

Table 3.3: The values of Morton and Eotvos numbers for simulations of bubbles in different regimes according to the bubble diagram Grace [87]

Bubble Regime	Series Fluid	Mo	Eo	$v_{\infty P}$	$v_{\infty R}$	Code in the Grace Diagram, Figure 3.6
Spherical(s)	S1	7.5287	1.7501	1.574	0.9508	A
Intermediate Oblate ellipsoidal (oe) +Oblate ellipsoidal cap (oec)	S1	7.5287	15.7512	10.85	10.3151	B
Spherical (s)	S3	0.1057	1.7221	3.53	3.4012	C
Intermediate Oblate ellipsoidal (oe) +Oblate ellipsoidal cap (oec)	S3	0.1057	15.4990	17.3284	17.3015	D
Spherical (s)	S5	7.4493×10^{-4}	1.6607	10.9055	9.6213	E
Oblate ellipsoidal (oe) (disk-like and wobbling) (oed)	S5	7.4493×10^{-4}	14.9464	-	-	F
Spherical (s)	S6	9.7757×10^{-5}	1.6400	13.0446	12.9316	G
Intermediate Oblate ellipsoidal (oe) +Oblate ellipsoidal wobbling (oed)	S6	9.7757×10^{-5}	14.7602	-	-	H

$*v_{\infty P}$ and $v_{\infty R}$ represent the terminal velocity obtained from the present computations and that of Raymond et al. [97], respectively.

after reaching steady state are represented as functions of Mo and Eo. Spherical to ellipsoidal shapes are observed as Eo increases. For a fixed value of Mo, the bubble becomes ellipsoidal shape as the Eo increases. The change in shape is small for the higher values of the Mo number whereas this is high for lower values of Morton number. When $Mo = 0.1057$, it becomes ellipsoidal for $Eo = 15.75$ while it becomes ellipsoidal for $Eo = 9.52$ when $Mo = 7.449 \times 10^{-4}$. It can be noticed from Table 3.4 that, for a fixed value of Eo, the bubble further changes its shapes from spherical to ellipsoidal as Mo decreases, as a fourth power of the decreasing viscosity of the background fluid (Eq. (3.2)). This means that a relatively small change in viscosity can induce significant change in the bubble behaviour. For example (see Table 3.4), this effect can clearly be noticed as the bubble becomes ellipsoidal in shape with a significant increase in its velocity.

Table 3.4: Computed terminal bubble shapes as a function of diameter of the bubble and series fluids

Bubble Diameter (mm)		3	5	7	9
		Eötvös Number (Eo)			
Series	Mo	≈ 2	≈ 5	≈ 10	≈ 15
S1	7.5287		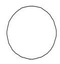	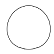	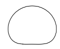
S3	0.1057		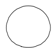	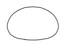	
S5	7.4493×10^{-4}		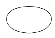		
S6	9.7757×10^{-5}		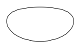		

3.2.6 Drag Coefficient

In the present simulations, the pressure jump at the interface is not sharp but spreads over a certain number of grid cells. Therefore, it is difficult to calculate accurately the drag coefficient from the pressure distribution on the interface. Another way to evaluate the drag coefficient (C_d) is to consider the balance between the buoyancy force and hydrodynamic drag, which leads to the following relation (Clift et al. [4]):

$$C_d = \frac{14.9}{Re^{0.78}} \tag{3.4}$$

Equation (3.4) is valid for larger values of Re (i.e. $Re > 2$). The drag coefficient is calculated based on the Reynolds number, which is again a function of the terminal velocity. Another useful correlation exists, which defines the Weber number, in terms of Re and Mo. The following relationship (Eq. (3.5)) is valid over the range of $Mo = [9 \times 10^{-7}$, 7] (Raymond et al. [97]):

$$We = f(Mo)Re^{5/3} \tag{3.5}$$

where the function $f(Mo)$ is given by

$$f(Mo) = 0.42Mo^{0.35} \tag{3.6}$$

The values of Reynolds and Weber numbers for different sized bubbles are presented in Table 3.5 for fluids S3, S5 and S6. The reason why the series S1 fluid is not considered for calculating drag coefficient is that the range of the values of Re and We is outside the comparable limits of the work of Ryskin et al. [88] and Raymond and Rosant [97]. The present results are compared in Table 3.6 to the drag coefficients calculated in these numerical studies. Again, they are found to be in close agreement.

The drag coefficient is also plotted with results from Ryskin et al. [88] and Raymond et al. [97] for various We and Re values, in Fig. 3.8. A good agreement is found between the present results and those of Ryskin et al. [88] and Raymond et al.[97]. It can be noted that the drag coefficient increases as We increases for a given value of Re. For a given value of We, the drag coefficient decreases as Re increases, suggesting that the drag coefficient value for an ellipsoidal terminal bubble is lower than that for a spherical bubble.

Table 3.5: The values of Reynolds and Weber numbers for the rising of different sized bubbles in the series fluids

Diameter (mm)	S3		S5		S6	
	Re	We	Re	We	Re	We
3	-	-	5.3806	0.5579	11.0315	0.9068
5	2.2676	0.7486	14.6063	2.9471	25.9431	3.7714
7	4.6643	2.4907	19.931	4.9473	32.9647	5.6219

Table 3.6: Comparison of calculated and measured values of drag coefficient of different sized bubbles in the series fluids

Diameter(mm)	S3		S5		S6	
	C_d	$C_{d,RR}$	C_d	$C_{d,RR}$	C_d	$C_{d,RR}$
3	-	-	4.01	3.9119	2.2905	2.422
5	7.9674	8.519	1.8401	2.01	1.1756	1.45
7	4.5394	4.511	1.440	2.27	0.9752	1.3501

C_d and $C_{d,RR}$ represent the present computed drag coefficient and that of Raymond and Rosant [97], respectively.

3.2.7 Comparison with Bhaga and Weber Experimental Observations

Simulations of rising bubbles are compared here with data taken from the experimental work of Bhaga et al. [77] to assess the present numerical method for higher values of Mo and Eo. The parameters used in these simulations are taken from corresponding experimental values as listed in Table 3.7. In Figs. 3.9 and 3.10, snapshots of the computed bubble shapes are compared with experimental visualizations. It can be seen that the computed bubble shapes compare reasonably well with the experimentally determined shapes of Bhaga et al. [77]. The oblate ellipsoidal cap bubbles are predicted as expected from the diagram for these values of Mo and Eo.

Table 3.7: The values of Eotvos and Morton numbers used in the simulations taken from corresponding experimental values of Bhaga et al. [77]

Cases	Eotvos Number (Eo)	Morton Number (Mo)	Shape
a	116	848	Oblate ellipsoidal cap
b	116	266	Oblate ellipsoidal cap
b	116	41.1	Oblate ellipsoidal cap
d	116	5.51	Oblate ellipsoidal cap

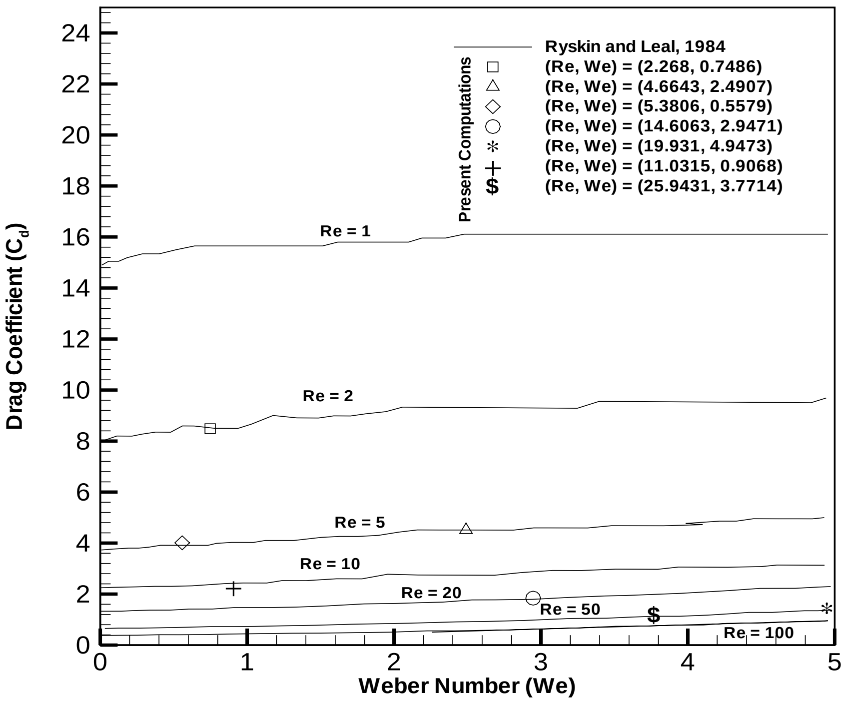

Figure 3.8: Comparison between measured and calculated values of the drag coefficient as a function of the Weber number.

3.2.8 Air Bubble in Water

Next, the simulations of an air bubble rising in quiescent water are performed. For these simulations, the true physical properties (see Table 3.8) for the air-water system are used. The 2D computational grid is a uniform orthogonal mesh of 140×280 cells and the time step is constant and equal to 10^{-4} s. Initially a spherical bubble of air is released from the bottom of the column. For comparison, the terminal velocity of the bubble is calculated using the following equation, proposed by Clift et al. [4]:

$$v_\infty = \sqrt{\frac{2.14\sigma}{\rho_l d_e} + 0.505 g d_e} \tag{3.7}$$

Equation (3.7) was obtained experimentally for air bubbles in water and is valid for the equivalent diameter of bubble greater than 1.3 mm.

The simulations are carried out with different grid sizes, as shown in Fig. 3.11a and the terminal velocities are compared with predictions from Eq. (3.7). The computed terminal velocity is 0.21 m/s and the corresponding value calculated using Eq. (3.7) is

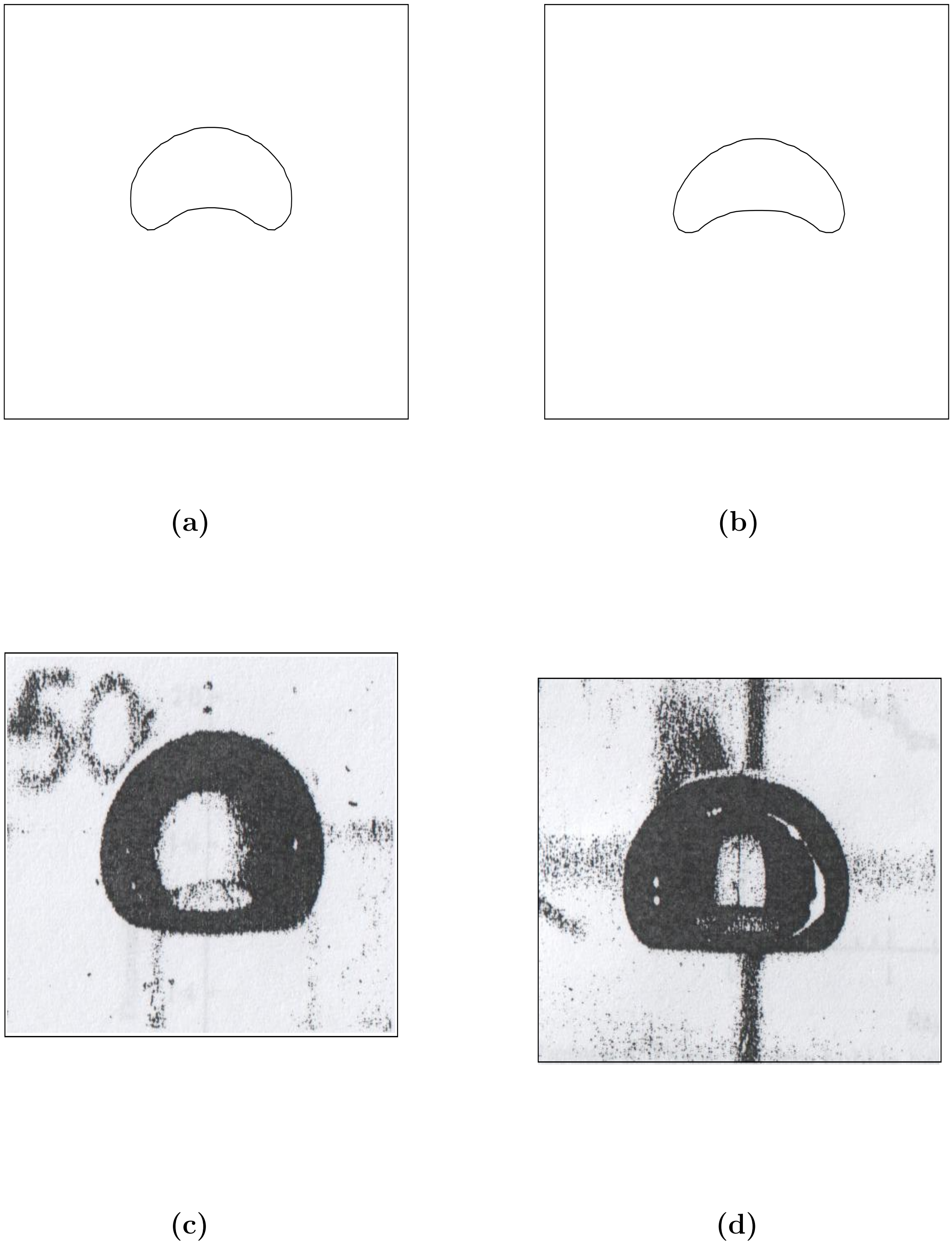

Figure 3.9: Comparison of the computed terminal bubble shapes with that of Bhaga and Weber [77] experimental findings: Left: $Eo = 116$ and $Mo = 848$, Right: $Eo = 116$ and $Mo = 266$; (a & b) Computations and (c & d) Experiments.

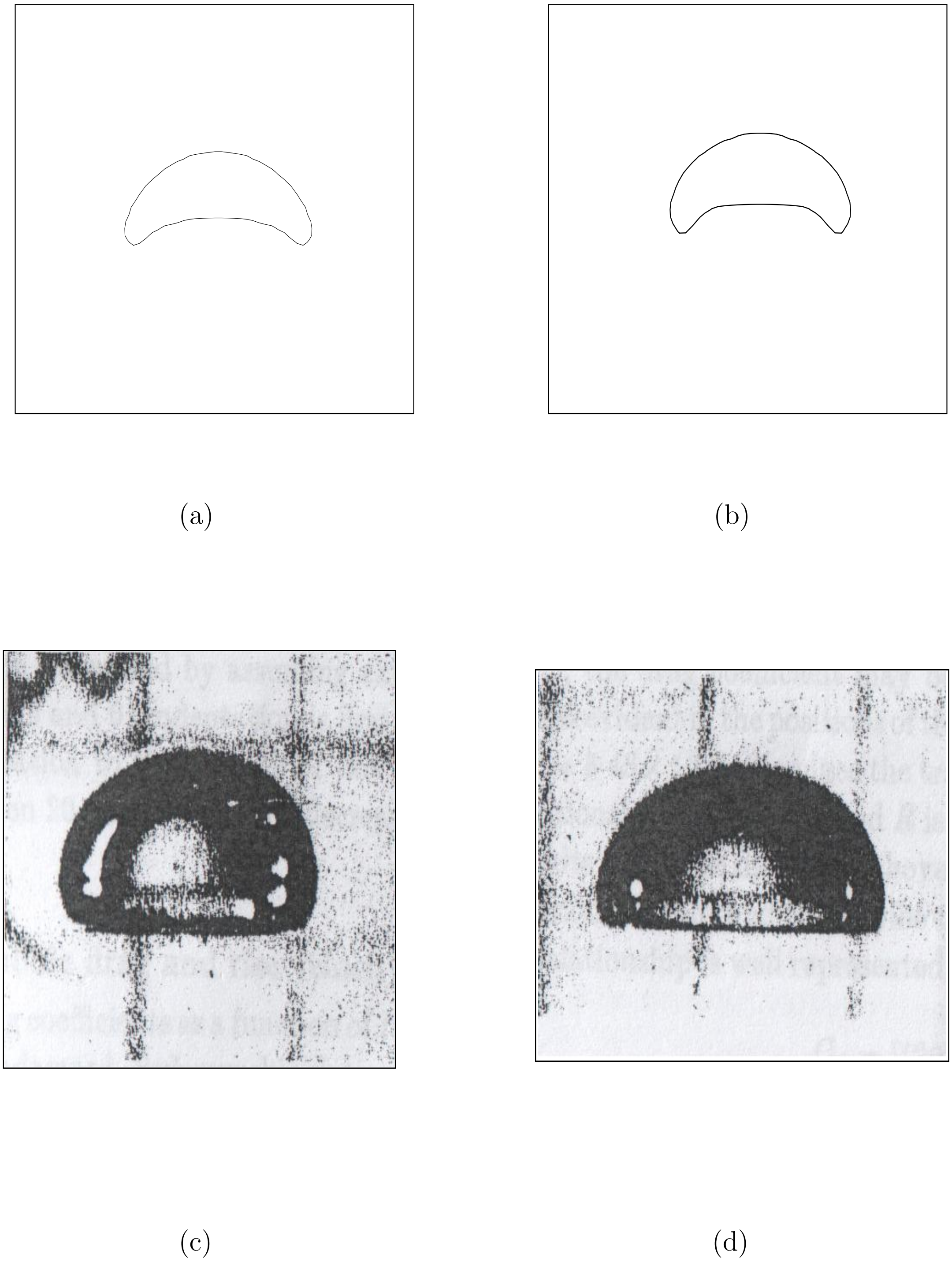

Figure 3.10: Comparison of the computed terminal bubble shapes with the experimental results presented by Bhaga and Weber [77]: Left: $Eo = 116$ and $Mo = 41.1$, Right: $Eo = 116$ and $Mo = 5.51$; (a & b) Computations and (c & d) Experiments.

Table 3.8: Physical Properties of the Air-Water System

Properties	Values	Units
Liquid density	1000	kg/m^3
Liquid viscosity	0.001	$kg/m^{-1}s^{-1}$
Gas density	1.225	kg/m^3
Gas viscosity	0.000018	$kg/m^{-1}s^{-1}$
Surface tension	0.0728	N/m

0.26 m/s. Hence comparison between the terminal velocity of bubble obtained from the present computation and those of experimental equation gives a non negligible percentage error of 19.23%. This is significantly larger than differences observed in Table 3.3. For the 3 mm diameter air bubble, the Morton number (Mo) is equal to 10^{-6} and the Eötvös number is 1.21. For these values, it is predicted from the shape regime map in Figs. 3.6 and 3.7 that the bubble will attain a shape of intermediate stage between spherical and oblate ellipsoidal. This is found to be the case in the computed results as shown in Fig. 3.11b.

Here, the drag coefficient is calculated using different equations suggested by Bhaga and Weber [77], Ryskin and Leal [88], and Ishii and Zuber [134], since Eq. (3.4) for C_d used in Section 3.2.6 is not valid for the Re value of 630, corresponding to a terminal velocity of 0.21 m/s.

$$C_d = \frac{2}{3}\sqrt{E_o} \tag{3.8}$$

$$C_d = \frac{4gd}{3v_\infty^2} \tag{3.9}$$

The drag coefficient (C_d) is calculated using Eq. (3.9), which is a function of the terminal velocity of bubble, and compared with that of Eq. (3.8) of Ishii and Zuber [134]. The computed value of C_d is 0.869 for the terminal velocity of 0.21 m/s. It has a reasonably good agreement with the value of 0.733 obtained using the Eq. (3.8) with a percentage error of 15.65%.

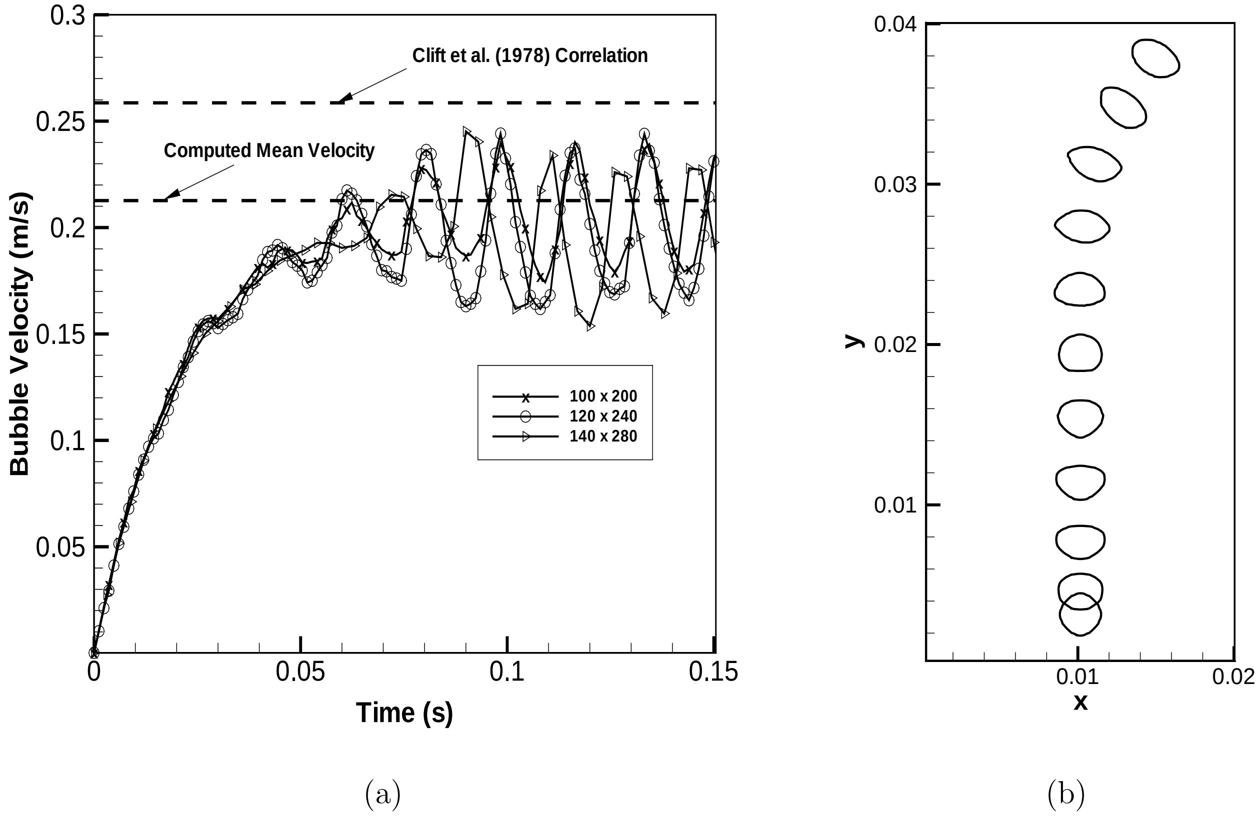

Figure 3.11: (a) Effect of grid size on the terminal velocity of bubble versus time, and (b) Instantaneous shapes of air bubble of diameter 3 mm rising in water.

3.3 Summary

Numerical simulations of rising bubbles are performed to assess the capability and accuracy of the present method. Comparisons are made with published numerical and experimental data in terms of terminal velocity, aspect ratio, terminal shape and drag coefficient of bubbles. The effects of fluid properties, wall effects, grid refinement, and dimensional parameters, are all investigated in some details. Overall, the present numerical method performs adequately for bubble dynamics, in spite of the two-dimensional assumption. The main exception to this is in the case of larger diameter bubbles of fluids S5 and S6. This suggests a necessity of three dimensional model for this kind of bubbles.

CHAPTER 4

DYNAMICS OF A SLIDING BUBBLE IN AN ISOTHERMAL VISCOUS LIQUID

In this chapter, the dynamics of a sliding bubble in an isothermal viscous liquid are presented and discussed. The computations are performed with an air bubble sliding along the lower surface of an inclined plate immersed in water. Three different plate inclination angles (θ) ranging from 10° to 30° are considered. The simulation results are compared with experimental results obtained, as part of the project, at a collaborating institute, the Thermodynamics group in the Trinity College Dublin (TCD), Ireland. The comparisons are carried out with the experimental observations of terminal bubble shapes, terminal velocities, sliding bubble paths and aspect ratios.

4.1 Objectives

Comparison with experimental results is made in spite of the two dimensional limitation of the computational model. This is justified by the fact that the primary objective of the study is to assess the suitability of the numerical modelling methods adopted to represent the main mechanisms affecting the dynamic behaviour of the sliding bubbles. Comparison with experimental results is therefore on a primarily qualitative basis.

The objectives of this chapter are to

- assess the Navier-Stokes and VOF solvers for multi-fluid flow modelling without heat transfer,
- study the effect of static contact angle on the predictions of the VOF solver,
- discuss and compare the results obtained numerically with the experimental results,

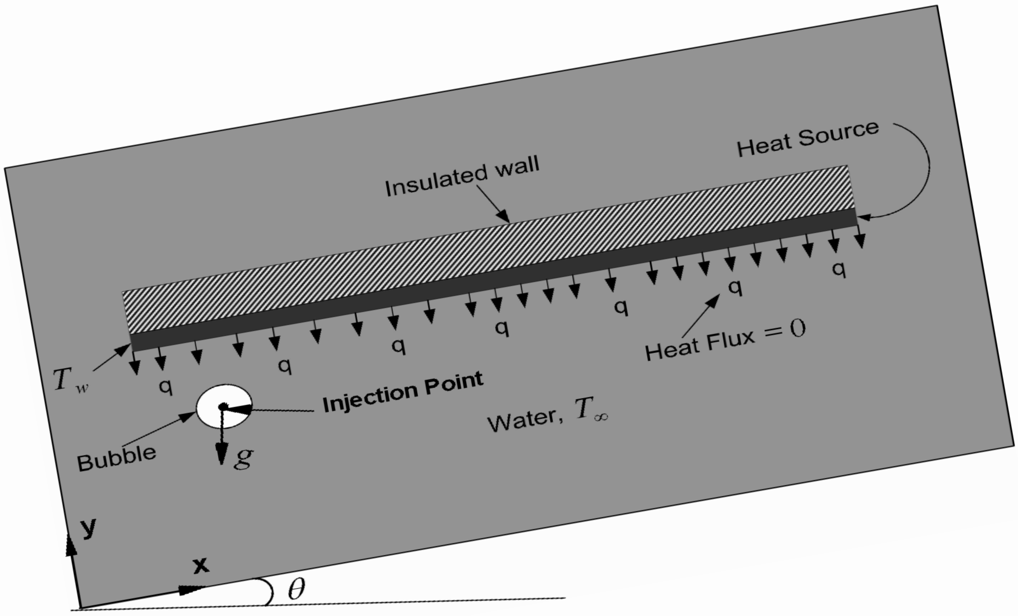

Figure 4.1: Schematic diagram of computational domain setup for sliding bubble motion.

- study the dynamics of the air bubble sliding along the lower surface of an inclined plate immersed in water, for different inclination angles, and
- study the effect of inclination angles on the dynamics of the sliding air bubble in water.

4.2 Problem Definition

4.2.1 Experimental Setup

The experimental setup is illustrated in Section C.1 of Appendix C. This setup is used to perform experiments for the sliding bubbles without heat transfer. Here there is no heat supplied to the foil which covers the lower part of the inclined plate so isothermal conditions are maintained throughout the investigations. The same setup is also used for sliding bubbles with heat transfer by supplying heat to the foil.

4.2.2 Computational Setup

The schematic diagram of the computational domain and set up for sliding bubble motion is shown in Fig. 4.1. Initially the surrounding fluid velocity is zero everywhere, the plate and the tank are fixed at an angle from the horizontal, and a spherical air bubble is initialised below the plate. The center of the bubble is positioned at a distance of 6.5 mm measured perpendicularly from the lower surface of the inclined plate over which it slides, for each angle of inclination. The gravity vector is aligned with the vertical direction and is at an angle with the y-axis, which is perpendicular to the plate surface. As a result, the bubble rises upward in the direction of the gravity vector due to buoyancy force. Once it hits the plate surface, it may bounce and wobble before it starts sliding along the bottom wall of the plate. The time required for the bubble to start sliding depends upon the density and viscosity differences between the surrounding fluid and the bubble, the plate inclination angle, the size of the bubble and the surface tension coefficient.

For the computations discussed in this chapter, there is no heat flux supplied to the lower surface of the plate over which the bubble slides, while the upper surface of the plate is insulated. No-slip boundary conditions are applied at all confining walls and inclined plate surfaces. For temperature, an isothermal boundary condition is used for the walls of the tank and for the lower surface of the plate, and the adiabatic boundary condition is used for the left, right and top walls of the plate to replicate the same conditions used in the experiments. In the experiments, the lower surface is made of 25 micron thick AISI 321 stainless steel foil and the upper side is covered with a perspex sheet. It can be approximated as one layer at the bottom surface of the plate in the computations and is modelled with a finite thickness.

Three different plate inclination angles (θ), 10°, 20° and 30° from horizontal, are used to perform the simulations. The parameters used in these simulations are listed in Table 4.1. Computations are performed with a grid of 800×200 cells and a time step of 10^{-4} s. This mesh means that the number of cells inside the bubble is 15, which was found to be sufficient to capture the bubble interface as discussed in Section 3.2.2 of Chapter 3. The mesh is uniform and orthogonal with square cells of width and height equal to

Table 4.1: The Parameters Used in the Sliding Bubble Computations

Parameters	Values	Units
Liquid density	1000	$\mathrm{kg/m^3}$
Liquid viscosity	0.001	$\mathrm{kg/m^{-1}s^{-1}}$
Gas density	1.225	kg/m^3
Gas viscosity	0.000018	$\mathrm{kg/m^{-1}s^{-1}}$
Surface tension	0.0728	N/m
Gravitational acceleration	9.81	$\mathrm{m/s^2}$
Plate inclination angles	$10°$, $20°$, and $30°$	-
Plate dimensions	length = 0.073, width = 0.002	m
Tank dimensions	length = 0.08, width = 0.02	m

10^{-4} m. The maximum Courant number based on the maximum bubble velocity is 0.2.

4.3 Effects of Various Forces on Sliding Bubble Dynamics

Sliding bubble dynamics can be characterised by the effects of various forces that act on the bubble while it slides along the surface of the inclined plate. The main forces that have significant effects on the sliding bubble dynamics are the buoyancy, surface tension and drag forces. Fig. 4.2a shows the various forces acting on a sliding bubble. Here the buoyancy force can be resolved into two components, namely one in the x-direction, and the other in the y-direction. The x-component of the buoyancy force acts parallel to the plate surface and induces the bubble slide while the y-component of the buoyancy force acts perpendicular to the plate surface and flattens the bubble.

In general, when the bubble rises in an infinite channel, the surface tension force attempts to maintain the initial spherical shape of the bubble while buoyancy forces the bubble to rise upward in the direction of the gravity vector. Drag forces oppose the motion of the bubble and are primarily due to adverse pressure gradients. Pressure drag increases with the bubble frontal cross section area and the rise or slide velocity.

When the bubble touches a solid surface, surface tension influences the angle formed between the air-water interface and the solid surface. For a static problem, the so-called contact angle can be measured relatively easily and is known to be a property of the two fluids and of the solid. If the bubble is in motion, the contact angle is also a property of the dynamics of the interface. This dependance however is generally neglected in computational models, which means that a fixed and constant contact angle is used. The influence of surface tension on a stationary bubble against a flat surface will depend on the bubble shape as well as on the contact angle. If the bubble is flattened, as shown in Fig. 4.2a, surface tension will attempt to reduce the stretching ratio. On the other hand, if the bubble is initially stretched in the y direction, surface tension will pull the bubble closer to the surface (see Fig. 4.2b).

The contact angle formed by the interface is a result of the interaction of buoyancy and surface tension forces. In a numerical model, it is imposed a priori rather than being a result of force balance. This means that a change in the imposed θ_c may affect the shape and dynamics of the bubble in a way that that does not represent actual physical phenomenon. In particular, it can be anticipated that by increasing the contact angle, the bubble will be forced to stretch in the y direction, and vice versa. There is one further undesirable effect of the numerical method for modelling surface tension near a wall by imposing a constant angle whether it is done statically or dynamically. As soon as a small volume fraction of air enters a wall adjacent cell, the model assumes that the interface is in contact with the wall. As a result, the model attempts to impose an orientation to the interface as a function of the contact angle. This will effectively attract the bubble towards the wall. It also means that the bubble interface can not remain continuously connected. The interface is broken as soon as the bubble touches a wall. Experimental observations see to show, on the other hand, that as a bubble slides along a surface a very thin layer of liquid isolates the bubble from the solid. If the bubble interface remains intact, surface tension can be expected to promote oscillations at the bubble interface and to promote bouncing of the bubble away from the surface. Away from the wall the bubble is able to change its shape so as to minimise pressure drag. The result should be an increase in bubble slide velocity. We can therefore expect that if the numerical model suppresses or reduces the bubble bounces, its velocity and trajectory can be affected significantly.

Gravitational flattening against the plate surface is more predominant for lower inclination angles than for higher inclination angles. The y-component of the buoyancy force decreases as the plate inclination angle (θ) increases, whereas the x-component of the buoyancy force increases as the plate inclination angle (θ) increases. The primary effect is that the bubble velocity increases with inclination angle. This, in turn, increases the drag force which acts in the direction opposite to the bubble trajectory. The effect on the bubble shape is to stretch it in the y-direction, perpendicular to the plate surface provided that it overcomes surface tension. Hence the stretching of the bubble in the y-direction depends on the relative strength of the surface tension and drag forces.

When the plate is placed horizontally (i.e., $\theta = 0$), the y-component of the buoyancy force is equal to the density difference between the bubble and the surrounding fluid times the gravity acceleration and the volume of the bubble while the x-component of the buoyancy force is zero (see Fig. 4.2b). In this case the bubble is squeezed against the wall by the y-component of the buoyancy force and remains stationary with small oscillations of bubble interface for a short period of time after it impacts on the wall.

When the plate is placed vertically (i.e., $\theta = 90$), the x-component of the buoyancy force is equal to the y-component of it in the case of $\theta = 0$ while the y-component of the buoyancy force is zero. The bubble will move upward against the wall as it rises in an infinite fluid, but with wall adhesion effects. The bubble may move away from the surface of the plate at some stages due to the effects of vortex structure created by its trailing wake. This vortex structure pushes the bubble away from the surface with the help of fluid that the bubble brings to back portion of it from the frontal portion.

4.4 Assessment of Static Contact Angle

The present mathematical formulation uses a fixed or static contact angle between the bubble interface and the solid surface to model the dynamics of the air-water interface as it interacts with the wall. It is necessary to estimate the contact angle which best approximates the experimental results.

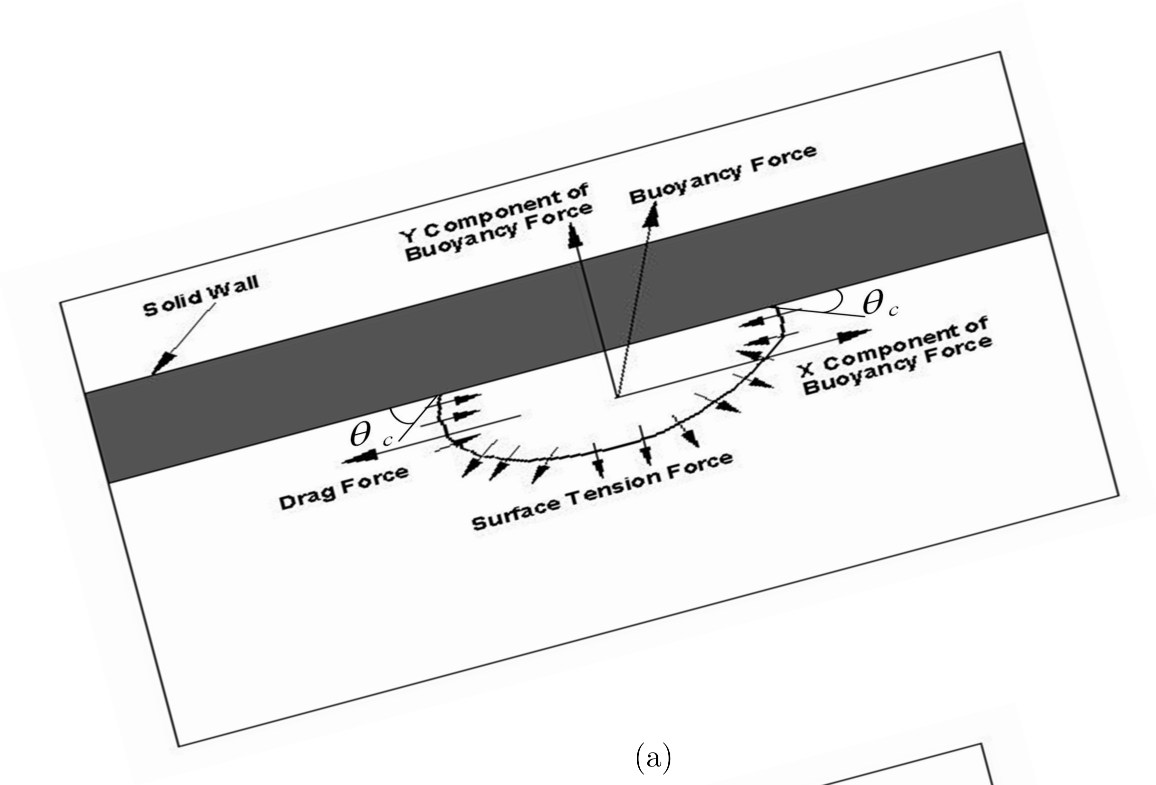

(a)

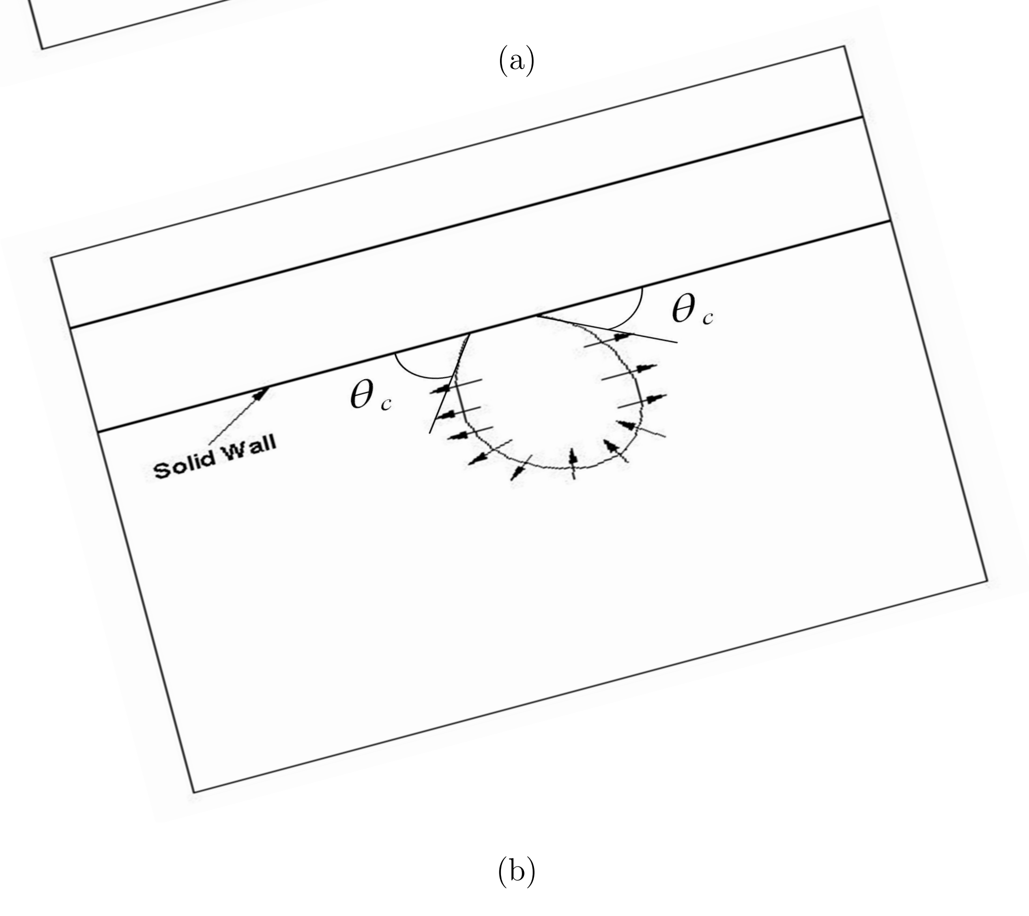

(b)

Figure 4.2: Forces acting on a sliding bubble: (a) for a bubble stretched in x-direction (b) for a bubble stretched in y-direction.

Experiments were performed carefully twice to get repeatability for each plate inclination angle. Snapshots of experimental sliding bubbles for different plate inclination angles are presented in Figs. 4.7, 4.8 and 4.9. Each image is presented with a time interval of 0.04 s. In the experiment, the static contact angle was calculated from side view images of the sliding bubble at different time instants. It was found that the value of contact angle is in a range between 20° to 30°.

In order to verify the dependance of computational predictions on the value of the contact angle, simulations were carried out with three different contact angles, namely $\theta_c = 20°$, $25°$ and $30°$ for all plate inclination angles, $\theta = 10°$, $20°$ and $30°$. These results are assessed in this section by comparison with experimental results. Evolutions of the bubble motion from computational results for the plate inclination angle $\theta = 10°$ are presented in Figs. 4.3a, b and c for different contact angles $\theta_c = 30°$, $25°$ and $20°$, respectively. Figs. 4.4a, b and c show the evolutions of the bubble motion from computational results for the plate inclination angle $\theta = 20°$ for different contact angles $\theta_c = 30°$, $25°$ and $20°$, respectively. Figs. 4.5a, b and c show the evolutions of the bubble motion from computational results for the plate inclination angle $\theta = 30°$ for different contact angles $\theta_c = 30°$, $25°$ and $20°$, respectively. The time interval between the two consecutive bubble shapes is 0.04 s for each plate inclination angle after the second bubble shape.

It can be seen from Fig. 4.3 that the results are almost similar for the contact angles $\theta_c = 25°$ and $30°$, whereas there is a noticeable difference in the bubble shapes with $\theta_c = 20°$. It is observed from Fig. 4.3b that the evolution of bubble motion for the plate inclination of 10° with $\theta_c = 25°$ compare reasonably well with the experimental results shown in Fig. 4.7. For $\theta = 20°$, as shown in Fig. 4.4, the results are almost similar for contact angles $\theta_c = 20°$ and $25°$, whereas there is a noticeable difference in the bubble shapes with $\theta_c = 30°$. In particular, it can be seen that the bubble stretches more in the y-direction, perpendicular to the plate surface. Again the evolution of bubble motion for the plate inclination of 20° with $\theta_c = 25°$, as shown in Fig. 4.4b, predicts the experimental results (see Fig. 4.8) reasonably well.

For $\theta = 30°$, as shown in Fig. 4.5, differences in the evolutions of bubble motion are clearly noticeable with different contact angles. The contact area of the bubble on the surface of the plate reduces as the contact angle increases. With $\theta_c = 30°$, lift off occurs while it slides over the surface of the plate. Here, the evolution of bubble motion obtained computationally with a contact angle of 30° (see Fig. 4.5a) is closely comparable with the experimental results shown in Fig. 4.9. These results tend to suggest that using a static contact angle is a valid approximation for the range of plate inclination angles chosen since it successfully predicts a number of mechanisms observed in the experiments. These are (i) the bubble lifting off the surface for the inclination angle $\theta = 30°$ (ii) gradual stretching in y direction with increased inclination angle and the resulting slide velocity.

Similarly, Computational results of the bubble velocities for three contact angles, namely $\theta_c = 20°$, 25° and 30° for all plate inclination angles, $\theta = 10°$, 20° and 30°, are compared with the experimental results. The bubble velocity is calculated over a time period before the bubble leaves the plate surface. In the computations, it is estimated by calculating the distance between the centroid of two consecutive bubbles and dividing by the time interval between those positions. This same procedure above, as followed by Brian et al. [135], was used to calculate the bubble velocities from the experimental images shown in Figs. 4.7, 4.8 and 4.9, respectively.

Figures 4.10a, b and c show the time evolution of the bubble velocity for different contact angles and plate inclination angles. The results are compared with the bubble velocity obtained experimentally for each plate inclination angle. It is observed that computational results compare reasonably well with the experimental results with a contact angle of 25° for the plate inclination angles $\theta = 10°$ and 20°. For $\theta = 30°$, the computational bubble velocity approaches the experimental values for a contact angle of 30°. It is worth mentioning here that contact angle plays a major role in the sliding bubble motion, as even small changes in the contact angle makes a noticeable difference in the bubble velocity.

When $\theta = 10°$, trends in the bubble velocity are not uniform with different contact angles, as shown in Fig. 4.10a. Since the velocity of the bubble with $\theta_c = 20°$ is higher than that obtained with $\theta_c = 25°$ while the velocity of the bubble with $\theta_c = 30°$ is less than that with $\theta_c = 20°$ and is higher than that with $\theta_c = 25°$. This suggests

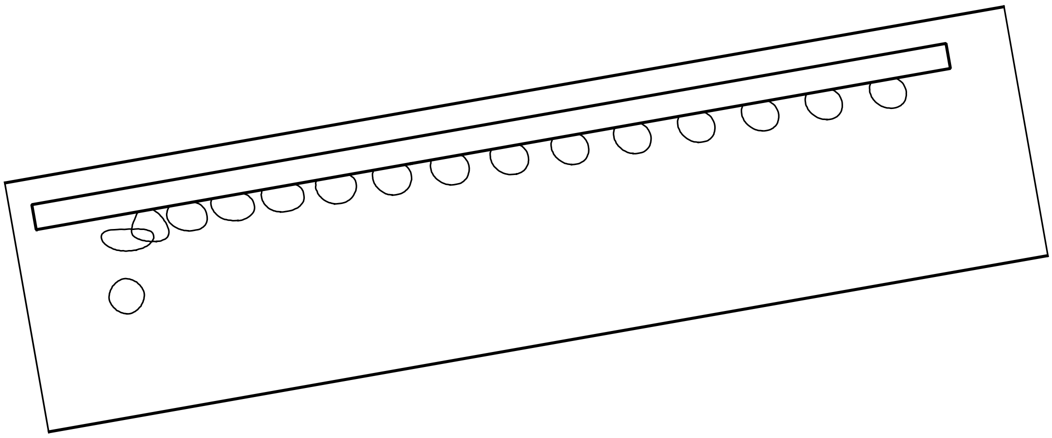

(a)

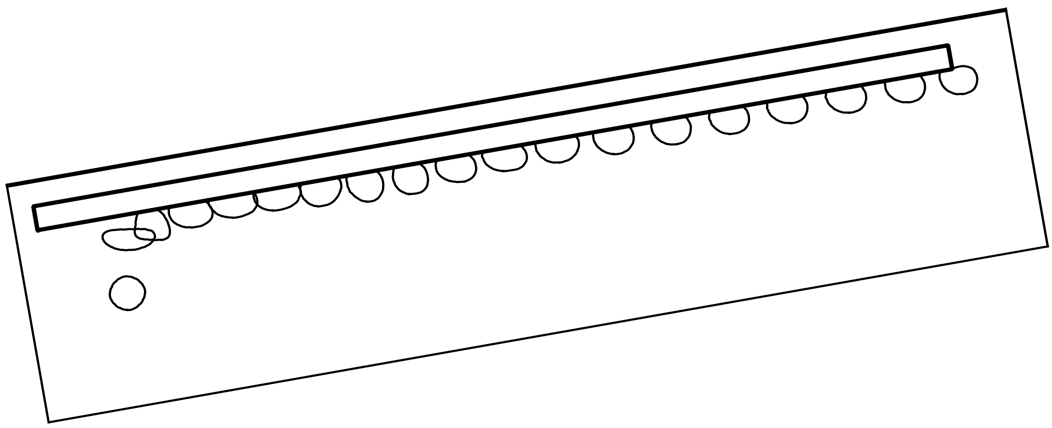

(b)

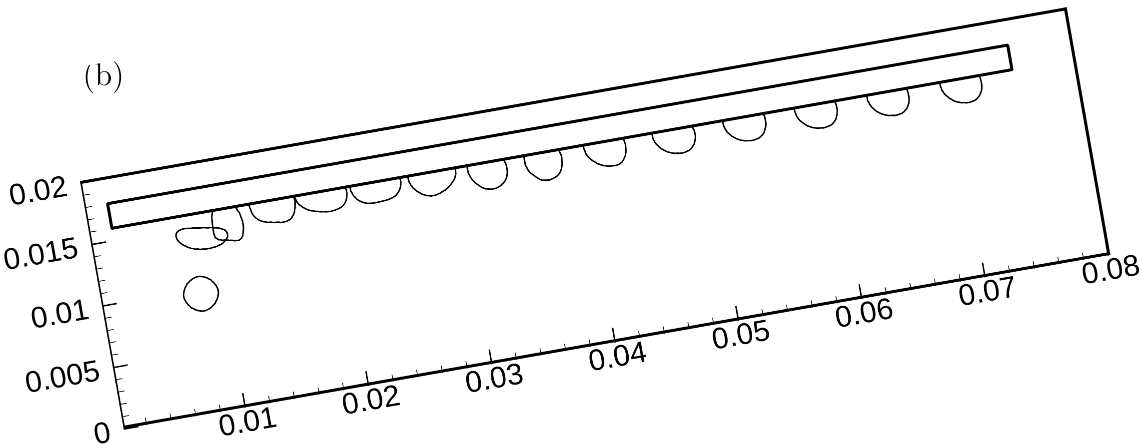

(c)

Figure 4.3: Numerical Computation: Evolutions of sliding bubble motion at a plate inclination angle of 10° for different contact angles; (a) $\theta_c = 30°$, (b) $\theta_c = 25°$ and (c) $\theta_c = 20°$.

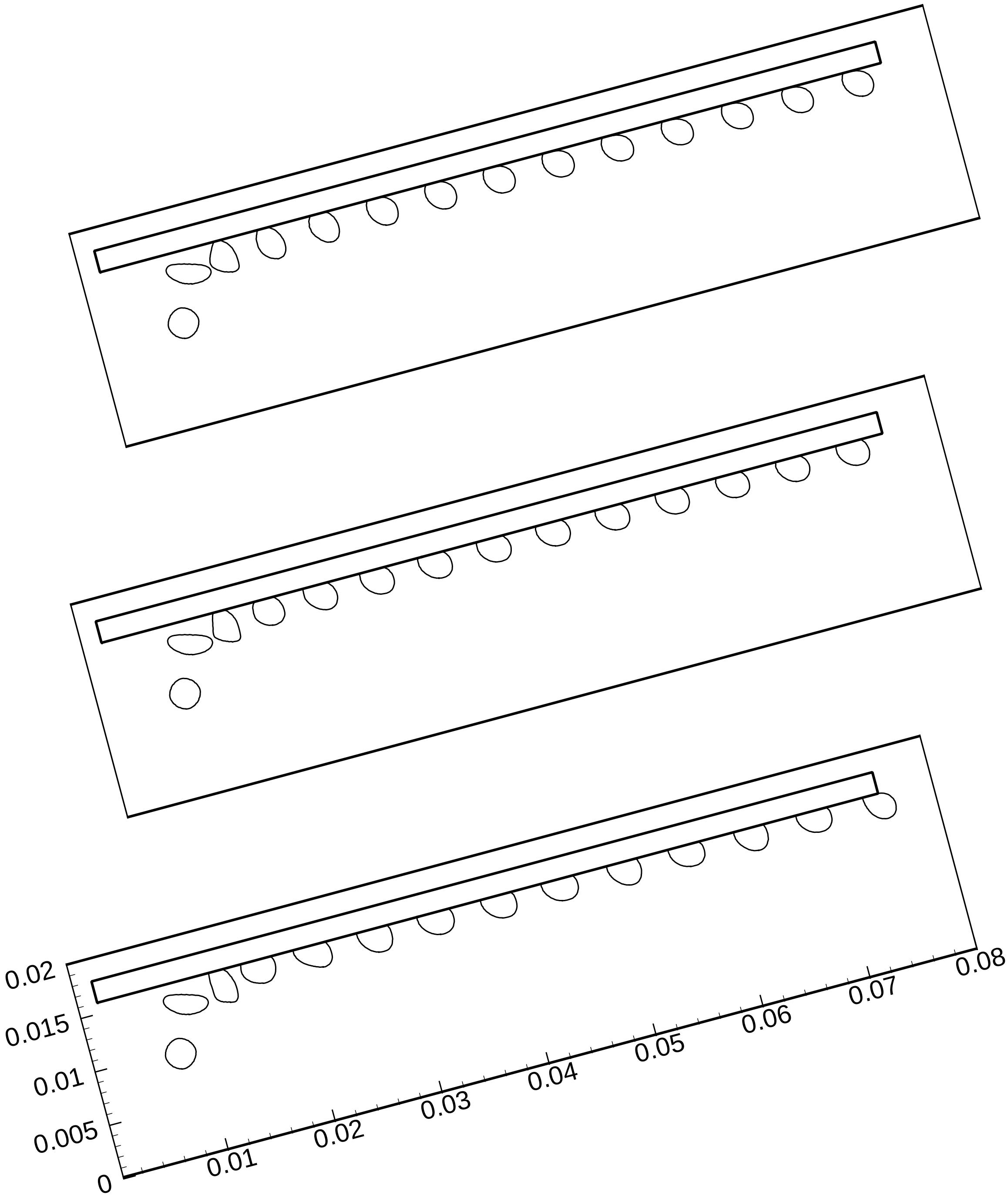

(a)

(b)

(c)

Figure 4.4: Numerical Computation: Evolutions of sliding bubble motion at a plate inclination angle of 20° for different contact angles; (a) $\theta_c = 30°$, (b) $\theta_c = 25°$ and (c) $\theta_c = 20°$.

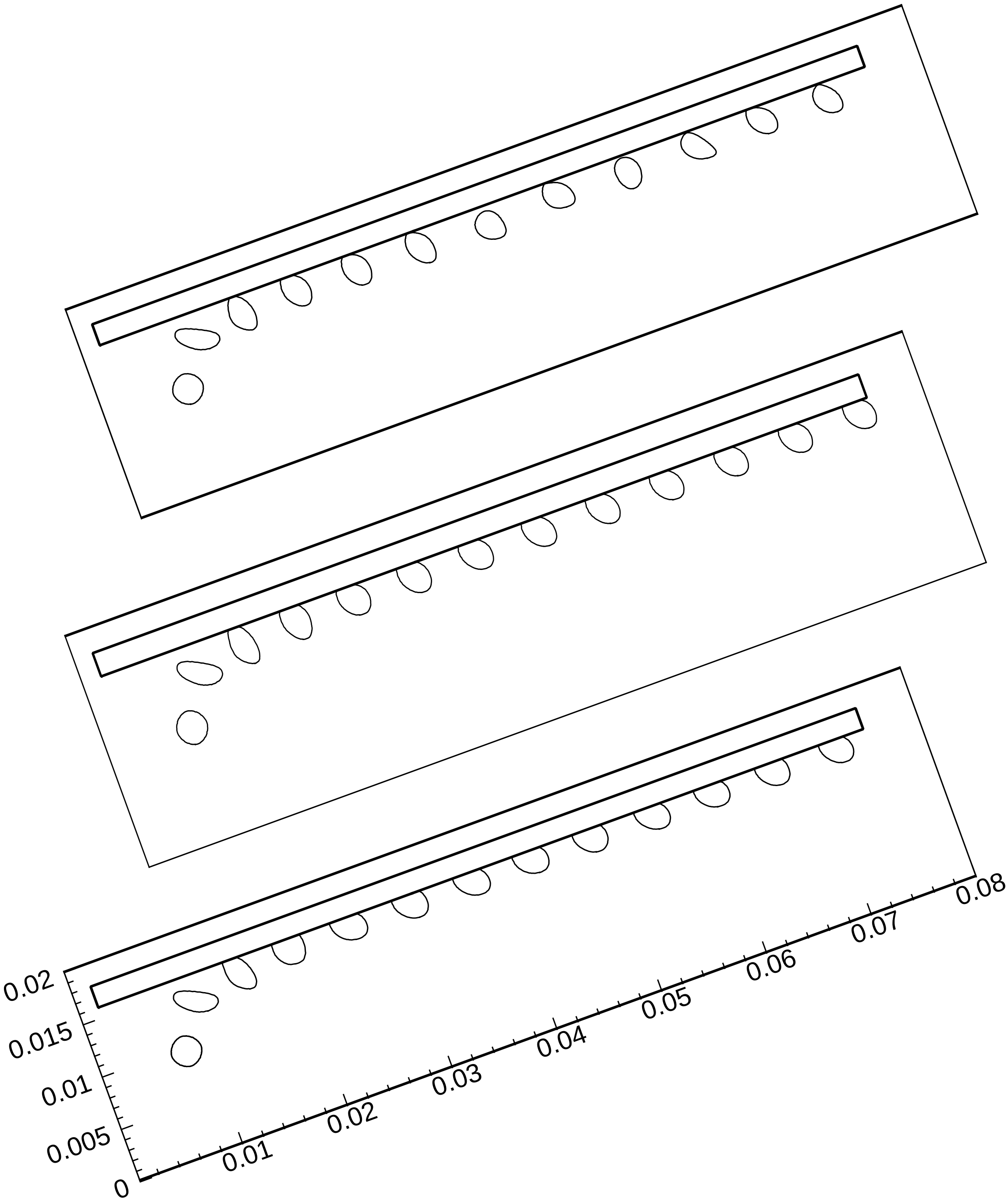

(a)

(b)

(c)

Figure 4.5: Numerical Computation: Evolutions of sliding bubble motion at a plate inclination angle of 30° for different contact angles; (a) $\theta_c = 30°$, (b) $\theta_c = 25°$ and (c) $\theta_c = 20°$.

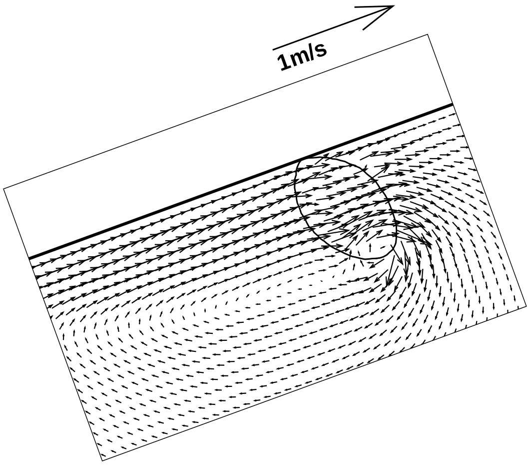

(a) (b)

Figure 4.6: Vector plots of sliding bubble motion at an angle $\theta = 30°$ with $\theta_c = 30°$: (a) Just before lifts off (b) While lifts off.

that increasing θ_c has two opposite effects. On the one hand, an increase in the bubble stretching in the y direction induces an increase in the bubble frontal surface area. This can be assumed to increase pressure drag and hence reduce the bubble velocity. On the other hand, as can be observed in Fig. 4.3, as the bubble is stretched in the y direction, its lower section also appears to slide at a higher velocity deforming the bubble. Since the bubble is found to move faster in this case, it can be assumed that the resulting shape is more aerodynamic (i.e. offers less resistance). This means that, although stretching in the y direction can increase drag, resulting deformation of the bubble can improve its aerodynamics. However, periodic oscillations are noticeable with all contact angles. These oscillations may be attributed to the periodic oscillations in the bubble shape while it slides along the plate surface. This is more predominant with $\theta = 10°$, suggesting that surface tension, buoyancy and drag forces, are of comparable magnitude and interact in a dynamic fashion. However, for $\theta = 10°$ the average velocity of the bubble agrees with the experimental results with the contact angle $\theta_c = 25°$.

When $\theta = 20°$ and $30°$, trends in the bubble velocity for different contact angles are not the same as those obtained with $\theta = 10°$, as shown in Figs. 4.10b and c. A

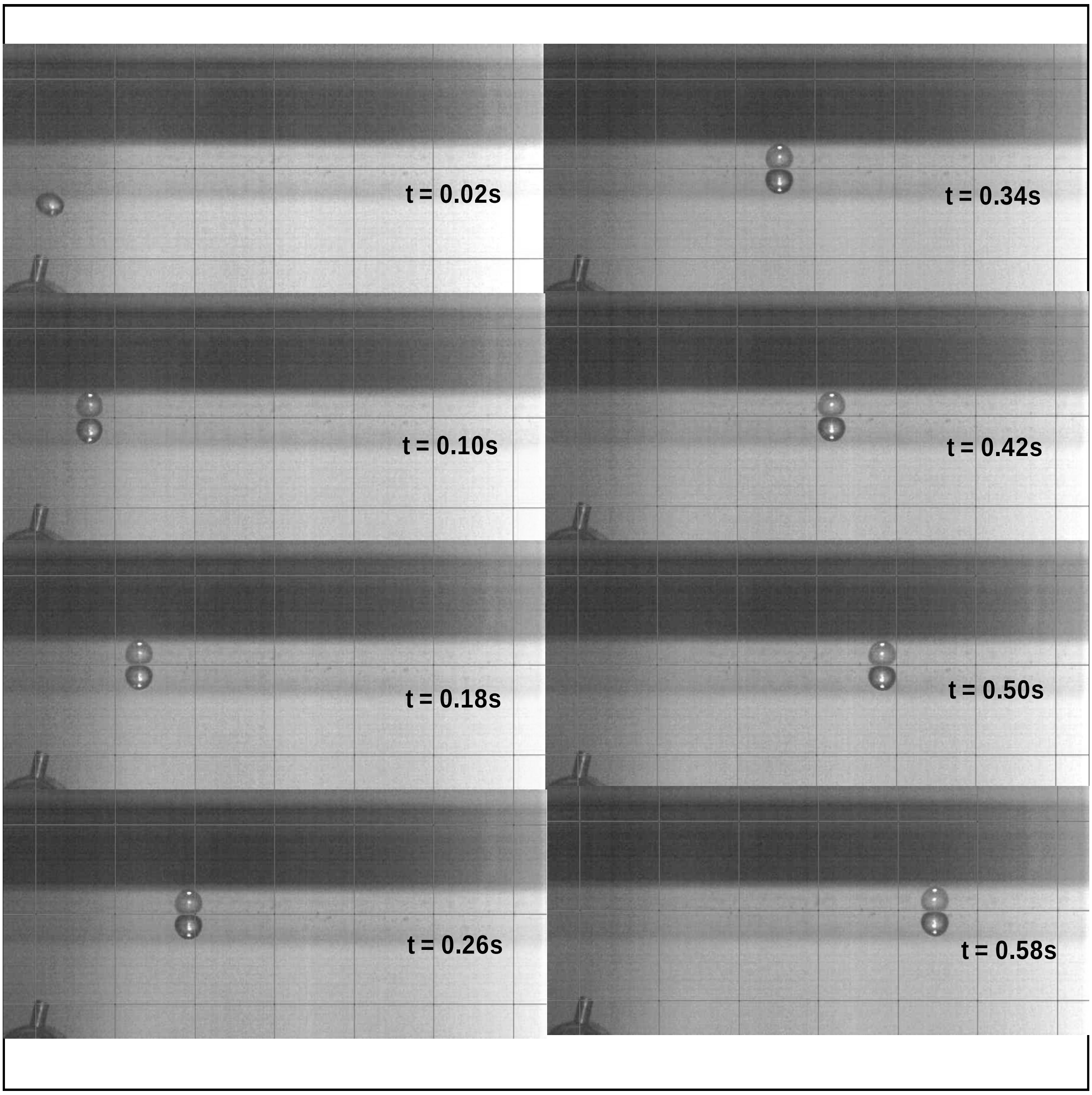

Figure 4.7: Evolution of sliding bubble motion at a plate angle of 10° - Experimental Results.

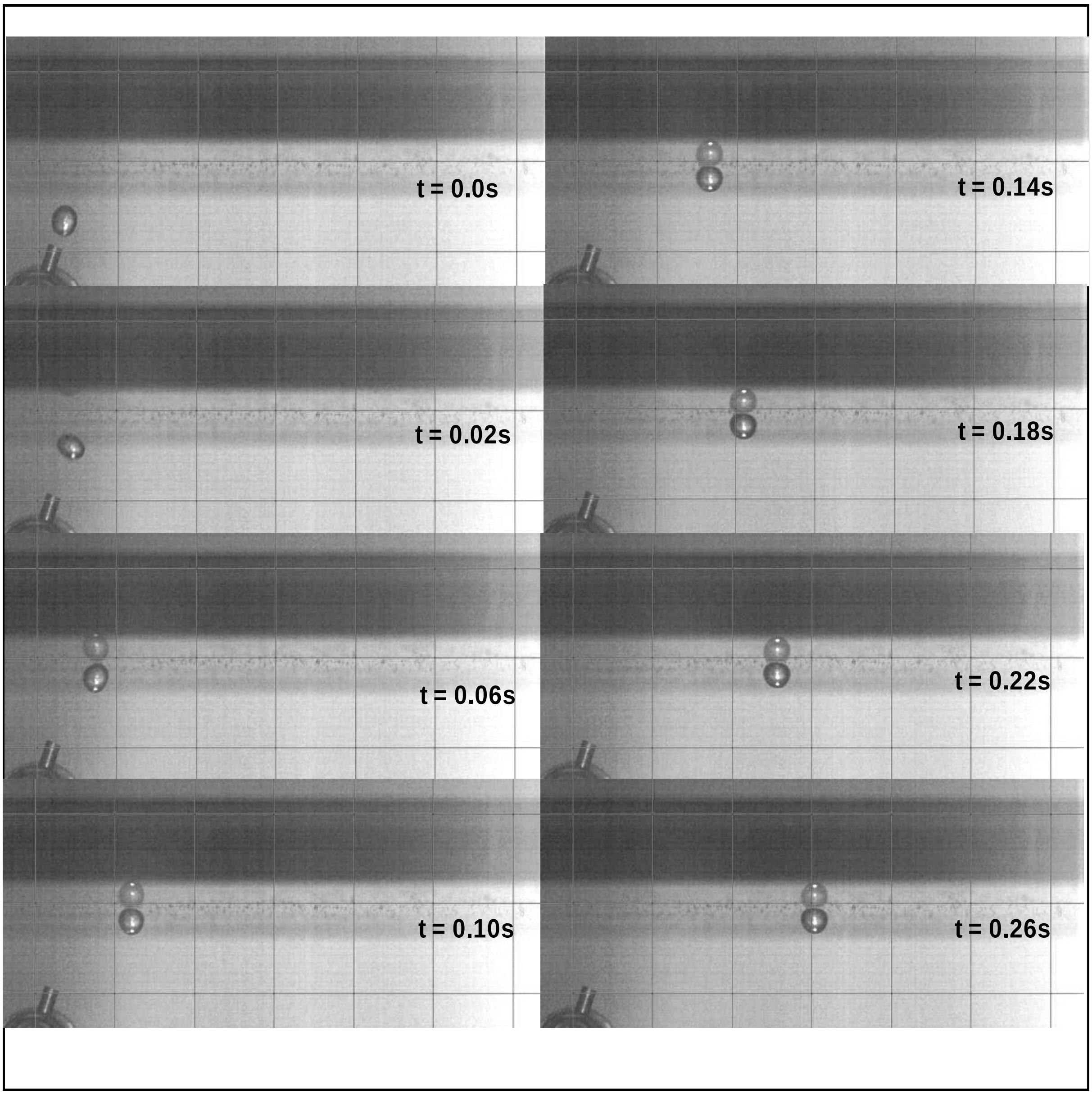

Figure 4.8: Evolution of sliding bubble motion at a plate angle of 20° - Experimental Results.

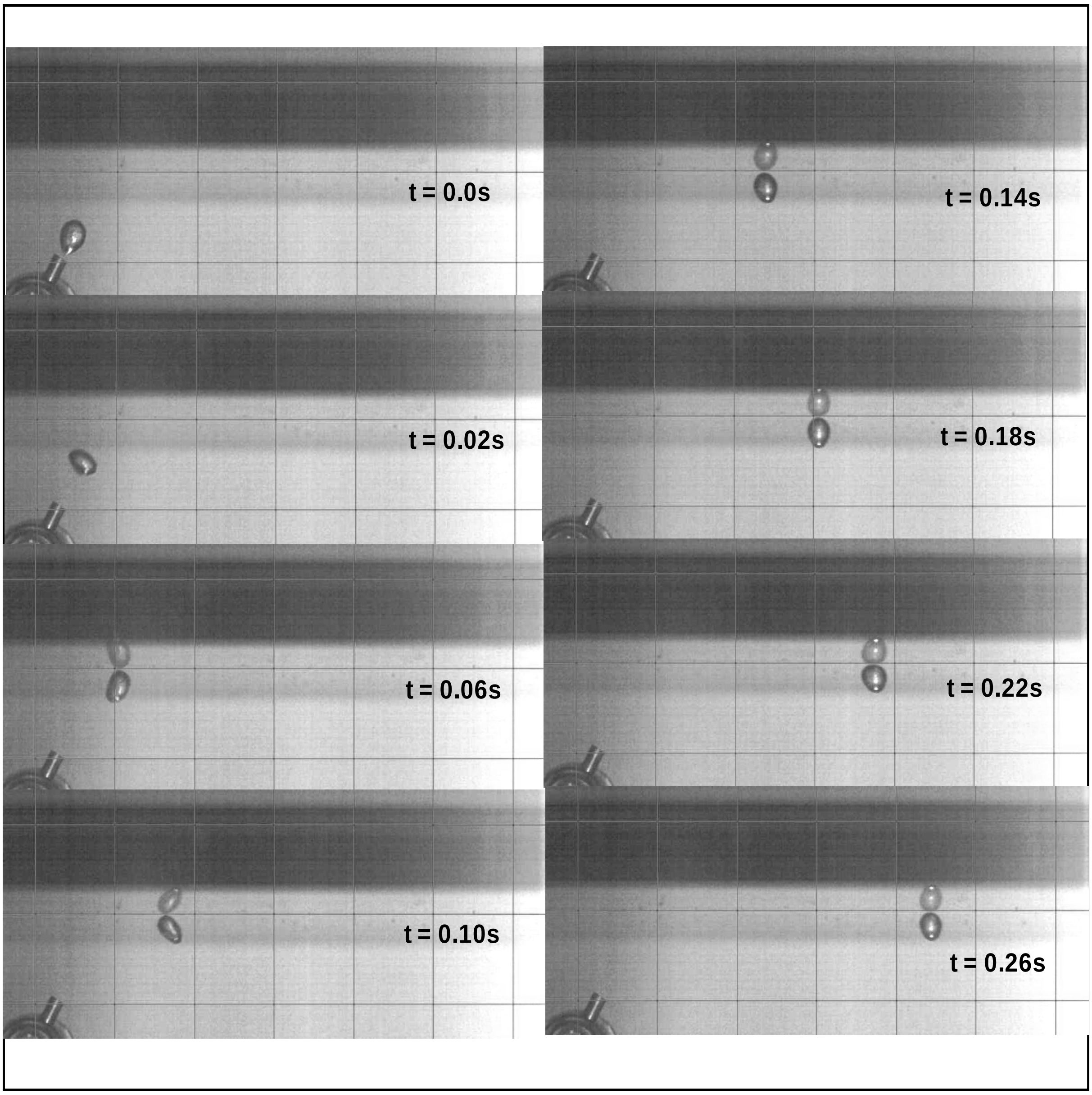

Figure 4.9: Evolution of sliding bubble motion at a plate angle of 30° - Experimental Results.

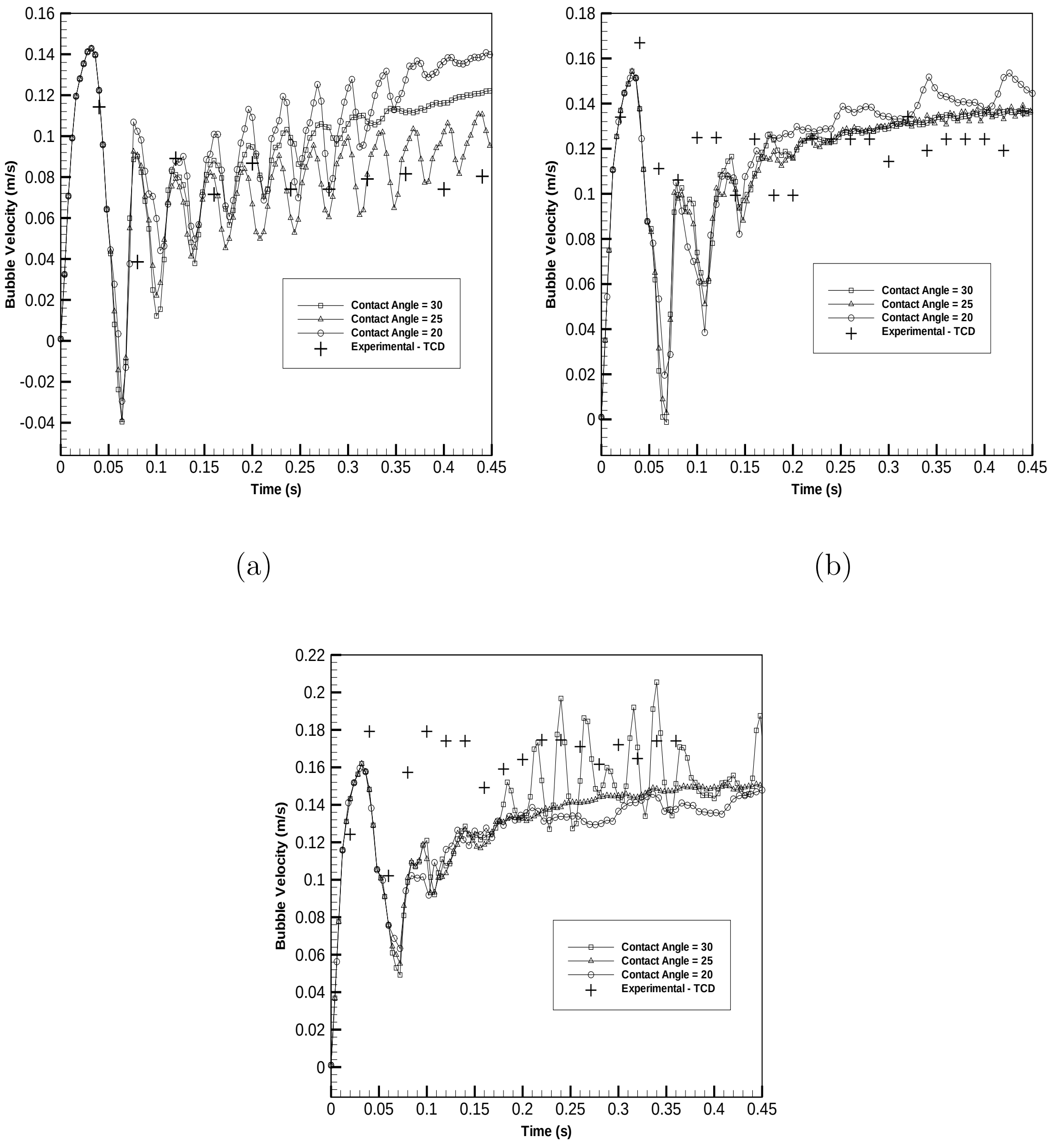

(a) (b)

(c)

Figure 4.10: Comparison of terminal velocity of sliding bubble for different plate inclination angles (θ) and contact angles; (a) $\theta = 10°$, (b) $\theta = 20°$ and (c) $\theta = 30°$.

similar increase in velocity is not obtained as θ_c increases for $\theta = 20°$ and $30°$. Here the velocity of the bubble increases as the contact angle increases. This suggests that, as the buoyancy x-component increases, it becomes the predominant driving and controlling force. With $\theta_c = 20°$ and $25°$, the bubble velocities are almost equal for $\theta = 20°$ and $30°$ and oscillations are significantly less. Since the bubble slides with a higher speed periodic oscillations might be damped out. However, large oscillations appear in the bubble velocities with $\theta_c = 30°$. This may be due to the fact that, as the contact area reduces with contact angle, the bubble shape is increasingly stretched away from the plate surface. For example, this can clearly be observed from Fig. 4.5a for $\theta = 30°$. This, in turn, leads to a detachment of the bubble from the wall. This effect is more pronounced for $\theta = 30°$ as the bubble lifts off the surface (see Fig. 4.5a), as shown in Fig. 4.10c. The lift off mechanism creates even more oscillations in the bubble shape, path and velocity. These oscillations are also observed in the experimental results.

Several contributing factors leading to lift off can be suggested. The lift off mechanism can be explained by the effects of vortex structure created by trailing wake of the bubble. This vortex structure brings the surrounding fluid into the gap between the air-water interface and the solid surface. This can clearly be observed from the vector plots of sliding bubble motion before and while the bubble lifts off from the surface, as shown in Figs. 4.6a and b, respectively. When the contact area of the bubble with the surface is less and the velocity of the bubble is higher, the surrounding fluid at the trailing wake can easily push the bubble away from the surface. This effect is evident with $\theta_c = 30°$ for $\theta = 30°$. This suggests that, when $\theta < 30°$, the effects of surface tension/wall adhesion and the y-component of buoyancy forces are capable of keeping the bubble against the surface of the plate even with higher contact angles .

4.5 Computational Results with Fixed Contact Angle

As discussed in Section 4.4, computational results obtained with a contact angle of 25° for the plate inclination angles 10° and 20° and with a contact angle of 30° for the plate inclination angles 30° provide realistic predictions. The corresponding computational

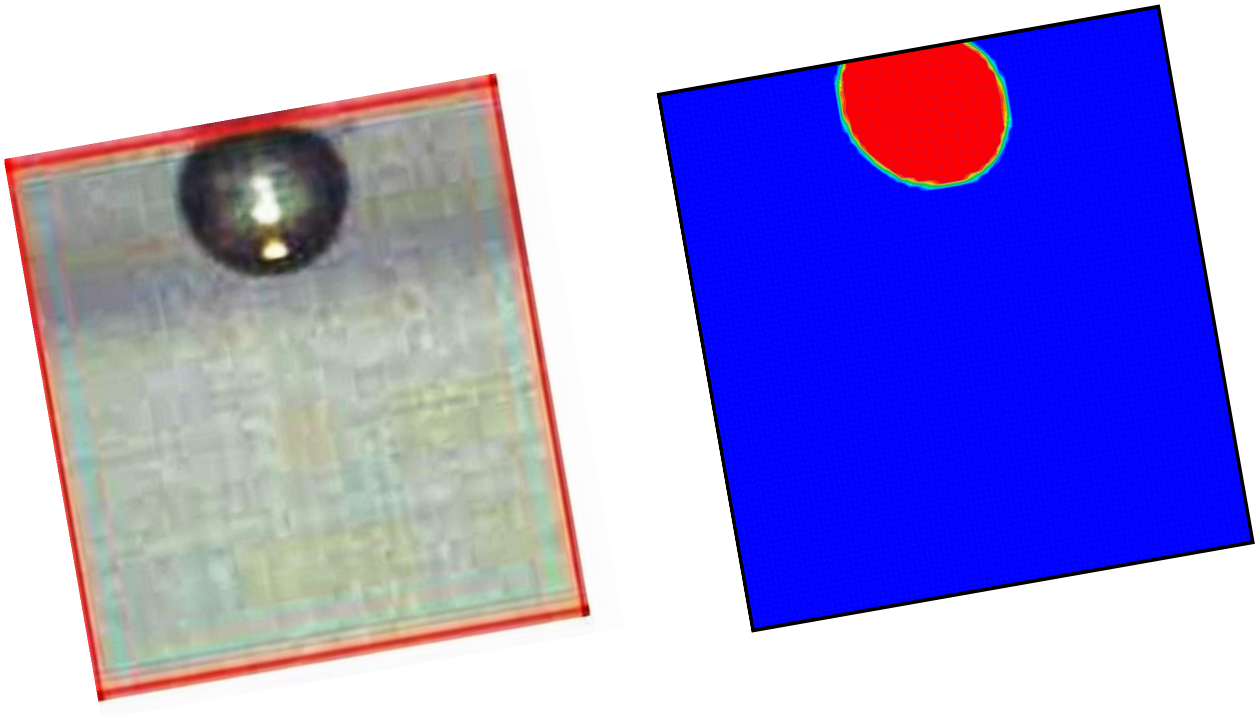

Figure 4.11: Shape of the sliding bubble at an angle of 10° when time (t) = 0.44 s (Left: Experiment, Right: Numerical Computation).

results obtained with the contact angles which best approximate the experimental results are assessed, and the main conclusions from Section 4.4 are summarised.

4.5.1 Sliding Bubble Dynamics

The shape of the sliding bubble at a plate inclination angle of 10° is compared qualitatively with the experimental results at time $t = 0.44$ s. It can be seen from Fig. 4.11 that the numerical computation is in reasonably good agreement with the experimental prediction of bubble shape. A difference in the computed and experimental bubble shapes is however noticeable. This is most likely due to the fact that a static contact angle is used in the numerical simulations.

Evolutions of the bubble motion for different plate inclination angles are presented in Figs. 4.12, 4.13 and 4.14 for the plate inclination angles 10°, 20° and 30°, respectively. The time interval between each consecutive bubble is 0.04 s for all plate inclination angles. In these figures, the bubble sliding mechanism can be seen clearly. The bubble rises by buoyancy and hits the surface. For $\theta = 10°$ and 20° of plate inclination, the bubble oscillates around the impact point, before starting to slide. With $\theta = 30°$, the bubble slides immediately without any delay from the impact point. This point on the plate surface is called starting point of sliding which separates the area of interest into two regions, namely B-I region and sliding region as indicated on the results in Fig. 4.15a. Then the velocity of the bubble increases from zero to an average velocity as time increases. For example, its value is 0.08 m/s for $\theta = 10°$. The B-I region is the region between the bubble injection point and the point, where the bubble first impacts the plate. The region where the bubble velocity changes from zero to an average constant velocity is called the sliding region. For $\theta = 10°$, as shown in Fig. 4.12, it can be seen that the bubble flattens in the x-direction, more than in the y-direction. The reason for this effect has been discussed in Section 4.3.

For such low inclination angles, the effect of surface tension, when the air-water interface comes in contact with the surface of the plate and before it reaches its terminal sliding speed, is predominant compared to inertia force. This explains why the bubble initially wobbles without sliding. Eventually it slowly gains momentum to slide along the plate surface. This suggests that the increase in the buoyancy force along the plate surface is larger than the increase in the impeding force due to drag, as discussed by Qiu et al. [109]. This can be illustrated by the velocity plot with respect to time, as shown in Fig. 4.15a. It can be seen that the increase in the bubble velocity is significantly less than the increases predicted for inclination angles $\theta = 20°$ and $\theta = 30°$ respectively. After the bubble has slid a certain distance, it moves with a constant average velocity.

For the inclination angles $\theta = 20°$ and $\theta = 30°$, shown in Figs. 4.13 and 4.14 respectively, the bubble stretching in the x-direction is not as pronounced compared with that of the inclination angle $\theta = 10°$. Stretching in the y-direction, perpendicular to the plate surface, becomes more predominant. This can be explained by the relative strength of buoyancy and drag forces compared to surface tension, as explained in Section 4.3.

For $\theta = 20°$, similar sliding characteristics to those discussed above for $\theta = 10°$, (see Fig. 4.13), are observed. The velocity increases from zero to an average slide velocity of 0.15 m/s as time evolves, in the sliding region as shown in Fig. 4.15b.

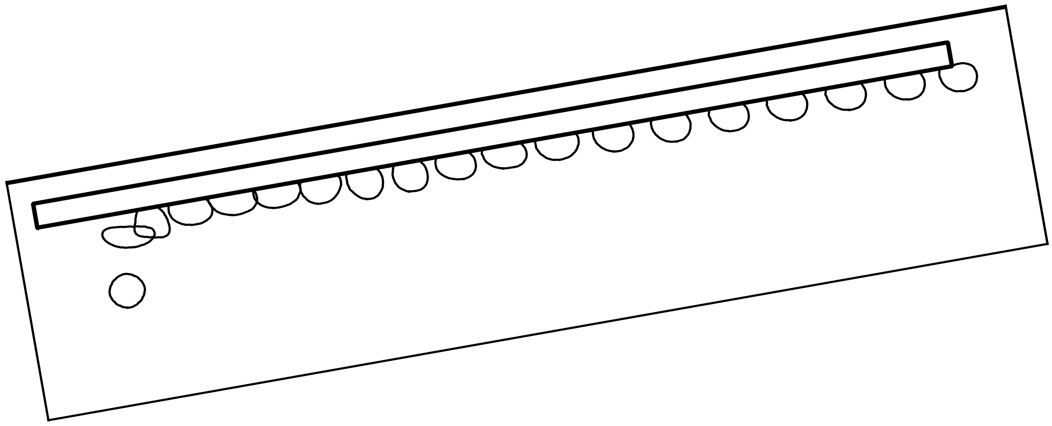

Figure 4.12: Evolution of sliding bubble motion at a plate angle of 10° - Numerical prediction of bubble interface shown for $t = 0$ and 0.02 s and every 0.04 s thereafter.

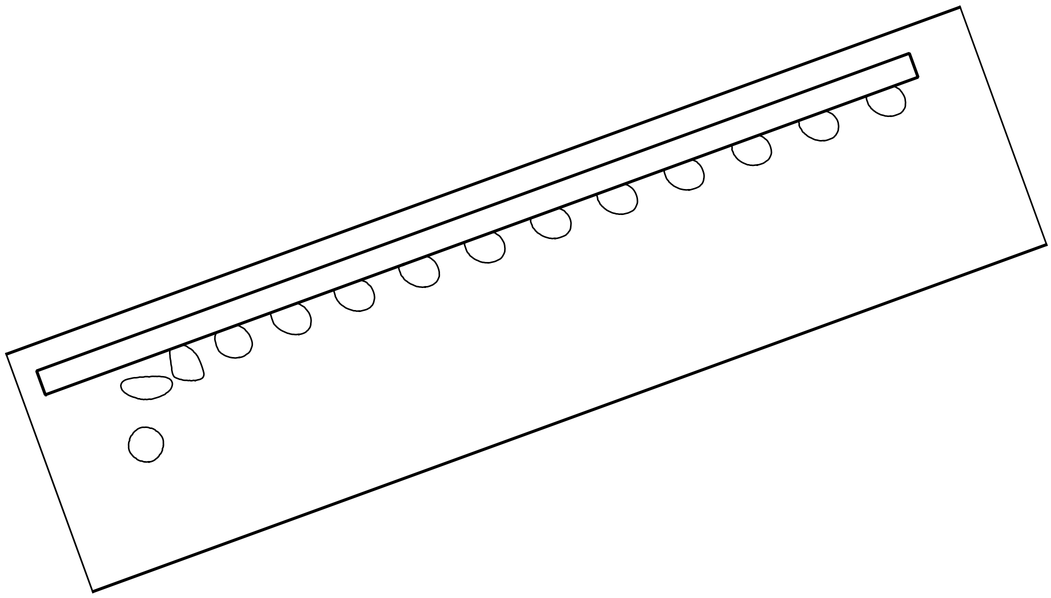

Figure 4.13: Evolution of sliding bubble motion at a plate angle 20° - Numerical prediction of bubble interface shown for $t = 0$ and 0.02 s and every 0.04 s thereafter.

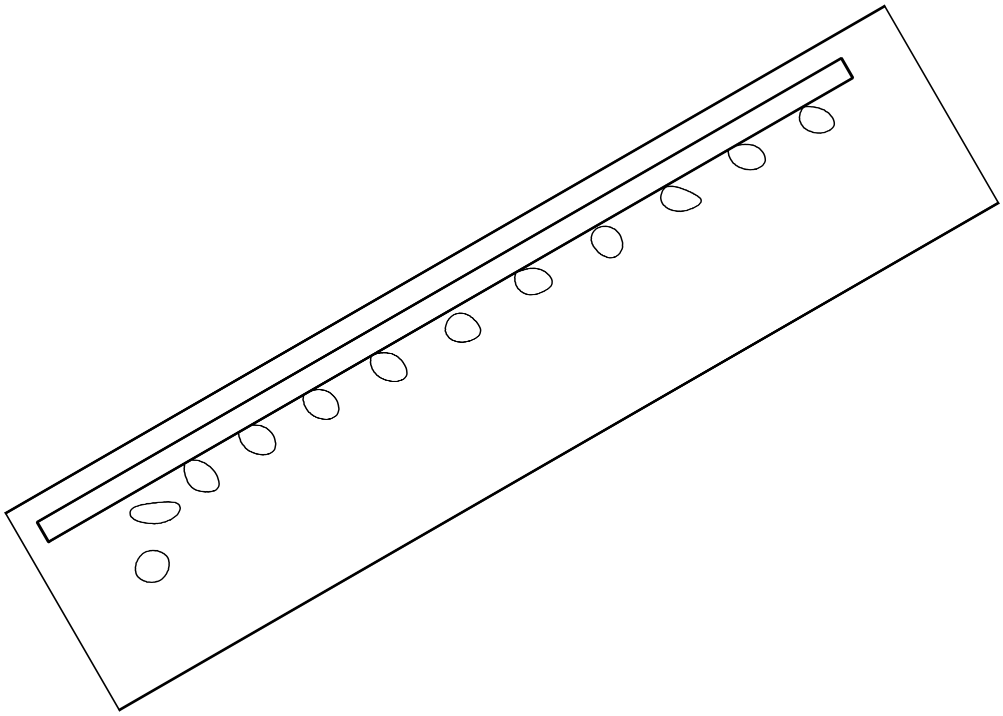

Figure 4.14: Evolution of sliding bubble motion at a plate angle of 30° - Numerical prediction of bubble interface shown for $t = 0$ and 0.02 s and every 0.04 s thereafter.

For $\theta = 30°$, similar mechanisms are as for the two previous cases (i.e. $\theta = 10°$ and $\theta = 20°$). However, the time evolution of bubble velocity shows an interesting behavior. Here the bubble rises up from the point of injection, then hits the plate surface as it did for the lower inclination angles (i.e. for $\theta = 10°$, and $\theta = 20°$). It starts sliding without delay after impact. The sliding velocity is also higher than that of for lower inclination angles. This may be explained by the fact that the x-component of buoyancy force is higher than the drag and surface tension forces for this angle. The velocity increases from 0.05 m/s to approximately 0.16 m/s in the sliding region as shown in Fig. 4.15c.

It is found that the qualitative assessments of bubble shapes are in reasonably good agreement with the experimental results, as shown in Figs. 4.7, 4.8 and 4.9. For quantitative assessment, the bubble velocities, the sliding bubble paths, the bubble displacements along the x-direction, and aspect ratios of the bubble are compared with the experimental results and are presented in the following sections.

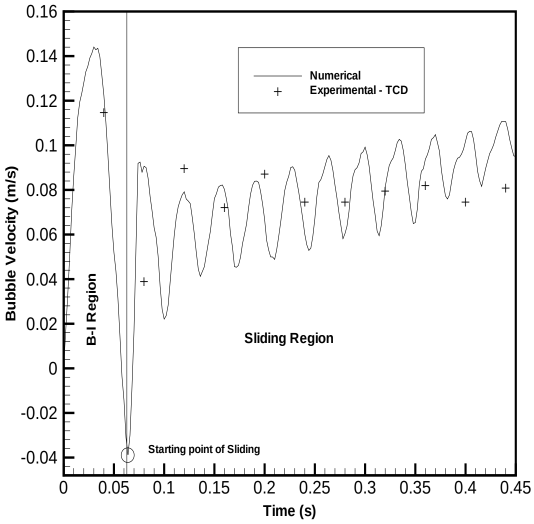

(a)

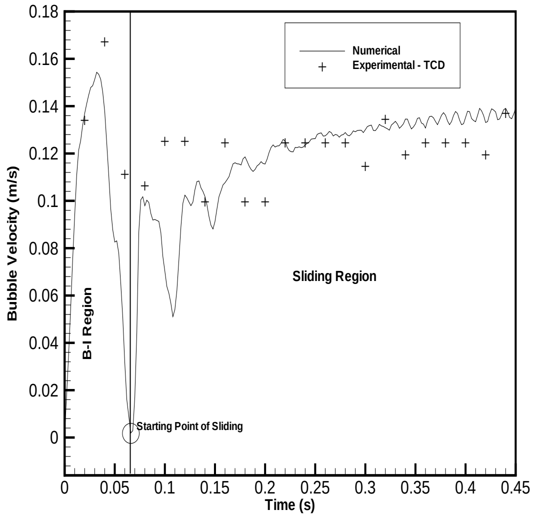

(b)

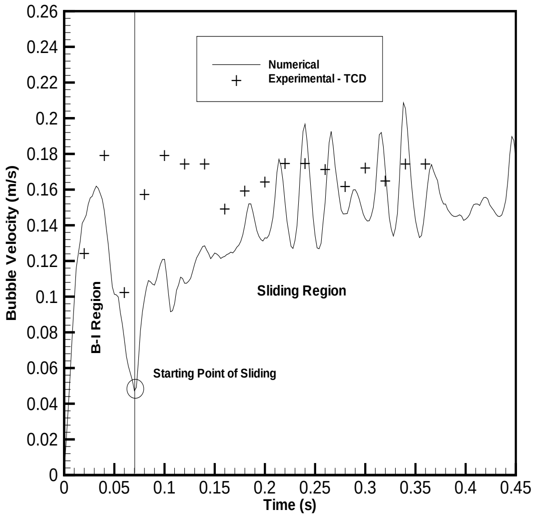

(c)

Figure 4.15: Comparison of terminal velocity of sliding bubble for different plate inclination angles (B-I: Before Impact); (a) $\theta = 10°$, (b) $\theta = 20°$ and (c) $\theta = 30°$.

4.5.2 Bubble Velocity

The comparisons of the terminal velocities of sliding bubbles are presented in Figs. 4.15a, b and c for different inclination angles $\theta = 10°$, $\theta = 20°$ and $\theta = 30°$ respectively. In the computation, the bubble is started from rest and rises under buoyancy effects. Likewise, the experimental procedure was adapted to ensure that the bubble rises due to buoyancy force rather than an injection pressure. This was achieved by keeping the bubble at rest for a while at the tip of a syringe needle (i.e. injection point). Differences in the initial bubble shapes could not be avoided, and can be expected to have an effect on the bubble velocity and its shape. After detachment and an initial rise, the bubble hits the bottom surface of the plate and its velocity oscillates around zero (for $\theta = 10°$ and $20°$). This point is the starting position of the sliding region. After an initial stagnation period, it starts sliding over the length of the plate due to the buoyancy force. These successive stages are illustrated in Figs. 4.12, 4.13 and 4.14. The velocity of the bubble slowly increases from zero and reaches a steady state after a time ranging from approximately 0.2 s to 0.45 s (see Figs. 4.15a, b and c). It is found that the average rising velocity of an air bubble sliding along the inclined plate increases monotonously as the inclination angle increases toward the vertical, as shown in Fig. 4.15. The same behaviour was observed by Maxworthy [100], and Brian et al. [135] in their experimental studies. This increase in the bubble velocity is due to the fact that, as explained before in Section 4.5.1, the x-component of buoyancy force along the plate surface increases as the inclination angle increases, whereas the impeding force due to drag decreases as the inclination angle increases, which was observed by Qiu et al. [109].

4.5.3 Sliding Bubble Path

Figures 4.16a, b and c, compare the experimental and computational results of the sliding bubble path for different inclination angles $\theta = 10°$, $\theta = 20°$ and $\theta = 30°$, respectively. These figures plot the center of the bubble position calculated from the instant of injection with respect to the distance from the plate surface. It means that for the center of the bubble is positioned in a coordinate system with the x-direction, aligned with the plate

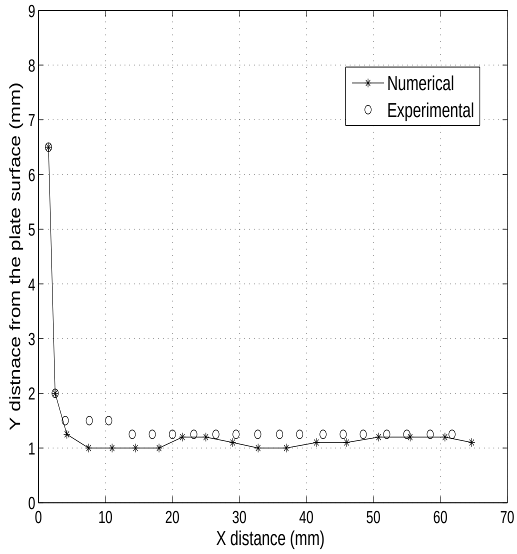

(a)

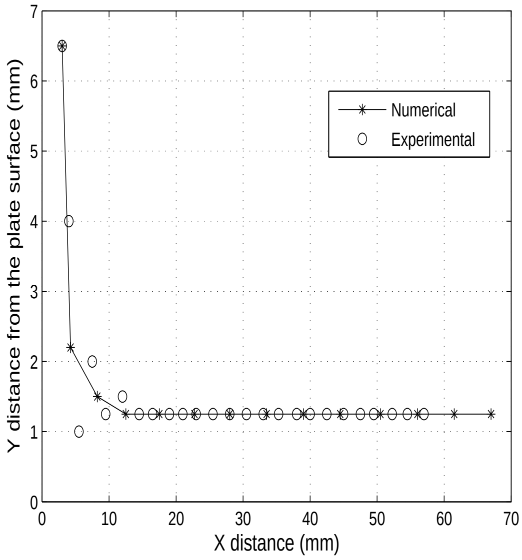

(b)

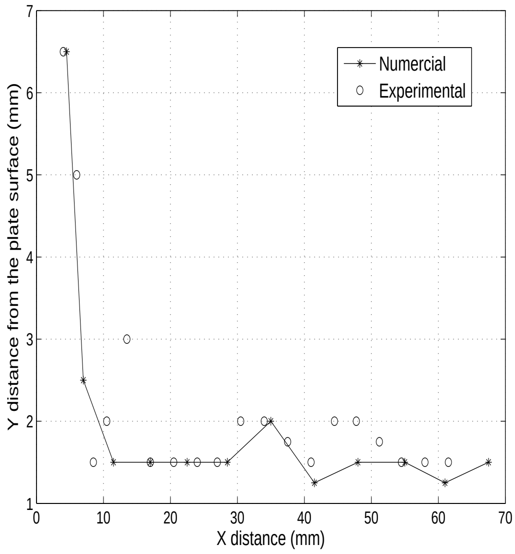

(c)

Figure 4.16: Comparison of bubble sliding path for different plate inclination angles; (a) $\theta = 10°$, (b) $\theta = 20°$ and (c) $\theta = 30°$.

surface and used as the origin of the x-axis. The y position is measured from the plate surface. For each angle of inclination, the bubble is injected at a distance of 6.5 mm below the plate surface. It is found that for lower inclination angles ($\theta < 30°$), the bubble moves along the plate surface, whereas it lifts off from the plate surface at some places for the higher inclination angle of 30°. The bubble shape is also found to oscillate with some stretching in the direction perpendicular to the plate surface.

It can be seen from Fig. 4.16 that the higher the angle of plate inclination, the more the bubble stretches and the more its path oscillates in the y-direction. For smaller angles of plate inclination, the bubble maintains a near spherical shape for most of its slide. This can be explained by the effects of surface tension and of the components of the buoyancy forces. When the inclination angle is small, as discussed in Section 4.3, the y-component of the buoyancy force is larger than the x-component of the buoyancy force and the surface tension forces the bubble to keep the same size and with little oscillation in the y-direction. When the inclination angle is high, the effect of surface tension force is smaller than the buoyancy force so the bubble lifts off more easily from the surface and, in particular, again it reaches the lower surface of the plate, as shown in Fig. 4.14. The lift off mechanism has been well explained in Section 4.4.

From Figs. 4.16a and b, there is a good agreement between the numerical and experimental findings for inclination angles of 10° and 20°, while for the inclination angle $\theta = 30°$, there are some discrepancies. It may be due to the static contact angle approach used for modelling interaction with the wall or due to unevenness/roughness of the surface over which bubble slides in the experiments or due to oscillations in the third direction that affect the bubble motion. The 2D model can not model 3D effects and this has to have an influence on bubble dynamics.

4.5.4 Sliding Bubble Displacement in the x-direction

Figures 4.17a, b and c, show the comparisons of bubble displacement along the x-direction parallel to the plate surface versus time for different inclination angles 10°, 20° and 30°, respectively. It is noticed from each figure that the increase in the displacement of the bubble in the x-direction is mostly linear as time evolves. When $\theta = 10°$, after $t = 0.4$ s, the bubble had travelled a distance of approximately 32 mm, measured from the injection point, while it travelled a distance of approximately 48 mm during the same time period when $\theta = 20°$. This shows the effect of the inclination angle on the movement of the sliding bubble. For $\theta = 10°$ and $20°$, the agreement between the experiments and numerical computations is very good before the bubble has reached the distance of approximately 32 mm from the injection point, as shown in Figs. 4.17a and b. After this, there is a noticeable difference between those results, as the bubble moves at a lower speed in the experimental observations. For $\theta = 30°$, this difference is noticed immediately after the injection point and is larger. It must be highlighted that in this case the bubble path is not linear but is seen in experiments to oscillate in the plane of the wall. It can be explained that in this case the bubble trajectory becomes increasingly 3D in nature which means that a quantitative comparison with experimental results becomes less meaning. Computations would have to be performed in three-dimension to assess this hypothesis.

4.5.5 Aspect Ratio

The bubble aspect ratio is defined as a ratio between the distance measured between the two extreme positions of the outer surface of the bubble in the x-direction to that in the y-direction. Figs. 4.18a and b, show computational and experimental bubble aspect ratios as a function of time for different inclination angles, $10°$ and $20°$, respectively. It should be mentioned here that the aspect ratio for the plate inclination angle, $\theta = 30°$ is not calculated. It is observed that the aspect ratio decreases as the inclination angle of the plate increases. This is due the fact that gravitational flattening of the bubble is more significant for the smaller angles. This, in turn, increases the contact area of the bubble with the plate surface and also the length of the bubble in the x-direction. This can be noticed in Figs. 4.12, 4.13 and 4.14 of computational results. The same behaviour is noticeable in Figs. 4.7, 4.8 and 4.9 of experimental results. This was also observed by Maxworthy [100] in his experimental observations.

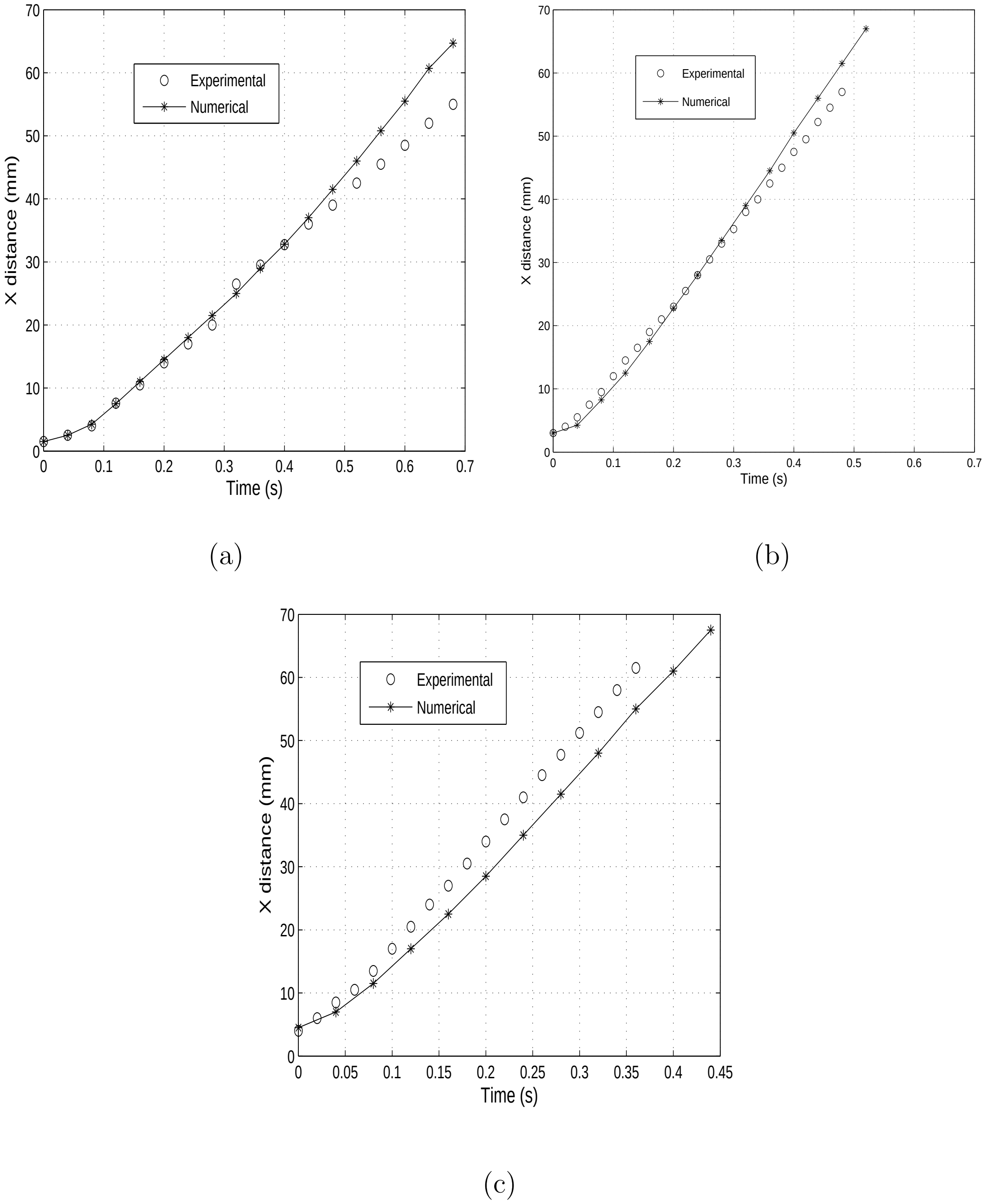

Figure 4.17: Comparison of bubble displacement along x-direction for different plate inclination angles; (a) $\theta = 10°$, (b) $\theta = 20°$ and (c) $\theta = 30°$.

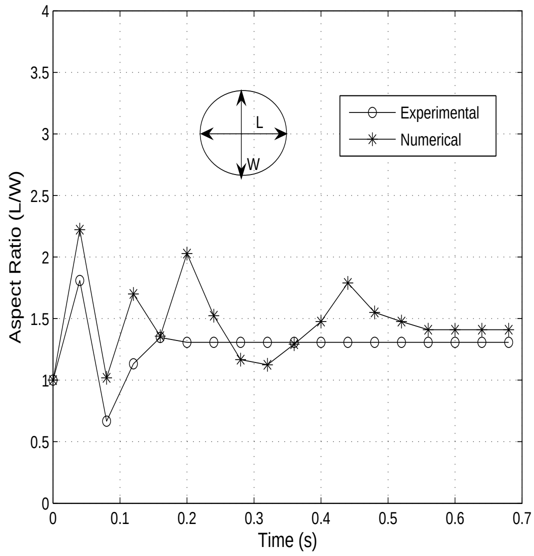

(a)

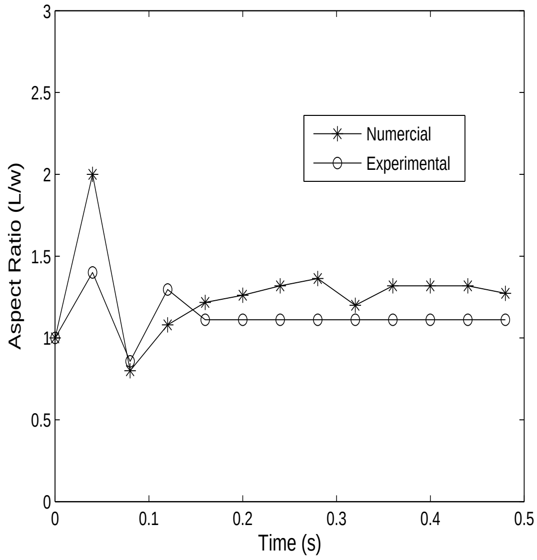

(b)

Figure 4.18: Comparison of bubble aspect ratio (L/W) for different plate inclination angles; (a) $\theta = 10°$ and (b) $\theta = 20°$.

4.6 Summary

Numerical simulations of an air bubble sliding along the lower surface of an inclined plate immersed in water were presented and discussed for different inclination angles. Numerical results were compared with experimental data in terms of evolution of bubble motion, terminal velocity, bubble path, bubble displacement along the x-direction, and aspect ratio. The effect of the inclination angle of the plate on the bubble shape, terminal velocity, aspect ratio and bubble path, were investigated and compared with the experimental results. It was found that the rising velocity of the bubble sliding along the inclined plate increases monotonously as the inclination angle increases toward the vertical. It was observed that a flattening of the bubble due to buoyancy forces is most noticeable for the smaller angles. This, in turn, increases the aspect ratio of the bubble for the smaller angles. It was also found that the results obtained by the present numerical model are in good agreement with the experimental results, however there are some discrepancies in the bubble displacement along the x-direction and aspect ratios. This is due to the fact that the lift offs were not fully observed in the numerical results, whereas they were observed in the experimental results and that the bubble might have oscillations in the third direction for higher inclination angles that affect its motion. Overall, the present numerical method was found to reproduce the main aspects of the behaviour of the sliding bubble that were observed experimentally.

CHAPTER 5

DYNAMICS OF A SLIDING BUBBLE WITH HEAT TRANSFER

This chapter presents and discusses computational results for sliding bubbles in a viscous liquid with heat transfer. Computations are carried out with an air bubble sliding along the lower surface of a heated inclined plate immersed in water, for different inclination angles. The simulation results are compared with experimental results obtained, as part of the project, at a collaborating institute, the Thermodynamics group in the Trinity College Dublin (TCD), Ireland. The comparisons are carried out with experimental measurements of surface temperatures.

5.1 Objectives

The objectives of this chapter are to

- assess the suitability of two fluid and heat flow modelling methods for the problem under consideration,
- study the heat transfer enhancement caused by an air bubble sliding along the lower surface of an inclined plate immersed in water for different inclination angles,
- study the effect of inclination angles on the heat transfer from the lower surface of the plate due to sliding air bubble motion in water, and
- discuss and compare the results obtained numerically with experimental results

The chapter is arranged as follows. Problem definition is described in Section 5.2. The dynamics of moving bubbles for different angles is discussed in Section 5.3. Assessment of the effect of contact angle on heat transfer is presented in Section 5.4. The temperature distribution along the lower surface of the inclined plate is presented in Section 5.5. Interaction of bubble wake with thermal boundary layer is discussed in Section 5.6. The wake size behind the bubble is discussed in Section 5.7. Experimental measurement and computational predictions of temperature profiles are presented and discussed in Section 5.8. Finally, the conclusions drawn from this study are summarised in Section 5.9.

5.2 Problem Definition

5.2.1 Experimental Setup

The experimental setup is illustrated in Section C.1 of Appendix C and the procedure used for extracting and analysing results from the experimental observations is also described in Section C.3 of Appendix C. This setup is used to perform experiments of the sliding bubble with heat transfer. Here heat is supplied to the foil which covers the lower part of the inclined plate so a constant heat flux condition is maintained throughout the numerical investigations.

5.2.2 Computational Setup

The domain for computations is illustrated in Fig. 5.1. A flat plate containing a heat source at the bottom surface is immersed in water inside a rectangular tank. Initially the plate and the tank are fixed at an angle to the horizontal and the surrounding fluid is at rest. The initial bulk water and lower surface of plate temperatures are set to 299 K. In the experiments, the foil used is a 25 micron thick AISI 321 stainless steel, so it can be approximated as one layer at the bottom surface of the plate in the computations and is modelled with a finite thickness. A uniform heat source is then supplied to the foil until the temperature of the bottom surface of the plate reaches 312 K, which corresponds to the surface temperature measured experimentally after 5 minutes with the same uniform heat flux and initial temperature condition.

The resulting wall temperature field T_w, is produced by a natural convection boundary layer on a uniform heat flux surface. T_w increases towards the trailing edge of

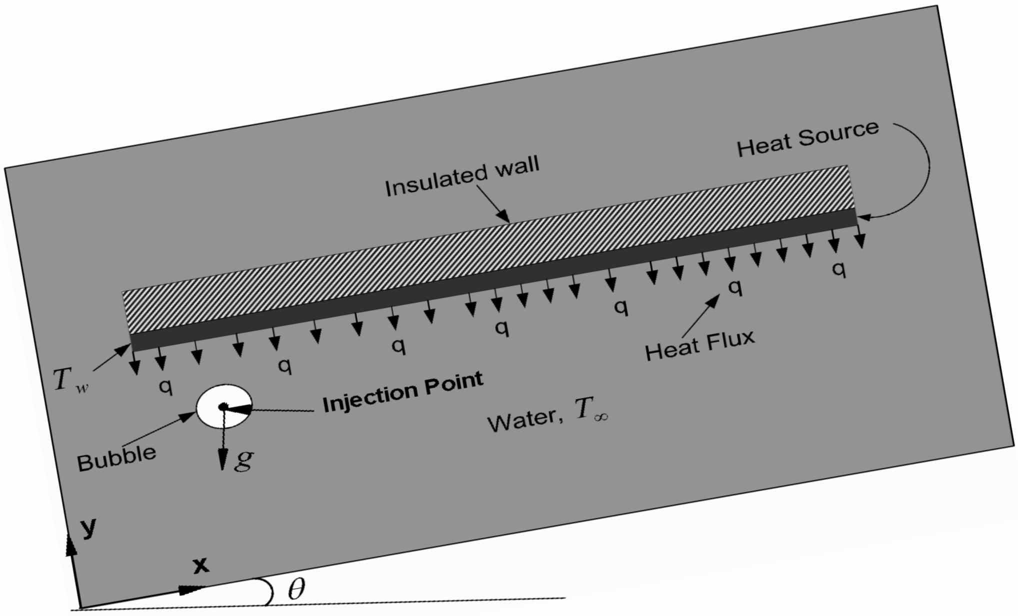

Figure 5.1: Schematic diagram of computational domain setup for sliding bubble motion.

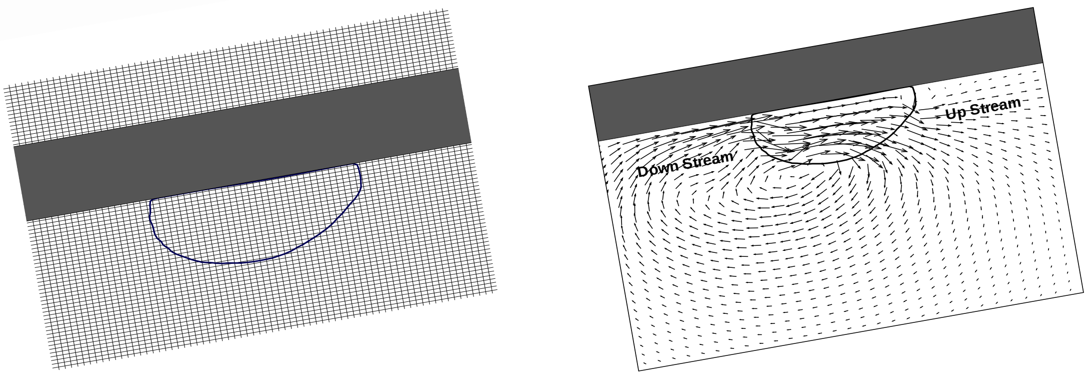

(a)

(b)

Figure 5.2: (a) Typical uniform mesh used for simulations, (b) Locations of upstream and downstream for sliding bubble flow.

the plate as the natural convection in the leading edge of the inclined plate is higher than that of the trailing edge.

Once this is achieved the flow and the temperature variables are stored in a file to provide initial temperature, T, and flow velocity conditions for the bubble flow model. At this point, the computation is restarted and a spherical air bubble is injected below the plate, in this flow field. The bubble rises upward in the direction of the gravity vector due to buoyancy force. Once it hits the plate surface, it will start sliding along the bottom wall of the plate as shown in Fig. 5.3. The bubble is sliding upwards from left to right. As the bubble slides along the heated test surface, heat transfer from the wall increases due to increased liquid velocity in the thermal boundary layer caused by the penetration of the bubble but also, and to a larger extent, as a result of the mixing of heated fluid from the boundary layer with the cold fluid drawn from the bubble wake.

For velocity, no-slip boundary conditions are applied at all the confining and inclined plate walls. For temperature, a constant temperature boundary condition (i.e., $T = 299$ K) is used for the walls of the tank. In the experiments, the heated foil is backed by a perspex sheet of 10 mm thickness. Heat transfer by conduction through perspex sheet is negligible by comparison with the convective heat flux through water. Over the 1 s duration of the bubble test, this boundary can be approximated as an adiabatic boundary. Therefore the adiabatic boundary condition is used for the left, right and top walls of the plate to replicate the same conditions used in the experiments.

Three different plate inclination angles (θ), 10°, 20° and 30° from horizontal, are used to perform the simulations. The parameters used for these simulations are listed in Table 5.1. The thermo-fluid properties used in the computations are presented in Table 5.2. Computations were performed with a grid of 800×500 cells and a time step of 10^{-4} s. Therefore the number of cells inside the bubble is 15, which was found to be sufficient to capture the bubble interface as discussed in Section 3.2.2 of Chapter 3. The mesh is uniform and orthogonal with square cells of width and height equal to 10^{-4} m. A typical close-up view of uniform mesh structure used for simulations is shown in Fig. 5.2a. Initially the center of a spherical bubble of air is positioned at a distance of 6.5 mm below the lower surface of the inclined plate and 3.5 mm from the left corner of the plate, for each angle of inclination. The upstream and downstream locations of sliding bubble flow are indicated in Fig. 5.2b.

Table 5.1: The Parameters Used in the Sliding Bubble Computations

Parameters	Values	Units
Gravitational acceleration	9.81	m/s^2
Surface tension	0.0728	N/m
Contact angle	20°, 25°, and 30°	-
Plate inclination angles	10°, 20°, and 30°	-
Heat Input	4889.3	W/m^2
Plate dimensions	length = 0.076, width = 0.002	m
Tank dimensions	length = 0.08, width = 0.05	m

Table 5.2: The Initial Thermo-Fluid Properties Used in the Sliding Bubble Computations at 299 K

Properties	Liquid	Gas	Units
Density(ρ)	1000	1.225	kg/m^3
Viscosity(μ)	0.001	0.000018	kg/m s
Conductivity(κ)	0.6	0.02624	W/m K
Specific heat (C_p)	4179.	1005.7	J/kg K

5.3 Dynamics of Sliding Bubble

In this section, the dynamic behaviour of the sliding bubble for three plate inclination angles (θ), 10°, 20° and 30° from horizontal, are discussed. As discussed in Chapter 4, computational results obtained with a contact angle of 25° for the plate inclination angles 10° and 20° and with a contact angle of 30° for the plate inclination angles 30° provide realistic predictions. The corresponding computational results with the estimated contact angles which best approximate the experimental results are compared. Fig. 5.3

shows the dynamic behaviour of the sliding bubble for 10°, 20° and 30°. Contour plots showing the bubble interface at regular time intervals, are superimposed on single plots. The time separation between the bubbles in the 10, 20 and 30° tests is 0.04 s. The effects of increasing angle on bubble shape can be seen from these figures.

When the plate inclination angle is $\theta = 10°$, the bubble sticks momentarily to the heated surface and stays for a time at the point of impact, whereas for higher angles, the bubble starts sliding immediately after hitting the plate surface. This can be explained by the fact, as discussed in Chapter 4, that for higher angles, the value of the y-component of buoyancy force is low as compared to that for lower angles. In the present case, however, the natural convection boundary layer has a noticeable effect on the bubble behaviour and shape just after impact. It can be seen that the bubble stretches significantly more in the plate direction as a result of the shearing induced by the boundary layer flow. The delay between impact and the onset of the bubble slide is also reduced as the boundary layer provides momentum to the bubble

The bubble velocity increases monotonically with respect to time as the plate inclination angle increases. The reason for this is that the x-component of the buoyancy force in the bubble flow direction, parallel to the plate surface, increases as the inclination angle (θ) increases while the y-component of the buoyancy force perpendicular to the plate surface decreases. This, in turn, increases the bubble velocity. As can clearly be observed from Fig. 5.3, the contact area of the bubble with the heated surface reduces as the plate inclination angle increases. This change in the contact area can again be attributed to the higher buoyancy force in the bubble flow direction compared to that for higher angles.

Figure 5.3 - Middle shows the evolution of the bubble motion when the plate inclination angle is 20° from horizontal. In this case, it can be observed from the figure that the gap between consecutive bubbles is more than that of for the plate inclination angle $\theta = 10°$. This means that the bubble moves faster than in the previous case when the inclination angle = 10°. The contact area of bubble with the plate is reduced, as expected. This shows the effect of fluid-solid surface interaction. This effect is more significant when the inclination angle is small whereas this is less significant for higher

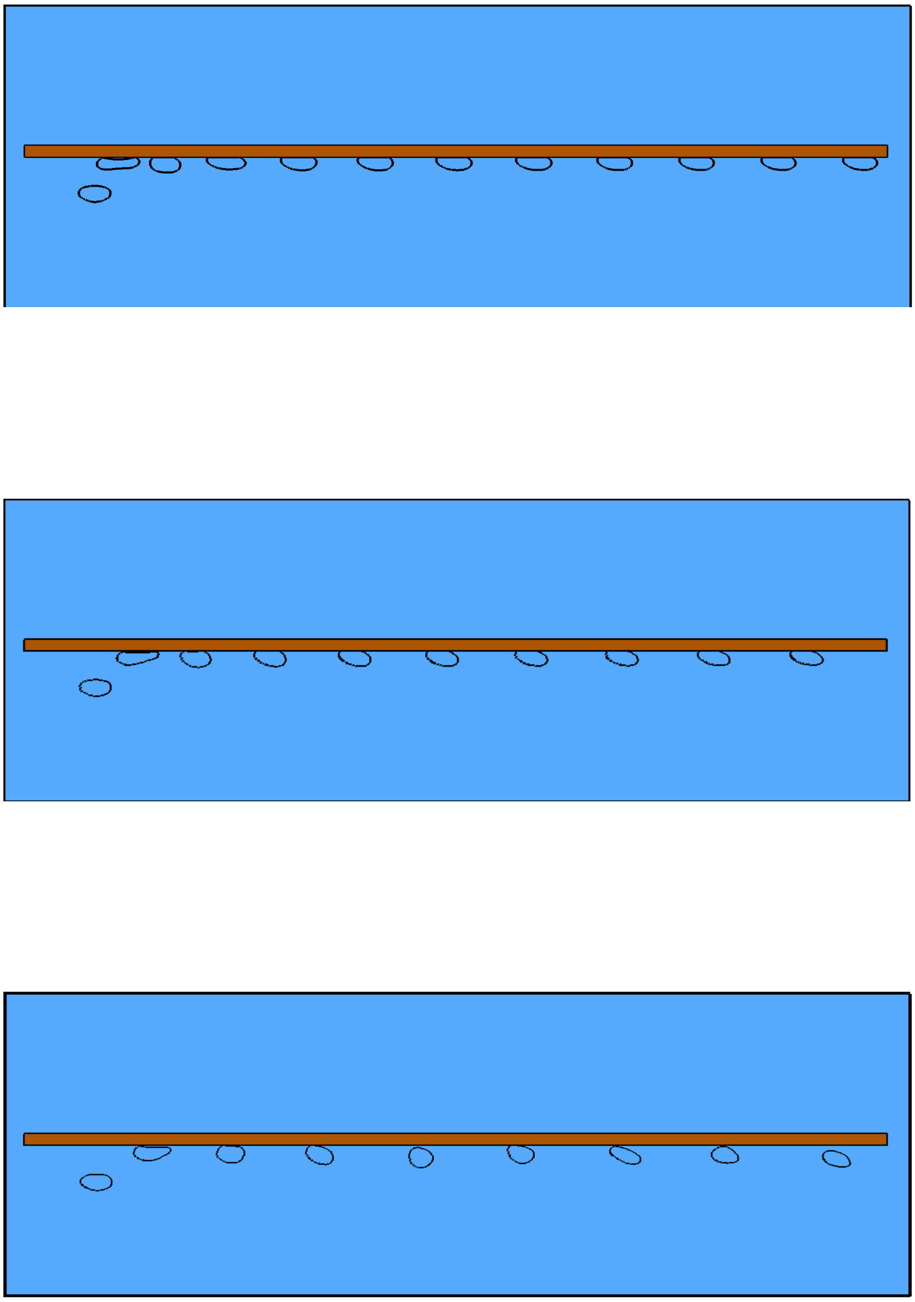

Figure 5.3: Evolution of sliding bubble motion for different plate inclination angles; Top: $\theta = 10°$; Middle: $\theta = 20°$; Bottom: $\theta = 30°$.

inclination angles. This is again evident from Fig. 5.3 - Bottom for the inclination angle of 30°. For this angle, the bubble is again shown to lift off the plate and bounce and the contact area is small compared with that for smaller angles. It is also observed that, as noticed in Chapter 4, stretching in the y direction increase as θ increases, whereas stretching in the x direction decreases as θ increases. These results are consistent with those of Chapter 4. However, stretching in the y direction for the higher inclination angles is less compared to that of for the cases in Chapter 4. This is most likely due to the velocity field created below the surface in the thermal boundary layer by natural convection alone. This velocity field is responsible for stretching the bubble further in the bubble direction. It can also be seen from Fig. 5.3 that the bubble is elongated, not only at the start of the slide, but also over the length of the plate. The stretching is slightly less significant when the bubble lifts off the plate with $\theta = 30°$.

5.4 Assessment of Contact Angle Effects on Temperature Field

Although all results discussed in this chapter refer to results obtained with the fixed contact angle values deemed most suitable, it is worth analysing the effect of contact angle on the wall surface temperature. Computations were carried out with different contact angles (θ_c) for each plate inclination angle. Figs. 5.4a and b show the temperature along the bottom surface of the plate inclined at an angle of 10° with different contact angles for times t = 0.3 and 0.4 s, respectively. An almost similar behaviour is noticed for all contact angles, but there is a small difference in the location of temperature reduction as the bubble velocity changes with the contact angle. The main difference in temperature profiles is a shift towards larger x values of the zone of influence of the bubble as the bubble velocity increases. This is consistent with the predicted dependence of the bubble velocity on θ_c. The remainder of the chapter will consider $\theta_c = 25°$ for the inclination angle $\theta = 10°$. Another noticeable difference concerns the temperature spike ahead of the sharp drop in the wake of the bubble. This temperature increase affects the air trapped in the bubble. Since air has a significantly lower heat capacity, it heats up much faster than water. The amount of heat transferred to the air depends on the contact area between the bubble and the plate which changes with the contact angle θ_c. Since it seems from experiments, that a water film isolates the bubble from the plate, we can expect this spike to be absent from experimental results. This spike in temperature can be used to locate the position of the bubble.

Figures 5.5a and b show the temperature along the bottom surface of the plate inclined at an angles of $\theta = 20°$ with different contact angles for times t = 0.3 and 0.4 s, respectively. Almost the same behaviour is noticed for all contact angles, as those discussed above for $\theta = 10°$.

For $\theta = 30°$, the same analysis is carried out with different contact angles. Figs. 5.6a and b show the temperature along the bottom surface of the plate inclined at an angle of 30° with different contact angles for times $t = 0.3$ and 0.4 s, respectively. Again almost the same behaviour is noticed for the contact angles $\theta_c = 20$ and 25°, but for $\theta_c = 30$, the temperature in the wake region is higher than that of for $\theta_c = 20$ and 25°. This may be justified by the fact that more hot fluid comes back to the rear side of the bubble. This is because, as discussed in Chapter 4, the bubble sticks along the lower surface of the plate for $\theta_c = 20$ and 25°, whereas the bubble lifts off from the surface and reattaches to the surface again with $\theta_c = 30°$. This creates more acceleration in the bubble and fluid flow. This mechanism is evident in the heat transfer behaviour as well for $\theta_c = 30$. Due to the lift off and the greater acceleration along the bubble path, hot fluid enters into the gap created between the bubble surface and the lower surface of the plate. This increases the lower surface temperature significantly. As a result the heat transfer enhancement is decreased. This behaviour is noticeable at times $t = 0.3$ and 0.4 s and can clearly be observed from the superimposed vector and temperature field plot (see Figs. 5.12c and d). It must be mentioned here that this increase in the temperature in the wake region is not noticeable with $\theta_c = 20$ and 25°. This suggests that the effect of contact angles is more significant for higher plate inclination angles, that is, when the bubble slides at a higher velocity and, hence, is more likely to lift off from the plate. In fact reduction in the plate surface temperature drop in the wake of the bubble is already noticeable for $\theta = 20°$ and $\theta_c = 30°$ (Fig. 5.5b), suggesting that the bubble is also lifting off slightly in this case.

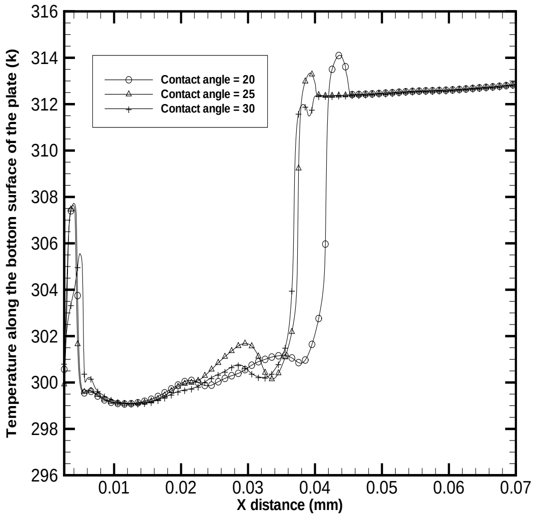

(a)

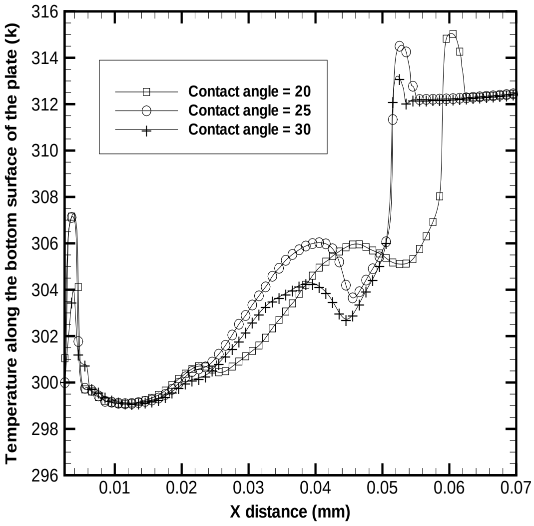

(b)

Figure 5.4: Temperature along the bottom surface of the plate for different contact angles when the plate inclination angle $\theta = 10°$; (a) $t = 0.3$ s and (b) $t = 0.4$ s.

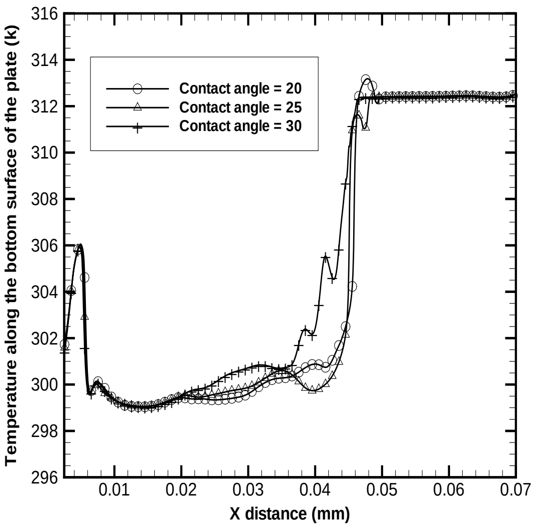

(a)

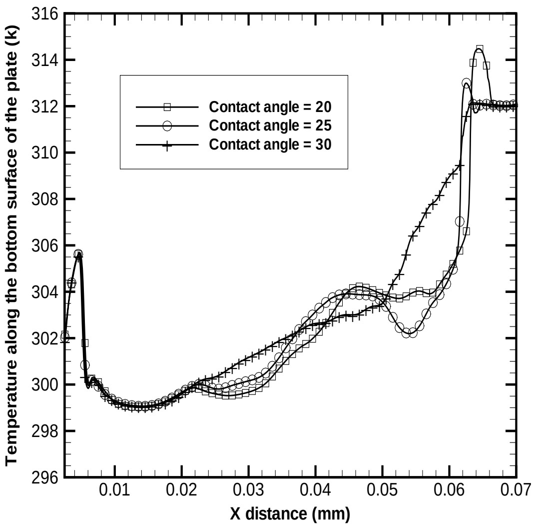

(b)

Figure 5.5: Temperature along the bottom surface of the plate for different contact angles when the plate inclination angle $\theta = 20°$; (a) $t = 0.3$ s and (b) $t = 0.4$ s.

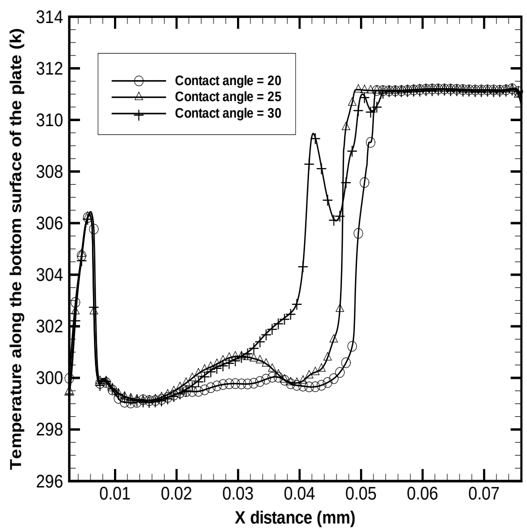

(a)

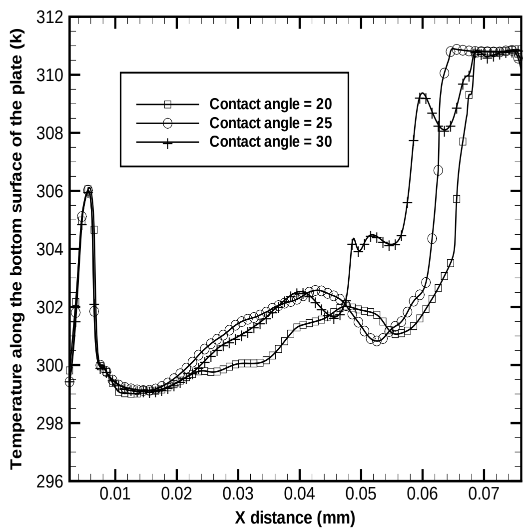

(b)

Figure 5.6: Temperature along the bottom surface of the plate for different contact angles when the plate inclination angle $\theta = 30°$; (a) t = 0.3 s and (b) t = 0.4 s.

5.5 Temperature Distribution

In order to investigate how the passage of the bubble alters the temperature along the lower surface of the plate, the contact angle $\theta_c = 25°$ is chosen for the plate inclination angles $\theta = 10°$ and $20°$ and the contact angle $\theta_c = 30°$ is chosen for the plate inclination angle $\theta = 30°$. To clearly understand the mechanism of heat transfer enhancement, variations of temperature along the lower surface of the plate and the bubble centred positions are shown on the same figure (see Figs. 5.7, 5.9 and 5.10) at different time instants for each plate inclination angle. The bubble positions are plotted here for the corresponding times as shown on the right hand side vertical axis. These plots are assessed by comparison with temperature contour and fluid velocity plots shown on Figs. 5.8, 5.11 and 5.12.

Figure 5.7 shows the bubble centred positions and the local temperature along the lower surface of the inclined plate as a function of distance along the x-direction for different time instants, with a time interval of 0.1 s when the plate inclination angle θ is 10°. The circle is used to indicate the position of the bubble centroid and does not

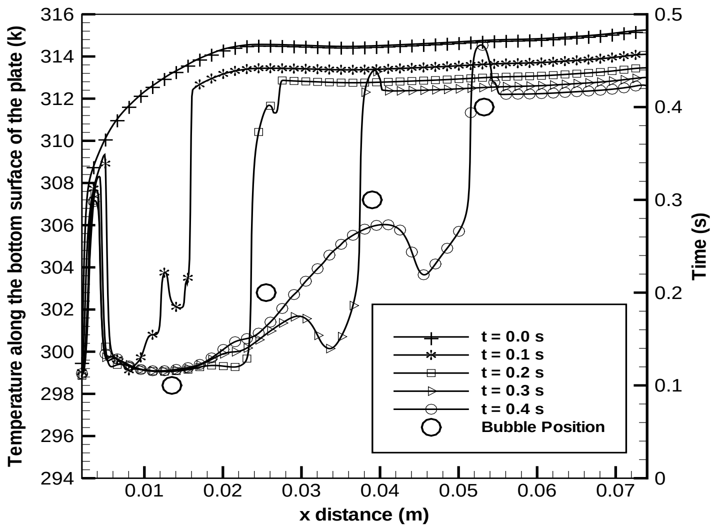

Figure 5.7: Temperature along the bottom surface of the plate and the bubble centroid positions for different time instants when the plate inclination angle $\theta = 10°$.

represent the bubble shape.

At time $t = 0.0$ s, before the bubble has been injected, the temperature increases gradually from the leading edge of the plate to the trailing edge as a result of natural convection alone. At time $t = 0.1$ s, the temperature at the bubble position and its wake region has decreased drastically to approximately 299.56 K that is slightly higher than the free stream initial temperature. This is the result of mixing between the cold water from the surrounding bulk water and the hot water trapped in the wake region of the bubble which is confined in the thermal boundary layer at the surface (see Fig. 5.8a). Thus, the more mixing created in the wake region, the greater the heat transfer experienced, as the cold wake has a great potential to remove heat from the plate surface.

Temperature continues to decrease at time $t = 0.2$ sec reaching a temperature of 299 K at the bubble position and in its wake, which is equal to the bulk liquid temperature. Now, the bubble has travelled a distance of 25.5 mm, and the width of the wake area whose temperature has been affected by the motion of the bubble has increased significantly as can be noticed from Fig. 5.8b.

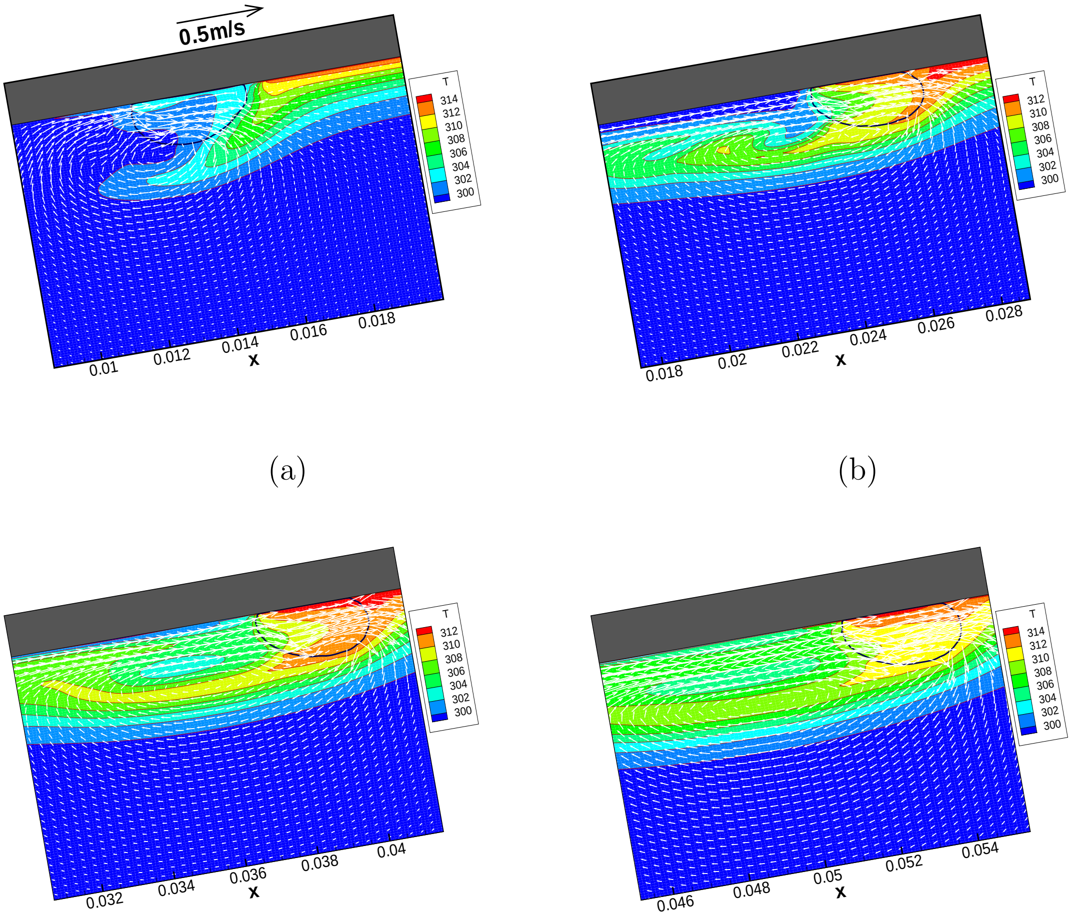

(a) (b)

(c) (d)

Figure 5.8: Vector plot and temperature field of sliding bubble motion at different times for a plate inclination angle $\theta = 10°$ when $\theta_c = 25°$: (a) $t = 0.1$ s (b) $t = 0.2$ s (c) $t = 0.3$ s (d) $t = 0.4$ s.

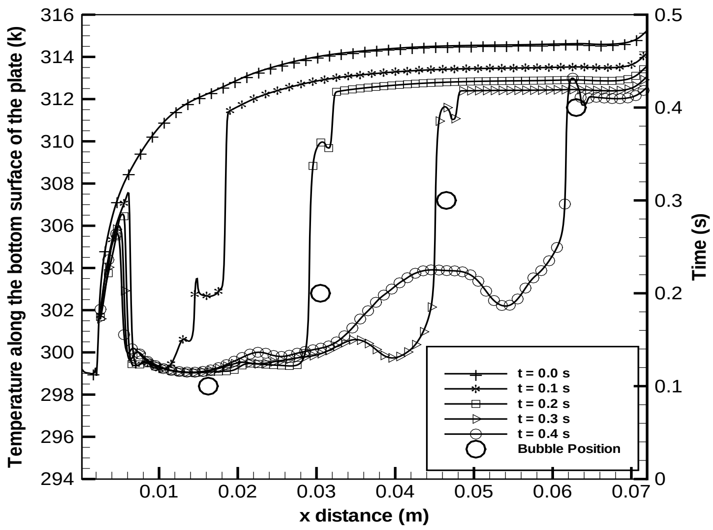

Figure 5.9: Temperature along the bottom surface of the plate and the bubble centroid positions for different time instants when the plate inclination angle $\theta = 20°$.

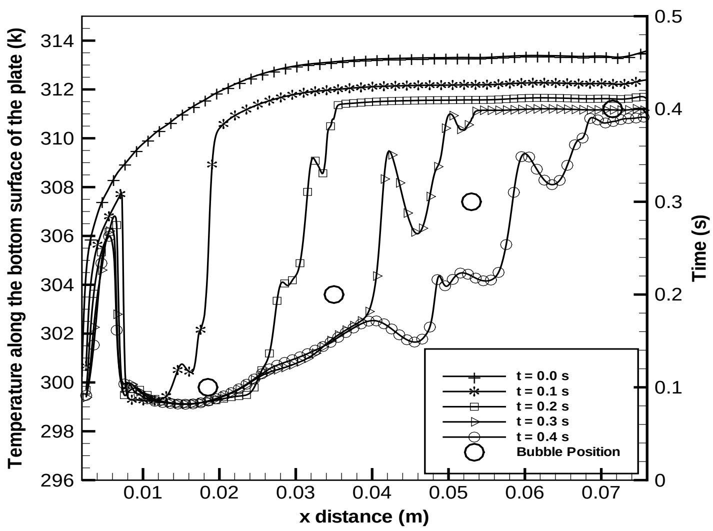

Figure 5.10: Temperature along the bottom surface of the plate and the bubble centroid positions for different time instants when the plate inclination angle $\theta = 30°$.

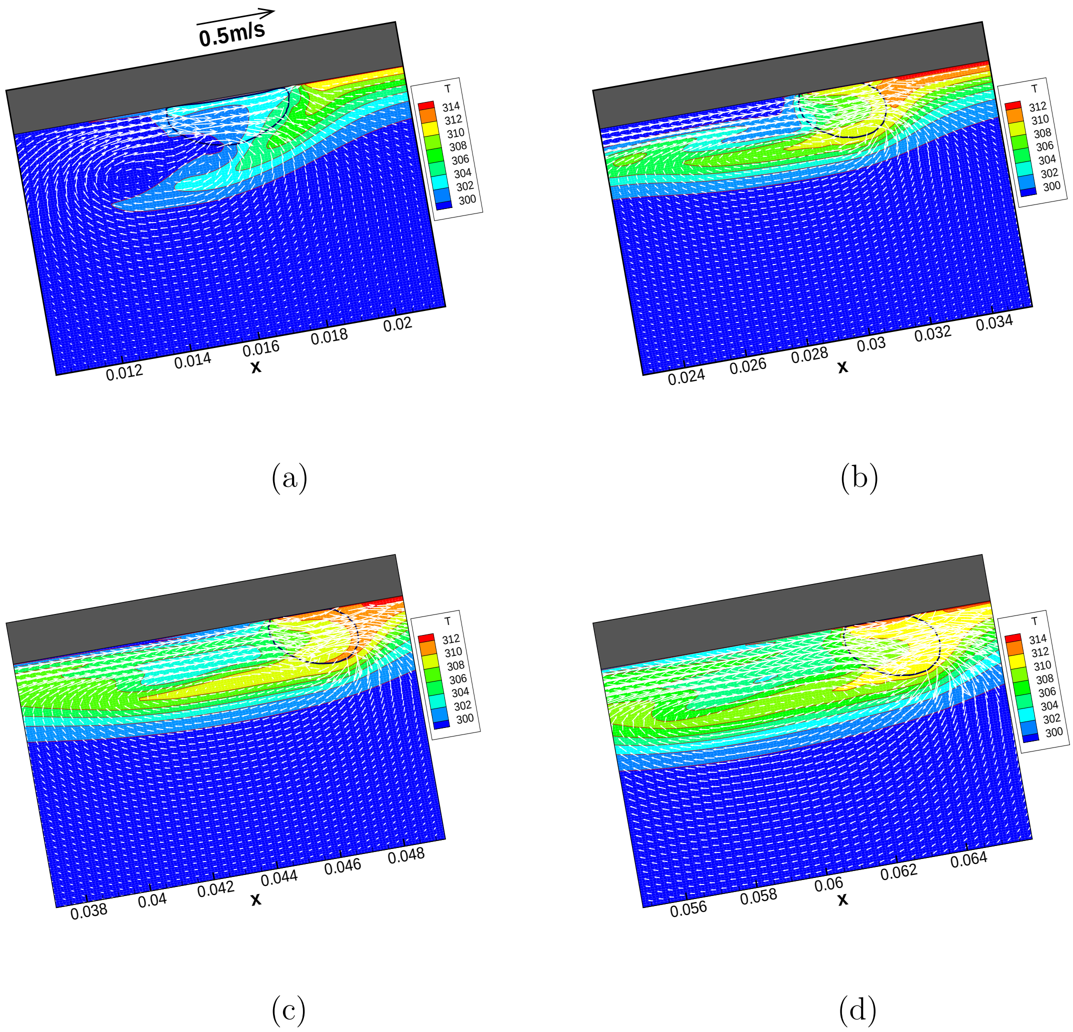

Figure 5.11: Vector plot and temperature field of sliding bubble motion at different times for a plate inclination angle $\theta = 20°$ when $\theta_c = 25°$: (a) $t = 0.1$ s (b) $t = 0.2$ s (c) $t = 0.3$ s (d) $t = 0.4$ s.

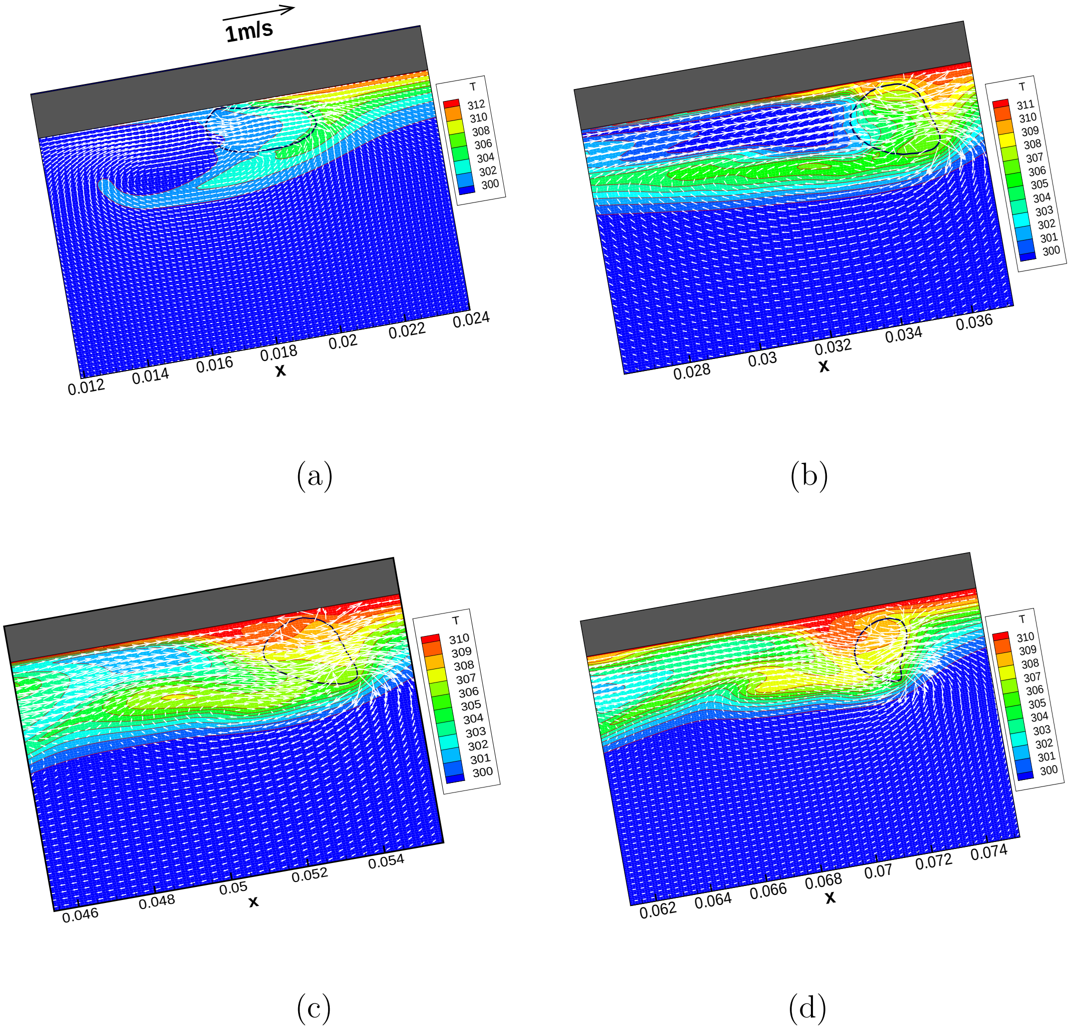

Figure 5.12: Vector plot and temperature field of sliding bubble motion at different times for a plate inclination angle $\theta = 30°$ when $\theta_c = 30°$: (a) $t = 0.1$ s (b) $t = 0.2$ s (c) $t = 0.3$ s (d) $t = 0.4$ s.

When the time is $t = 0.3$ s, the bubble has moved a distance of 39 mm from the injection point. At this time, the temperature at the bubble position and its wake has dropped to 300 K, which is higher than the downstream temperature at time $t = 0.2$ s, suggesting that the temperature drop is decreasing after time $t = 0.2$ s and the wake is losing its ability to absorb heat from the plate surface. In the downstream wake region, where the bubble was at $t = 0.2$ s, the temperature is still lower and maintaining the value of 299 K. The width of the wake area whose temperature has been affected by the motion of the bubble has increased further. From Figs. 5.14 and 5.15, it can be observed that the bubble wake continues to grow outwards for a significant time after the bubble has passed. The temperature is increased in the downstream as the wake brings hot fluid to that region. This is clearly seen in Fig. 5.8c.

When the time is $t = 0.4$ s, the bubble has reached a distance of 53.25 mm. At this stage, the temperature can be seen to decrease slightly in the downstream region whereas it keeps the same value in the upstream region of the plate, again suggesting that the wake grows in size (see Fig. 5.8d) but loses its ability to absorb as much heat from the plate as it did at earlier stages (i.e. before time $t = 0.2$ s). Although the downstream region does experience a significant temperature drop after the bubble has passed, the reduction in the temperature in the downstream region is lower compared to that in the downstream regions at times $t = 0.1$ and 0.2 s, respectively. This is due to the fact that the level of liquid mixing by the bubble wake is strongest near the point of impact on the plate surface and hence the heat transfer levels are a maximum in this region. Another reason is that the bubble wake brings hot fluid to the rear side of the bubble that increases the lower surface temperature of the plate after it slides progressively to the trailing edge of the plate.

It is worth noting that the plate surface plots alone do not fully explain the impact of the sliding bubble on the heat and fluid flow processes taking place. The temperature plots show a significant decrease in the wake of the bubble and show that this effect remains significant over most of the slide region. The temperature contour plots of Fig. 5.8 show that this effect is due to the penetration of the cold wake into the thermal boundary layer but also that this mass of cold water is pulled into the boundary layer by the bubble. As the bubble slides, the cold water mass is stretched into a gradually thinner film, which is forced against the plate. It can be assumed that this would not be observed in the simulation results.

The effects of bubble passage on the surface temperature field will now be studied for the inclination angles $\theta = 20^\circ$ and 30°. Figs. 5.9 and 5.10 show the centres of the bubble position and the temperature profile along the bottom surface of the inclined plate at various time instants for inclination angles of 20° and 30° respectively. From Fig. 5.9, it can be seen that at time $t = 0.0$ s, before a bubble is injected, the trailing edge of the plate is quite uniform in temperature, with a temperature of 312 K, whereas the leading edge of the plate shows a gradual increase from the free stream temperature 299 K to 312 K within 0.015 m. It can be seen, from Figs. 5.11a, b, c and d, how the bubble passage changes the temperature of the plate and how its wake brings cold fluid from the surrounding area and creates mixing at the rear of the bubble. These mechanisms are similar to those observed with an inclination angle 10° but the bubble locations vary as it moves faster with this angle.

With an inclination angle is 30°, the same trends in temperature drops as those observed with inclination angles 10° and 20°, can be seen in Fig. 5.10. Again the locations of the temperature drops vary since the bubble moves faster as the inclination angle increases. So at a fixed point on the plate surface the temperature drop occurs earlier in the case of higher angles, whereas this will happen a bit later in the case of lower inclination angles. It is also found that, as discussed before, the temperature drop is less at the later stages, say time $t = 0.3$ and 0.4 s, for the plate inclination angle of 30°. It is clearly noticeable from Figs. 5.11c and d, however, that the bubble behaves as it did for the lower angles at times $t = 0.1$ and 0.2 s (see Figs. 5.12a and b).

For a fixed value of inclination angle, the temperature drop in the near wake of the bubble reduces as time increases. Although the trailing edge of the plate does experience a significant temperature drop after the bubble passes, the temperature never drops down as much as it did in the leading edge of the plate suggesting that the ability of bubble wake to absorb heat in the area is not as great as it was in the early stages of its travel. As explained before, this could be due to the fact that the wake brings hot fluid back to

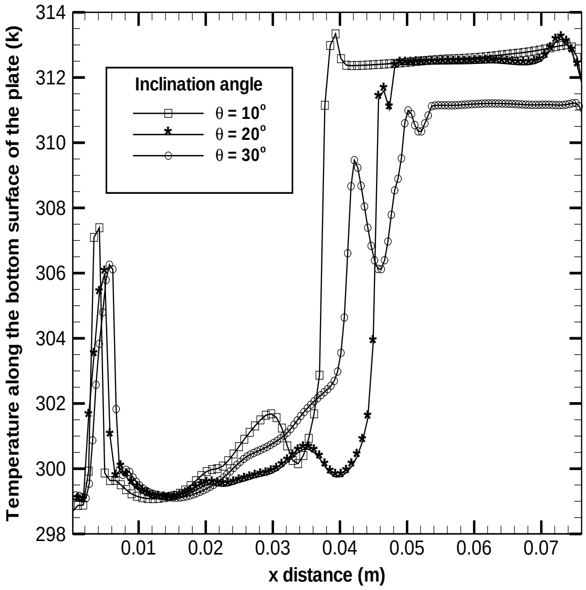

Figure 5.13: Temperature along the bottom surface of the plate at time t=0.3 s for different plate inclination angles.

the rear portion of the bubble thereby reducing the heat adsorption capacity of the wake. This can be observed clearly from Figs. 5.11c and d, and Figs. 5.12c and d, for $\theta = 20°$ and $30°$, respectively.

Figure 5.13 shows the local temperature of the lower surface of the inclined plate as a function of distance along the x-direction for various plate inclination angles. This is to provide a summary snapshot of differences in temperature profile resulting from changes in θ. It can be noted that the plate surface temperature drop for lower angles is higher than that for higher angles and shows the effect of plate inclination angles.

5.6 Interaction between Bubble Wake and Thermal Boundary Layer

The interaction of the bubble wake with the thermal boundary layer plays a major role in the convective heat transfer from the inclined plate. In order to get more insight into the underlying physical phenomena of the convective heat transfer enhancement, the bubble interface and temperature field are superimposed on a single plot for different times for each plate inclination angle for the whole computational domain. Figs. 5.14 and 5.15 show the temperature field and bubble interface for different time instants when the inclination angle is $\theta = 10°$. Fig. 5.14a shows the temperature field at time $t = 0.0$ s, before the bubble has been injected. This is the typical thermal boundary layer formed below the lower surface of the inclined plate since the plate has started heating up. It is seen that the thermal boundary layer at the leading edge of the plate is thinner than at the trailing edge, as expected.

At time $t = 0.1$ s, the bubble penetrates into the thermal boundary layer and disturbs it, as shown in Figs. 5.14b and 5.8. It can be seen from the figure that as the bubble penetrates into the boundary layer, the heated liquid moves around the bubble. This is a sign that the hot liquid originally in the boundary layer is diverted by the sliding bubble. This can be clearly seen from Fig. 5.8a, showing the velocity vector in the vicinity of the bubble interface, that the bubble enhances mixing with the bulk fluid which is at 299 K. As can be seen from Fig. 5.7 and 5.14b, the plate surface temperature has dropped drastically to approximately 299.56 K at this stage. The interaction with the thermal boundary layer continues until the bubble reaches the end point of the plate and is responsible for carrying the heat away from the plate surface.

From Fig. 5.14c, it can be observed that the bubble brings the hot fluid back in its wake. It is seen that in comparison to the undisturbed thermal boundary layer at $t = 0.0$ s, an expansion of the thermal layer occurs at $t = 0.2$ s just downstream of the bubble. The expansion of the thermal layer occurs as the fluid tries to flow over the bubble. The same observation was noticed by Qiu and Dhir [109] in their experimental work. The outer portion of the thermal layer is found to stretch out and the stretching is caused by the increased velocity of the bubble as it slides over the surface. This can be explained by a close view of the velocity vector around the bubble, as shown in Fig. 5.20. At time $t = 0.1$ s, a vortex starts forming behind the bubble. This vortex is responsible for enhancing the heat transfer from the surface by bringing the colder fluid from the bulk to the thermal boundary layer. As time progresses, the vortex behind the bubble elongates in the direction of bubble flow, along the length of the plate. This, in turn, expands the thermal layer. A striking mechanism, which can be drawn from an observation of Fig. 5.20, is that the wake following the bubble path may give siginificant pushing power to the bubble motion.

It is worth seeing how the bubble interacts with the thermal boundary layer for different inclination angles. The same mechanism of interaction is noticed in Figs. 5.16 and 5.17, 5.18 and 5.19 for the inclination angles 20° and 30°, respectively. However, the bubble is sliding faster as the inclination angle increases. For higher inclination angles, for example $\theta = 30°$, the bubble bounces more and this, in turn, sheds the vortex behind the bubble. This allows more cold fluid to the surface of the plate and the thermal boundary layer mixes with the surrounding fluid. This creates more than one peak in the temperature profile of the plate surface at later times, say $t = 0.3$ s and 0.4 s, as shown in Fig. 5.10.

It is particularly intuitive to correlate the temperature profile at $t = 0.4$ s shown on Fig. 5.10 with velocity vector and temperature contour plots. In this case, the bubble is shown to have lifted off the plate and to force hot fluid against the plate. This explains why the cooling effect is not felt until the bubble has passed the temperature measurement point. A cold liquid mass is also shown to have been trapped between a hot liquid layer against the plate and the part of the thermal boundary layer that has been deflected by the bubble. At some point in the near wake, this cold mass is pushed against the plate and the hot water layer, bringing the plate surface temperature slightly lower. Temperature fluctuations in the wake in this case, that is when the bubble lifts off, is the result of a relatively complex interaction of cold and hot fluid masses which are stretched and deformed by the effect of the sliding bubble and the vortices shed in its wake. When the bubble does not lift off the plate, the main mechanism influencing the plate surface temperature is linked to the gradual stretching and thinning of the cold water masses trapped in the wake of the bubble and pulled against the plate (see Figs. 5.8, 5.11, 5.12 and 5.15). In this case, the temperature of the plate shows a more gradual decrease with less fluctuation.

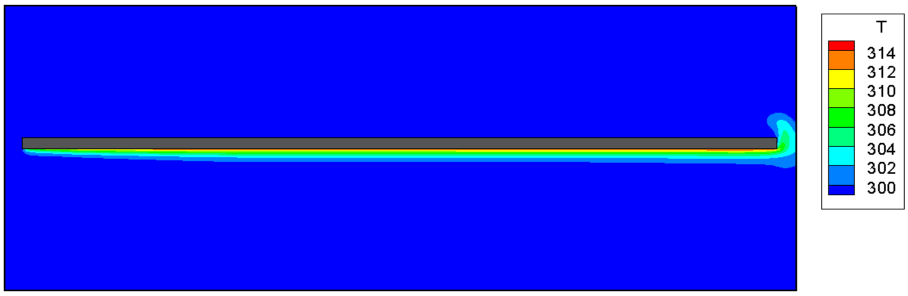

(a)

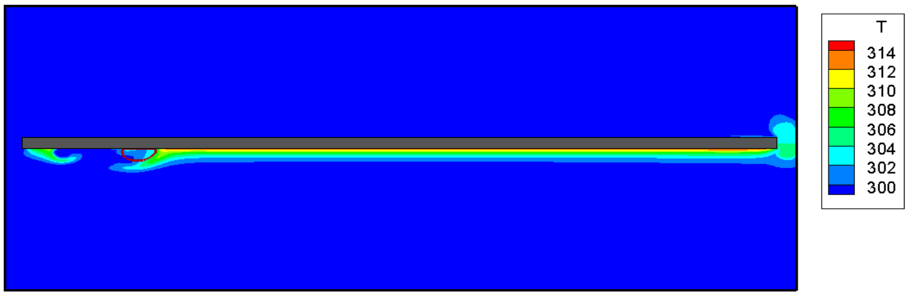

(b)

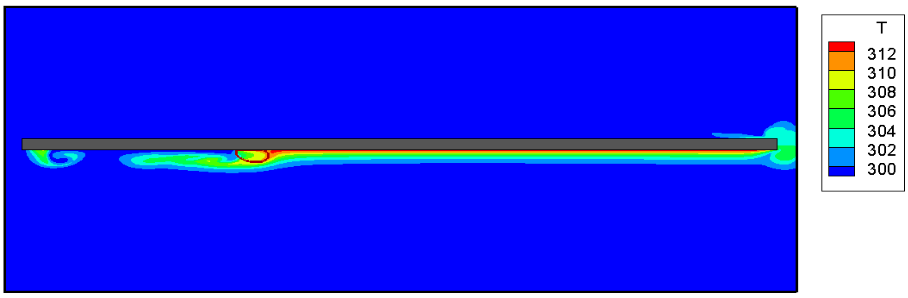

(c)

Figure 5.14: Temperature field and bubble interface of the sliding bubble motion for different times when the plate inclination angle $\theta = 10°$: (a) t = 0.0 s (b) t = 0.1 s (c) t = 0.2 s.

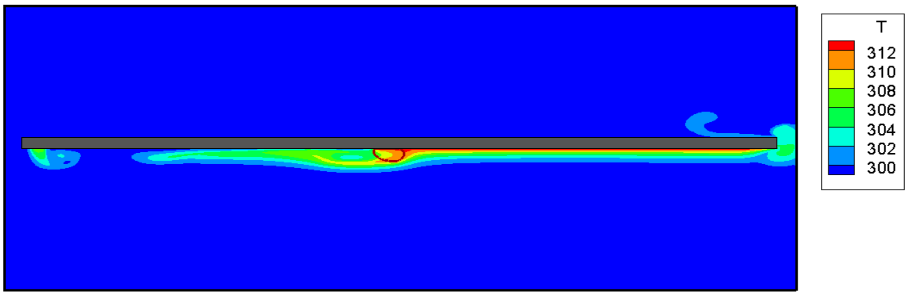

(d)

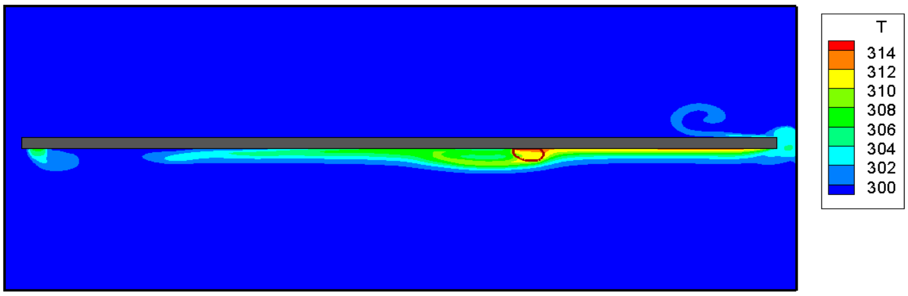

(e)

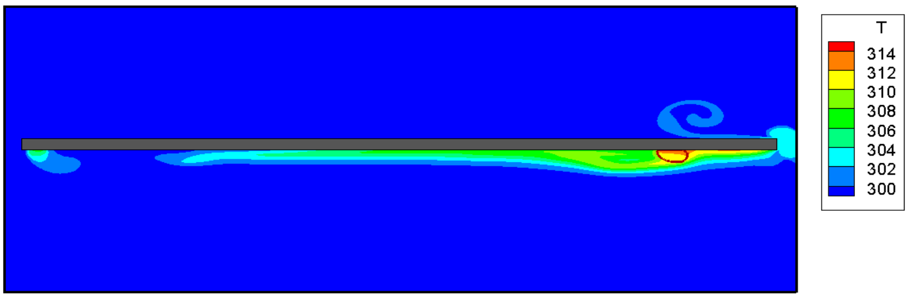

(f)

Figure 5.15: Temperature field and bubble interface of the sliding bubble motion for different times when the plate inclination angle $\theta = 10°$: (d) $t = 0.3$ s (e) $t = 0.4$ s (f) $t = 0.5$ s.

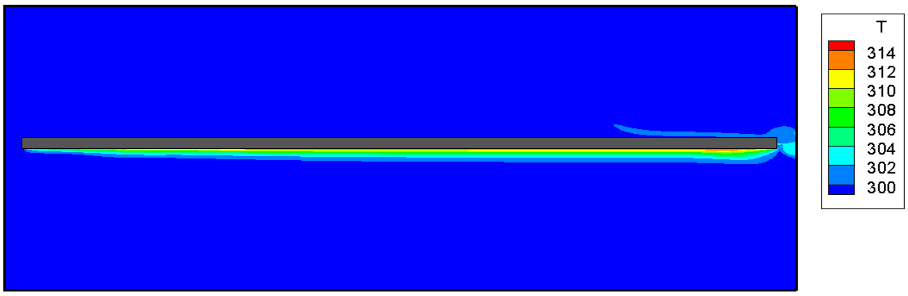

(a)

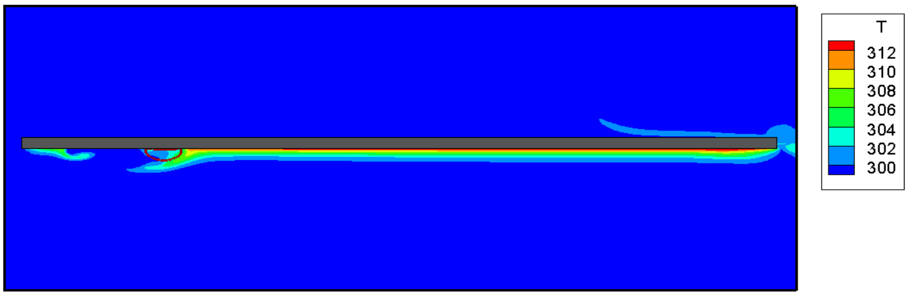

(b)

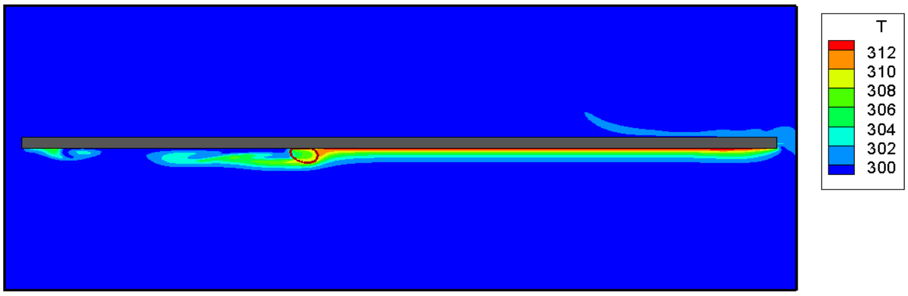

(c)

Figure 5.16: Temperature field and bubble interface of the sliding bubble motion for different times when the plate inclination angle $\theta = 20°$: (a) $t = 0.0$ s (b) $t = 0.1$ s (c) $t = 0.2$ s.

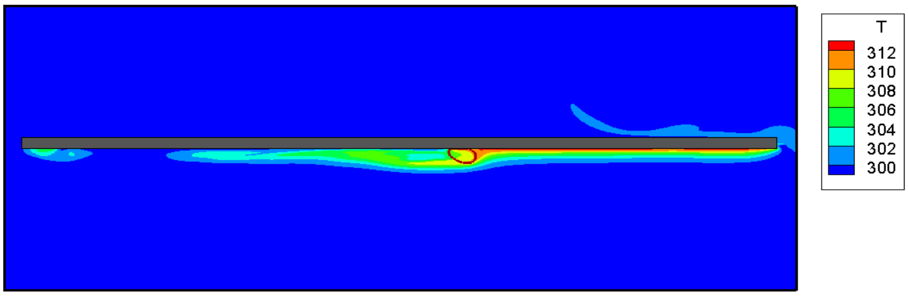

(d)

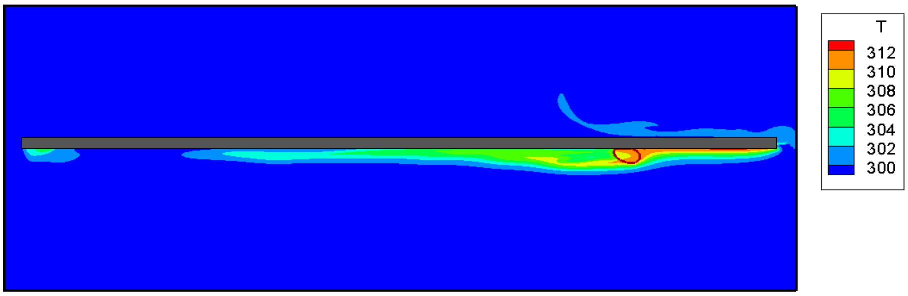

(e)

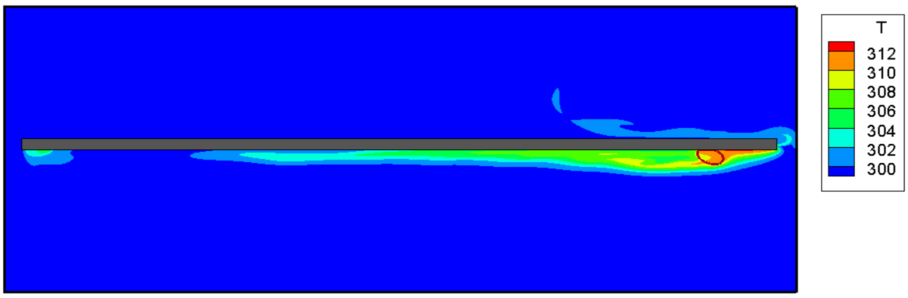

(f)

Figure 5.17: Temperature field and bubble interface of the sliding bubble motion for different times when the plate inclination angle $\theta = 20°$: (d) $t = 0.3$ s (e) $t = 0.4$ s (f) $t = 0.45$ s.

5.7 Wake Structure

In order to see the effect of bubble dynamics on heat transfer, the velocity vectors are plotted for different angles 10°, 20° and 30°. The evolution of wake structure is shown in Fig. 5.20 for the inclination angle of 10°. It can be seen from Fig. 5.20 that the length of the wake increases in the bubble flow direction, parallel to the plate surface, as time progresses. This vortical structure is responsible for dropping the temperature of the plate surface by bringing the cold fluid onto the surface in the back portion of the sliding bubble. This is carried out by disturbing the thermal boundary layer formed over the plate surface by a contact heat flux. This could be illustrated by showing a close view of the velocity vectors surrounding the sliding bubble.

The velocity vectors in the front and the back portions of a sliding bubble, when the plate inclination angle is $\theta = 10°$ and time $t = 0.2$ s, are shown in Fig. 5.21a and b, respectively. In the front portion, the liquid is pushed outwards away from the wall. In the rear of bubble, liquid is pulled inwards and a vortex structure is seen to exist behind the bubble. The sliding bubble acts like a bluff body, creating a wake structure behind it. This is the result of mixing and vortex-shedding causing increased liquid agitation in the wake region of the bubble and encouraging the hot liquid at the surface to mix with colder liquid from the surrounding bulk liquid. It has a significant potential to remove heat from the plate surface. The more mixing created in the wake region the greater the heat transfer experienced. These mechanisms are consistent with the observations drawn by Qiu and Dhir [109] and Delauré et al. [85].

Figures 5.22 and 5.23 show the velocity vector for inclination angles of 20° and 30°, respectively. It should be noted that the velocity vectors are plotted in Fig. 5.23 with different scales in order to show the full wake structure of the bubble. The same trend is noticed in the vortex structure for both the cases as in the case when the inclination angle is $\theta = 10°$. The length of the wake in the x-direction parallel to the plate surface for higher angles is larger than that of for $\theta = 10°$. This is again due to the fact that the buoyancy force in the bubble flow direction increases as the inclination angle increases. This buoyancy force helps the sliding bubble to overcome the effect of the solid-fluid

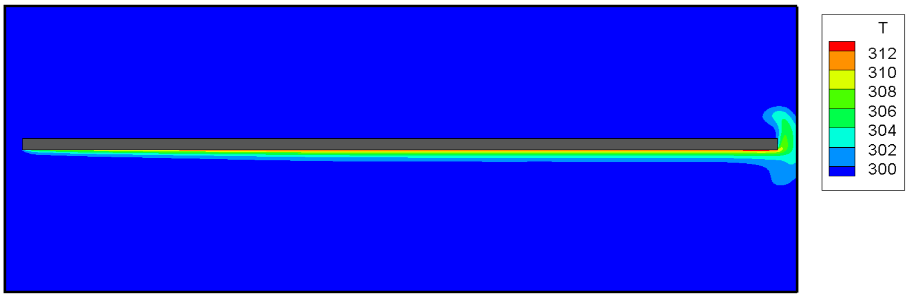

(a)

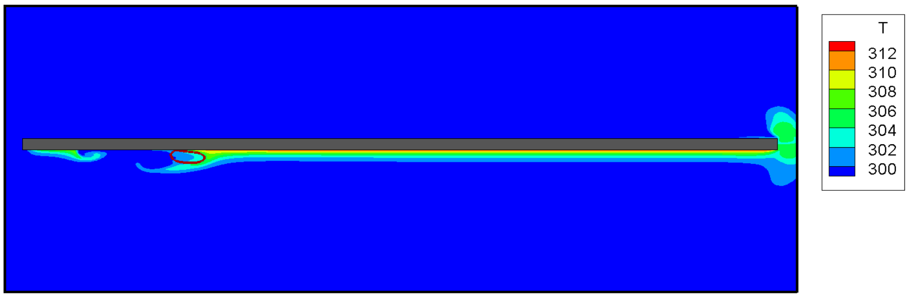

(b)

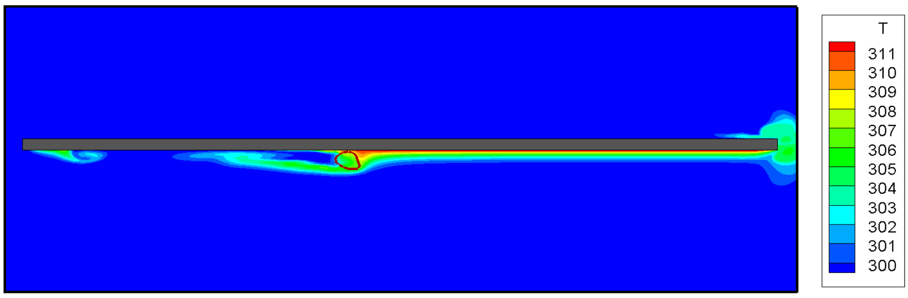

(c)

Figure 5.18: Temperature field and bubble interface of the sliding bubble motion for different times when the plate inclination angle $\theta = 30°$: (a) $t = 0.0$ s (b) $t = 0.1$ s (c) $t = 0.2$ s.

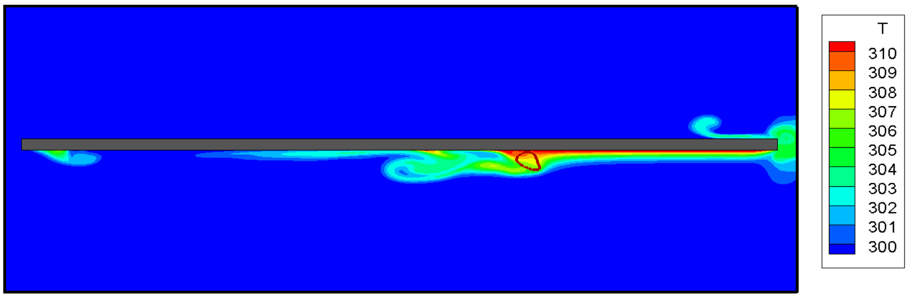

(d)

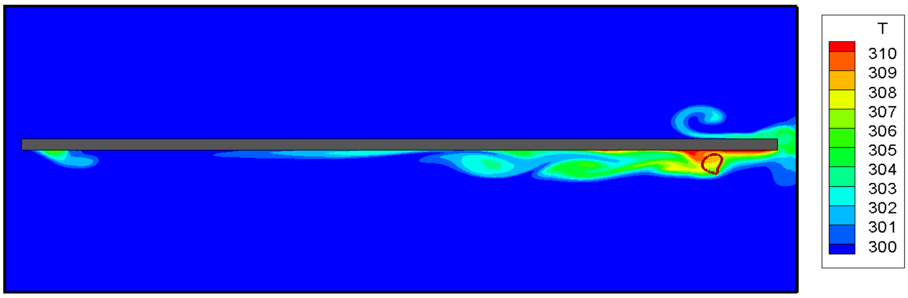

(e)

Figure 5.19: Temperature field and bubble interface of the sliding bubble motion for different times when the plate inclination angle $\theta = 30°$: (d) $t = 0.3$ s (e) $t = 0.4$ s.

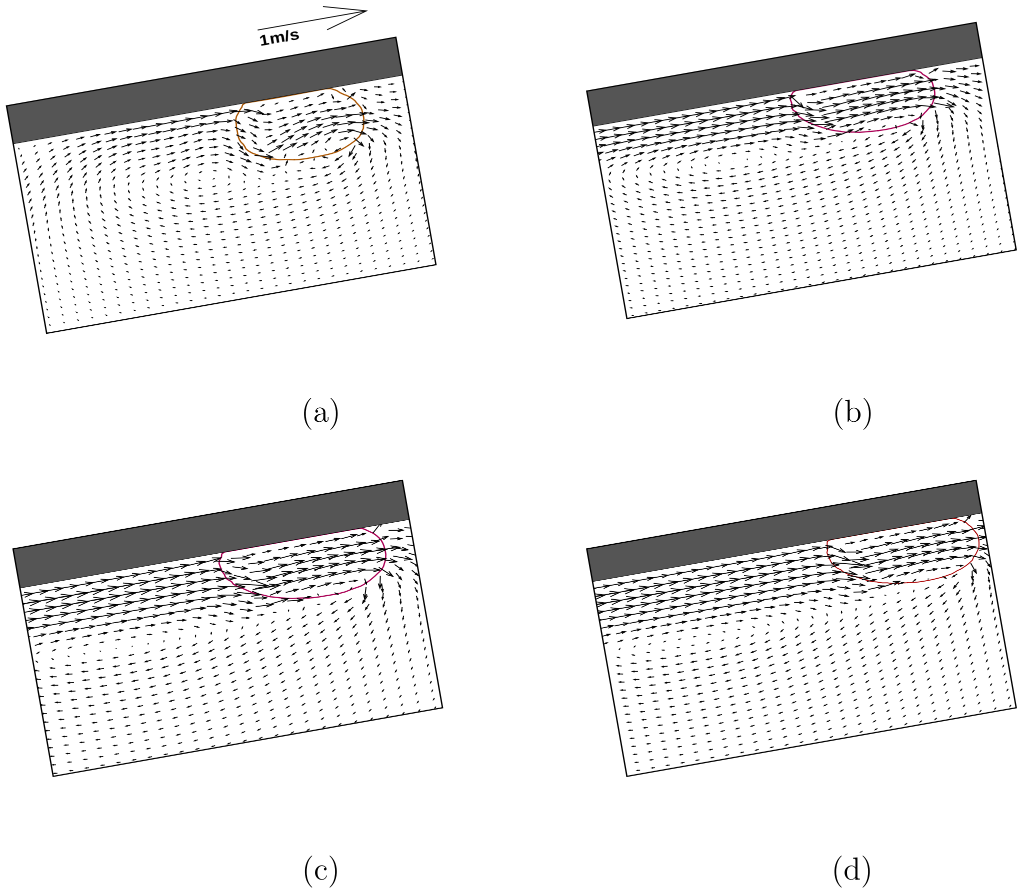

Figure 5.20: Vector plot of sliding bubble motion for different time instants at an angle $\theta = 10°$: (a) $t = 0.1$ s (b) $t = 0.2$ s (c) $t = 0.3$ s (d) $t = 0.4$ s.

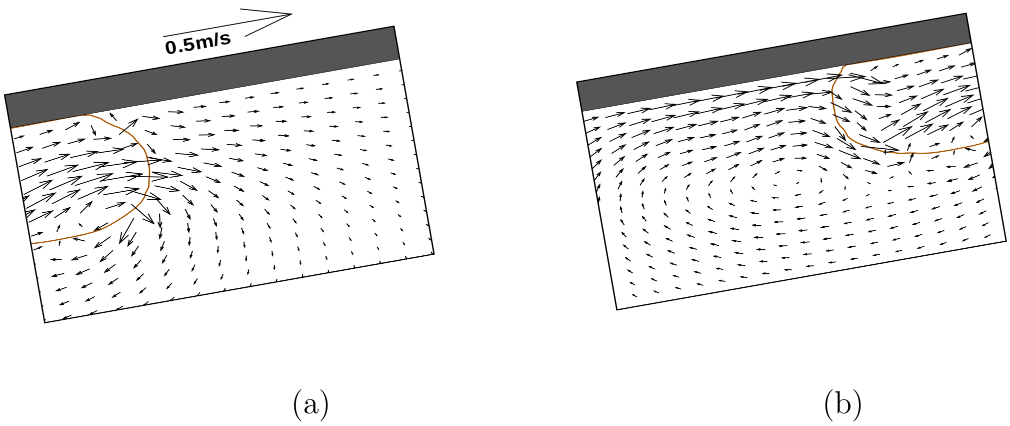

Figure 5.21: Vector plot of frontal and back portions of the sliding bubble when the inclination angle $\theta = 10°$ and time $t = 0.2$ s: (a) Front portion (b) Back portion.

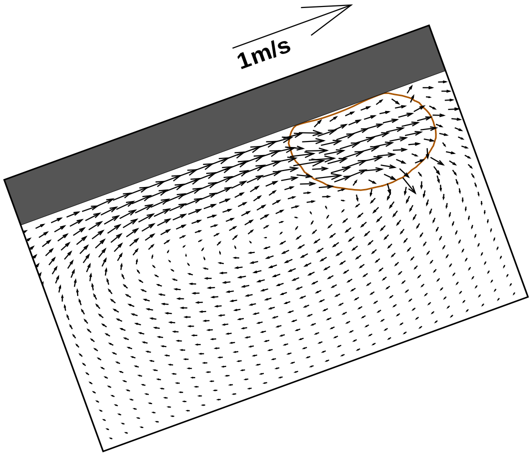

(a)

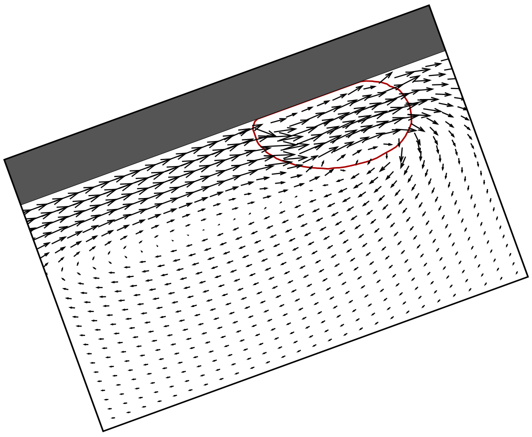

(b)

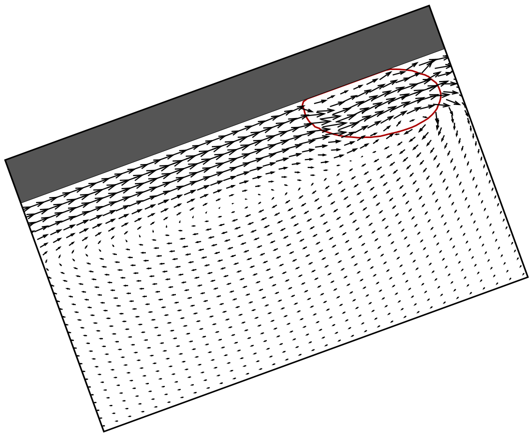

(c)

Figure 5.22: Vector plot of sliding bubble motion for different time instants at an angle $\theta = 20°$: (a) $t = 0.1$ s (b) $t = 0.2$ s (c) $t = 0.3$ s.

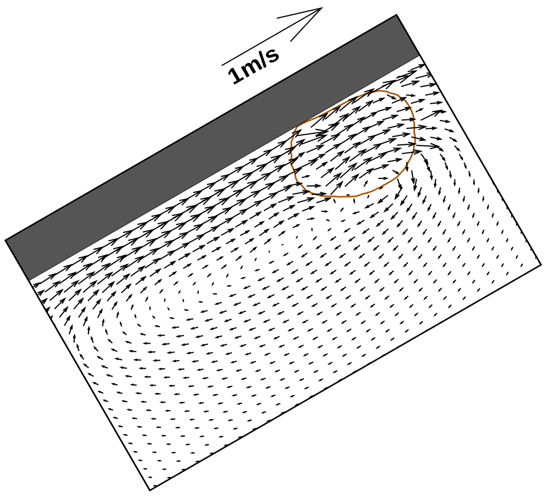

(a)

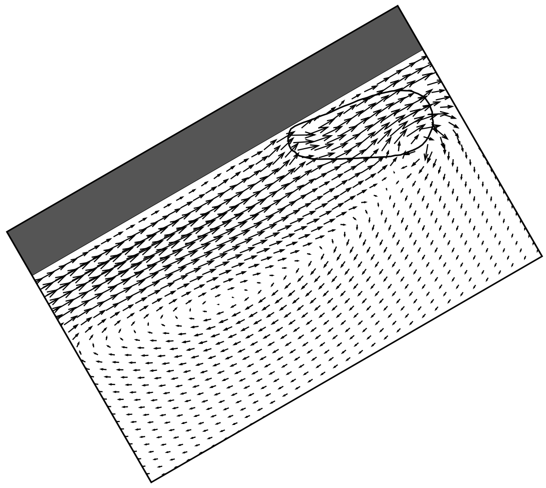

(b)

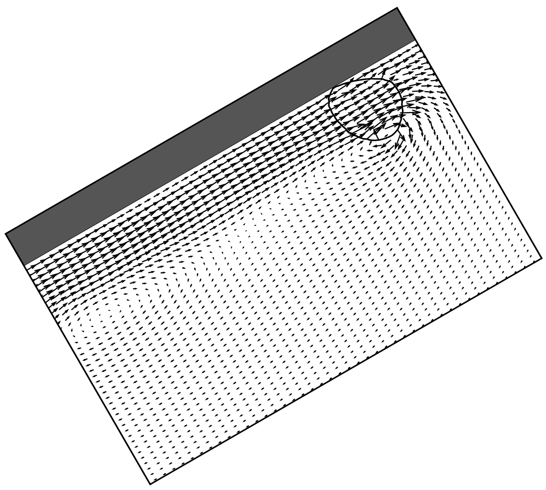

(c)

Figure 5.23: Vector plot of sliding bubble motion for different time instants at an angle $\theta = 30°$: (a) $t = 0.1$ s (b) $t = 0.2$ s (c) $t = 0.3$ s.

interaction force and makes it to move faster as the plate angle increases.

5.8 Comparison of Temperature Profiles

Experimental results of bubble positions, plate surface temperature contour plots, and surface temperature profiles along the bubble path over the lower surface of the plate, for the inclination angle of 10° are presented in Figs. D.1, D.2, D.3 and D.4 of Appendix D for different times 0.1, 0.2, 0.3 and 0.4 s, respectively. The plot at the left hand side shows the shape and position of the bubble and the plot at the center shows the temperature map of the plate surface with the color bar showing its corresponding values, while the plot at the right hand side shows the temperature profile along the path of the sliding bubble motion. Similar results for $\theta = 20°$ are plotted in Figs. D.5, D.6, D.7 and D.8 of Appendix D for different times 0.1, 0.2, 0.3 and 0.4 s, respectively. For $\theta = 30°$, similar plots are presented in Figs. D.9, D.10, D.11 and D.12 of Appendix D for different times 0.1, 0.2, 0.3 and 0.4 s, respectively.

It can be seen from Fig. D.1 of Appendix D and from Fig. 5.7 that the upstream and downstream temperatures are 314.25 and 311.5 K, respectively in the experiment whereas these values are 313.5 and 299.5 K, respectively in the computation, when $\theta = 10°$ and at time $t = 0.1$ s. This means that the predicted temperature drop is more in the computations than in the experiments.

This discrepancy continues for all time instants for a given value of the inclination angle, during the sliding bubble motion. This can be observed from the corresponding figures of Appendix D at times 0.1, 0.2, 0.3 and 0.4 s for each plate inclination angle. The corresponding upstream and downstream temperature values are listed in Table 5.3. Likewise, the temperature values are listed in Table 5.4 from computational results. These differences in the temperature can be explained by the fact that in the computations, the calculations are carried out using a 2D model while in the experiments, it is a 3D problem. Conduction in the third direction might be having an effect in the experimental observations. This brings heat from the surrounding region of the plate surface in that direction. This effect can not be considered in the 2D computational model. This explains the limitation of the present model. The low temperature predicted by the computational model is caused by the cold water mass trapped against the plate by the thermal boundary layer in the wake of the bubble. As discussed in Section 5.4, it is quite likely that in three dimensions such a cold water mass would be quickly mixed with hotter liquid, pushed latterly by the sliding bubble brought back in the wake from the side. In a 2D model, such lateral mixing is not accounted for.

The table 5.3 shows the experimental results of temperature ratios between downstream temperature and upstream temperature for different plate inclination angles $10°, 20°$ and $30°$, respectively. This is calculated for different time instants with a time interval of 0.1 s. The same calculations of temperature ratios for different plate inclination angles $10°, 20°$ and $30°$ are calculated from the computational results and are presented in Table 5.4. The values of temperature ratio are almost same (i.e. till the first decimal accuracy) in both the experimental and computational findings.

Computational results that are in agreement with the temperature profiles of Figs. D.1 - D.12 are:

- There is a significant temperature reduction immediately after the bubble.
- The extent of the zone of influence grows with time after impact although there is a more significant dilation of the strength of the wake (measured in terms of its influence on temperature reduction) which may be explained by three dimensional mixing between the wake and the boundary layer.
- There are fluctuations in the temperature when the plate inclination angle is $30°$ due to the bouncing of the bubble.

Table 5.3: Ratio of upstream temperature to downstream temperature for various time instants - Experimental Results

Plate Inclination Angle, $\theta = 10$ degree			
Time (seconds)	Up stream wall temperature, T_u (K)	Down stream wall temperature, T_d (K)	Temperature ratio $\left(\frac{T_d}{T_u}\right)$
0.1	314.25	311.5	0.9912
0.2	314.25	313.2	0.9967
0.3	314.25	313.6	0.9979
0.4	314.25	313.4	0.9973

Plate Inclination Angle, $\theta = 20$ degree			
Time (seconds)	Up stream wall temperature, T_u (K)	Down stream wall temperature, T_d (K)	Temperature ratio $\left(\frac{T_d}{T_u}\right)$
0.1	314.25	311.5	0.9912
0.2	314.25	311.0	0.9897
0.3	314.25	312.0	0.9928
0.4	314.25	311.5	0.9912

Plate Inclination Angle, $\theta = 30$ degree			
Time (seconds)	Up stream wall temperature, T_u (K)	Down stream wall temperature, T_d (K)	Temperature ratio $\left(\frac{T_d}{T_u}\right)$
0.1	313.25	310.25	0.9904
0.2	313.25	309.50	0.9880
0.3	313.25	309.75	0.9888
0.4	313.25	310.00	0.9896

Table 5.4: Ratio of upstream temperature to downstream temperature for various time instants - Computational Results

Plate Inclination Angle, $\theta = 10$ degree			
Time (seconds)	Up stream wall temperature, T_u (K)	Down stream wall temperature, T_d (K)	Temperature ratio $\left(\frac{T_d}{T_u}\right)$
0.1	313.5	299.5	0.9553
0.2	312.75	299.0	0.956
0.3	312.5	300.5	0.9616
0.4	312.0	303.75	0.9736

Plate Inclination Angle, $\theta = 20$ degree			
Time (seconds)	Up stream wall temperature, T_u (K)	Down stream wall temperature, T_d (K)	Temperature ratio $\left(\frac{T_d}{T_u}\right)$
0.1	313.5	299.50	0.955
0.2	312.5	299.25	0.958
0.3	312.25	299.50	0.959
0.4	311.5	302.00	0.970

Plate Inclination Angle, $\theta = 30$ degree			
Time (seconds)	Up stream wall temperature, T_u (K)	Down stream wall temperature, T_d (K)	Temperature ratio $\left(\frac{T_d}{T_u}\right)$
0.1	312.0	299.5	0.959
0.2	311.5	299.5	0.960
0.3	311.0	306.0	0.984
0.4	310.5	307.5	0.992

5.9 Summary

Numerical simulations of an air bubble sliding along the lower surface of a heated inclined plate immersed in water, for different inclination angles were presented and discussed. The effects of contact angles on temperature field were assessed. Numerical results were compared with experimental data in terms of the evolution of bubble motion, temperature distribution along the lower surface of the plate and temperature ratios. The effect of the inclination angle of the plate on the bubble shapes and temperature distributions were investigated and compared with the experimental results. It was found that the rising velocity of the bubble sliding along the inclined plate increases monotonously as the inclination angle increases toward the vertical.

It was also found that the results obtained by the present numerical model are in reasonable qualitative agreement with the experimental results, however there are discrepancies in the predictions of temperature. The predicted temperature drop was higher in the computations than in the experiments. This discrepancy continued for all time instants for a fixed value of the inclination angle, during the sliding bubble motion. This may be explained by the fact that, in the computations, the calculations are carried out using a 2D model which can not account for lateral mixing as the bubble slides in the boundary layer. Conduction from the third direction might be having an effect on the experimental observations. This would bring heat from the surrounding region of the plate surface in that direction. This effect can not be considered in the 2D computational model. This is the limitation of the present model. However, it gives an insight into the underlying mechanisms of mixing and vortex-shedding that are responsible for increases in the heat transfer from the surface and has qualitative agreement with the experimental results. It is worth mentioning here is that it is difficult to gain a good insight into the processes taking place in the thermal boundary layer and how the bubble interacts with it through experiments. Computational results, on the other hand, help in understanding the mechanisms responsible for temperature reduction.

The advantage of the present formulation is that the combined effects of both surface tension and convective heat transfer components are modelled directly. Although limited by static contact angle approximation, the present formulation may be used as a tool for the analysis of the complex unsteady flow of a bubble sliding along the lower surface of an inclined plate. It is observed that the present formulation provides the solution for a variety of unsteady flows of sliding bubble with heat transfer.

CHAPTER 6

CONCLUSIONS

6.1 Conclusions

The conclusions of the numerical study of bubble dynamics with heat transfer are summarised in this Section:

A numerical tool has been developed to solve the multi-fluid problems with or without heat transfer. The mathematical formulation and the numerical methodology employed have been described. The main aspects are summarised below:

- A SIMPLE algorithm is employed to solve the mass, momentum and energy conservation equations. The equations are discretized using the finite volume formulation. A multigrid technique is implemented to accelerate the calculation of the pressure equation.The solution of mass and momentum equations was validated by the study of lid driven cavity benchmark problem. The coupling of the mass and momentum equations with the energy equation was validated by the study of natural convection in a square cavity having its vertical walls differentially heated. The variable thermo-physical properties formulation was investigated through the problem of natural convection of water with empirical relationships of properties with temperature.
- The two-fluid problem was solved numerically using the volume of fluid (VOF) method. The interface was tracked by the piecewise linear interface construction technique. The surface tension force was modelled as a continuum body force in the momentum equations. The accuracy and the implementation of the method were investigated through a series of tests of translation of different interfaces and of the Rider and Kothe [19] single vortex problem.

To further assess the capability and accuracy of the present method for multi-fluid flows with large property jumps, the dynamics of an isothermal bubble in an enclosed rectangular domain was investigated for different fluid properties and flow parameters. The simulation results of rising bubbles were compared with reported numerical and experimental observations of terminal bubble shapes, terminal velocities, and aspect ratios. Drag coefficients were also calculated for a range of bubble types and compared with results presented by Raymond and Rosant [97]. The SIMPLE-VOF solver developed in this study was assessed as it relies on a specific density interpolation in cells containing the multi-fluid interface and also limitations of a 2D model approach were assessed. It was found that, overall, the present numerical method performed adequately for bubble dynamics, in spite of the two-dimensional assumption. The main exception to this was in the case of larger diameter bubbles of fluids S5 and S6. This suggested a necessity of three dimensional model for this kind of bubbles.

To assess the suitability of the numerical modelling methods adopted to represent the main mechanisms affecting the dynamic behaviour of the sliding bubbles, simulations of an air bubble sliding along the lower surface of an inclined plate immersed in water were performed for different inclination angles. Numerical computation relied on two significant simplifications. First, the numerical model assumed two dimensional flow which meant that any comparison with experimental data was considering two different situations. Second, surface tension effects at the bubble interface with a solid surface were modelled assuming a fixed contact angle between the solid surface and the bubble interface. In spite of this difference, comparison between numerical and experimental results helped to assess qualitatively, the suitability of the model to account for all main mechanisms. In particular, the VOF model was shown to reproduce

- bubble flattening against the solid surface for lower angle as a result of buoyancy and surface tension
- bubble velocity increases with plate inclination angle
- bubble lift off from the surface with larger plate inclination angle

It was found that the velocity of the bubble sliding along the inclined plate increases monotonously as the inclination angle increases toward the vertical. It was observed that a flattening of the bubble due to buoyancy forces is most noticeable for smaller angles. This, in turn, increases the aspect ratio of the bubble for the smaller angles. It was also found that the results obtained by the present numerical model are in good agreement with experimental results, however there are some discrepancies in the bubble displacement along the x-direction and the aspect ratios. This was due to the fact that the lift offs were not fully observed in the numerical results, whereas they were observed in the experimental results and that the bubble might have oscillations in the third direction for higher inclination angles that may affect its motion. Overall, the present numerical method performs adequately for sliding bubble dynamics.

Numerical simulations of an air bubble sliding along the lower surface of a heated inclined plate immersed in water, for different inclination angles, were presented and discussed. The effect of contact angle on the temperature field was assessed. Numerical results were compared with experimental data in terms of the evolution of bubble motion, temperature distribution along the lower surface of the plate and temperature ratios. The effect of the inclination angle of the plate on the bubble shapes and temperature distributions were investigated and compared with the experimental results. It was found that the rising velocity of the bubble sliding along the inclined plate increases monotonously as the inclination angle increases toward the vertical.

It was also found that the results obtained by the present numerical model are in reasonable qualitative agreement with the experimental results, however, there are discrepancies in the predictions of temperature. The predicted temperature drop was more in the computations than in the experiments. This discrepancy continued for all time instants for a fixed value of the inclination angle during the sliding bubble motion. This can be explained by the fact that, in the computations, the calculations are carried out using a 2D model while in the experiments, it is a 3D problem. Conduction from the third direction might be having an effect on the experimental observations. This brings heat from surrounding region of the plate surface in that direction. This effect can not be considered in the 2D computational model. This may also be explained by the fact that, in the experiments, the bubble rising with higher initial velocity caused by the injection pressure of the syringe and it is very difficult to avoid, whereas, in the computations, the bubble starts from rest. Because of the higher initial velocity, a bubble may stay for a shorter time at the point of impact. It may not be able to absorb as much heat from the surface of the plate. This may explain the reduced temperature drop at the early stage of the impact in the experiments when compared with the computations. These are limits of the present computational model. However, the model does give an insight into the underlying mechanisms of mixing and vortex-shedding that are responsible for increases in the heat transfer from the surface and has qualitative agreement with the experimental results. It is worth mentioning here that it is hard to see the thermal boundary layer and how the bubble interacts with it in the experiments.

The advantage of the present formulation is that the solution is obtained directly for the combined effects of both surface tension and convective heat transfer components. Although limited by the static contact angle approximation, the present formulation may be used as a tool for the analysis of complex unsteady flow of a bubble sliding along lower surface of an inclined plate. It is observed that the present formulation provides the solution for a variety of unsteady flows of sliding bubble with heat transfer.

6.2 Future Scope

The focus of the present work was on the numerical simulation of bubble impact and sliding and lift off from wall for a wide range of inclinations of flat plate to help understand the hydrodynamic and heat transfer characteristics. A significant increase in heat transfer is observed when the bubble is sliding. In the present work, numerical simulations were carried out using a 2D approximation. Even though it agreed qualitatively with experimental studies, more details on fluid flow and heat transfer characteristics could be obtained using 3D numerical simulations.

A number of aspects of the research that require more study, and areas of the computational framework in which improvements may be made in future work are listed below:

- The spatial resolution in the Volume of Fluid Method can be improved using the adaptive mesh refinement technique, especially around the interface and contact point.

- A range of bubble sizes should be studied to examine any possible relationship between bubble size and heat transfer experienced.
- A wider range of inclination angles should be studied to highlight the effect of inclination angle variation on the heat transfer experienced.
- Conduction should be taken into account in the solid surface to perform realistic simulations of the thermo-fluid dynamics involved in the sliding bubble over inclined surface.
- Dynamic contact angle behaviour needs to be considered using a mathematical model that should take into account the effect of bubble velocity on contact angle.
- The bubble-sliding phenomenon is also observed in nucleate boiling over vertical and inclined flat surfaces and horizontal and vertical pipes and plays an important role in heat transfer. In saturated nucleate boiling, the size of the bubble continuously increases because of the mass transfer at the interface. Even though many experimental studies were conducted to understand the bubble sliding and lift off phenomenon of nucleate boiling, almost no work has been carried out numerically. Hence, numerical simulation of bubble sliding and lift off in nucleate boiling will help in establishing good CFD tools for designing thermal system which involve two-phase flows.

APPENDIX A

TABLE A.I. SIDE FRACTION CALCULATIONS USING PLIC METHOD

		Sub-Case (1)	Sub-Case (2)	Sub-Case (3)	Sub-Case (4)
	s_t	0	0	$1-\sqrt{2F\tan\alpha}$	$\sqrt{2F\tan\alpha}$
	s_r	0	$\sqrt{2F\cot\alpha}$	$1-\sqrt{2F\cot\alpha}$	0
Case I	s_b	$\sqrt{2F\tan\alpha}$	$1-\sqrt{2F\tan\alpha}$	0	0
	s_l	$\sqrt{2F\cot\alpha}$	0	0	$1-\sqrt{2F\cot\alpha}$
	s_t	$F-\frac{1}{2}\tan\alpha$	$(1-F)-\frac{1}{2}\tan\alpha$	$(1-F)+\frac{1}{2}\tan\alpha$	$F+\frac{1}{2}\tan\alpha$
	s_r	0	0	0	0
Case II	s_b	$F+\frac{1}{2}\tan\alpha$	$(1-F)+\frac{1}{2}\tan\alpha$	$(1-F)-\frac{1}{2}\tan\alpha$	$F-\frac{1}{2}\tan\alpha$
	s_l	0	0	0	0
	s_t	0	0	0	0
	s_r	$F-\frac{1}{2}\cot\alpha$	$F+\frac{1}{2}\cot\alpha$	$(1-F)+\frac{1}{2}\cot\alpha$	$(1-F)-\frac{1}{2}\cot\alpha$
Case III	s_b	0	0	0	0
	s_l	$F+\frac{1}{2}\cot\alpha$	$F-\frac{1}{2}\cot\alpha$	$(1-F)-\frac{1}{2}\cot\alpha$	$(1-F)+\frac{1}{2}\cot\alpha$
	s_t	$1-\sqrt{2(1-F)\tan\alpha}$	$\sqrt{2(1-F)\tan\alpha}$	0	0
	s_r	$1-\sqrt{2(1-F)\cot\alpha}$	0	0	$\sqrt{2(1-F)\cot\alpha}$
Case IV	s_b	0	0	$\sqrt{2(1-F)\tan\alpha}$	$1-\sqrt{2(1-F)\tan\alpha}$
	s_l	0	$1-\sqrt{2(1-F)\cot\alpha}$	$\sqrt{2(1-F)\tan\alpha}$	0

APPENDIX B

TABLE B.I. FLUX CALCULATIONS FOR YOUNGS' METHOD.

Case I.1	Case I.2	Case I.3	Case I.4
if $x_e \le (1 - S_b)$ $F_e = 0$ else $F_e = \frac{1}{2}[(x_e - (1 - S_b))^2]cot\theta$	$x_e \le (1 - S_t)$ $F_e = 0$ if $(1 - S_t) > x_e > (1 - S_b))$ $F_e = \frac{1}{2}[(x_e - (1 - S_b))^2]cot\theta$ if $x_e \ge (1 - S_t)$ $F_e = \frac{1}{2}[(x_e - (1 - S_t)) + (x_e - (1 - S_b))]$	$F_e = [S_r + \frac{1}{2}(S_r + x_e cot\theta)]x_e$	if $x_e \le (1 - S_t)$ $F_e = \frac{1}{2}[S_r + (S_r + x_e cot\theta)]x_e$ else $F_e = x_e - \frac{1}{2}(1 - S_r)(1 - S_t)]$
if $x_w \le S_b$ $F_w = \frac{1}{2}[S_l + (S_l - x_w cot\theta)]x_w$ else $F_w = (S_b S_l)/2$	if $x_w \le S_t$ $F_w = x_w$ if $S_b > x_w > S_t$ $F_w = x_w - \frac{1}{2}[(x_w - S_t)^2]cot\theta$ if $x_w \ge S_b$ $F_w = \frac{1}{2}[S_t + S_b]$	$F_w = \frac{1}{2}[Sl + (Sl - x_w cot\theta)]xw$	if $x_w \le S_t$ $F_w = x_w$ else $F_w = x_w - \frac{1}{2}[(x_w - S_t)^2 cot\theta]$

Case I.1	Case I.2	Case I.3	Case I.4
$y_n \leq (1 - S_l)$ $F_n = 0$ else $F_n = \frac{1}{2}[(y_n - (1 - S_l))^2]tan\theta$	$F_n = \frac{1}{2}[S_t + (S_t + y_n tan\theta)]y_n$	if $y_n \leq (1 - S_l)$ $F_n = 0$ if $(1 - S_r) > y_n > (1 - S_l)$ $F_n = \frac{1}{2}[(y_n - (1 - S_l))^2]tan\theta$ if $y_n \geq (1 - Sr)$ $F_n = y_n - \frac{1}{2}[(1 - S_r) + (1 - S_l)]$	if $y_n \leq (1 - S_r)$ $F_n = \frac{1}{2}[S_t + (S_t + y_n tan\theta)]y_n$ else $F_n = y_n - \frac{1}{2}[(1 - S_t)(1 - S_r)]$
$y_s \leq S_l$ $F_s = \frac{1}{2}[S_b + (S_b - y_s tan\theta)]y_s$ else $F_s = (S_l S_b)/2$	$F_s = \frac{1}{2}[S_b + (S_b - y_s tan\theta)]y_s$	if $ys \leq Sr$ $F_s = y_s$ if $y_s > Sr$ and $ys < Sl$ $F_s = y_s - [(y_s - S_r)^2 tan\theta]$ if $y_s >= S_l$ $F_s = (S_r + S_l)/2$	if $y_s \leq S_r$ $F_s = y_s$ else $F_s = y_s - \frac{1}{2}[(y_s - S_r)^2 tan\theta]$

APPENDIX C - EXPERIMENTAL PROCEDURE

C.1 Experimental Setup

The experimental apparatus includes of a tilting test tank which can be set to any angle between 0 and 45° by rotating a winding jack, see Fig. 6.2. The tank is constructed from 6 mm thick glass of dimensions $420 \times 420 \times 420$ mm and is supported by aluminium structural members. An inclinometer mounted on the tank provides the angle of inclination. Additional structural elements connected to the tank allow cameras to be mounted above and below the test surface.

The test surface for this experiment measures 300×100 mm and consists of a liquid crystal layer backed by black paint applied to a thin electrically heated foil mounted on a 10 mm thick perspex sheet. The foil used is 25 micron thick AISI 321 stainless steel supplied by Goodfellow Ltd. Both the black paint and liquid crystal (Hallcrest: MB/R33C7W/S40) layers are applied using an Aztek A4702 artists airbrush in conjunction with a compressed air supply at 1.5 bar. Thermal adhesive bonds the foil to the surface with electrical contact being made by two machined copper bars at each end as can be seen in Fig. 6.2.

The test surface requires high intensity lighting both to enhance the visibility of the liquid crystal layer from above and to image the bubble flow from below for bottom view or from front side for side view. This is provided by 4 high intensity light emitting diode (LED) strips mounted to the tank which illuminate the test surface. Each strip contains 15 LED bulbs angled to provide maximum light intensity at the test surface. This method of lighting provides ample uniform light at low temperatures so as not to interfere with the liquid crystal's color play. Mounting both the camera and the lighting to the tilting tank ensures consistency obtained for all angles of the tank.

Bubble generation is achieved by use of a surgical syringe machined to remove the tip. It is mounted to the foil assembly as shown in Fig. 6.2. The bubble is released by pressing a plunger connected to the syringe via rubber tubing: the bubble immediately impacts on the foil and starts sliding along its length. Bubbles have a hydraulic diameter

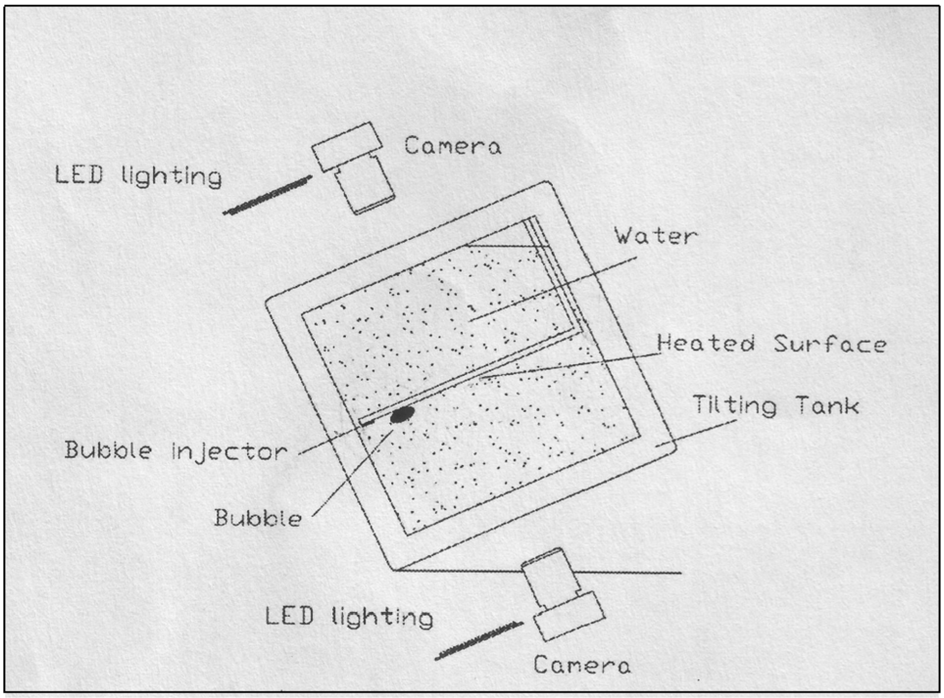

Figure C.1: Schematic diagram of experimental setup for sliding bubble motion [135].

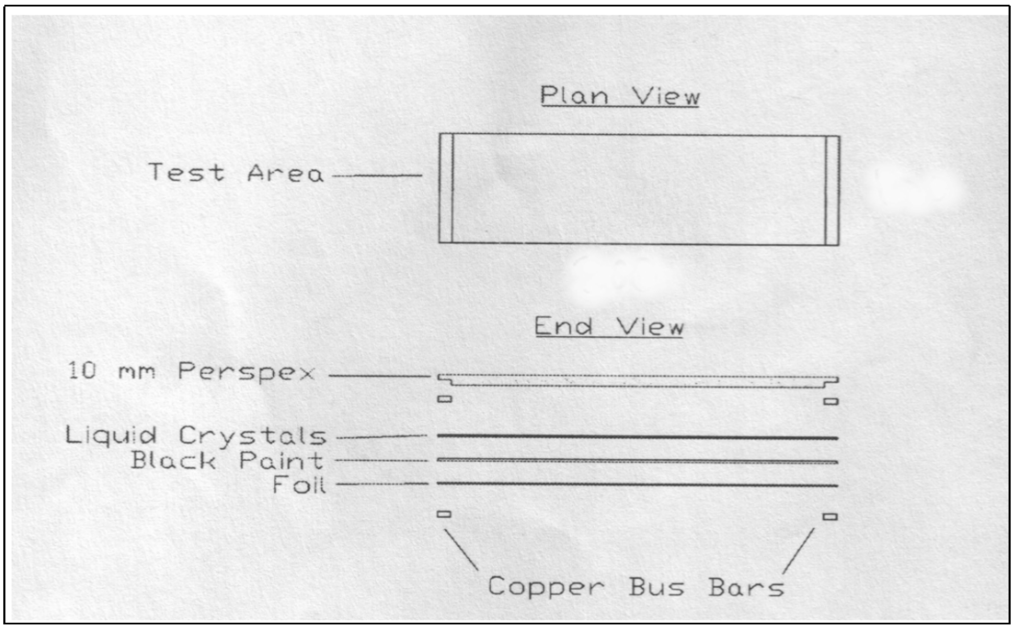

Figure C.2: Schematic of test surface [135].

of approximately 3 mm upon release.

The imaging system used in these experiments is an NAC Hi-Dcam II digital high-speed color camera capable of recording at frame rates of up to 20000 fps and its image resolutions of up to 1280×1024 pixels per frame. The camera is PC controlled via the manufacture's PCI card. This high-speed camera is used to record images of both bubble movement and the response of the thermochromic liquid crystal layer. Although the camera is capable of recording images at very high frame rate, for these experiments frame rates of 250 fps were deemed suitable for both the liquid crystal and the bubble motion due to the dynamic response of the system.

C.2 Water Treatment

Bubble development and motion is strongly influenced by the presence of surfactants and impurities in water. In order to carry out experiments which focus on bubble behaviour the presence of unwanted impurities in the water must be minimised. It was also found that using normally oxygenated water for testing led to growth of air bubbles on the thermochromic liquid crystal test surface when the surface was heated. This made it difficult to obtain clear color images of the test surface, so it was decided to de-oxygenate the water prior to testing.

The water used for these experiments is first de-ionised and then filtered through a 1 μm fibre filter. It is then pumped into a chamber where it is brought to boiling point, using an electrical heating element, in order to de-oxygenate it. The liquid is then allowed to cool in the chamber before carefully being transferred to the test tank, ensuring that minimal air is re-introduced to it by pouring or splashing. This process is repeated for each day of testing in order to keep test conditions uniform.

C.3 Analysis

C.3.1 Heat Transfer Imaging and Analysis System

The foil is heated by passing 50.8 amps at 4.73 volts through it, resulting in

240.3 Watts being dissipated from the foil. The heat generated brings the foil to 39° C under natural convection conditions; this is the clearing point of the liquid crystals i.e. the upper limit above which no colours are visible. The bulk water is maintained at approximately 26° C. A bubble is introduced to the flow and slides along the plate through the test area (see Figs. C.1 and C.2). This causes local regions on the plate surface to cool and thus the liquid crystals change colour from blue to green, then yellow and finally red before the lower temperature limit is reached. Any temperature measurement below or above the limits, or bandwidth, is not possible and the temperature in such regions is replaced with a maximum or minimum value of 39° C and 35° C respectively. Images of the liquid crystal layer are recorded at 250 fps; they are then stored for further analysis. The conversion of the raw images to MatLAB^{TM} temperature plots is done using a third order polynomial calibration curve obtained during liquid crystal calibration.

Images are first converted from RGB (red, green, blue) to HSV (hue, saturation, value) image format using MatLAB^{TM} rgb2hsv function. The hue value of each pixel is then used in conjunction with a calibration curve to retrieve the temperature of the plate.

C.3.2 Bubble Image Capture and Analysis

While the liquid crystal layer is being observed on the upper surface of the foil, the bubble is also being monitored from the side using another NAC Hi-Dcam II digital high-speed color camera. The progress of the bubble is recorded at a frame rate of 250 frames per second, and the still images saved as individual files in the windows bitmap format. Analysis of these images is carried out using MatLAB^{TM} code developed for this purpose. The code subtracts a reference background image which does not contain a bubble, from each of the images which show the bubble's progress. In this way a series of images are produced which show the position and shape of the bubble at various stages of its travel.

APPENDIX D

TEMPERATURE ALONG THE LOWER WALL OF THE PLATE - EXPERIMENTAL RESULTS

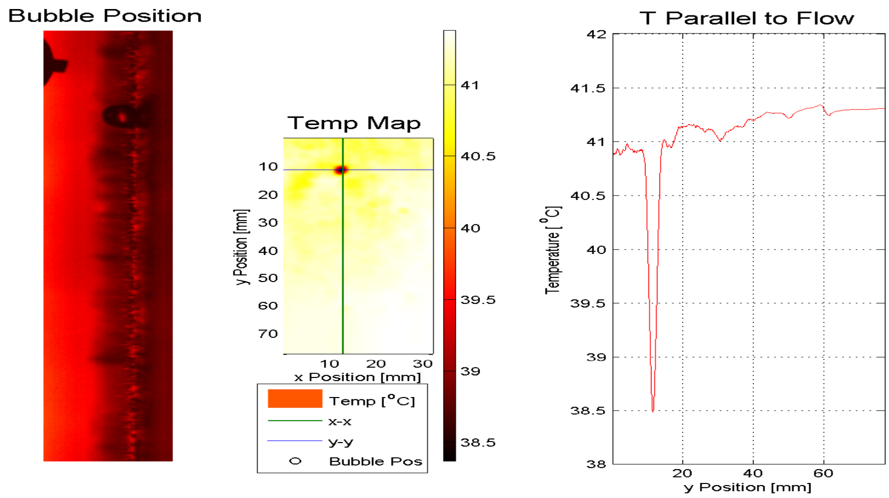

Figure D.1: Left: Snap shot of sliding bubble motion, Middle: Temperature Map and Right: Temperature along the bubble path; when the angle of inclination = 10° and time, $t = 0.1$ s.

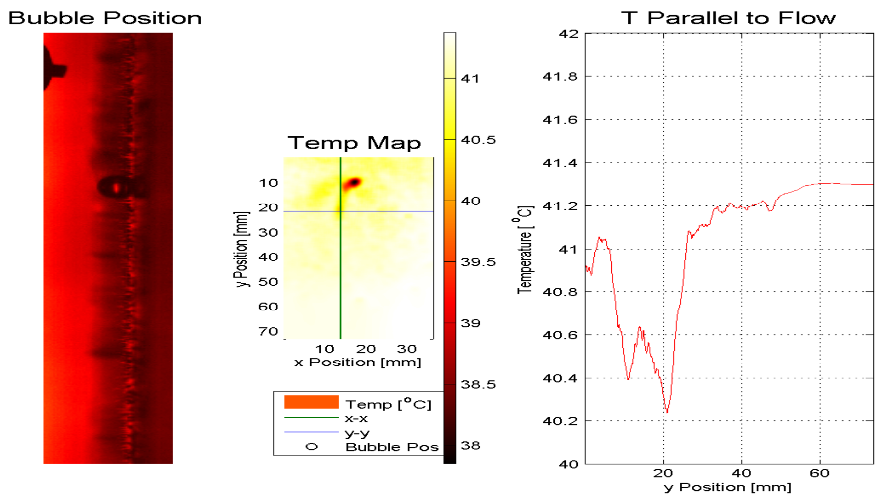

Figure D.2: Left: Snap shot of sliding bubble motion, Middle: Temperature Map and Right: Temperature along the bubble path; when the angle of inclination = 10° and time, $t = 0.2$ s.

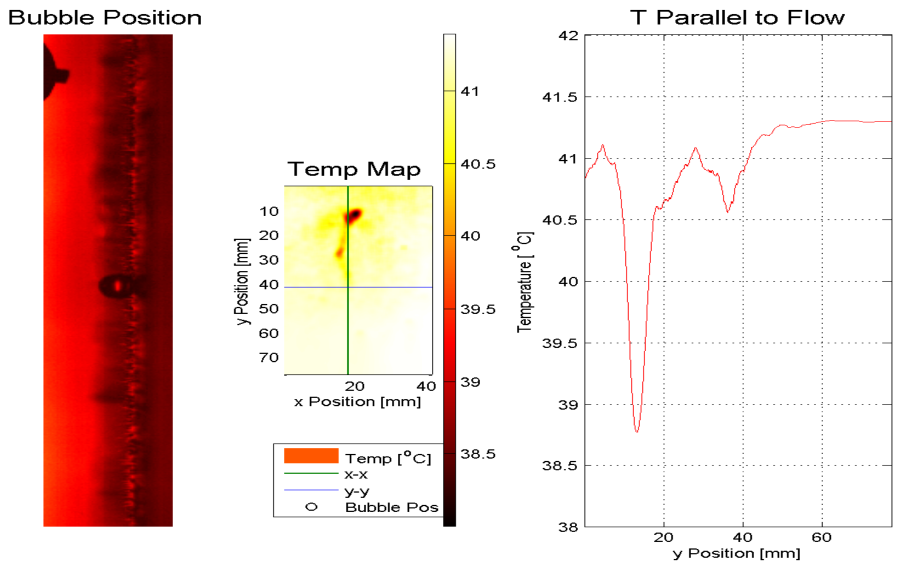

Figure D.3: Left: Snap shot of sliding bubble motion, Middle: Temperature Map and Right: Temperature along the bubble path; when the angle of inclination = 10° and time, $t = 0.3$ s.

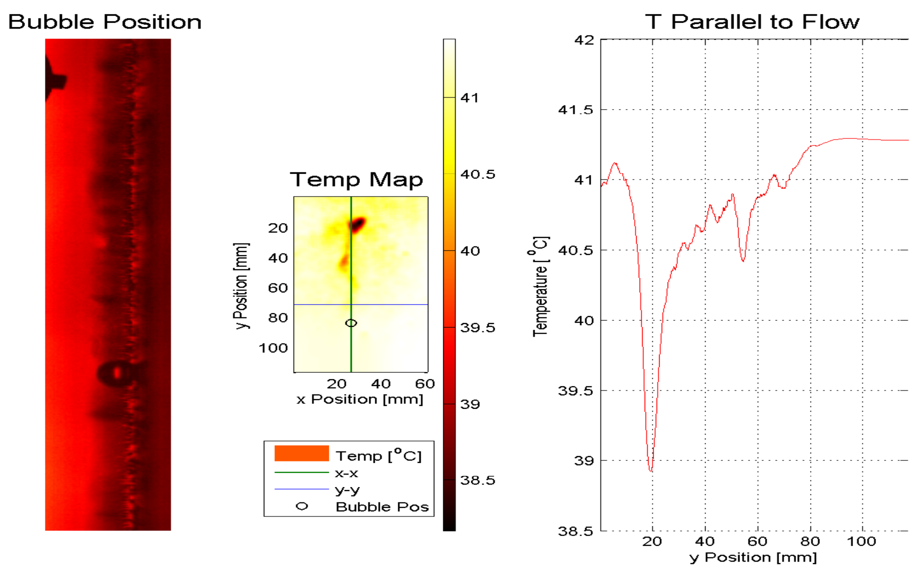

Figure D.4: Left: Snap shot of sliding bubble motion, Middle: Temperature Map and Right: Temperature along the bubble path; when the angle of inclination = 10° and time, $t = 0.4$ s.

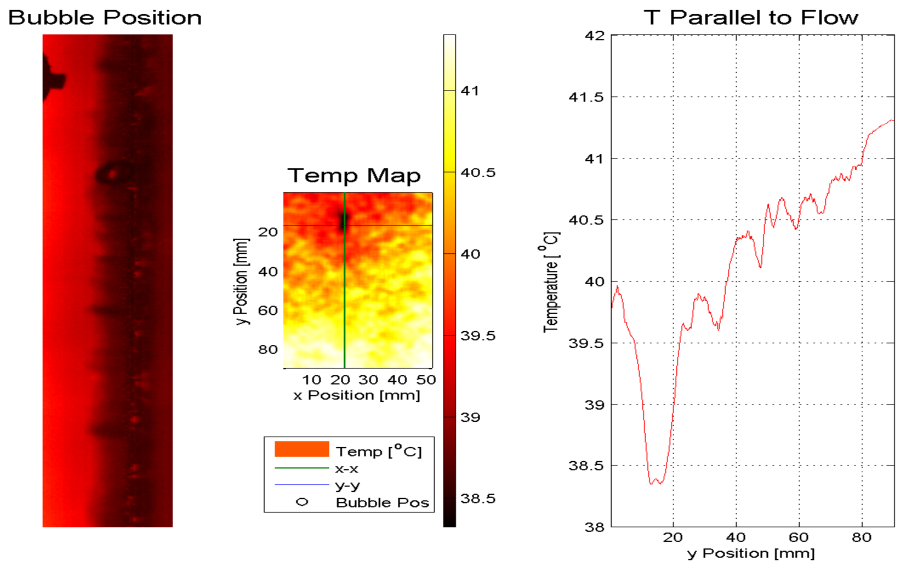

Figure D.5: Left: Snap shot of sliding bubble motion, Middle: Temperature Map and Right: Temperature along the bubble path; when the angle of inclination = 20° and time, $t = 0.1$ s.

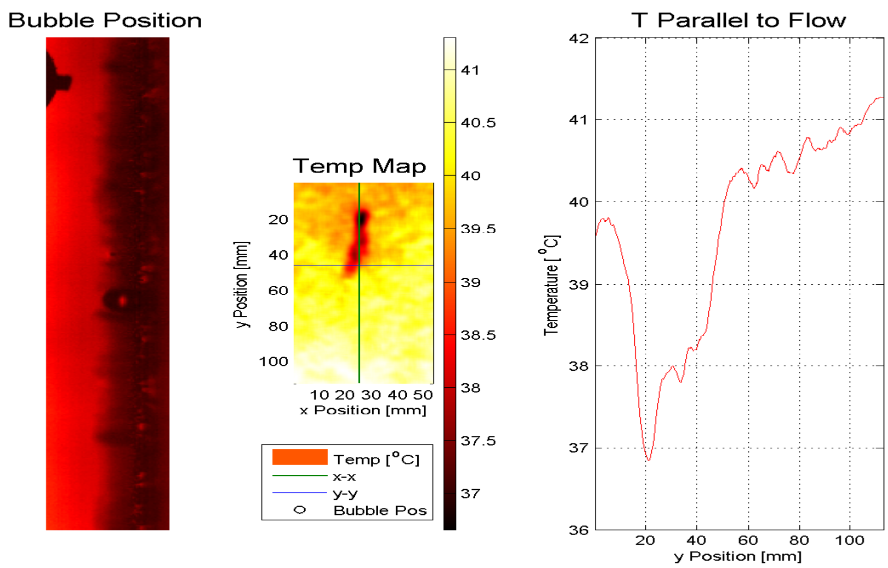

Figure D.6: Left: Snap shot of sliding bubble motion, Middle: Temperature Map and Right: Temperature along the bubble path; when the angle of inclination = 20° and time, $t = 0.2$ s.

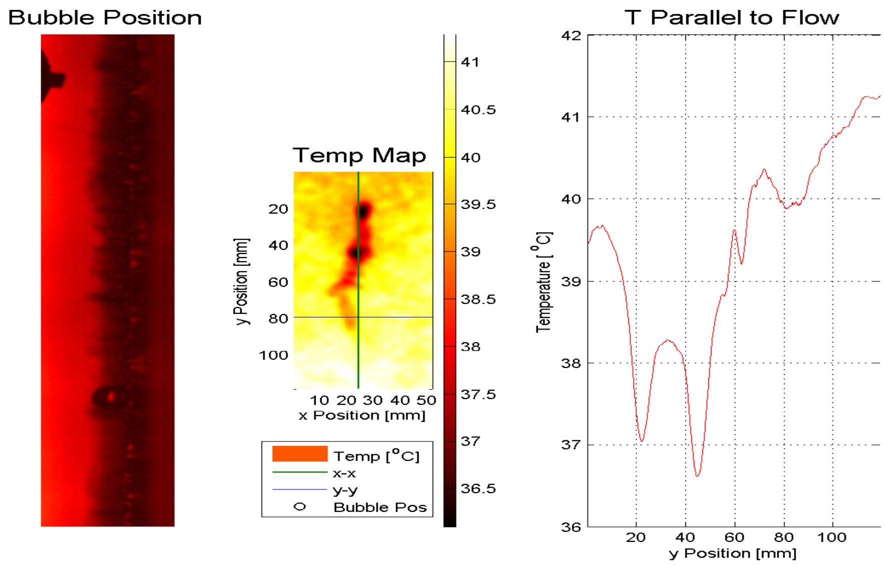

Figure D.7: Left: Snap shot of sliding bubble motion, Middle: Temperature Map and Right: Temperature along the bubble path; when the angle of inclination = 20° and time, $t = 0.3$ s.

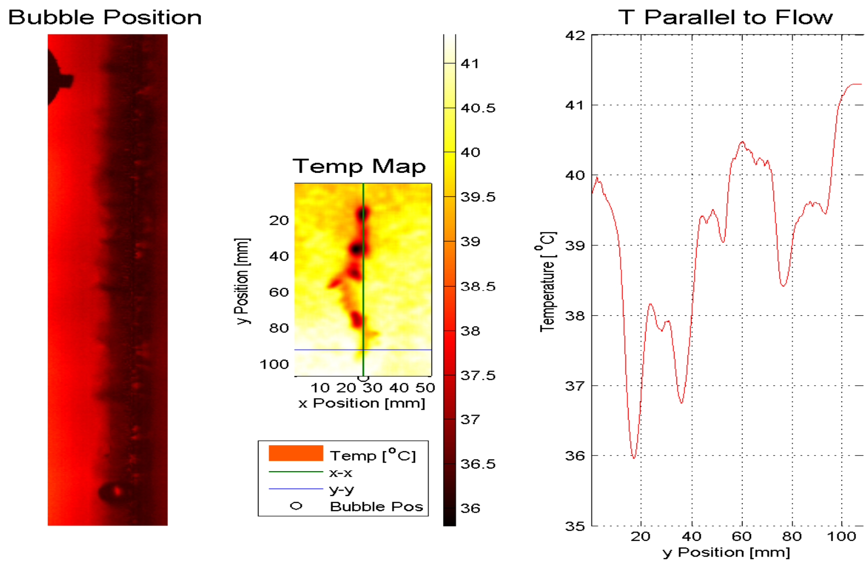

Figure D.8: Left: Snap shot of sliding bubble motion, Middle: Temperature Map and Right: Temperature along the bubble path; when the angle of inclination = 20° and time, $t = 0.4$ s.

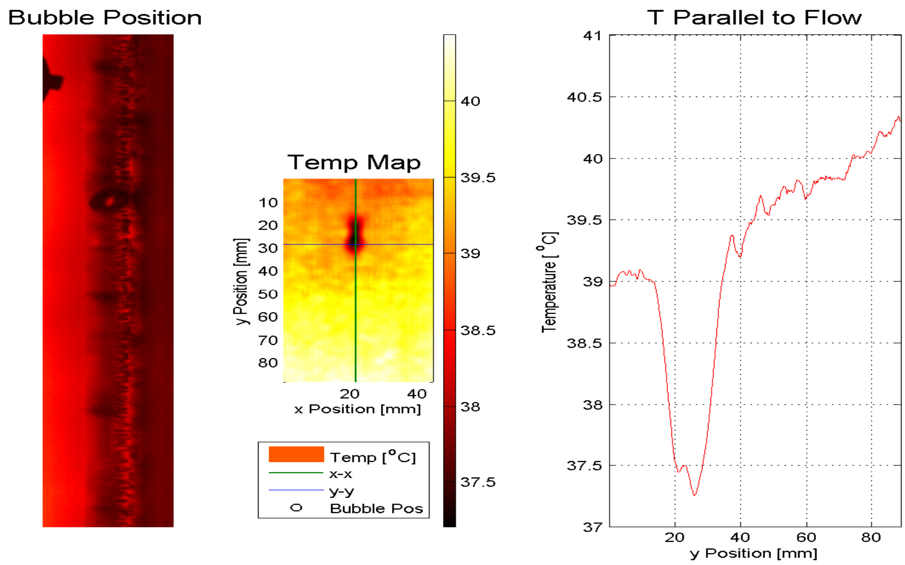

Figure D.9: Left: Snap shot of sliding bubble motion, Middle: Temperature Map and Right: Temperature along the bubble path; when the angle of inclination = 30° and time, $t = 0.1$ s.

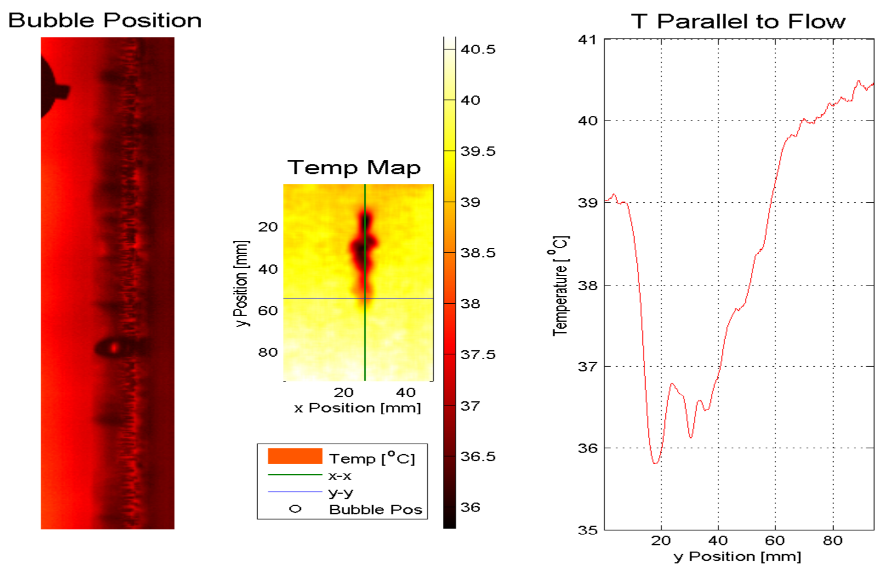

Figure D.10: Left: Snap shot of sliding bubble motion, Middle: Temperature Map and Right: Temperature along the bubble path; when the angle of inclination = 30° and time, $t = 0.2$ s.

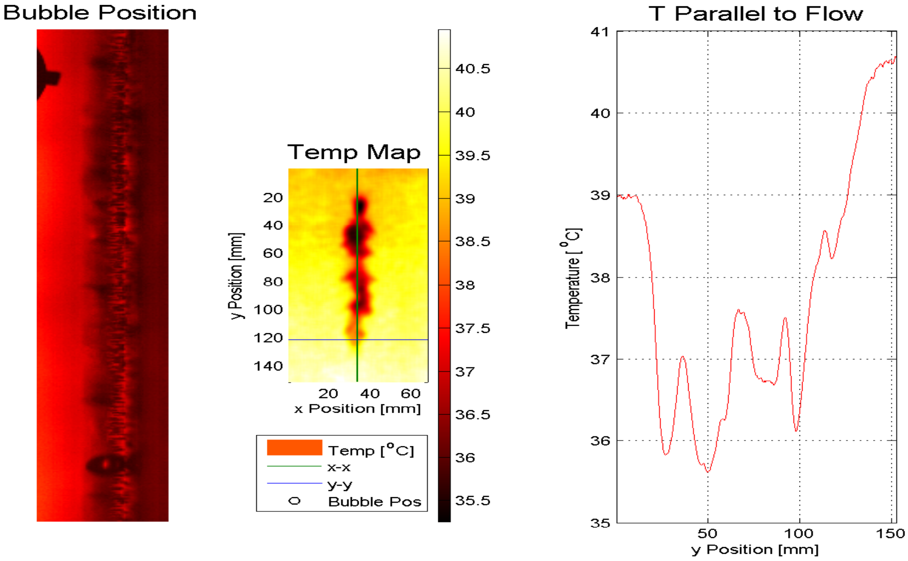

Figure D.11: Left: Snap shot of sliding bubble motion, Middle: Temperature Map and Right: Temperature along the bubble path; when the angle of inclination = 30° and time, $t = 0.3$ s.

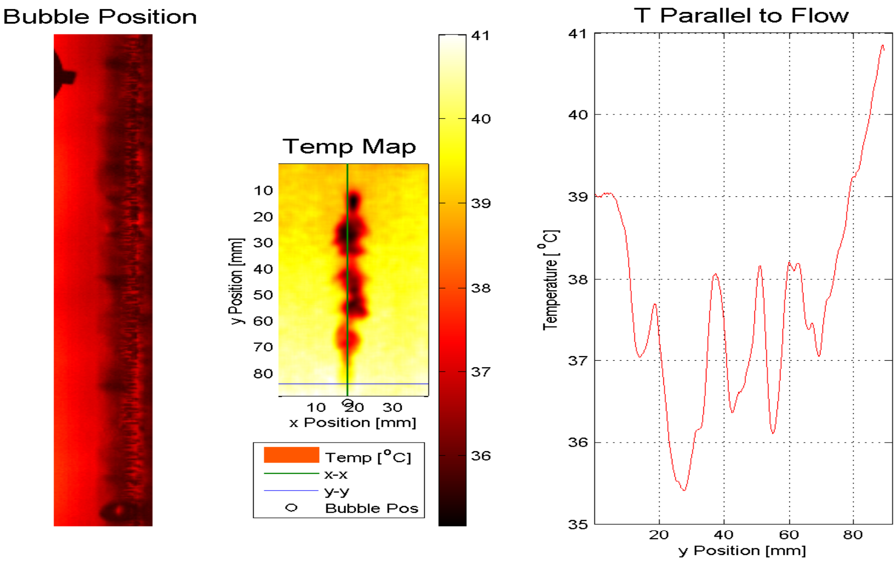

Figure D.12: Left: Snap shot of sliding bubble motion, Middle: Temperature Map and Right: Temperature along the bubble path; when the angle of inclination = 30° and time, $t = 0.4$ s.

BIBLIOGRAPHY

[1] **G. E. Thorncroft, J. F. Klausner and R. Mei**, An experimental investigation of bubble growth in vertical upflow and downflow boiling, *Int. J. Heat and Mass Transfer*, **41**: 3857-3871, (1998).

[2] **H. Y. Yoon, S. Koshizucha,, Oka, Y**, Direct calculation of bubble growth and rise in nucleate pool boiling, *Int. J. Multiphase Flow*, **27**: 277-298, (2002).

[3] **K. Cornwell**, The influence of bubbly flow on boiling from a tube bundle, *Int. J. Heat and Mass Transfer*, **33**: 2579-2584, (1991).

[4] **R. Clift, J. R. Grace and M. E. Weber**, *Bubbles, drops and particles.* Academic Press, New York, (1978).

[5] **M. Sussman, P. Smereka, and S. Osher**, A level set approach for computing solutions to incompressible two-phase flow, *J. Comput. Phys.*, **114**: 146-159, (1994).

[6] **M. Sussman, A. S. Almgren, J. B. Bell, P.Colella, and L. H. Howell**, Welcome ML. An adaptive level set approach for incompressible two-phase flows, *J. Comput. Phys.*, **48**: 81-124, (1999).

[7] **J. A. Sethian**, Level Set Methods, Cambridge, UK: Cambridge Univ. Press; (1996).

[8] **Y. C. Chang, T. Y. Hou, B. Merriman, and S. Osher**, A level set formulation of Eulerian interface capturing methods for incompressible fluid flows, *J. Comput. Phys.* **124**: 449-464, (1996).

[9] **M. Sussman and P. Smereka**, Axi-symmetric free boundary problems, *J. Fluid Mech.*, **341**: 269-294, (1997).

[10] **M. Sussman and E. Fatemi**, An efficient interface-preserving level set redistancing algorithm and its application to interfacial incompressible fluid flow, *SIAM J. Sci. Comput.*, **20**: 1165-1191, (1999).

[11] **R. P. Fedkiw and S. Osher**, Level-set methods: An overview and some recent results. *J. Comput. Phys.*, **169**: 463, (2001).

[12] **M. Ida**, An improved unified solver for compressible and incompressible fluids in-

volving free surfaces: Part I. Convection, *Comput. Phys. Commun.*, **132**: 44-65, 2000.

[13] **W. J. Rider and D. B. Kothe**, Stretching and tearing interface tracking methods, *http://laws.lanl.gov/XHM/personnel/wjr/Web_papers/pubs.html*; (1995).

[14] **J. E. Welch , F. H. Harlow, J. P. Shannon and B.J. Daly**, The MAC method: A computing technique for solving viscous incompressible transient fluid flow problems involving free surfaces, *Report LA-3425. Emeryville, CA*: Los Alamos Scientific Laboratory; (1965).

[15] **S. Scardovelli and S. Zaleski**, Direct numerical simulation of free-surface and interfacial flow, *Annu. Rev. Fluid Dyn.*, **31**: 567-603, (1999).

[16] **C. W. Hirt and B. D. Nichols**, Volume of fluid (VOF) method for the dynamics of free boundaries, *J. Comput. Phys.*, **39**: 201, (1981).

[17] **D. L. Youngs**, Time-dependent multi-material flow with large fluid distortion. In: Morton KW, Bianes MJ, eds, *Numerical Methods for Fluid Dynamics*, New York, NY: Academic Press; 273-285, (1982).

[18] **M. Rudman**, Volume-tracking methods for interfacial flow calculations, *Int. J. Numer. Methods Fluids*, **24**: 671-691, (1997).

[19] **W. J. Rider and D. B. Kothe**, Reconstructing volume tracking, *J. Comput. Phys.*, **141**: 112-152, (1998).

[20] **S. Popinet and S. Zaleski**, A front-tracking algorithm for accurate representation of surface tension, *Int. J. Numer. Methods Fluids*, **30**: 775-793, (1999).

[21] **M. Bussman, J. Mostaghimi and S. Chandra**, On a three-dimensional volume tracking model of droplet impact, *Phys. Fluids*, **11**: 1406- 1417, (1999).

[22] **W. F. Noh and P. R. Woodward**, SLIC (Simple Line Interface Calculation) method. In: van Vooren AI, Zandbergen PJ, eds, *Lecture Notes in Physics*, **59**, Berlin: Springer-Verlag: 330, (1976).

[23] **M. Sint Annaland van, N. G. Deen and J. A. M. Kuipers**, Numerical simulation of gas bubbles behaviour using a three-dimensional volume of fluid method, *Chem. Eng. Sci.*, **60**: 2999-3011, (2005).

[24] **A. J. C. Ladd**, Numerical simulations of particulate suspensions via a discretised Boltzmann equation. Part 1. Theoretical foundation, *J. Fluid. Mech.*, **271**: 285-309, (1994).

[25] **A. J. C. Ladd**, Numerical simulations of particulate suspensions via a discretised Boltzmann equation. Part 2. Numerical results, *J. Fluid. Mech.*, **271**: 311-339, (1994).

[26] **K. Sankaranarayanan, X. Shah, I. G. Kevrekidis and S. Sundaresan** , Analysis of drag and added mass forces in bubbly suspensions using an implicit formulation of the lattice Boltzmann method, *J. Fluid. Mech.*, **452**: 61-96, (2002).

[27] **K. Sankaranarayanan and S. Sundaresan**, Lift force in bubble suspensions, *Chem. Eng. Sci.*, **57**: 3521-3542, (2002).

[28] **S. O. Unverdi and G. Tryggvason**, A front-tracking method for viscous, incompressible multi-fluid flows, *J. Comput. Phy.* **100** : 25-37, (1992).

[29] **A. Esmaeeli and G. Tryggvason**, Direct numerical simulation of bubble flows. Part I. Low Reynolds number arrays, *J. Fluid. Mech.*, **377**: 313-345, (1998).

[30] **A. Esmaeeli and G. Tryggvason**, Direct numerical simulation of bubble flows. Part II. Moderate Reynolds number arrays, *J. Fluid. Mech.*, **385**: 325-358, (1998).

[31] **G. Tryggvasson, B. Bunner, A. Esmaeeli**, A front tracking method for the computations of multiphase flow, *J. Comput. Phys.*, **169**: 708-759, (2001).

[32] **B. DeBar**, Fundamentals of the KRAKEN code, *Technical Report*, **UCIR-760**, LLNL, (1974).

[33] **J.D. Ramshaw, J.A. Trapp**, A numerical technique for low speed homogeneous two-phase flows with sharp interface, *J. Comput. Phys.*, **21**: 438-453, (1976).

[34] **C.S. Peskin**, Numerical analysis of blood flow in the heart, *J. Comput. Phys.*, **25**: 220-252, (1977).

[35] **B.D. Nichols, C.W. Hirt, R.S. Hotchkiss**, SOLA-VOF: a solution algorithm for transient fluid flow with multiple free boundaries, *Los Alamos Scientific Laboratory Report*, **LA-8355**, (1980).

[36] **D.L. Youngs**, An interface tracking method for a 3D Eulerian hydrodynamics code, *Technical report*, **44/92/35**, AWRE, (1984).

[37] **S.T. Zaleski**, Full multi-dimensional flux corrected transport algorithm that works, *J. Comput. Phys.*, **31**: 335-362, (1979).

[38] **A.J. Chorin**, Flame advection and propagation algorithms, *J. Comput. Phys.*, **35**: 1, (1980).

[39] **N. Ashgriz, J.Y. Poo**, FLAIRflux line-segment model for advection and interface reconstruction, *J. Comput. Phys.*, **93**: 449, (1991).

[40] **E.G. Puckett, A.S. Almgren, J.B. Bell, D.L. Marcus, W.J. Rider**, A high-order projection method for tracking fluid interface in variable density incompressible flow, *J. Comput. Phys.*, **130**: 269-282, (1997).

[41] **D.J.E. Harvie, D.F. Fletcher**, A new volume of fluid advection algorithm: the stream scheme, *J. Comput. Phys.*, **162**: 1-32, (2000).

[42] **W.J. Rider, D.B. Kothe**, Stretching and tearing interface tracking methods, in: *12th AIAA CFD Conference*, San Diego, USA, (1995).

[43] **V. Maronnier, M. Picasso, J. Rappaz**, Numerical simulation of free surface flows, *J. Comput. Phys.*, **155**: 439-455, (1999).

[44] **L. Duchemin, S. Popinet, C. Josserand, S. Zaleski**, Jet formation in bubbles bursting at a free surface, Available from *¡http://www.lmm.jussieu.fr/ zaleski/zaleski.html¿*, (2002).

[45] **J. Zhang, Y. Li, L.-S. Fan**, Discrete phase simulation of gasliquidsolid fluidization systems: single bubble rising behaviour, *Powder Technol.*, **113**: 310-326, (2000).

[46] **Y. Li, G.Q. Yang, J.P. Zhang, L.-S. Fan**, Numerical studies of bubble formation dynamics in gasliquidsolid fluidization at high pressure, *Powder Technol.*, **116**: 246-260, (2001).

[47] **G. Černe, S. Petelin, I. Tiselj**, Coupling of the interface tracking and the two-fluid models for the simulation of incompressible two-phase flow, *J. Comput. Phys.*, **171**: 776-804, (2001).

[48] **S.W.J. Welch, J. Wilson**, A volume of fluid based method for fluid flows with phase change, *J. Comput. Phys.*, **160**: 662-682, (2000).

[49] **Y.F. Zhang, W.K. Liu, H.P. Wang**, Cast filling simulation of thin-walled cavities, *Comput. Methods Appl. Mech. Eng.*, **128**: 199-230, (1995).

[50] **X.Y. Wang, H. Zhang, L.L. Zheng, S. Sampath**, An integrated model for interaction between melt flow and non-equilibrium solidification in thermal spraying, *Int. J. Heat Mass Transfer*, **45**: 2289-2301, (2002).

[51] **W. Sussman, E.G. Puckett**, A coupled level set and volume of fluid method for computing 3d and axisymmetric incompressible two-phase flows, UCD, unpublished report.

[52] **J.M. Hyman**, Numerical methods for tracking interfaces, *Physica D*, **12**: 396-407, (1984).

[53] **D.J. Benson**, Volume of fluid interface reconstruction methods for multi-material problems, *Annu. Rev. Fluid Mech.*, **55**: 151-165, (2002).

[54] **W.T. Tsai, D.K.P. Yue**, Computation of nonlinear freesurface flows, *Annu. Rev. Fluid Mech.*, **28**: 249-278, (1996).

[55] **D.B. Kothe, W.J. Rider**, Comments on modelling interface flows with volume-of-fluid methods, *Los Alamos National Laboratory*, **LA-UR-94-3384**, (1995).

[56] **G. Černe, S. Petelin, I. Tiselj**, Numerical errors of the volume-of-fluid interface tracking algorithm, *Int. J. Numer. Methods Fluids*, **38**: 329-350, (2002).

[57] **P. Colella, L.F. Henderson, E.G. Puckett**, A numerical study of shock wave refractions at an interface, in: T. Pulliam (Ed.), *Proceedings of the AIAA 9th Computational Fluid Dynamics Conference*, 426, (1989).

[58] **I. Ginzburg, G. Wittum**, Two-phase flows on interface refined grids modelled with VOF, staggered finite volumes, and spline interpolants, *J. Comput. Phys.*, **66**: 302-335, (2001).

[59] **B.T. Helenbrook, L. Martinelli, C.K. Law**, A numerical method for solving incompressible flow problems with a surface of discontinuity, *J. Comput. Phys.*, **148**: 366-396, (1999).

[60] **J.U. Brackbill, D.B. Kothe, C. Zemach**, A continuum method for modeling surface tension, *J. Comput. Phys.*, **100**: 335-354, (1992).

[61] **S. Guignard, R. Marcer, V. Rey, C. Kharif, P. Fraunie**, Solitary wave breaking on sloping beaches: 2D two phase flow numerical simulation by SL-VOF method, *Eur. J. Mech. B/Fluids*, **20**: 57-74, (2001).

[62] **P. Brufau, P. Garcia-Navarro**, Two-dimensional dam break flow simulation, *Int. J. Numer. Methods Fluids*, **33**: 35-57, (2000).

[63] **J.E. Park, M.A. Rezvani**, In-tank fluid sloshing impact effects during earthquakes: a preliminary computational simulation in fluid-sloshing and fluid-structure, in: *ASME Pressure Vessels and Piping Conference*, **PVP-314**: 73-78, (1995).

[64] **R.A. Ibrahim, V.N. Pilipchuk**, Recent advances in liquid sloshing dynamics, *Appl. Mech. Rev.*, **54**: 133-199, (2001).

[65] **D. Lakehal, M. Meier, M. Fulgosi**, Interface tracking towards the direct simulation of heat and mass transfer in multiphase flow, *Int. J. Heat Fluid Flow*, **23**: 242-257, (2002).

[66] **G.J. Storr, M. Behnia**, Comparisons between experimental and numerical simulation using a free surface technique of free-falling liquid jets, *Exper. Therm. Fluid Sci.*, **22**: 79-91, (2000).

[67] **T. Iwasaki, K. Nishimura, M. Tanaka, Y. Hagiwara**, Direct numerical simulation of turbulent Couette flow with immiscible droplets, *Int. J. Heat Fluid Flow*, **22**: 332 342, (2001).

[68] **H. Tang, L.C. Wrobel, Z. Fan**, Numerical evaluation of immiscible metallic ZnPb binary alloys in shear-induced turbulent flow, in: *1st International Conference on Multiscale Material Modelling*, London, June, (2002).

[69] **H. Tang, L.C. Wrobel, Z. Fan**, Numerical evaluations of immiscible metallic ZnPb alloys in shear-induced turbulent flow, *Mater. Sci. Engng. A*, (in press).

[70] **J. Li, Y.Y. Renardy, M. Renardy**, Numerical simulation of breakup of a viscous drop in shear flow through a volumeof- fluid method, *Phys. Fluids*, **12**: 269-282, (2000).

[71] **P. Gueyffier, A. Nadim, R. Scardovelli and S. Zaleski**, Volume-of-fluid interface tracking with smoothed surface stress methods for three-dimensional flow, *J. Comp. Phys.*, **152**: 423-456, (1999).

[72] **D. B. Kothe, R. C. Mjolsness and M. D. Torrey**, RIPPLE: A Computor Program for Incompressible Flows with Free Surfaces, Technical Report LA-12007-MS, Los Almos National Laboratory, April, (1991).

[73] **S. Popinet and S. Zaleski**, A front-tracking algorithm for accurate representation of surface tension, *Int. J. Num. Methods in Fluids*, **30**: 775-793, (1999).

[74] **A. V. Coward, Y. Y. Renardy, M. Renardy, and J. R. Richards**, Temporal evolution of periodic disturbances in two-layer Couette flow, *J. Comput. Phys.* **132**, 346 (1997).

[75] **F. Mashayek and N. Ashgriz**, A hybrid finite-element-volume tracking model for simulating free surface flows and interfaces, *Int. J. Num. Methods in Fluids*, **20**: 1363, (1995).

[76] **D. M. Gao**, A three-dimensional finite element-volume tracking model for mould filing in casting process, *Int. J. Num. Methods in Fluids*, **29**: 877, (1999).

[77] **D. Bhaga and M. E. Weber**, Bubbles in viscous liquids; shapes, wakes and velocities, *J. Fluid Mech.* **105**, 61-85, (1981).

[78] **J. Mercier, A. Lyrio and R. Forslund**, Three dimensional study of the nonrectilinear trajectory of air bubble rising in water, *Trans. ASME, J Appl. Mech*, **40**: 650-654, (1973).

[79] **P.G. Saffman**, On the rise of small air bubbles in water, *J. Fluid Mech.*, **1**: 249-275, (1956).

[80] **K. Lünde and R. Perkins**, Observations on wakes behind spheroidal bubbles and particles, *Proc. ASME Fluids Eng. Div. Summer Meeting*, Vancouver, Canada, 97-3530, (1997).

[81] **T. A. Johnson and V.C. Patel**, Flow past a sphere up to a Reynolds number of 300, *J. Fluid Mech.*, **378**: 19-70, (1999).

[82] **R. A. Hartunian and W. R. Sears**, On the instability of small gas bubbles moving uniformly in various liquids, *J. Fluid Mech.*, **3**: 27-47, (1957).

[83] **C. Brücker,** , Structure and dynamics of the wake of bubbles and its relevance for bubble interaction, *J. American Institute of Physics*, **11**: 1781-1796, (1999).

[84] **R. Bel Fdhila and P. C. Duineveld** , The effect of surfactant on the rise of a spherical bubble at high Reynolds and Peclet numbers, *Phys. Fluids*, **8**: 310-321, (1996).

[85] **Y. M. C. Delauré, V. S. S. Chan and D. B. Murray**, A simultaneous PIV and heat tarnsfer study of bubble interaction with free convection flow, *Experimental Thermal and Fluid Science*, **27**, 911-926, (2003).

[86] **C. W. Stewart**, Bubble interactions in low viscosity fluids, *Int. J. Multiphase Flow*, **21(6)**: 1037-1046, (1995).

[87] **J. R. Grace**, Shapes and velocities of bubbles rising in infinite liquids, *Trans. IChemE.* **51**, 116-120, (1973).

[88] **G. Ryskin and L. G. Leal**, Numerical solution of free-boundary problems in fluid mechanis. Part 1, Part 2,Part 3, *J. Fluid Mech.* **148**, 1-43, (1984).

[89] **L. Chen, S. V. Garimella, J. A. Reizes and E. Leonardi**, The development of a bubble rising in a viscous liquid, *J. Fluid Mech.* **387**, 61-96, (1999).

[90] **G. Son**, A numerical method for bubble motion with phase change, *Numer. Heat Transfer B*, **39**: 509-523, (2001).

[91] **M. Ohta, E. Iwasaki, E. Obata and Y. Yoshida**, A numerical study of the motion of a spherical drop rising in shear-thinning fluid systems, *J. Non-Newtonian Fluid Mech.*, **116**: 95-111, (2003).

[92] **M. Ohta, S. Haranaka, Y. Yoshida and M. Sussman**, Three-dimensional numerical simulations of the motion of a gas bubble rising in viscous liquids, *J. Chem. Eng.*, **37**: 968-975, (2004).

[93] **M. Wu, M. Gharib**, Experimental studies on the shape and path of small air bubbles rising in clean water, *Phys. Fluids*, **14**: 49-52, (2002).

[94] **A. Tomiyama, G.P. Celata, S. Hosokawa and S. Yoshida**, Terminal velocity of single bubbles in surface tension force dominant regime, *Int. J. Multiphase Flow*, **28**: 1497-1519, (2002).

[95] **B. Yang, A. Prosperettia and S. Takagi**, The transient rise of a bubble subject to shape or volume changes, *Phys. Fluids*, **15**: 2640-2648, (2003).

[96] **B. G. M. van Wachem and J. C. Schouten**, Experimental validation of 3-D lagrangian VOF model: bubble shape and rise velocity, *AIChe J.* **48**, 2744-2753, (2002).

[97] **F. Raymond and J. M. Rosant**, A numerical and experimental study of the terminal velocity and shape of the bubbles in viscous liquids, *Chem. Engg. Sci.* **55**, 943-955, (2000).

[98] **S. D. Houston and K. Cornwell**, Heat Transfer to Sliding Bubble on a Tube Under Evaporation and Non-Evaporation Conditions, *Int. J. Heat Mass Transfer*, **39**: 211214, (1996).

[99] **C. C. Maneri, and N. Zuber**, An experimental study of plane bubbles rising at inclination, *Int. J. Multiphase Flow*, **1**: 623-645, (1974).

[100] **T. Maxworthy**, Bubble rise under an inclined plate, *J. Fluid Mech.*, **220**, 650-674, (1991).

[101] **A. J. Addlessee and K. Cornwell**, Liquid film thickness above a bubble rising under an inclined plate, *Chem. Eng. Res. Design*, **75**: 663-667, (1997).

[102] **K. Cornwell and R. B. Schller**, A Study of Boiling Outside a Tube Bundle Using High Speed Photography, *Int. J. Heat Mass Transfer*, **25**: 683690, (1982).

[103] **K. Cornwell and I. A. Grant**, Heat transfer to bubbles under a horizontal tube, *Int. J. Heat Mass Transfer*, **41**: 1189-1197, (1998).

[104] **G. E. Thorncroft, J. F. Klausner and R. Mei**, Suppression of flow boiling nucleation, *J. Heat Transfer*, **119**: 517-523, (1997).

[105] **G. E. Thorncroft and J. F. Klausner**, The Influence of Vapor Bubble Sliding on Forced Convection Boiling Heat Transfer, *J. Heat Transfer*, **121**: 73-79, (1999).

[106] **Y. Yan, D.B.R. Kenning and K. Cornwell**, Sliding and sticking vapor bubbles under inclined plane ad curved surfaces, *Int. J. of Refrigeration*, **20, No.8**: 583-591, (1997).

[107] **D. B. R. Kenning, O. E. Bustenes and Y. Yan**, Heat transfer to a sliding vapor bubble, *Proc. of Boiling 2000: Phenomena and Emerging Applications*, Girdwood, Alaska, April 30-May 5, 253-27, (2000).

[108] **B. B. Bayazit, D. K. Hollingsworth and L. C. Witte**, Heat Transfer Enhancement Caused by Sliding Bubbles, *J. Heat Transfer*, **125**: 503 509, (2003).

[109] **D. Qiu and V. K. Dhir**, Experimental Study of Flow Pattern and Heat Transfer Associated With a Bubble Sliding on Downward Facing Inclined Surfaces, *Exp. Therm. Fluid Sci.*, **26**: 605616, (2002).

[110] **R. I. Isa** , Solution of Implicitly Discretised Fluid Flow Equations by Operator-Splitting, *J. Comput. Phys.*, **62**: 40-65, (1985).

[111] **S. V. Patankar**, *Numerical Heat Transfer and Fluid Flow. Series in computational methods in mechanics and thermal sciences*, Taylor and Francis Pubs, (1980).

[112] **H. K. Versteeg and W. Malalasekera**, *An introduction to Computational Fluid Dynamics - The Finite Volume Method*, Pearson, Prentice Hall, (1995).

[113] **C. de Boor**, *A Practical Guide to splines*, Springer-verlag, New York, (1967).

[114] **G. Son**, Numerical Study on a Sliding Bubble During Nucleate Boiling, *KSME Int. J.*, **15**: 931940, (2001).

[115] **U. Ghia, K. N. Ghia and C. T. Shin**, High-Re Solutions for Incompressible Flow Using the Navier-Stokes Equations and a Multigrid Method, *J. Comput. Phys.*, **18**: 387-411, (1982).

[116] **T. Gjesdal and M. E. H. Lossius**, Comparison of pressure correction smoothers for multigrid solutions of incompressible flow, *Int. J. Num. Meth. Fluids*, **25**: 393-405, (1997).

[117] **G. de Vahl Davcis**, Natural Convection of air in a square cavity: a bench-mark numerical solutions, *Int. J. Numer. Methods in Fluids*, **3**: 249-264, (1983).

[118] **J. H. Hortmann, M. Peric and G. Scheuerer**, Finite Volume Multigrid prediction of Laminar Natural Convection: Bench-Mark Solutions, *Int. J. Numer. Methods in Fluids*, **11**: 189-207, (1990).

[119] **S. L. Braga and R. Viskanta**, Transient Natural Convection of Water near its Density Extremum in a Rectangular Cavity, *Int. J. Heat and Mass Transfer*, **35**: No.4, 861-875, (1992).

[120] **M. W. McDonough and A. Faghri**, Experimental and Numerical Analyses of the Natural Convection of Water through its Density Maximum in a Rectangular Enclosure, *Int. J. Heat and Mass Transfer*, **37**: No.5, 783-801, (1994).

[121] **T. Nishimura, A. Wake, and E. Fukumori**, Natural Convection of Water near its Density Extremum for a Wide Range of Rayleigh Numbers, *Numerical Heat Transfer, A*, **27**: 433-449, (1995).

[122] **J. Banaszek, Y. Jaluria, T. A. Kowalewski, and M. Rebow**, Semi-implicit FEM Analysis of Natural Convection of Freezing Water, *Numerical Heat Transfer, A*, **26**: 449-472, (1999).

[123] **C. J. Ho and F. J. Tu**, Visualization and prediction of Natural Convection of Water Near its Density Maximum in a Tall Rectangular Enclosure at High Rayleigh Numbers, *J. Heat Transfer*, **123**: 84-95, (2001).

[124] **P. Kandaswamy, and K. Kumar**, Buoyancy-Driven Nonlinear Convection in a Square Cavity in the presence of a Magnetic field, *Acta Mechanica*, **136**: 29-40, (1999).

[125] **A. Pantokratoras**, Laminar Natural Convection in Water near the Density Extremum along a vertical plate with sinusoidal surface temperature variation, *Acta Mechanica*, **172**: 211-218, (2004).

[126] **W. Tong and J. N. Koster**, Density Inversion Effect on Transient Natural Convection in a Tall Rectangular Enclosure, *Int. J. Heat and Mass Transfer*, **37**: 927-938, (1994).

[127] **P. Kandaswamy, and K. Kumar**, Buoyancy-Driven Convection of Water Near its Density Maximum with partially active vertical walls, *Int. J. Heat and Mass

Transfer, **50**: 942-948, (2007).

[128] **D. Y. Shang, B. X. Wang, Y. Wang and Y. Quan**, Study on liquid laminar free convection with consideration of variable thermophysical properties, *Int. J. Heat and Mass Transfer*, **36**: 3411, (1993).

[129] **Flow Science Inc., Santra Fe, NM.**

[130] **D. Lörsatd and L. Fuchs**, Higher-order surface tension VOF model for 3D bubble flows with high density ratio, *J. Comput. Phys.*, **200**: 153-176, (2004).

[131] **J. G. Hnat and J. D. Buckmater**, Spherical cap bubbles and skirt formation, *Phys. Fluids*, **19**: 182-194, (1976).

[132] **D. S. Dandy and G. L. Leal**, Buouancy driven motion of a deformable drop through a quiscent liquid at intermediate Reynolds numbers, *J. Fluid Mech.* **208**, 161-192, (1989).

[133] **T. Ye and J. N. Chung**, A fixed-grid, sharp-interface method for bubble dynamics and phase change, *J. Comput. Phys.*, **174**: 781-815, (2001).

[134] **M. Ishii and N. Zuber**, Drag coefficient and relative velocity in bubble droplet or particulate flow, *AIChE J.* **25**, 843-855, (1979).

[135] **Brian G. Donnelly, Darina B. Murray and Tadhg O′Donovan**, Enhancement of heat transfer from a submerged inclined surface due to sliding bubble motion, *Proceedings of ASME-JSME Thermal Engineering Summer Heat Transfer Conferrence*, Vancouver, British Columbia, Canada, July 8-12 (2007).

LIST OF PAPERS SUBMITTED BASED ON THIS THESIS

1. **S. Senthil Kumar and Y. Delauré**, Convective Heat Transfer Modelling of a Multi-Fluid Flow using a VOF Method, *The Proceeding of the 9th ICFD Conference on Numerical Methods for Fluid Dynamics*, 26-29 March 2007, University of Reading, UK.

2. **S. Senthil Kumar and Y. Delauré**, A SIMPLE VOF-CSF Multi-Fluid Flow Solver, *The Proceeding of European Conference on Computational Fluid Dynamics*, ECCOMAS CFD 2006, 5-8 September 2006, TU Delft, The Netherlands.

3. **Y. Delauré, S. Senthil Kumar and S. Kumar**, A Multigrid Navier-Stokes Solver for Unsteady Incompressible Multi-Fluid Flow Modelling, *The Proceeding of Fifth International Conference on Computational and Experimental Engineering and Sciences*, ICCES-05, 2005, Chennai, India.